



University of Kentucky  
UKnowledge

---

Theses and Dissertations--Chemical and  
Materials Engineering

Chemical and Materials Engineering

---

2014

## Structure and Catalytic Properties of Ultra-Small Ceria Nanoparticles

Xing Huang

University of Kentucky, [jerry.x.huang@uky.edu](mailto:jerry.x.huang@uky.edu)

[Right click to open a feedback form in a new tab to let us know how this document benefits you.](#)

---

### Recommended Citation

Huang, Xing, "Structure and Catalytic Properties of Ultra-Small Ceria Nanoparticles" (2014). *Theses and Dissertations--Chemical and Materials Engineering*. 25.  
[https://uknowledge.uky.edu/cme\\_etds/25](https://uknowledge.uky.edu/cme_etds/25)

This Doctoral Dissertation is brought to you for free and open access by the Chemical and Materials Engineering at UKnowledge. It has been accepted for inclusion in Theses and Dissertations--Chemical and Materials Engineering by an authorized administrator of UKnowledge. For more information, please contact [UKnowledge@lsv.uky.edu](mailto:UKnowledge@lsv.uky.edu).

## **STUDENT AGREEMENT:**

I represent that my thesis or dissertation and abstract are my original work. Proper attribution has been given to all outside sources. I understand that I am solely responsible for obtaining any needed copyright permissions. I have obtained needed written permission statement(s) from the owner(s) of each third-party copyrighted matter to be included in my work, allowing electronic distribution (if such use is not permitted by the fair use doctrine) which will be submitted to UKnowledge as Additional File.

I hereby grant to The University of Kentucky and its agents the irrevocable, non-exclusive, and royalty-free license to archive and make accessible my work in whole or in part in all forms of media, now or hereafter known. I agree that the document mentioned above may be made available immediately for worldwide access unless an embargo applies.

I retain all other ownership rights to the copyright of my work. I also retain the right to use in future works (such as articles or books) all or part of my work. I understand that I am free to register the copyright to my work.

## **REVIEW, APPROVAL AND ACCEPTANCE**

The document mentioned above has been reviewed and accepted by the student's advisor, on behalf of the advisory committee, and by the Director of Graduate Studies (DGS), on behalf of the program; we verify that this is the final, approved version of the student's thesis including all changes required by the advisory committee. The undersigned agree to abide by the statements above.

Xing Huang, Student

Dr. Matthew J. Beck, Major Professor

Dr. Fuqian Yang, Director of Graduate Studies

STRUCTURE AND CATALYTIC PROPERTIES  
OF ULTRA-SMALL CERIA NANOPARTICLES

---

DISSERTATION

---

A dissertation submitted in partial  
fulfillment of the requirements for  
the degree of Doctor of Philosophy  
in the College of Engineering at the  
University of Kentucky

By  
Xing Huang  
Lexington, Kentucky

Director: Dr. Matthew J Beck, Professor of Chemical and Materials Engineering  
Co-Director: Dr. Yang-Tse Cheng, Professor of Chemical and Materials Engineering  
Lexington, Kentucky 2014

Copyright© Xing Huang 2014

## ABSTRACT OF DISSERTATION

### STRUCTURE AND CATALYTIC PROPERTIES OF ULTRA-SMALL CERIA NANOPARTICLES

Cerium dioxide (ceria) is an excellent catalytic material due to its ability to both facilitate oxidation/reduction reactions as well as store/release oxygen as an oxygen buffer. The traditional approach to assess and improve ceria's catalytic behavior focuses on how efficiently O-vacancies can be generated and/or annihilated within the material, and how to extend established understandings of "bulk" ceria to further explain the greatly enhanced catalytic behavior of ultra-small ceria nanoparticles (uCNPs) with sizes less than 10 nm. Here, using density functional theory (DFT) calculations, we reexamine the atomic and electronic structures of uCNPs, especially their surface configurations. A unique picture dissimilar to the traditional point of view emerges from these calculations for the surface structure of uCNPs. uCNPs similar to those obtained by experimental synthesis and applied in catalytic environments exhibit core-shell like structures overall, with under-stoichiometric, reduced CNP "cores" and over-stoichiometric, oxidized surface "shells" constituted by various surface functional groups, e.g.,  $-O_x$  and/or  $-OH$  surface groups. Therefore, their catalytic behavior is dominated by surface chemistry rather than O-vacancies. Based on this finding, reaction pathways of two prevalent catalytic reactions, namely CO oxidation and the water-gas shift reaction over uCNPs are systematically investigated. Combined, these results demonstrate an alternative understanding of the surface structure of uCNPs, and provide new avenues to explore and enhance their catalytic behavior, which is likely applicable to other transition metal oxide nanoparticles with multivalent ions and very small sizes.

KEYWORDS: density functional theory, ceria nanoparticles, surface, catalysis, thermodynamics

Author's signature: Xing Huang

Date: February 20, 2014



STRUCTURE AND CATALYTIC PROPERTIES  
OF ULTRA-SMALL CERIA NANOPARTICLES

By  
Xing Huang

Director of Dissertation: Dr. Matthew J Beck

Co-Director of Dissertation: Dr. Yang-Tse Cheng

Director of Graduate Studies: Dr. Fuqian Yang

Date: February 20, 2014

“What things were gains to me, these I have counted as loss on account of Christ. But moreover I also count all things to be loss on account of the excellency of the knowledge of Christ Jesus my Lord, on account of whom I have suffered the loss of all things and count them as refuse that I may gain Christ.” —Phil.3:7-8

“For it is God who operates in you both the willing and the working for His good pleasure. Do all things without murmurings and reasonings that you may be blameless and guileless, children of God without blemish in the midst of a crooked and perverted generation, among whom you shine as luminaries in the world.”  
—Phil.2:13-16

“And do not be fashioned according to this age, but be transformed by the renewing of the mind that you may prove what the will of God is, that which is good and well pleasing and perfect.” —Rom.12:2

## ACKNOWLEDGMENTS

The following dissertation, while an individual work, benefited from the insights and direction of several people. First, my dissertation advisor, Matthew J Beck, has fully exemplified the high quality scholarship to which I aspire and pursue. He has indeed provided abundant instruction as well as in-depth and invaluable discussions, comments and evaluation at every stage of my doctoral study. Next, I wish to thank the complete Dissertation Committee, respectively: Dr. Eric A. Grulke, Dr. Bruce J. Hinds, Dr. Yang-Tse Cheng, Dr. Gang Cao, and Dr. Kaveh Tagavi. Each has provided constructive guidance and challenged my thinking to improve and shape my dissertation. I also would like to thank Dr. Binghui Wang for his cooperative work.

In addition to the scientific assistance above, I greatly appreciate my parents of their long-lasting supports and encouragements over the past 30 years both materially and spiritually, which leads and motivates me to obtain the PhD degree. Finally, I own significant gratitude to my dear and precious Lord Jesus and His members in the church of Lexington. Without His shepherding and direction, I will not know the meaning of my human life. It is Himself who gives me the controlling vision and sets my destination of my future living.

# TABLE OF CONTENTS

Acknowledgments . . . . .	iii
Table of Contents . . . . .	iv
List of Figures . . . . .	vii
List of Tables . . . . .	xii
Chapter 1 Overview . . . . .	1
1.1 Introduction . . . . .	1
1.2 Cerium oxides, catalysis and O-storage capacity (OSC) . . . . .	2
1.3 Motivation and overview of the entire research work . . . . .	6
Chapter 2 Background . . . . .	9
2.1 Previous experimental techniques to identify $\text{Ce}^{\text{III}}$ cations . . . . .	9
2.2 Computational methods used previously to study bulk ceria, ceria surface and CNPs . . . . .	10
2.2.1 Molecular mechanics calculation . . . . .	10
2.2.2 Embedded cluster method . . . . .	12
2.2.3 DFT electronic structure calculation . . . . .	13
2.3 Previous computational studies on semi-infinite ceria surfaces . . . . .	15
2.4 Previous computational studies on mall ceria clusters and CNPs . . . . .	19
2.4.1 Semi-empirical calculations . . . . .	19
2.4.2 Quantum mechanical calculations of small ceria clusters . . . . .	21
2.4.3 Quantum mechanical calculations of ceria crystallites (nanoparticles) . . . . .	22
2.5 Previous experimental studies on $-\text{OH}$ groups adsorbed at surfaces of CNPs . . . . .	26
2.6 Previous perspective on the catalytic behavior of CNPs to oxidize CO . . . . .	27
2.7 Previous experimental and computational studies of water-gas shift reaction catalyzed by ceria . . . . .	28
2.7.1 Introduction . . . . .	28
2.7.2 The variables influencing the reaction rate <sup>141</sup> . . . . .	29
2.7.3 Former studies of WGS reaction mechanism on ceria-based catalysts . . . . .	30
2.7.3.1 Experimental studies . . . . .	31
2.7.3.2 Computational studies . . . . .	35
2.7.4 Brief summary of previous studies . . . . .	36
2.8 Challenges in computational modeling of ultra-small ceria nanoparticles (uCNPs) . . . . .	37

2.8.1	Problems arising from constructing uCNPs with ideal, stoichiometric, bulk-cut surface configurations . . . . .	37
2.8.2	Challenges to construct realistic, physically-representative uCNPs . . . . .	39
2.9	Brief proposal to address the challenges in studying the surface structure of uCNPs . . . . .	42
Chapter 3	Theoretical backgrounds and computational methods . . . . .	44
3.1	Quantum mechanical calculation methods . . . . .	44
3.1.1	Introduction . . . . .	44
3.1.2	The Schrödinger equation and Hartree-Fock approximation . . . . .	45
3.1.3	Density functional theory (DFT) . . . . .	47
3.1.4	The pseudopotential method . . . . .	49
3.2	Computational settings and and convergence . . . . .	50
3.2.1	Introduction . . . . .	50
3.2.2	Choice of k points . . . . .	51
3.2.3	Choice of cutoff energy . . . . .	52
3.2.4	Choice of exchange-correlation functional . . . . .	53
3.2.5	Choice of Hubbard U correction . . . . .	54
3.2.6	Bader charge analysis . . . . .	54
3.2.7	Nudged elastic band calculation . . . . .	55
3.2.8	Dynamical matrix calculation . . . . .	55
3.2.9	Relaxation convergence criterion . . . . .	56
3.2.10	Calculation precision . . . . .	56
3.2.11	Other calculation settings . . . . .	57
3.3	Thermodynamics of uCNPs . . . . .	58
3.3.1	Introduction . . . . .	58
3.3.2	Excessive energy of formation per Ce atom of uCNPs as a function of size, shape and composition in a pure oxygen environment . . . . .	58
3.3.3	Excessive energy of formation uCNPs with different surface configurations as a function of chemical potentials of O and H atoms in a humid environment . . . . .	61
3.3.4	Activation energy . . . . .	65
3.4	Constructing computational cells containing uCNPs . . . . .	66
3.4.1	Experimentally reported shapes and quantitative atom counts . . . . .	66
3.4.2	Construction of bulk-cut uCNP structures . . . . .	68
3.4.3	Initial placement of surface groups . . . . .	70
Chapter 4	The surface configuration of ultra-small CNPs in a pure oxygen environment . . . . .	71
4.1	Excess energy of formation per Ce atom of uCNPs as a function of oxygen concentration . . . . .	72
4.2	Atomic structures of uCNPs . . . . .	74
4.3	Electronic density of states . . . . .	78
4.4	Infrared spectrum . . . . .	82

4.5	Size-dependent surface terminations . . . . .	88
4.6	Summary . . . . .	88
Chapter 5	Direct oxidation of CO over ultra-small CNPs terminated with $-O_x$ surface groups . . . . .	92
5.1	Catalytic properties of uCNPs terminated with $-O_x$ surface groups . . . . .	92
5.2	Summary . . . . .	97
Chapter 6	The surface configuration of ultra-small CNPs in a humid environment . . . . .	99
6.1	Individual $-O_x$ group at surfaces of uCNPs interacting with H atoms . . . . .	100
6.2	Surface configuration of uCNPs in a humid environment . . . . .	103
6.3	Densities of $-OH$ surface groups bound to cubic uCNPs as a function of particle size . . . . .	108
6.4	Electronic density of states of OH-terminated uCNPs . . . . .	112
6.5	Infrared spectrum . . . . .	116
6.6	Summary . . . . .	124
Chapter 7	Water-gas shift reaction over OH-terminated ultra-small CNPs . . . . .	126
7.1	Catalytic pathway of WGS reaction over pure OH-terminated uCNPs . . . . .	126
7.1.1	Formate mechanism . . . . .	126
7.1.2	Dehydrogenation mechanism . . . . .	134
7.2	Summary . . . . .	137
Chapter 8	Conclusions and future work . . . . .	139
8.1	Concluding results of this research work . . . . .	139
8.2	Future research directions . . . . .	141
8.3	Overall conclusions . . . . .	142
	Appendix: Exemplary input files for DFT calculations performed in this study . . . . .	144
	Bibliography . . . . .	149
	Vita . . . . .	178

## LIST OF FIGURES

1.1	Schematic illustration of the four-step mechanistic hypothesis explaining ceria's excellent catalytic activity. . . . .	4
2.1	Atomic structure of of $\{111\}$ , $\{110\}$ and $\{100\}$ ceria surfaces. Purple balls represent O atoms and yellow balls represent Ce atoms. . . . .	15
2.2	The process of O-vacancy formation in ceria: a neutral O atom is removed, leaving behind an empty O lattice site, and returning electrons to nearby Ce atoms. At right are the calculated electronic density of states (eDOS) for relevant Ce and O bands. Solid lines correspond to the eDOS of fully oxidized bulk $\text{CeO}_2$ , while dashed lines are for partially reduced bulk $\text{CeO}_{2-x}$ . The zero of energy for each system has been set to the Fermi energy. Note the energy shift down of the Ce states. This plot shows that electrons returned to Ce states due to O-vacancy formation (that is, the reduction of ceria) appear in <i>Ce 4f</i> states. . . . .	17
2.3	Three CNPs with different initial structures evolved into final configurations after MD simulation <sup>105</sup> . . . . .	21
2.4	Chemical structures of absorbed intermediates on ceria surfaces <sup>182</sup> . . . . .	34
2.5	Most stable configurations of intermediates on Cu (111) <sup>183</sup> . . . . .	34
2.6	$n(\text{Ce})/n(\text{O})$ as a function of CNP size for Ce-terminated (blue) cubic CNPs and O-terminated (red) cubic CNPs. . . . .	37
2.7	$n(\text{Ce})/n(\text{O})$ as a function of CNP size for Ce-terminated (blue) octahedral CNPs and O-terminated (red) octahedral CNPs. . . . .	39
3.1	Calculated total energy as a function of the number of k points for the primitive cell of $\text{CeO}_2$ . . . . .	51
3.2	Calculated total energy as a function of the cutoff energy for the primitive cell of $\text{CeO}_2$ . . . . .	52
3.3	High resolution TEM images of cubic CNPs. (a) fast Fourier transform (FFT) analysis together with HRTEM image confirm cubic CNPs are single-crystalline and enclosed by $\{200\}$ planes <sup>194</sup> ; (b) interplanar spacing of 0.27 nm corresponds to $\{001\}$ lattice fringe, indicating cubic CNPs are enclosed by $\{100\}$ facets <sup>11</sup> . . . . .	67

3.4	(a) Unit cell of bulk $\text{CeO}_2$ showing cubic fluorite structure; (b) schematic illustration of building the solid atomic assembly of Ce and O atoms by randomly expanding the unit cell of bulk $\text{CeO}_2$ (enclosed by black solid lines) x, y, and z times in three orthonormal directions, respectively; (c) the supercell of cubic CNPs of $\sim 1$ nm for relaxation calculation; (d) zoom-in image of the solid atomic assembly in (c) to show the atomic structure of $\{001\}$ -terminated cubic uCNPs. (e) the supercell of octahedral CNPs of $\sim 1$ nm for relaxation calculation; (f) zoom-in image of the solid atomic assembly in (e) to show the atomic structure of $\{111\}$ -terminated octahedral uCNPs. Yellow balls represent Ce atoms, purple balls represent bulk O atoms, and blue balls represent all possible surface O lattice sites that can be partially or fully occupied by individual O atom. . . . .	69
4.1	Calculated excess energies of formation per Ce atom of various sized and shaped uCNPs. $E_f$ are referenced to the energy of formation of the same sized bulk $\text{CeO}_2$ as a function of $n_O/n_{\text{Ce}}$ in various uCNPs at the corrected chemical potential of O atoms. . . . .	72
4.2	Atomic structures of various shaped uCNPs with reduced, stoichiometric and oxidized chemical compositions. Yellow balls represent Ce atoms while larger sized balls represent O atoms and they are colored according to their type and charge states. . . . .	74
4.3	Calculated projected electronic density of states (eDOS) of some interested atomic orbitals for (a) bulk $\text{CeO}_2$ ; (b) bulk $\text{H-Ce}_2\text{O}_3$ ; (c) $\text{Ce}_{32}\text{O}_{57}$ ; (d) $\text{Ce}_{32}\text{O}_{179}$ ; (e) $\text{Ce}_{44}\text{O}_{152}$ and (f) $\text{Ce}_{40}\text{O}_{152}$ under LDA+U algorithm. . . . .	79
4.4	Calculated projected electronic density states (eDOS) of some interested atomic orbitals for (a) bulk $\text{CeO}_2$ ; (b) bulk $\text{H-Ce}_2\text{O}_3$ ; (c) $\text{Ce}_{32}\text{O}_{57}$ ; (d) $\text{Ce}_{32}\text{O}_{179}$ ; (e) $\text{Ce}_{44}\text{O}_{152}$ and (f) $\text{Ce}_{40}\text{O}_{152}$ under GGA+U algorithm. . . . .	80
4.5	Spatial orientation for diatomic and triatomic $-\text{O}_x$ groups adsorbed at surfaces of uCNPs: (1) $\text{O}_2^-$ laying; (2) $\text{O}_2^{2-}$ bridging; (3) $\text{O}_2$ standing; (4) $\text{O}_3$ laying; (5) $\text{O}_3^-$ bridging and (6) $\text{O}_3^{2-}$ standing. Note that yellow balls represent Ce atoms, while other colored balls represent O atoms within different $-\text{O}_x$ surface groups, and the coloring is consistent with Figure 4.2. . . . .	84
4.6	Ratio of Ce to O atoms in cubic and octahedral CNPs as a function of CNP size. Cubic CNP and octahedral CNP <sup>a</sup> structures are fully oxidized, while octahedral CNP <sup>b</sup> structures exhibit stoichiometric $\{111\}$ facets, but fully coordinated (oxidized) edges and corners. . . . .	87
5.1	Three different situations of an incoming CO molecule attacking the surface of uCNPs. These are zoom-in pictures showing the reaction sites pertaining to partial surface of considered uCNPs. Yellow greenish balls represent Ce atoms, pink balls represent O atoms within considered uCNP structures, light green balls represent C atoms, and blue balls represent O atoms bound to C atoms. Some balls are enlarged to clearly show the atoms actively participating in the CO oxidation process. . . . .	93



6.1	Evolution of the surface configuration of $O_x$ -terminated uCNPs when approached by H atoms. Those cases corresponding to singular H atom interacting with negative charged $-O_x$ surface groups are shown in the parenthesis. . . . .	101
6.2	Phase diagram of ground state surface configurations for a series of considered uCNP structures as a function of $\mu_O$ and $\mu_H$ in a gas phase environment containing $O_2$ gas and $H_2O$ vapor. Warm colors indicate structures terminated solely with $-OH$ surface groups (see atomic structures in Figure 6.3). Cool colors indicate structures terminated with mixed $-OH$ and $-O_x$ surface groups (see atomic structures in Figure 6.4). Black parallel lines indicate the experimentally relevant limits of the partial pressure of $H_2O$ vapor. The white trapezoid $abcd$ indicates the region of experimental conditions most relevant for the synthesis and application of uCNP structures. . . . .	104
6.3	The relaxed, ground-state atomic structures of three OH-terminated cubic uCNPs with different densities of $-OH$ surface groups. Yellow balls represent Ce atoms, purple balls represent O atoms, and green balls represent H atoms. For increasing densities of $-OH$ surface groups, $-OH$ groups are first adsorbed on uCNP $\{001\}$ facets, then edges and corners. . . . .	105
6.4	The relaxed, ground-state atomic structures of three cubic uCNPs terminated with mixed $-OH$ and $-O_x$ surface groups. Yellow balls represent Ce atoms, purple balls represent either bulk O atoms or O atoms in $-OH$ surface groups, green balls represent H atoms, blue balls represent O atoms in $-O_2^-$ surface groups, and pink balls represent O atoms in $-O_3^-$ surface groups. For increasing numbers of adsorbed $-O_x$ surface groups, $-O_x$ groups are first adsorbed on uCNP corners, then edges and $\{001\}$ facets. . . . .	106
6.5	Density of adsorbed $-OH$ surface groups as a function of cubic CNP size calculated from the scaling relationship invoking full oxidation of Ce atoms (see text for details). Yellow, blue and cyan curves are plotted for cubic CNPs of surface configurations consistent with the $Ce_{32}O_{101}H_{74}$ , $Ce_{32}O_{125}H_{54}$ and $Ce_{32}O_{120}H_{40}$ structures, respectively. In addition, the yellow curve represents the case where $-OH$ surface groups are the only surface group to balance net positive charges from $Ce^{IV}$ cations, while blue and cyan curves represent the case where both $-OH$ and $-O_x$ surface groups are present. Colors have been selected to match subsequent figure (Figure 6.2). . . . .	109
6.6	Calculated projected electronic density states (eDOS) of some interested atomic orbitals for (a) bulk $CeO_2$ ; (b) $Ce_{32}O_{101}H_{74}$ ; (c) bulk $H-Ce_2O_3$ and (d) $Ce_{32}O_{81}H_{54}$ . . . . .	113
6.7	Calculated IR absorption spectra for $Ce_{32}O_{81}H_{54}$ (a) and $Ce_{32}O_{101}H_{74}$ (b); (c) experimental measured IR absorption spectrum for as-synthesized $\sim 30$ nm CNPs; (d) relaxed atomic structures of $Ce_{32}O_{81}H_{54}$ and $Ce_{32}O_{101}H_{74}$ . . . . .	116

6.8	Schematic illustration of three measurands used to describe the status of a facet –OH group. The green ball represent an O atom as the base of a –OH surface group under consideration, which is leaning towards a nearest –OH surface group adsorbed at edges/corners whose base O atom is colored in purple. Their spatial relationship is determined by the distance between the centers of these two base O atoms, $d$ , the angle between the O-H vector of a considered facet –OH group and the vector normal to the surface ( $n$ ), $\theta$ , and the angle between the O-H vector of this considered facet –OH group and the direction lining up the centers of these two base O atoms, $\phi$ .	117
6.9	Calculated IR absorption spectrum of $\text{Ce}_{32}\text{O}_{125}\text{H}_{54}$ within the vibration frequency range of adsorbed $-\text{O}_x$ surface groups: (a) $\text{O}_2^-$ ; (b) $\text{O}_3^-$ ; and (c) combined.	121
6.10	Calculated IR absorption spectrum of $\text{Ce}_{32}\text{O}_{120}\text{H}_{40}$ within the vibration frequency range of adsorbed $-\text{O}_x$ surface groups: (a) $\text{O}_2^-$ ; (b) $\text{O}_2^{2-}$ ; (c) $\text{O}_3^-$ ; (d) $\text{O}_3^{2-}$ and (e) combined.	122
7.1	Three possible WGS reaction pathways realized via OH-terminated uC-NPs following formate mechanism. Chemical elements marked with single/double/triple prime symbols represent atoms adsorbed to different surface Ce atoms of OH-terminated uCNPs. Letter “u” stands for “unidentate” and letter “b” stands for “bidentate”.	127
7.2	Key products during WGS reaction along pathway 1 following the formate mechanism. Yellow greenish balls represent Ce atoms, pink balls represent O atoms of the OH-terminated uCNP, cyan balls light green balls represent C atoms, blue balls represent O atoms from the CO molecule, light purple balls represent O atoms from the $\text{H}_2\text{O}$ molecule, and yellow balls represent H atoms from the $\text{H}_2\text{O}$ molecule. Some balls are enlarged to clearly show the atoms actively participating in the WGS reaction. Note that different color is also used to track the movement of interested atoms.	130
7.3	Key products during WGS reaction along pathway 2 following the formate mechanism. Yellow greenish balls represent Ce atoms, pink balls represent O atoms of the OH-terminated uCNP, cyan balls light green balls represent C atoms, blue balls represent O atoms from the CO molecule, light purple balls represent O atoms from the $\text{H}_2\text{O}$ molecule, and yellow balls represent H atoms from the $\text{H}_2\text{O}$ molecule. Some balls are enlarged to clearly show the atoms actively participating in the WGS reaction. Note that different color is also used to track the movement of interested atoms.	132
7.4	Key products during WGS reaction along pathway 3 following the formate mechanism. Yellow greenish balls represent Ce atoms, pink balls represent O atoms of the OH-terminated uCNP, cyan balls light green balls represent C atoms, blue balls represent O atoms from the CO molecule, light purple balls represent O atoms from the $\text{H}_2\text{O}$ molecule, and yellow balls represent H atoms from the $\text{H}_2\text{O}$ molecule. Some balls are enlarged to clearly show the atoms actively participating in the WGS reaction. Note that different color is also used to track the movement of interested atoms.	133

7.5	The possible WGS reaction pathway realized via OH-terminated uCNPs following dehydrogenation mechanism. Chemical elements marked with single/double prime symbols represent atoms adsorbed to different surface Ce atoms of OH-terminated uCNPs. . . . .	135
7.6	Key products during WGS reaction along the pathway following the dehydrogenation mechanism. Yellow greenish balls represent Ce atoms, pink balls represent O atoms of the OH-terminated uCNP, cyan balls light green balls represent C atoms, blue balls represent O atoms from the CO molecule, light purple balls represent O atoms from the H <sub>2</sub> O molecule, and yellow balls represent H atoms from the H <sub>2</sub> O molecule. Some balls are enlarged to clearly show the atoms actively participating in the WGS reaction. Note that different color is also used to track the movement of interested atoms. . . . .	136

# LIST OF TABLES

3.1	Summary of computationally calculated (Cal.) energies and experimentally measured (Expt.) energies . . . . .	60
4.1	Properties of assigned $-O_x$ surface groups in representative uCNP structures.	75
4.2	Average Bader charge of Ce atoms in cubic uCNPs with different O concentrations obtained from LDA+U calculations ( $U = 5$ eV). . . . .	77
4.3	Comparison of calculated vibration frequencies under IBRION=5 and IRBION=7 settings and assigned vibration modes to $-O_x$ surface groups in a representative oxidized uCNP structure, $Ce_{32}O_{101}$ . . . . .	84
4.4	Comparison of calculated vibration frequencies under IBRION=5 settings and assigned vibration modes to $-O_x$ surface groups in three representative oxidized uCNP structures, cubic shaped $Ce_{32}O_{179}$ , octahedral shaped $Ce_{44}O_{152}$ , and cuboctahedral shaped $Ce_{40}O_{152}$ obtained via LDA+U calculations ( $U=5$ eV). . . . .	91
5.1	The information on the relaxed structure of $\sim 1$ nm cubic uCNPs interacting with an incoming CO molecule . . . . .	95
6.1	Summary of required measurands used to describing two neighboring facet $-OH$ groups . . . . .	119
6.2	Comparison of calculated vibration frequencies under IBRION=5 and IRBION=7 settings and assigned vibration modes to $-O_x$ surface groups in two representative cubic uCNP structures terminated with mixed $-OH$ and $-O_x$ surface groups. . . . .	120

## Chapter 1 Overview

### 1.1 Introduction

Catalysts are essential engineering materials used to promote specific chemical reactions in a host of applications and processes. Typical catalysts influence target reactions by enhancing the binding or localization of reactant molecules at catalyst surfaces while lowering reaction barriers and allowing desorption of product molecules. Ideal catalysts have high activity, specificity and stability, as well as low contamination rates under operating conditions. Various pure metals and, increasingly, metal oxides are widely applied as catalysts. Reversible reduction/oxidation catalysts have particular technological value in energy, environmental and biomedical applications. Cerium dioxide ( $\text{CeO}_2$ , ceria) has served as an excellent reduction/oxidation catalyst for 30 years. In fact, ceria has been shown to have wide applications in environmental remediation, energy generation and biomedicine, in addition to other important applications in microelectronics, optical films, gas sensors, and polishing materials<sup>1-13</sup>.

The effects of a catalyst on a chemical reaction are necessarily surface effects. That is, the physical and chemical action of a catalyst occurs at the interface between the catalyst and its environment—namely, at the catalyst’s surfaces. Enhancing or tailoring a catalyst’s behavior, therefore, first requires an understanding of the structure and properties of catalyst surfaces. In ceria or ceria-supported catalysis, the discovery that *bulk* cubic fluorite  $\text{CeO}_2$  can be reduced through the formation of O-vacancies and reversibly (re-)oxidized via the annihilation of O-vacancies has led to the development of a general understanding that the presence of (or potential to form) O-vacancies on ideal, bulk-terminated  $\text{CeO}_2$  surfaces drives the catalytic activity of ceria in reduction/oxidation reactions. In fact, explanations for the mechanism of ceria catalysis have, to date, assumed ideal, bulk-like  $\text{CeO}_2$  surface structures, or minor

perturbations thereof. But does this picture apply to *ultra-small ceria nanoparticle* (uNCPs)? Do uNCPs actually exhibit ideal, bulk-like surface configurations? Are the redox properties, or catalytic behavior in general, of uNCPs simply dominated by O-vacancies? Is tuning the thermodynamics and kinetics of O-vacancies within uNCPs the correct and unique means that can be resorted to for realizing the functionalities of uNCPs targeted at multiple applications, especially in energy and biomedical related fields?

## 1.2 Cerium oxides, catalysis and O-storage capacity (OSC)

Cerium is the most abundant rare-earth element, and easily donates three or four electrons to oxygen. Ce forms two stable, distinct bulk stoichiometric cerium oxides:  $\text{H-Ce}_2\text{O}_3$  (hexagonal, space group  $\text{P}\bar{3}\text{m1}$ ) and  $\text{CeO}_2$  (cubic fluorite, space group  $\text{Fm}\bar{3}\text{m}$ ). In  $\text{CeO}_2$ , referred to as ceria, Ce cations occupy every site of a face-centered cubic (FCC) unit cell and O anions occupy all octahedral interstitial sites. Each Ce cation is assigned a formal charge of 4+ ( $\text{Ce}^{\text{IV}}$ ) and is coordinated to eight nearest-neighbor O anions with formal charges of 2- ( $\text{O}^{\text{II}}$ ). Each  $\text{O}^{\text{II}}$  anion is coordinated to four nearest-neighbor  $\text{Ce}^{\text{IV}}$  cations. In  $\text{CeO}_2$ , the four  $\text{Ce}^{\text{IV}}$  valance states ( $4\text{f}^1$ ,  $5\text{d}^1$ , and  $6\text{s}^2$ ), are formally empty, and reducing  $\text{CeO}_2$  (that is, generating  $\text{Ce}^{\text{III}}$  cations) returns electrons to the Ce  $4\text{f}$  band.

The excellent catalytic properties of ceria were first harnessed in the late 1970s when ceria was utilized for the treatment automobile exhaust, serving as a key component in three-way catalysts (TWC)<sup>14,15</sup>. During the same time period, studies on the phase diagram of the cerium oxide system were carried out. It was discovered that bulk ceria (cubic fluorite  $\text{CeO}_2$ ) can be reduced at elevated temperatures to form a range of O-deficient, non-stoichiometric oxides ( $\text{CeO}_{2-x}$ ), referred to collectively as “reduced” ceria. In addition, it was shown that ceria is able to reversibly transform among these various reduced phases<sup>16–18</sup>. Further studies<sup>19–21</sup> directly exploring

these transformations found that bulk  $\text{CeO}_2$  retains a cubic fluorite structure despite removal of 25% of lattice O atoms when subjected to reduction below 900K. While these studies noted an anomalous lattice expansion during reduction, they found that O-vacancy-containing reduced ceria could be completely recovered to stoichiometric  $\text{CeO}_2$  when exposed to an oxidizing environment, even at room temperature.

These discoveries implied that ceria can *store* O by adsorbing it (via the annihilation of O-vacancies) under O-rich conditions, and controllably release it by (re-)forming O-vacancies under O-poor or reducing conditions. The number of  $\text{O}^\text{II}$  anions (per volume or unit mass) that can be reversibly extracted and recovered during a particular reaction (e.g., oxidation or reduction of  $\text{CO}/\text{CO}_2$ ) is quantitatively characterized as the “oxygen storage capacity” (OSC) of a ceria system<sup>22,23</sup>. Hence, ceria has two related, technologically important capabilities: (i) the ability to strongly catalyze redox reactions, and (ii) the ability to serve as a solid state oxygen buffer for redox reactions.

Since the 1970s substantial experimental and computational effort has been expended to understand, control, and ultimately optimize ceria’s natural ability to support and catalyze redox reactions. Over the course of these investigations the experimentally measurable OSC of ceria and ceria-containing systems has become a kind of litmus test for catalytic activity. That is, the realizable potential of a ceria system to form and annihilate O-vacancies during reduction and oxidation has become both the lens through which the general catalytic properties of all ceria-based materials are viewed, and the default basis for understanding all reduction/oxidation mechanisms in such materials. Specifically, the existence of O-vacancy-containing cubic fluorite “reduced ceria” phases and low-barrier reversible transformation paths between them (simply the formation/annihilation of O-vacancies) suggests a straightforward mechanistic hypothesis explaining ceria’s excellent catalytic activity, as schematically illustrated in Figure 1.1. For oxidation this is:

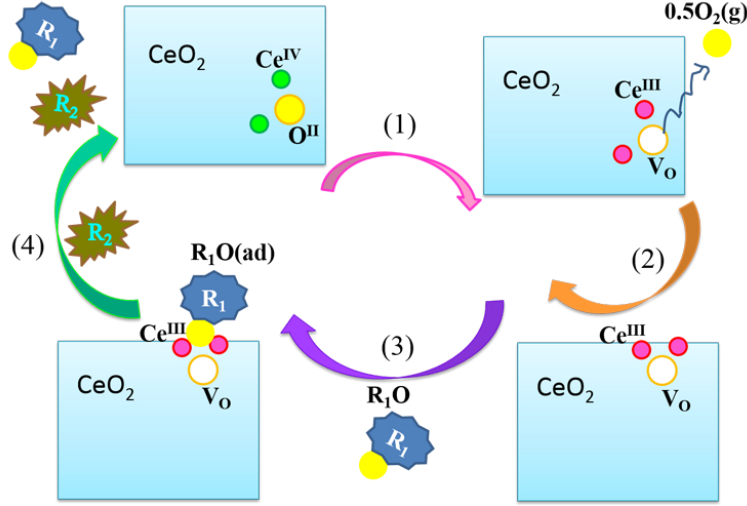


Figure 1.1: Schematic illustration of the four-step mechanistic hypothesis explaining ceria's excellent catalytic activity.

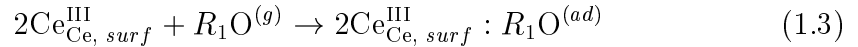
1. Formation of O-vacancies and associated  $\text{Ce}^{\text{III}}$  cations.



2. Migration of bulk  $\text{Ce}^{\text{III}}$  cations to the surface.



3. Adsorption of O-containing molecule ( $\text{R}_1\text{O}$ ) at surface  $\text{Ce}^{\text{III}}$  cations.



4. Interaction of adsorbed O-containing molecule with another O-containing molecule leading to catalyzed reaction enabled by (re-)oxidation of  $\text{Ce}^{\text{III}}$  cations.



The above “four-step” mechanism operates on the basis of two assumptions: (i) that reactive  $\text{Ce}^{\text{III}}$  cations are present only in conjunction with vacant  $\text{O}^{\text{II}}$  lattice sites, and (ii) that the intrinsic ceria surface itself has no direct role in the catalytic reaction—that is, redox catalysis by ceria requires that a vacant O lattice site



must migrate, along with its concomitant  $\text{Ce}^{\text{III}}$  cations, to the surface, and that this (surface) defect structure, not any intrinsic feature of the stable surface itself, is catalytically active. These assumptions have important consequences, namely implying that optimizing the activity of ceria catalysts requires increasing the concentration of surface O-vacancies (e.g., by reducing surface O-vacancy formation energies, or increasing bulk O-vacancy concentrations). Given that, this implication drives much of the recent research on optimizing or enhancing ceria and ceria-supported catalysts, it is worth considering under what conditions the assumptions leading to the “four-step” mechanism are applicable.

The first assumption (that  $\text{Ce}^{\text{III}}$  cations are present in conjunction with O-vacancies) is well-justified in bulk  $\text{CeO}_2$  systems with fixed charge, where reducing bulk  $\text{CeO}_2$  (that is, generating  $\text{Ce}^{\text{III}}$  cations) while maintaining charge neutrality requires the formation of one lattice O-vacancy for every two  $\text{Ce}^{\text{III}}$  cations. On this basis, it is general practice to consider the reduction of  $\text{CeO}_2$ , the creation of  $\text{Ce}^{\text{III}}$  cations, and/or the creation of lattice O-vacancies to be equivalent processes *in bulk  $\text{CeO}_2$* . The existence of large numbers of reactive  $\text{Ce}^{\text{III}}$  cations in ceria systems is itself justified by the existence of a range of sub-stoichiometric cubic fluorite reduced ceria phases ( $\text{CeO}_{2-x}$ ) which can be reversibly oxidized or reduced.

The second assumption upon which the “four-step” mechanism is based, that catalytically-active surface sites are  $\text{Ce}^{\text{III}}$  cations present as lattice O-vacancies on ceria surfaces, implies by extension that stable ceria surface structures do not intrinsically exhibit  $\text{Ce}^{\text{III}}$  cations, and that no other stable surface structures (other than surface  $\text{Ce}^{\text{III}}$  cations) are catalytically active. An argument can be made that this assumption is applicable for ideal, bulk-terminated surfaces on semi-infinite  $\text{CeO}_2$  samples, particularly on the basis of STM images of such surfaces revealing ideal, unreconstructed structures populated with finite concentrations of vacant O lattice sites<sup>24</sup>. The “four-step” mechanism of ceria catalysis (and the assumptions it is

based upon) is therefore well-supported for bulk  $\text{CeO}_2$  samples (or more correctly, for structures with surfaces well-approximated as ideal, unreconstructed, semi-infinite and stoichiometric bulk cuts). But the direct translation of the above assumptions to nanoparticle structures ignores the possibility of completely new atomic arrangements and catalytic mechanisms accessible only on the surfaces of nanoscale systems.

### 1.3 Motivation and overview of the entire research work

Over the past 30 years of exploring ceria as a catalyst, numerous experimental studies have proven that ceria is indeed an excellent catalytic material. The development of experimental techniques to synthesis nanoscale ceria materials, especially uCNPs, has raised their catalytic performance and significantly broadened their applications in the energy and biomedical related fields. More and more researchers are investing time and efforts to drive uCNPs into various practical applications. A key hurdle to realize practical applications of uCNPs, in particular in biomedical applications<sup>1-3,7,9,10</sup>, is that uCNPs tend to agglomerate into bigger sized clusters, thereby diminishing their high-activity and oxygen modulating characteristics<sup>11,25,26</sup>. Although various surfactants have been tested to alleviate this problem, it is still not possible to coat uCNPs with appropriate surfactants that meet all following requirements: (a) prevent agglomeration; (b) enhance biocompatibility; (c) retain high catalytic activity; (d) allow controlled and tunable redox property. To address these needs, and more generally, to realize improving and designing functional uCNPs targeted towards various specific and practical applications requires clear and thorough understandings concerning the microscopic structure of uCNPs, critically the structure of their surfaces, where catalytic reactions are expect to occur. In terms of exploring the surface structure of uCNPs, especially on the atomic level and resolution, experimental characterization techniques are limited and indirect. Although state-of-the-art microscopy techniques can provide direct and distinguishable atomistic images of nanoscale ceria

materials, it is difficult to directly reveal molecular species adsorbed at surfaces of uCNPs as they can hardly remain under high vacuum environment. In addition, the intrinsic electronic properties of functional groups decorating the surface of uCNPs, for instance, the interaction of an individual surface species with another incoming species from the environment, are very hard to be properly characterized experimentally. Moreover, in this age of fast advancement of science and technology, it strongly calls a more effective, efficient, and reliable research paradigm established through joint computational and experimental study.

Here, we apply DFT calculations to address the problems related to understanding and controlling the structure and catalytic properties of uCNPs. Chapter 1 is a general introduction on the well-established understanding concerning the structure and catalytic mechanism of bulk  $\text{CeO}_2$  materials, as well as the motivation of studying the structure and catalytic properties of uCNPs along with the overview of my entire research work. Chapter 2 presents the background information pertinent to my research work including a brief review of current perspective on the structure and property of various kinds of ceria materials from both experimental and computational studies, an account of problems arising from constructing CNPs with ideal, stoichiometric surface configurations, and associated challenges of constructing realistic, physically-representative structures compatible with experimentally synthesized and applied uCNPs as calculation inputs. Chapter 3 introduces the theoretical background as well as required computational tools, methods and settings to practically carry out this computational study. Starting from Chapter 4 up to Chapter 7 are the primary results of this computational study. In Chapter 4, we remove the constraint of ideal, stoichiometric, bulk-cut surface configuration, and systematically investigate what is the thermodynamically stable surface configuration and related structural properties of uCNPs in response to a pure oxygen environment. We show that after eliminating the constraint applied in all previous computational studies

to explore the surface configuration of CNPs, we have gained a new picture that various  $-O_x$  groups adsorbed at surfaces of uCNPs. Intuitively, those  $-O_x$  surface groups are hypothesized as active sites and potential factor dominating the catalytic behavior of uCNPs. Chapter 5 is a further test of this idea, and using a typical catalytic reaction (CO oxidation) realized by CNPs, we show that if uCNPs are decorated with various  $-O_x$  surface groups, their catalytic behavior is in fact critically dependent on those  $-O_x$  surface groups rather than surface O-vacancies. Chapter 6 considers a more complex and realistic case where the actual environmental effects (i.e. synthesis and application conditions) on the surface configurations of uCNPs is considered. We show that surface configurations of uCNPs are both sensitive to and determined by the environment they are in. This is a dynamic picture concerning the surface configuration of uCNPs in response to the real environment, a stark contrast to all previous computational studies that assume surface configurations of CNPs are static. The greater importance of these results is that we can provide recipes to direct experimental synthesis of uCNPs with desired and controlled surface structures, shedding light on using computational studies to facilitate experimental design and develop effective, highly efficient, and reliable experimental approach of producing new functional uCNPs, none of which has been exercised previously in ceria-based research world. In Chapter 7, we further show how water-gas shift reaction is likely to proceed over uCNPs with one of the stable surface configurations obtained through the typical synthesis condition. It elegantly provides an alternative perspective on what possibility can be achieved when exploring the catalytic behavior of uCNPs with surface configurations resulting from actual synthesis and application environments. Chapter 8 concludes this research work by highlighting some key results and discussing some future research directions.

## Chapter 2 Background

### 2.1 Previous experimental techniques to identify $\text{Ce}^{\text{III}}$ cations

$\text{Ce}^{\text{III}}$  cations are one of the basis for experimental “four-step” hypothesis used to explain ceria’s excellent catalytic activity (see **section 1.2**). Although “reduced” ceria refers to a range of sub-stoichiometric cubic fluorite ceria phases ( $\text{CeO}_{2-x}$ ), it is widely viewed as (stoichiometric)  $\text{CeO}_2$  containing a finite concentration of  $\text{Ce}^{\text{III}}$  cations. Therefore, experimental detection of  $\text{Ce}^{\text{III}}$  cations is the default method for identifying reduced ceria materials. Several techniques including X-ray photoelectron spectroscopy (XPS), X-ray absorption spectroscopy (XAS), valence band electron energy loss spectroscopy (EELS), and Fourier transform infrared spectroscopy (FTIR), have been employed to identify  $\text{Ce}^{\text{III}}$  cations<sup>27–30</sup>. In 1976, XPS was first used to examine the photoemission spectra of the Ce  $3d$  band in both  $\text{Ce}^{\text{III}}$  and  $\text{Ce}^{\text{IV}}$  compounds<sup>27</sup>. The XPS spectra indirectly provided some information about the coupled excitation of O  $2p$  to Ce  $4f$  associated with transformations between  $\text{Ce}^{\text{III}}$  and  $\text{Ce}^{\text{IV}}$  in cerium oxides.

Following this work, Ce  $3d_{5/2}$  core level spectra have been further investigated in order to clearly delineate  $\text{Ce}^{\text{III}}$  from  $\text{Ce}^{\text{IV}}$  cations<sup>28</sup>. Results have shown that a broad  $v''$  feature (binding energy around 888.6 eV) is characteristic of  $\text{Ce}^{\text{IV}}$  while two distinct  $v$  and  $v'$  lines (binding energy at 882.1 and 885.8 eV) are characteristic of  $\text{Ce}^{\text{III}}$ . In addition, XAS has been used to study the  $L_{\text{III}}$  edge of both  $\text{Ce}^{\text{IV}}$  and  $\text{Ce}^{\text{III}}$  compounds. In contrast to the multiple transitions observed for  $\text{Ce}^{\text{IV}}$  cations,  $\text{Ce}^{\text{III}}$  cations universally exhibit a single transition corresponding to the  $2p^5 4f^1 5d^{*1}$  final configuration. Hence XAS on the Ce  $L_{\text{III}}$  edge can serve as a fingerprint for the presence of  $\text{Ce}^{\text{III}}$  cations.

In 1998, a series of electron spectroscopy techniques were applied to explore the

features that can distinguish  $\text{Ce}^{\text{IV}}$  from  $\text{Ce}^{\text{III}}$  cations in fully oxidized  $\text{CeO}_2$ , sputtered  $\text{CeO}_{2-x}$  and  $\text{Ce}_2\text{O}_3$  oxide films<sup>29</sup>. It was found that the *Ce 4f* photoemission peak, the D peak in the *Ce 4d* spectra and the excitation in the band gap between 0 and 3 eV in the EELS spectra can be used to provide the evidence for the presence of  $\text{Ce}^{\text{III}}$  cations. In addition, XPS analysis of the *O 1s* photoemission is an alternative method to recognize the oxidation state of Ce cations<sup>31</sup>. The *O 1s* XAS peak at 535 eV was associated with  $\text{Ce}^{\text{III}}$  oxide while the *O 1s* XAS peak at 530 eV was assigned to the transition from *O 1s* to *Ce 4f*<sup>0</sup>, an ideal indicator of the presence of  $\text{Ce}^{\text{IV}}$  cations<sup>29</sup>. Finally, Binet has applied FTIR to  $\text{CeO}_2$  sample before and after reduction and pointed out that by comparing their IR spectra, a weak but well-defined peak at  $2127\text{ cm}^{-1}$  can be assigned to the electronic transition of  $\text{Ce}^{\text{III}}$  cations in bulk defective sites, as an marker for the existence of  $\text{Ce}^{\text{III}}$  cations<sup>30</sup>.

In summary, a range of experimental techniques exist which can identify  $\text{Ce}^{\text{III}}$  cations in bulk cerium oxides. These techniques do not provide direct information about the O-vacancies that are understood to be required in order to allow the existence of  $\text{Ce}^{\text{III}}$  cations in bulk ceria. None of these techniques can be applied directly to uCNPs in their application environment—which typically consists of uCNPs in gas or liquid environments.

## **2.2 Computational methods used previously to study bulk ceria, ceria surface and CNPs**

### **2.2.1 Molecular mechanics calculation**

In the early 1990s, a set of interatomic potentials were developed to describe ceria system<sup>32–35</sup>. These approaches generally separated the energy of a ceria structure into three contributions. The first of these is a Coulomb energy from pair interactions,

e.g.:

$$\sum_{i \neq j} \frac{q_i q_j}{r_{ij}} \quad (2.1)$$

, where  $q_i$  is the charge on atom (ion)  $i$ , and  $r_{ij}$  the interatomic distance between each  $ij$  pair of atoms. Note that this term explicitly requires that the oxidation state (that is, the charge,  $q_i$ ) be specified *a priori* for each atom (ion) in a given system. The second energy contribution is a short-range interaction arising jointly from the electronic repulsion and attractive van der Waals forces, expressed in the form of the Buckingham potential:

$$\sum_{i \neq j} A_{ij} \left\{ \exp \left( \frac{r_{ij}}{\rho_{ij}} \right) - \frac{C_{ij}}{r_{ij}^6} \right\} \quad (2.2)$$

The first part of this is a repulsive (Born) term, the second part an attractive (van der Waals) term, and  $A_{ij}$ ,  $\rho_{ij}$ , and  $C_{ij}$  are variable parameters. The final contribution is an ion polarizability induced by the electric field produced by all other ions as described by the shell model, assuming each ion is represented by a point core and a spherical shell, coupled by a harmonic spring:

$$\sum_i K_i \delta_i^2 \quad (2.3)$$

Here  $K_i$  is the force constant, and  $\delta_i$  the distance between core and shell centers for a particular ion. Studies employing these potentials have focused on the atomic structures of bulk ceria and ceria surfaces.

To test the applicability of such potentials to CNPs, Migani has examined the structure, energetics, and stability of ten configurational isomers of  $\text{Ce}_{19}\text{O}_{32}$  with distinct  $\text{Ce}^{\text{III}}/\text{Ce}^{\text{IV}}$  cationic ordering<sup>36</sup>. The results were compared with those obtained from DFT electronic structure calculations and quite similar trends on both structural parameters and relative energy ordering were observed. Such good agreement between interatomic potential calculations and DFT calculations was understood to highlight the key dependence of CNP energy on a sensitive balance between long range electrostatics and local bonding contributions to the energy, and to imply that

the empirical models employed were a reliable (and rapid) choice for seeking minimum energy cation (that is,  $\text{Ce}^{\text{III}}/\text{Ce}^{\text{IV}}$ ) arrangements. However, it does need to be noted that assigned charges are not able to vary during structural relaxation, limiting the ability to apply empirical potentials to seek complex atomic configurations that differ from initial (and presumably bulk-like) initial configurations.

### 2.2.2 Embedded cluster method

The embedded cluster method was specifically developed as an alternative to periodic boundary method to treat defects in ionic crystals and on their surfaces<sup>37,38</sup>. For the traditional embedded cluster method, the basic concept focuses on dividing the ionic defect-containing solid system into a number of local regions. Each local region consists of a defect structure treated by, e.g., quantum mechanical methods, as well as the defect surroundings, whose electrostatic potential is described with a point charge model. While such embedding schemes have been shown to accurately describe isolated point defects, it is challenging to calculate long range potential effects in complex systems or structures poorly represented as point charges<sup>39</sup>. Several different approaches have been developed to address this challenge, e.g. by including a calculated Madelung potential in embedded cluster schemes. One such approach, the periodic electrostatic embedded cluster method (PEECM)<sup>40</sup> leveraging recent development of the periodic fast multipole method (PFMM)<sup>41</sup> (in turn based on a multipole expansion<sup>42</sup>), has sought to provide a correct Madelung potential within the local quantum mechanical region in a periodic array of point charges of any dimensionality. Several studies have used the traditional and developed embedded cluster method to investigate the surface structure of ceria surfaces and clusters<sup>40,43–46</sup>.



### 2.2.3 DFT electronic structure calculation

Although interatomic potential models and the embedded cluster method are fast, they require *a priori* knowledge of the oxidation state of individual Ce and O atoms to calculate the energy of ceria structures. In contrast, quantum mechanical (QM) calculations do not necessarily require such knowledge, and can, in some cases, be used to solve for the oxidation state of atoms in ceria structures<sup>36,47–49</sup>.

When studying the structures and energetics of ceria based systems with QM techniques, conventional DFT calculations<sup>50–55</sup> adopt either one of the following two assumptions: (i) a core-state model (CSM), treating *Ce 4f* electron states in  $\text{Ce}_2\text{O}_3$  as part of the core and neglecting their contribution to the chemical bonds<sup>50,51</sup>, or (ii) a valence-band model (VBM), explicitly treating *Ce 4f* electrons in  $\text{CeO}_2$  as valence electrons and recognizing their contribution to the chemical bonds<sup>53–55</sup>. CSM-based methods accurately predict  $\text{Ce}_2\text{O}_3$  as an insulator, but have two drawbacks: (1) their predictive power is limited because the distribution of  $\text{Ce}^{\text{III}}$  or  $\text{Ce}^{\text{IV}}$  cations has to be assumed as an input of the calculation (similar to empirical models), and (2) it is not possible to directly obtain the energetics of the  $\text{CeO}_2/\text{Ce}_2\text{O}_3$  redox reaction<sup>56</sup>. In contrast, VBM-based methods accurately predict  $\text{CeO}_2$  as a metal, but do not accurately predict the band gap experimentally observed in partially reduced ceria ( $\text{CeO}_{2-x}$ ). This has been primarily attributed to a failure to correctly capture the electronic localization on the *Ce 4f* states—an important shortcoming, as these states have been shown to be key to controlling the oxygen-storage mechanisms in ceria<sup>52</sup>. In turn, inaccurate modeling of *Ce 4f* localization in conventional DFT has been attributed to incomplete cancellation of the Coulomb self-interaction in exchange-correlation functionals, and effect that stabilizes delocalized solutions.

The challenge, then, is to achieve a unified QM treatment of both oxidation states of Ce cations as well as to accurately capture both metal/insulator properties and *Ce 4f* electron localization. Both the LDA+U method<sup>57</sup> and various hybrid

exchange-correlation functionals<sup>58–60</sup> have been developed to overcome the limitations of conventional DFT in these regards. Hybrid functionals are computationally expensive, in particular when implemented on plane wave basis. Local Gaussian basis functions in combination with efficient integral screening have been attempted to reduce the computational cost<sup>59</sup>.

Given the computational cost of hybrid functionals, the most widely adopted unified treatment of the oxidation states of Ce cations is the LDA+U (or GGA+U) method. These DFT+U methods have been widely used to study bulk ceria, ceria surfaces, ceria clusters and CNPs, and they correct for errors in conventional DFT calculations by modifying the on-site Coulomb repulsion for *Ce 4f* electrons using an empirical parameter (Hubbard parameter). In the DFT+U formalism of Dudarev<sup>61</sup>, which has been widely and successfully applied to ceria systems<sup>56,62</sup>, a rotationally invariant simplification of the full Hubbard Hamiltonian results in a single parameter,  $U_{eff} = U - J$ .  $U$  reflects the strength of the on-site Coulomb interaction, and  $J$  adjusts the strength of the exchange interaction. From an *ab initio* point of view, it would be desirable to determine this parameter in a self-consistent way<sup>63</sup>. Moreover, the  $U_{eff}$  parameter has been shown to depend on the chosen exchange-correlation functional<sup>62,64,65</sup>. A number of studies have been conducted to optimize the value of  $U_{eff}$  to best reproduce experimental results (e.g., electronic structure properties such as band gaps<sup>56,62,64,65</sup>, the position of the occupied *Ce 4f* band with respect to the valence band edge<sup>56,62,64,65</sup>, and structural properties such as lattice constants and bulk modulus<sup>56,62,64–66</sup>) and have found no optimized single value of  $U_{eff}$  can be used appropriately throughout all calculations. The range of tested  $U_{eff}$  values from previous computational studies is between 2.5 and 6 eV<sup>56,62–74</sup> and the choice of  $U$  depends on what properties are most essential and need to be best captured for a particular computational study. In conclusion, it must be noted that given a properly chosen  $U$  parameter, DFT+U calculations have been shown to accurately model the

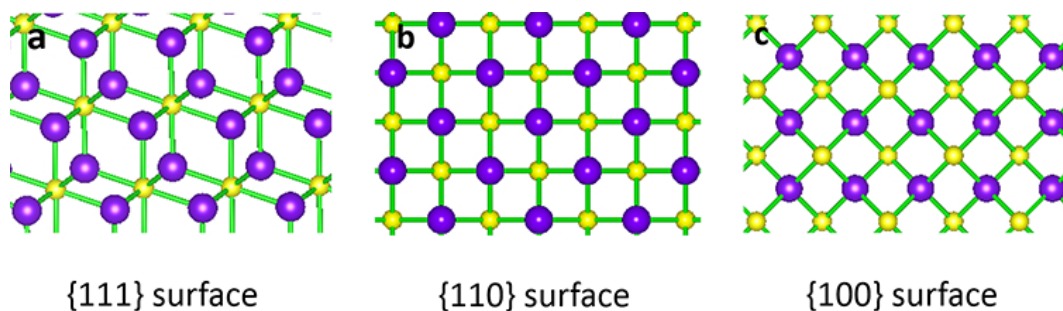


Figure 2.1: Atomic structure of  $\{111\}$ ,  $\{110\}$  and  $\{100\}$  ceria surfaces. Purple balls represent O atoms and yellow balls represent Ce atoms.

$\text{CeO}_2/\text{Ce}_2\text{O}_3$  system<sup>56,62–74</sup>.

### 2.3 Previous computational studies on semi-infinite ceria surfaces

Given the critical role of O-vacancy formation in the “four-step” model of catalysis by ceria, various computational studies aimed at understanding O-vacancy formation in bulk ceria and at ideal bulk ceria surfaces have been carried out. In 1992, Sayle<sup>75</sup> investigated O-vacancy formation (that is, step 1 from above) in stoichiometric bulk ceria, and on bulk  $\{111\}$  and  $\{110\}$  ceria surfaces. Both of these surfaces have stoichiometric ideal terminations—that is, cleaving a bulk sample along  $\{111\}$  or  $\{110\}$  planes results in ideal (unreconstructed) surfaces with  $\text{CeO}_2$  compositions (see Figures ??a and ??b). Sayle found that O-vacancy formation was energetically more favorable on ceria surfaces than in bulk, and more favorable on  $\{110\}$  surfaces than on  $\{111\}$  surfaces. Later the same group systematically studied the structures and energetics of and O-vacancy formation energies on three low-indexed ceria surfaces<sup>32</sup> in the context of CO oxidation over ceria. Again, all considered surfaces have stoichiometric ideal bulk terminations. Apart from confirming the conclusions of their earlier study<sup>32</sup>, Sayle, et al., found that along with  $\{110\}$  surfaces,  $\{310\}$  surfaces exhibited lower O-vacancy formation energies than  $\{111\}$  facets. Given the role of O-vacancies in enabling catalysis by ceria (see steps 1–4 in the “four-step” hypothesis

of ceria catalysis), surfaces with lower O-vacancy formation energies were predicted to exhibit higher catalytic activity.

In addition to  $\{111\}$ ,  $\{110\}$  and  $\{310\}$  surfaces, Conesa studied the structure and energetics of three other low-indexed ceria surfaces,  $\{100\}$ ,  $\{210\}$  and  $\{211\}$ , of which only  $\{211\}$  has a stoichiometric ideal termination<sup>33</sup>. This work found that  $\{211\}$  surfaces relaxed into stepped  $\{111\}$  configurations. Consistent with the previous Sayle results<sup>32,75</sup>, O-vacancy formation energies on  $\{110\}$  and  $\{100\}$  surface were found to be lower than on  $\{111\}$  surfaces; however, O-vacancy pairs were found to be more stable on  $\{111\}$  surfaces than  $\{110\}$  or  $\{100\}$ .

The results of Sayle, et al., and Conesa were generated using empirical interatomic potentials which required that the oxidation state of Ce atoms be assumed and fixed. That is, such methods could not be used to calculate the low-energy distribution of electrons—as required to predict the distribution of Ce oxidation states for a given atomic configuration.

In 2002, Skorodumova used DFT calculations to lift this limitation and directly explore the electronic structure of O-vacancies in ceria<sup>52</sup>. Considering both ceria and a cubic fluorite reduced ceria structure with  $\text{Ce}_2\text{O}_3$  stoichiometry, Skorodumova concluded that O-vacancies prefer to be located in the crystal bulk—in contrast to previous semi-empirical results<sup>75</sup>, and raising the question of why  $\text{Ce}^{\text{III}}$  cations should be expected to migrate to sample surfaces (step 2 in the “four-step” hypothesis of ceria catalysis). Importantly, they also concluded that the two excess electrons associated with a lattice O atom removed to form a vacancy localize into the 4f states of two of the four Ce atoms nearest neighbor to the vacant O lattice site (Figure 2.2). Therefore, the redox properties of ceria (and the “four-step” process of ceria catalysis described in **section 1.2**) must critically depend upon electron transitions from delocalized *O* 2*p* states to localized *Ce* 4*f* states that occur during O-vacancy formation. DFT+U techniques have made accurate quantum mechanical calculations of these transitions

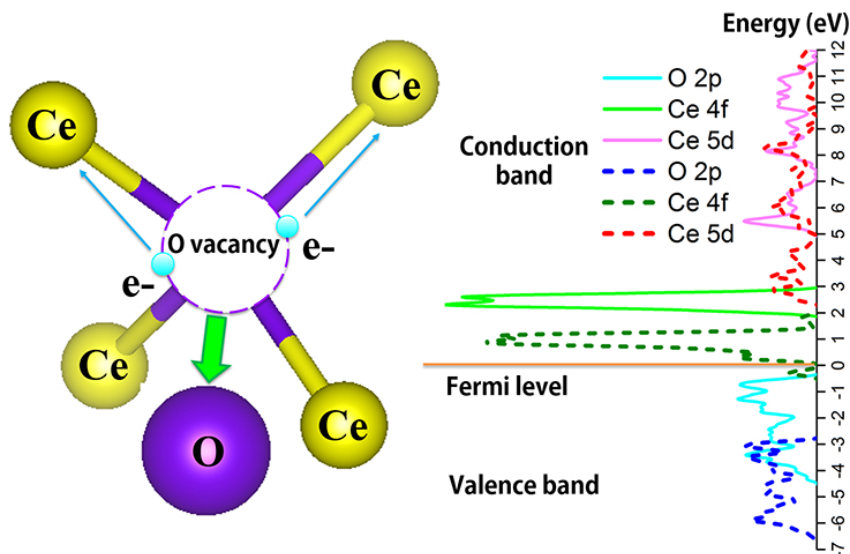


Figure 2.2: The process of O-vacancy formation in ceria: a neutral O atom is removed, leaving behind an empty O lattice site, and returning electrons to nearby Ce atoms. At right are the calculated electronic density of states (eDOS) for relevant Ce and O bands. Solid lines correspond to the eDOS of fully oxidized bulk CeO<sub>2</sub>, while dashed lines are for partially reduced bulk CeO<sub>2-x</sub>. The zero of energy for each system has been set to the Fermi energy. Note the energy shift down of the Ce states. This plot shows that electrons returned to Ce states due to O-vacancy formation (that is, the reduction of ceria) appear in *Ce 4f* states.

possible.

The results of Skorodumova, et al., are an important contribution to the conventional “four-step” mechanism of catalysis by ceria as they show that the Ce<sup>III</sup> cations generated by O-vacancy formation are located at Ce sites adjacent to the O-vacancy itself. This implies that identifying and characterizing O-vacancies in ceria is equivalent to identifying and characterizing Ce<sup>III</sup> cations. That is, because Ce<sup>III</sup> cations are preset in stoichiometric ceria only if O-vacancies are present and, when present, are physically adjacent to an O-vacancy, the thermodynamics and kinetics of O-vacancies are the thermodynamics of Ce<sup>III</sup> cations.

Note, though, the importance of stoichiometry in the above analysis. The conventional “four-step” picture of ceria catalysis requires interaction of reactants with *surface* Ce<sup>III</sup> cations. These cations appear only as a consequence of O-vacancy

formation *in stoichiometric ceria*, but only a subset of possible ceria surfaces have stoichiometric surface terminations. Therefore, *non-stoichiometric* ceria surfaces may exhibit a non-zero concentration of  $\text{Ce}^{\text{III}}$  cations without the formation of O-vacancy defects. Understanding ceria redox catalysis on these surfaces, even simply evaluating the applicability of the “four-step” hypothesis for the catalytic mechanism, first requires knowledge of the surface structure. In particular, assessing the role of vacant surface O lattice sites (whether as part of the thermodynamically stable surface reconstruction, or as surface defects) is therefore critical to correctly evaluating catalytic processes on arbitrary ceria surfaces.

Previous calculations of ceria surfaces have not directly or systematically addressed the role of variations in surface composition and/or structure. Calculations on stoichiometric ceria surfaces (e.g.,  $\{111\}$ ,  $\{110\}$ , and  $\{310\}$ ) have assumed ideal, bulk-like terminations. Calculations on non-stoichiometric ceria surfaces [e.g.,  $\{100\}$  (see Figure 2.1c), and  $\{211\}$ ] were first conducted by enforcing net stoichiometry in the calculation cell by constructing asymmetric slabs with differing top and bottom surfaces, namely one O-terminated surface and one Ce-terminated surface (e.g.,  $\{100\}$ ). While this avoids the issue of  $\text{Ce}^{\text{III}}$  cations present natively in systems with non-stoichiometric surfaces (in contrast to their presence in reduced ceria directly as a result of O-vacancy formation), these structural models do not address the issue of possible surface reconstructions. In addition, the resulting asymmetric computational cells result in electronic dipoles perpendicular to the slab surfaces. These dipoles distort the calculated electronic structure and give rise to errors in calculated surface and O-vacancy formation energies.

Calculations by Conesa<sup>33</sup> addressed the surface dipole problem by assuming symmetric slabs with model (top and bottom) surface structures composed of arbitrarily assigned arrangements of vacant and filled surface O lattice sites chosen to satisfy net stoichiometry (e.g., choosing half the surface O lattice sites to be unoccupied). While

this eliminates the problem of surface dipoles due to asymmetric slabs, the approach still does not fully account for possible compositional and structural variations at ceria surfaces. Therefore, calculated results for relative surface and O-vacancy formation energies may not be relevant to real ceria systems. In turn, this greatly limits the potential for calculated results to directly evaluate the experimentally-driven “four-step” hypothesis for ceria catalysis.

A number of other authors have considered semi-infinite ceria surfaces including the interaction of small molecules with those surfaces, and report results concerning the surface structure of ceria surfaces similar to those discussed above<sup>43,45,47–49,54,55,64,66,70,71,76–104</sup>. In all cases, the authors have limited their investigations to bulk-like surface terminations and net stoichiometric (or near stoichiometric) slabs. While these calculations consider the limiting case where the assumptions undergirding the “four-step” mechanism are applicable, they fail to consider potential surface configurations that strongly deviate from bulk ceria structure or stoichiometry.

## **2.4 Previous computational studies on small ceria clusters and CNPs**

### **2.4.1 Semi-empirical calculations**

To explore whether nanoceria (broadly meaning ceria materials with one or more dimension on the nanoscale) behaves similarly to larger ceria materials, computational studies have considered O-vacancy properties in small ceria clusters and nanoparticles. In 1996, Cordatos applied the empirical interatomic potentials developed by Sayle, et al., in Metropolis Monte Carlo simulations of an NVT ensemble to find the global minimum energy structures for stoichiometric and sub-stoichiometric ceria clusters.  $\text{Ce}_n\text{O}_{2n}$  clusters were considered for  $n = 2 - 20$  and  $n = 50$ <sup>34</sup>. Cluster structures were characterized with their angular-distribution and pair-distribution functions (ADF and PDF, respectively), and their stability evaluated on the basis of the zero temperature lattice energy (which consists of pure electrostatic energy, short-

range repulsion and attraction between ions, and effects of electronic polarizability, see **section 2.3.1**). Only large clusters formed fluorite crystallites with well-defined facets, and these exhibited  $\{111\}$  surfaces. Smaller clusters tended to form spherical agglomerations. Cluster stability increased nonlinearly with cluster size. The reducibility of ceria clusters was assessed based on the difference in lattice energy between  $\text{Ce}_n\text{O}_{2n}$  and  $\text{Ce}_n\text{O}_{2n-1}$  clusters, that is, by calculating the effective energy of formation of an O-vacancy. Reducibility (energy of formation of an O-vacancy) was found to be structure sensitive, but generally decreased (increased) with cluster size.

The use of empirical potentials in this study is notable because the oxidation state of Ce cations treated with empirical potentials must be fixed a priori (see **section 2.3.1**). Therefore, calculated lattice energies of sub-stoichiometric (reduced) nanoparticles and calculated reducibilities are constrained by an external assignment of  $\text{Ce}^{\text{III}}$  cation locations. In reduced clusters, Cordatos placed  $\text{Ce}^{\text{III}}$  cations at the nanoparticle surfaces in generally unpaired arrangements, in contrast to Skorodumova’s findings (reported six years after Cordatos’ study) on semi-infinite surfaces that  $\text{Ce}^{\text{III}}$  cations should be paired and nearest neighbor to vacant O lattice sites. Despite these limitations, a number of further empirical potential studies were conducted following Cordatos work.

In 1998, Vyas also used empirical potentials (in fact, comparing four different potentials), to study the surface structures and energetics of a set of ceria surfaces. Based on these results, stoichiometric ceria crystallites were predicted to exhibit an octahedral morphology<sup>35</sup> with  $\{111\}$  facets, in agreement with the Cordatos’ previous findings.

Sayle, et al.<sup>105</sup>, conducted molecular dynamics simulations of ceria nanoparticles using the same empirical potentials applied by Cordatos<sup>34</sup>, and in Sayle’s own previous work on ceria semi-infinite surfaces<sup>32,75</sup>. Sayle relaxed three 10 nm CNPs with different combinations of low-index surfaces to explore various CNP shapes. De-



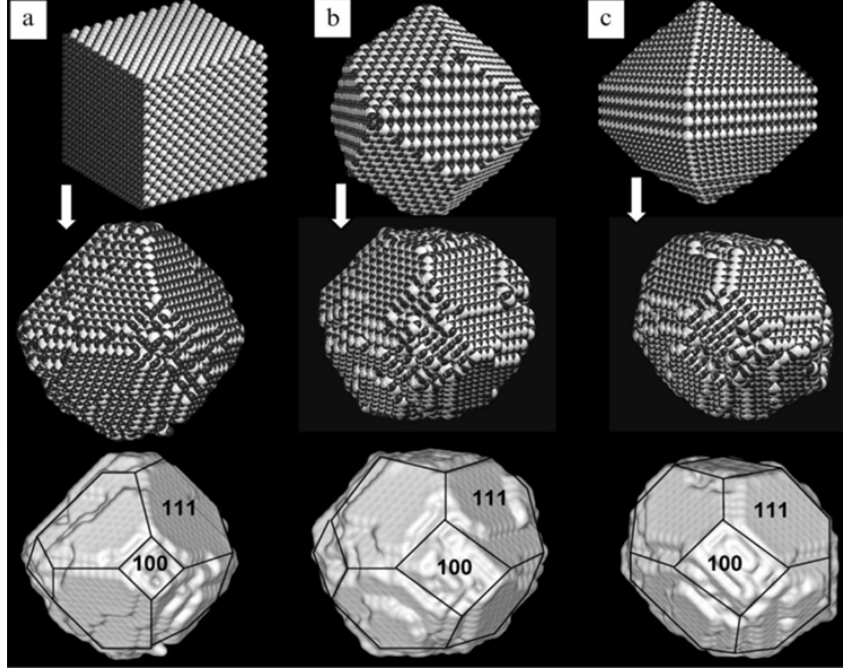


Figure 2.3: Three CNPs with different initial structures evolved into final configurations after MD simulation<sup>105</sup>.

spite beginning with completely different initial shapes, all three CNPs considered by Sayle, et al., relaxed to similar shapes: truncated octahedrons comprised of eight  $\{111\}$  facets and  $\{100\}$  mini-facets at the six corners (see Figure 2.3). It is notable that the  $\{110\}$  surfaces previously predicted<sup>32,33,75,76</sup> in semi-infinite slab calculations as more stable than  $\{100\}$  surfaces but less stable than  $\{111\}$  surfaces disappeared in small CNPs, leaving behind only  $\{111\}$  and  $\{100\}$  surfaces. The resulting  $\{100\}$ -truncated octahedral CNPs agreed well with experimentally determined shapes of certain synthesized CNPs<sup>106</sup>.

#### 2.4.2 Quantum mechanical calculations of small ceria clusters

In 2006, Tsunekawa, using GGA calculations not requiring a priori specification of the oxidation state of Ce cations, calculated the electronic density of states (eDOS) and band structure of two ceria clusters. Their study considered a fully oxidized  $(\text{CeO}_2)_{13}$  cluster and a fully reduced  $(\text{CeO}_{1.5})_{13}$  cluster<sup>107</sup>. HOMO-LUMO gap energies of the

clusters  $(\text{CeO}_2)_{13}$  and  $(\text{CeO}_{1.5})_{13}$  were calculated to be  $\approx 0$  and 3 eV, respectively.

Li subsequently employed both LDA+U and GGA+U calculations to investigate the geometric and electronic structures of small  $\text{Ce}_n\text{O}_m$  ( $n=1-4$ ,  $m=2n-1, 2n$ ) clusters and their reducibility<sup>108</sup>. They found the energy of formation of O-vacancies to be much *lower* in ceria clusters than in the bulk ceria, implying better catalytic properties. This result was supported by Zhang, et al., who used LDA+U method to calculate the energy of formation of one O-vacancy in a  $\text{Ce}_4\text{O}_8$  cluster<sup>109</sup>. Chen, et al., studied the eDOS of stoichiometric  $\text{Ce}_n\text{O}_{2n}$  ( $n=1-4$ ) clusters and analyzed the decomposed *spd* orbital distributions of both Ce and O atoms within clusters of  $n=2$  and  $n=3$  in detail<sup>110</sup>. The Fukui function<sup>111</sup> was used to identify different kinds of Ce and O atoms in terms of different coordination states, and to evaluate the chemical reactivity of a certain atoms. Results indicated that Ce atoms or O atoms with different numbers of nearest bonding atoms will have different chemical reactivity.

While these quantum mechanical studies allow calculation of the distribution of  $\text{Ce}^{\text{III}}$  and  $\text{Ce}^{\text{IV}}$  cations, in contrast to semi-empirical calculations, they are limited to small clusters without distinct facets. Given that catalysis by ceria occurs at ceria surface facets, such calculations offer limited insight into the mechanisms and properties of experimentally synthesized nanoceria samples.

### 2.4.3 Quantum mechanical calculations of ceria crystallites (nanoparticles)

In 2007, Loschen conducted DFT-based calculations aimed at understanding the atomic structure of ceria crystallites, which, although still small, possessed distinct crystallinity and faceted surfaces<sup>112</sup>. They studied  $\{111\}$ -terminated octahedral C-NPs which are partially reduced ( $\text{CeO}_{2-x}$ ) due to the sub-stoichiometric (meaning O-deficient) nanoparticle edge and corner structures considered. In contrast to previous experimental results, Loschen, et al.<sup>112</sup>, found that the ceria lattice spacing

decreased with decreasing nanoparticle size (based on calculated interatomic Ce-Ce and Ce-O distances). It was concluded that the presence of multiple O-vacancies, inherent to CNPs at finite temperature due to low O-vacancy formation energies, must account for the experimentally detected lattice expansion in small, partially-reduced nanoparticles. This was supported, in part, by included calculations of nanoparticles containing a single bulk O-vacancy showing that interatomic Ce-Ce distances of Ce atoms near O-vacancies increased. Loschen, et al., also reported that  $\text{Ce}^{\text{III}}$  cations (present in their nanoparticles due to non-stoichiometric CNP edges, not bulk O-vacancies) were located at the edges and corners of CNPs, whereas  $\text{Ce}^{\text{IV}}$  cations were located at fully O-coordinated sites.

A 2008 study by the same authors have systematically investigated the energetics and structure of octahedral CNPs containing up to 85 Ce atoms, as well as “cuboctahedral” CNPs of similar size and consisting of octahedral structures with six corner Ce atoms removed<sup>113</sup>. The truncated corners of cuboctahedral CNPs are small, O-terminated  $\{100\}$  facets, recalling the nanoparticle shapes predicted by Sayle, et al., using semi-empirical potentials and mimicking certain structures observed experimentally for 2–10 nm CNPs<sup>114,115</sup>. This 2008 study also calculates the energy of formation of a single O-vacancy in various CNPs, as well as  $\text{Ce}^{\text{III}}$  versus  $\text{Ce}^{\text{IV}}$  cation distribution within those CNPs<sup>113</sup>. In order to compare energies of different shaped and sized CNPs, an energy of formation of CNPs,  $E_f$ , was defined for  $n$  Ce atoms,  $m$  O atoms, and referenced to the energy of solid Ce metal  $\text{Ce}_{(s)}$  and molecular O in the gas phase  $\text{O}_{2(g)}$ :

$$E_f = \frac{1}{n}E(\text{Ce}_n\text{O}_m) - E(\text{Ce}_{(s)}) - \frac{m}{2n}E(\text{O}_{2(g)}) \quad (2.4)$$

Loschen, et al., considered partially-reduced, stoichiometric and, for the first time, super-oxidized ( $\text{CeO}_{2+x}$ ) nanoparticles<sup>113</sup>. While partially-reduced nanoparticles were found to have formation energies that converge to the the energy of formation of bulk  $\text{CeO}_{2(s)}$  with increasing size, stoichiometric CNPs had formation energies below this

trend, and oxidized CNPs had formation energies above this trend. The authors noted that the super-oxidized nanoparticles ( $\text{Ce}_{13}\text{O}_{32}$  and  $\text{Ce}_{38}\text{O}_{80}$ ), containing 6 and 4 excess O atoms respectively, exhibited isolated  $\text{O}^{-1}$  anions (“peroxide-like O-atoms”), likely causing the relative increase in the energy of formation of CNPs.

In a separate 2008 publication, the same research group sought to identify a “size-converged” model CNP that, on the one hand, would be as small as possible to minimize computational cost, but on the other hand, large enough to be representative of experimentally observed properties<sup>116</sup>. To seek such a model CNP structure, they examined CO adsorption at different CNP surface sites as a function of CNP size seeking a CNP size beyond which the energetics of CO interaction with the CNP became invariant. Using model CNPs similar to the 2008 Loschen’s study<sup>113</sup> (notably excluding the oxidized CNPs considered in that work), the authors concluded that adsorption properties were very sensitive to the CNP size, but converged to values within expected accuracy for computational studies ( $\approx 0.1$  eV) for CNPs approximately 1 nm in diameter.

In parallel work, Inerbaev, et al., have investigated the energy of formation of O-vacancies at the surface, the subsurface and inside CNPs as a function of CNP sizes,  $\text{Ce}^{\text{III}}$  versus  $\text{Ce}^{\text{IV}}$  cation ratios, and variations in details of the DFT methodology used<sup>117</sup>. They found that the energy of formation of O-vacancies decreased with increasing CNP size and decreasing  $\text{Ce}^{\text{III}}$  versus  $\text{Ce}^{\text{IV}}$  cation ratio. This implied that for a CNP of given size, there exists an equilibrium concentration of O-vacancies at finite temperature. The authors also compared formation energies of O-vacancies calculated with different DFT exchange-correlation potentials and different parameterizations of the semi-empirical Hubbard  $U_{eff}$  parameter, which is used to correct a known limitation of DFT in correctly modeling localized  $f$  orbitals (see Appendix B). Highlighting previous results showing that O-vacancy formation in ceria triggers electron transitions from delocalized  $\text{O } 2p$  states to localized  $\text{Ce } 4f$  states, Inerbaev

found strong variations in formation energies of O-vacancies with respect to  $U_{eff}$ . Strong variations in formation energies of O-vacancies were also reported between GGA and LDA calculations.

Migani then proposed that formation of O-vacancies was greatly facilitated in stoichiometric CNPs compared to extended surfaces<sup>118,119</sup>. The formation of O-vacancies in stoichiometric CNPs has been decomposed into three elementary steps and energies associated with each step was separately evaluated. The first step was two electrons transferred from one  $O^{II}$  anion to two  $Ce^{IV}$  cations that were subsequently reduced to  $Ce^{III}$  cations. The associated energy ( $E_1$ ) was calculated from the separation between the highest-occupied  $O\ 2p$  orbital of the  $O^{II}$  anion and the  $Ce\ 4f$  orbitals of the two  $Ce^{IV}$  cations involved in the two-electron transfer. The second step was removal of the neutral O atom from its lattice site, and the associated energy ( $E_2$ ) was calculated from change before and after eliminating a neutral O atom within considered CNPs. The third step was relaxation of the whole system, and the associated energy ( $E_3$ ) was calculated from the energy difference between the O-vacancy-containing systems with  $4f^1$  electrons localized at Ce sites first neighbouring to O-vacancies at the fixed geometry of the pristine model and at the relaxed geometry. The energy of formation of O-vacancies in stoichiometric CNPs ( $E_f$ ) was defined as  $E_f = E_1 + E_2 + E_3$ . They concluded that (1) it was easier to remove low-coordinated O atoms to form O-vacancies; (2) formation energies of O-vacancies decreased with increasing size of CNPs (considered size no more than 2 nm), indicating that the CNP of a certain size was expected to be most favorable to form O-vacancies; (3) size-dependent  $E_f$  was driven by electrostatics between  $O^{II}$  anions and  $Ce^{IV}$  cations, thus enabling the prediction that most easily removable are the low-coordinated O atoms experiencing the least attractive electrostatic potential in the pristine ceria systems without O-vacancies.

Most recently, Migani, et al., predicted that stoichiometric CNPs of tetrahedral

shape and size less than 2 nm was more stable than experimentally observed stoichiometric CNPs of truncated octahedral shape and larger size<sup>120</sup>.

To sum up, atomistic calculations focusing on stoichiometric or near-stoichiometric (particularly partially-reduced) nanoceria structures with bulk-like surface configurations have been conducted to study various nanoclusters and faceted octahedral, cuboctahedral and tetrahedral CNPs. Calculated results show that  $\text{Ce}^{\text{III}}$  cations, when present, are generally under-coordinated Ce atoms (e.g., those neighboring discrete O-vacancies, or those at under-coordinated surface, edge or corner sites) and that formation of O-vacancies involves electron transfers from *O* 2*p* states to *Ce* 4*f* states. Beyond this, calculations on faceted CNPs show that energetics of the O-vacancy formation, while generally lower at CNP surfaces than in bulk, are highly dependent on the CNP shape and composition, and that surface composition itself directly influences the number and distribution of  $\text{Ce}^{\text{III}}$  cations. While individual results suggest various low-energy overall configurations (combinations of CNP size, shape and composition), no definitive consensus has emerged to define a computational predicted configuration for actual CNP catalysts. Critically, calculations to date have not systematically explored the possibility of non-bulk-like CNP surface terminations, and have frequently limited consideration of possible CNP configurations on the basis of bulk stoichiometry.

## 2.5 Previous experimental studies on –OH groups adsorbed at surfaces of CNPs

As highly active CNPs are typically synthesized and applied in aqueous and/or humid environments, it is generally acknowledged that –OH groups are present on the surface of all as-prepared CNPs<sup>121,122</sup>. Furthermore, these –OH surface groups significantly affect not only the adsorption/desorption behavior of water at surfaces in related catalytic processes<sup>123</sup>, but also the rate and degree of surface modifications, such as

reactions between  $\text{-OH}$  surface groups and silane coupling agents<sup>124,125</sup>.

None of previous computational studies concerning CNPs has considered the origin and nature of adsorbed  $\text{-OH}$  surface groups other than focusing on bare, ideal, stoichiometric surface configurations. In contrast, the potential role of adsorbed  $\text{-OH}$  surface groups is highly desired to be understood by experimentalists. Fourier transform infrared spectroscopy (FTIR) and thermogravimetric analysis with mass spectroscopy (TGA-MS) have previously verified the presence of adsorbed  $\text{-OH}$  groups on CNPs, and estimated their binding energies and surface densities<sup>126–128</sup>. These techniques, though, are not able to directly reveal the structure of OH-terminated ceria surfaces<sup>121,129</sup>, nor the chemistry controlling the adsorption, distribution, and stable densities of  $\text{-OH}$  surface groups as a function of environmental conditions. On the contrary, we will show in this dissertation that DFT calculations can be combined with experimental synthesis and characterization methods, as well as thermochemical data, to address these limitations.

## **2.6 Previous perspective on the catalytic behavior of CNPs to oxidize CO**

CO is a typical by-product of car exhausts, energy-harvesting combustion including fuel cells and many industrial proceeds involving organic compounds that seriously contaminates the environment and sabotages our health. Converting CO to  $\text{CO}_2$  in the catalytic oxidation reaction is a practical means widely exploited in industry. However, such process typically processes under rather high oxidation temperature, which necessarily increases energy consumption and requires high selectivity, stability and activity of applied catalysts. Extensive researches have been carried out to find efficient catalysts that facilitate the oxidation of CO. CNPs have been shown to be a potential candidate given their application in three way catalysts<sup>130</sup> and fuel cells<sup>4,8</sup> as well as their role in lowering the oxidation temperature of CO<sup>131</sup>. It is

widely accepted that oxidation of CO by ceria is controlled by lattice O vacancies at surfaces of reduced ceria regardless of its shape, size and composition<sup>130–133</sup>. The basic reaction mechanism is the generation and annihilation of lattice O-vacancies via exchange between Ce<sup>IV</sup> and Ce<sup>III</sup> cations that are capable of providing the atomic oxygen that combines with CO at surfaces. It can be described as  $\text{Ce}^{\text{IV}} + \text{CO}(\text{g}) \longrightarrow \text{Ce}^{\text{III}} + \text{V}_{\text{O}}^{\bullet\bullet} + \text{CO}_2(\text{g})$ <sup>130</sup>. Hence, various strategies including increasing the surface-to-volume ratio have been developed to engineer ceria catalysts for the purpose of enhancing the density of available surface O-vacancies<sup>131,133–139</sup>. Is this the case for uCNPs to realize the oxidation of CO to CO<sub>2</sub>? We will show different viewpoints concerning the catalytic behavior of uCNPs in this dissertation.

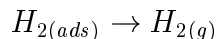
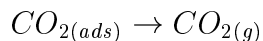
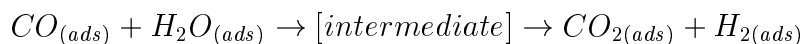
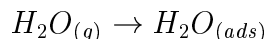
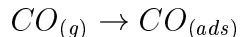
## **2.7 Previous experimental and computational studies of water-gas shift reaction catalyzed by ceria**

### **2.7.1 Introduction**

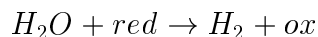
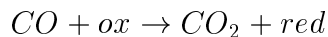
Water-gas shift (WGS) reaction has been extensively employed in industry to massively produce pure hydrogen. Based on the range of temperatures within which the catalyst functions, WGS reaction can be divided into low temperature reaction, medium temperature reaction and high temperature reaction. Typically, the low temperature reaction is operated between 190–250 °C over copper-zinc oxide based catalysts, and the high temperature reaction is carried out at 350–450 °C over iron oxide based catalysts, while the medium temperature reaction proceeds at 270–350 °C over modified copper-zinc catalysts<sup>140,141</sup>. Besides the above three types of catalysts, sulfur-tolerant catalysts using cobalt and molybdenum sulfides as active ingredients and precious metal based catalysts (mainly platinum and gold) are also under intensive investigation. Regarding the WGS reaction mechanism, two broadly classified pathways based on either associative mechanism or redox mechanism from the micro kinetic perspective have both been initially proposed by Armstrong and Hilditch<sup>142</sup>



in 1920s, and which one dominates the catalytic process pertinent to particular catalytic systems has always been the controversial topic since then. The key step of associative mechanism is the formation of an unspecified intermediate once  $\text{CO}_2$  and  $\text{H}_2\text{O}$  are absorbed onto the catalyst surface and subsequent dissociation of the intermediate into reaction products. Such mechanism can be illustrated by following equations<sup>143</sup>:



It is considered that the third reaction step determines the overall reaction rate<sup>141</sup>. In contrast, the redox mechanism involves a periodic change of the catalytic surface state in terms of first being reduced by incoming  $\text{CO}_2$  and then oxidized by incoming  $\text{H}_2\text{O}$ . This mechanism can be represented by following equations<sup>141</sup>:



In this mechanism, the dissociation of  $\text{H}_2\text{O}$  with surface O-vacancies or with surface O adatoms is recognized as the rate-determining step<sup>144</sup>.

### 2.7.2 The variables influencing the reaction rate<sup>141</sup>

The WGS reaction rate can be affected by a number of factors. Above all, it is intrinsically influenced by the nature of applied catalysts, which is closely related to their chemical composition and preparation method. Externally, processing variables such as temperature, steam/dry gas ratio and pressure will also influence the reaction kinetics. Since the WGS reaction is exothermic, the equilibrium will be likely to shift towards hydrogen production at low temperatures. However, in the case that is kinetically- rather than equilibrium-limited, higher gas/bed temperatures may favor

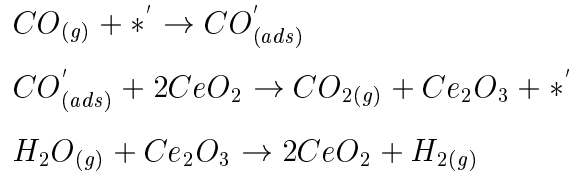
the reaction in the reactor. In addition, it is indicated that higher steam/dry gas ratios in commercial ranges increase the WGS reaction rate and benefit CO conversion, and so does the pressure.

### 2.7.3 Former studies of WGS reaction mechanism on ceria-based catalysts

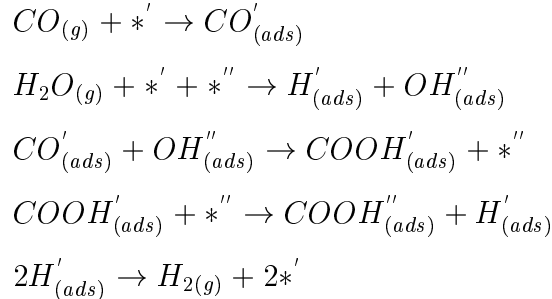
The traditional pyrophoric low temperature shift (LHS) catalysts ( $\text{Cu/ZnO/Al}_2\text{O}_3$ ) can not be well adjusted to the fuel cell application that requires rapid startup or shutdown processes, it is thus necessary to develop nonpyrophoric LHS catalysts with high activity and efficiency<sup>145</sup>. Following this idea, structures consisting of noble metal particles on the partially reducible oxide (PRO) support or inverse structures for low-temperature WGS reactions have been widely explored<sup>146–152</sup>. As a matter of fact, two prevalent viewpoints on the function of such particular catalytic systems similar to the general catalyzed WGS mechanism are supported by various experimental and computational studies<sup>153–157</sup>. In general, WGS reaction is explained by the redox mechanism and the associative mechanism, or the combination of these two<sup>158</sup>. Specifically, the former emphasizes the reduction role of noble metal facilitating its absorbed CO to capture oxygen absorbed on PRO at metal/PRO interface and creating a surface O-vacancy by releasing  $\text{CO}_2$  as well as the oxidation role of  $\text{H}_2\text{O}$  replenishing the surface O-vacancy by depositing an O adatom and generating  $\text{H}_2$ <sup>144,159,160</sup>. However, the latter stresses the decisive role of noble metal facilitating the dissociation of  $\text{H}_2\text{O}$  to germinate bridged  $-\text{OH}$  surface groups on PRO surface and subsequent formation of bidentate formate as the crucial intermediate by associating CO with  $-\text{OH}$  surface groups as well as the selective decomposition of formate to  $\text{H}_2$  and  $\text{CO}_2$  with co-adsorbed  $\text{H}_2\text{O}$ <sup>161–166</sup>.

### 2.7.3.1 Experimental studies

One of the big LHS catalyst families is the metal/ceria catalysts, for instance Au/CeO<sub>2</sub>, Pt/CeO<sub>2</sub>, Cu/CeO<sub>2</sub> and the corresponding inverse-structured catalysts. On the basis of oxygen storage capacity (OSC) of ceria, redox mechanism was proposed that CO absorbed on the metal reacted with an O atom donated from ceria and to form CO<sub>2</sub> and then H<sub>2</sub>O offered an O atom to reoxidize ceria and yield H<sub>2</sub><sup>167–170</sup>. The relevant reaction steps can be shown as:



where  $*'$  represents a free adsorption site on the metal surface and  $CO'_{(ads)}$  the adsorbed CO on the metal surface. Alternative formate mechanism (also known as associative mechanism) was suggested relying on FIIR spectroscopy investigation<sup>163,171</sup>. Similarly to the redox mechanism, the reaction pathways of formate mechanism can be summerized as:

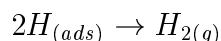
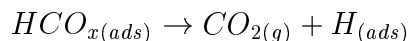
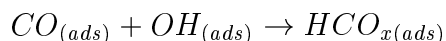
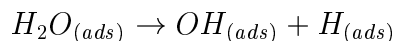
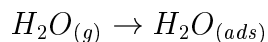
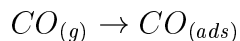


where  $*'$  and  $*''$  are the free adsorption sites on the metal surface and on the oxides, respectively;  $'_{(ads)}$  and  $''_{(ads)}$  represent adsorption on the metal and on the oxide, respectively. In this mechanism, –OH surface groups and intermediates (primarily formate) were recognized to be crucial chemicals dominating the WGS reaction on metal/ceria catalysts<sup>151</sup>. –OH surface groups are produced by dissociation of H<sub>2</sub>O on O-vacancy sites, and they needs to be further broken to regenerate O atoms<sup>172</sup>. There are two scenarios envisioned to generate the formate intermediates, either from

CO directly interacting with  $\text{-OH}$  surface groups on reduced ceria surfaces induced by precious metal<sup>173–176</sup> or from CO absorbed on active Au sites interacting with nearby  $\text{-OH}$  groups on ceria surfaces at the interface between Au particles and ceria support<sup>147</sup>. Extensive studies have been focused on the conditions that benefit the formation of  $\text{-OH}$  surface groups and dissociation of intermediates. One way is to internally tailor the surface structure of catalysts to achieve better catalytic performance. It has been evidenced that incorporating zirconia dopants into ceria lattice increases both the surface area and the concentration of  $\text{-OH}$  groups at surface  $\text{Ce}^{\text{III}}$  cation sites<sup>177</sup>. Another interesting phenomenon concerning this issue is that combining three separately catalytic inactive materials can create an extremely high active complex metal/ $\text{CeO}_2(111)/\text{TiO}_2(110)$  catalyst for WGS reaction<sup>150</sup>. In such system, CNPs are deposited on the  $\text{TiO}_2(110)$  to form nontypical coordinated ceria structures with considerable  $\text{Ce}^{\text{III}}$  states, which not only enhances its reaction activity but also induces a larger dispersion of supported metal nanoparticles on  $\text{TiO}_2(110)$ . The complex structure provides a one-stop arena and facile avenue for WGS reaction in that  $\text{H}_2\text{O}$  can easily dissociate to  $\text{-OH}$  surface groups on the oxide to form low stable intermediates with CO adsorbed on the admetal nanoparticles, and subsequently decompose intermediates to yield  $\text{H}_2$  and  $\text{CO}_2$  at the oxide-admetal interface. Moreover, increasing the size of metallic cations in PRO gives rise to stronger C-O bonds in formate and in turn weakens the C-H bond, which may fasten the dissociation of formate and thus the reaction rate<sup>145</sup>. Meanwhile, DRIFTS analysis suggests C-H bond of formate can be weakened by the incorporation of alkali promoter (for example Na) into Pt-zirconia catalysts<sup>178</sup>. Another way is to externally varying the reaction environment to affect the surface structure of catalysts and thus their catalytic behaviors. One study suggested that in realistic reaction, the content of atmosphere would significantly influence the reaction rate and activity<sup>179</sup>. The reaction kinetics were closely related to two competitive intermediate species, bidentate formate and

unidentate carbonate. The former actively participated in the forward WGS reaction to generate  $H_2$  and  $CO_2$  at the active sites where  $-OH$  surface groups were located, while the latter acted as the spectator but inhibited the forward WGS by blocking the active sites to accommodate formate and absorb  $CO$ . They found that high  $H_2$  concentration greatly reduced the initial reaction rate dependent on the buildup of  $-OH$  surface groups and reactive formate, but high  $CO$  concentration led to pronounced deactivation of forward WGS reaction as it produces a number of reaction-inhibiting unidentate carbonates. In addition, Burch has also pointed out the nature of active catalyst was strongly dependent on the reaction conditions, and the reaction temperature as well as the ratio of  $H_2O$  to  $CO_2$  can drive the dominant WGS reaction transit from a redox-type process to a surface species-mediated one<sup>146,180</sup>. Specifically, the redox mechanism would be anticipated in the presence of high concentrated  $H_2O$  and mainly oxidized surface of the catalyst at high temperatures while the associative mechanism would be generally expected at low temperatures as enough lifetime was given for the formation and dissociation of intermediate species. On the other hand, high  $H_2O$  to  $CO_2$  promoted the formation of formate rather than carbonate and verse visa.

Several studies have suggested inverse oxide/metal catalysts exhibit better performance than conventional metal/oxide catalysts<sup>181,182</sup>. The assumed mechanism for WGS reaction can be viewed as the combination of redox and associate mechanisms and undergo following pathways<sup>182</sup>:



$HCO_{x(ads)}$  stands for three possible intermediate species formed by interacting  $CO$

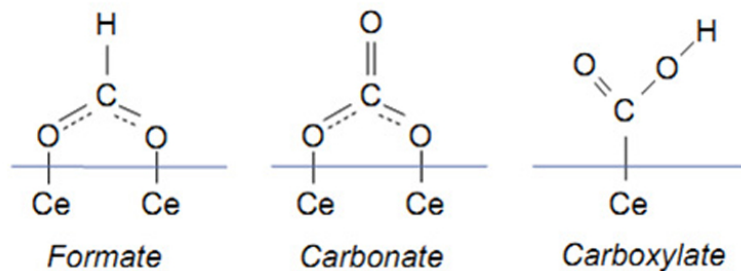


Figure 2.4: Chemical structures of absorbed intermediates on ceria surfaces<sup>182</sup>

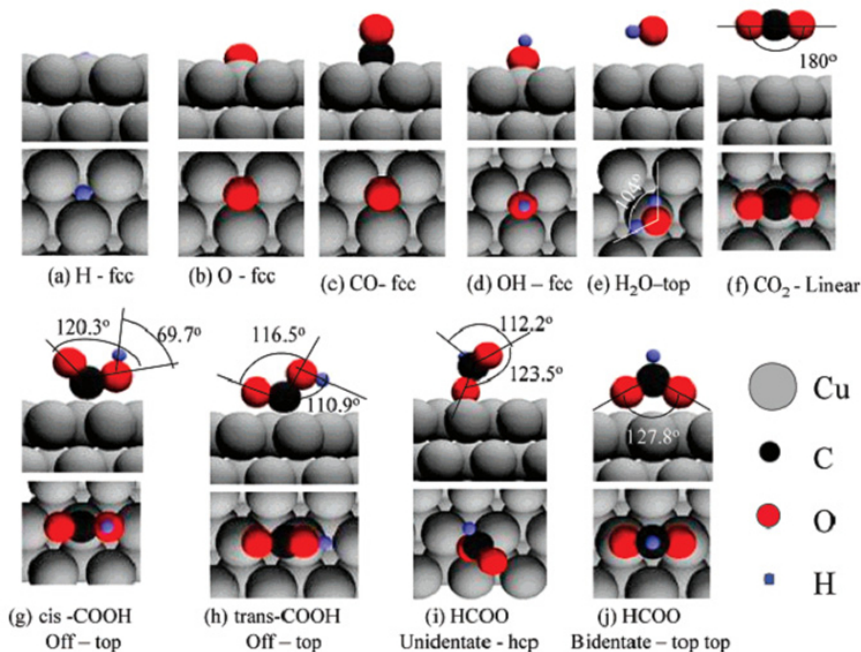


Figure 2.5: Most stable configurations of intermediates on Cu (111)<sup>183</sup>

with  $\text{-OH}$  surface groups, i.e. formate, carbonate and carboxylate, whose structures are shown in Figure 2.4. Compared to carboxylate, formate and carbonate are thermally stable species absorbed on reduced ceria surfaces<sup>182</sup>. The role of ceria involves both generating active sites for WGS reaction and stabilizing essential reaction intermediates<sup>182</sup>.

In the inverse  $\text{CeO}_x/\text{Cu}(111)$  system, a considerable amount of  $\text{Ce}^{\text{III}}$  cations in CNPs were indicated by Ce  $3d$  spectra observed in X-ray photoelectron spectroscopy (XPS), which was considered apparently increasing the catalytic activity and lowered

apparent activation energy of  $\text{CeO}_x/\text{Cu}(111)$  catalyst<sup>181</sup>.

### 2.7.3.2 Computational studies

In general, DFT+U approach has been adopted to study the WGS reaction mechanism of noble metal/ $\text{CeO}_2$  catalysts. The computational model commonly employed 5- to 9-layered ceria slab model with top 2-3 layers to be relaxed and metal clusters on the surface<sup>172</sup>. The basic procedure generally involves: (1) identifying stable species likely present during WGS reaction absorbed on the surface of either noble metal or ceria; (2) calculating the binding energy of identified stable species (including transition states) and analysing their atomic and electronic structural evolutions including bond break/formation and charge transfer; (3) determining the elementary reaction steps that provide the pathway for the transition from one identified stable structure to another based on previously proposed redox mechanism or associative mechanism; (4) calculating the reaction barrier of various elementary reaction steps according to nudged elastic band method; (5) evaluating of the feasibility of assumed mechanisms and mapping out the most possible pathway for those mechanisms. Figure 2.5 shows all the possible intermediates formed on the surface of pure metal during WGS reaction<sup>183</sup>.

DFT calculations have revealed a third mechanism governing the WGS reaction on  $\text{Au}/\text{CeO}_2$  or  $\text{Pt}/\text{CeO}_2$  catalyst system, carboxyl mechanism<sup>172,184–186</sup>, and it was indicated as the dominant WGS reaction mechanism on  $\text{Cu}(111)$ <sup>183</sup> and  $\text{Au}(111)$  catalysts<sup>155</sup>. DFT calculation showed that the decomposition of  $-\text{COOH}$  required overcoming the highest energy barrier<sup>184</sup>; however, the most difficult step was the dissociation of  $\text{H}_2\text{O}$  and reduced  $\text{CeO}_2(111)$  can facilitate this process<sup>185</sup>. Chen further argued that for  $\text{Au}/\text{CeO}_2$  catalysts, the active reaction site for  $\text{H}_2\text{O}$  dissociation was neither on Au cluster nor on ceria support as the relevant reaction on these two sites exhibited too high energy barrier<sup>172</sup>, but at the interface between Au cluster and

ceria surface with O-vacancies nearby<sup>186</sup>. CO was oxidized on Au cluster by tilting towards nearby OH to form *trans*-COOH. Instead of directly breaking O-H bond on Au cluster<sup>172</sup>, *trans*-COOH passed its H onto OH nearby to release CO<sub>2</sub>, through which the activation barrier of breaking O-H bond was significantly lowered. All DFT calculations have consistently indicated that H<sub>2</sub> was produced via combining two atomic H adsorbed on the metal<sup>155,183–188</sup>.

#### 2.7.4 Brief summary of previous studies

The WGS mechanism and reaction kinetics is controlled by the nature of catalytic systems and reaction environment. The panoramic picture of WGS reaction on metal/ceria catalyst involves three key step, namely CO oxidation, H<sub>2</sub>O dissociation and H<sub>2</sub> generation. CO will preferably adsorb onto the metal and its oxidation generally follow two pathways. One is directly oxidized by surface O atom on ceria support based on the redox mechanism while the other is first forming an intermediates with nearby –OH surface groups and then being decomposed by H<sub>2</sub>O or –OH surface groups to release CO<sub>2</sub> obeying the associative mechanism. It is worth noting that the decomposition of these intermediate species can be rate-determining step for overall WGS reaction and their concentration as well as stability are very environment-dependent, for instance, reaction temperature and partial pressures of CO, H<sub>2</sub>O and CO<sub>2</sub>. H<sub>2</sub>O dissociation is another crucial reaction step for both mechanisms and the feasible pathways occur at places where activation energy of breaking O-H bond is lowest, possibly at interfaces between metal and ceria support. H<sub>2</sub> production is unanimously realized through combining two surface H adatoms located on the metal. Both metal and ceria support are indispensable components for the WGS reaction as they both facilitate lowering the energy barrier of H<sub>2</sub>O dissociation and fasten the decomposition of intermediate species. Is this picture consistent with catalytic mechanism of uCNPs? Are there any alternative catalytic mechanism available for uCNPs? We will



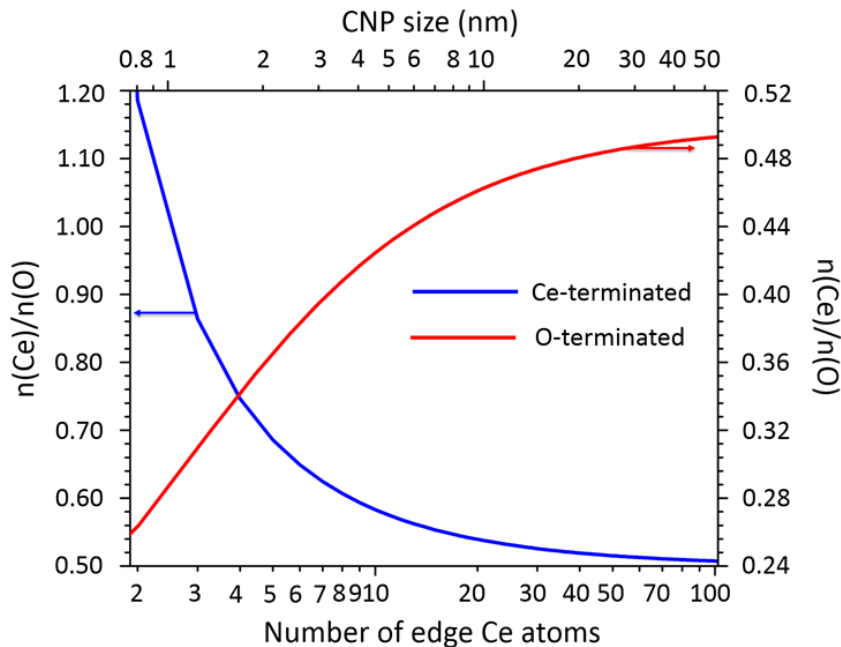


Figure 2.6:  $n(\text{Ce})/n(\text{O})$  as a function of CNP size for Ce-terminated (blue) cubic CNPs and O-terminated (red) cubic CNPs.

discuss different options for uCNPs to catalyze WGS reaction in this dissertation.

## 2.8 Challenges in computational modeling of ultra-small ceria nanoparticles (uCNPs)

### 2.8.1 Problems arising from constructing uCNPs with ideal, stoichiometric, bulk-cut surface configurations

Despite all previous computational studies on octahedral shaped and cuboctahedral shaped CNPs have constrained themselves to ideal, stoichiometric, bulk-cut surface configurations, in the following we will show that in fact, it is impossible to intuitively construct uCNPs of any experimentally observed shape with ideal stoichiometric, bulk-cut surface configurations.

For cubic  $\{001\}$ -terminated CNPs with  $N$  Ce atoms along each edge, there are  $4N^3$  Ce atoms and  $(2N - 1)^3$  “bulk” O atoms internal to the CNP. In the absence

of additional O atoms (e.g., for a Ce-terminated CNP) the ratio of Ce to O atoms,  $n_{Ce}/n_O$ , is:

$$\frac{n_{Ce}}{n_O} = \frac{4N^3}{(2N-1)^3} \quad (2.5)$$

If the CNP surface is fully O-terminated—that is, if every surface O lattice site is occupied by one O atom—there are 4 additional O atoms at the corners,  $12(2N-1)^2$  at edges and  $6(2N-1)^3$  at facets. Thus,  $n_{Ce}/n_O$  becomes

$$\frac{n_{Ce}}{n_O} = \frac{4N^3}{(2N-1)^3 + 6(2N-1)^2 + 12(2N-1) + 4} \quad (2.6)$$

Figure 2.6 plots  $n_{Ce}/n_O$  as a function of CNP size for cubic  $\{001\}$ -terminated CNPs with either Ce- or O-terminations. In both cases,  $\text{CeO}_2$  stoichiometry (that is  $n_{Ce}/n_O \equiv 0.5$ ) is a limiting case, and cannot be achieved for cubic  $\{001\}$ -terminated CNPs of finite size. Constructing a finite, cubic  $\{001\}$ -terminated CNP with exact  $\text{CeO}_2$  stoichiometry therefore requires either deleting some fraction of O atoms present in O-terminated CNPs, or deleting Ce atoms from Ce-terminated CNPs.

For octahedral  $\{111\}$ -terminated with  $N$  Ce atoms along each edge, there are  $N(2N^2+1)/3$  Ce atoms and  $4N(N-1)(N+1)/3$  “bulk” O atoms. In this case “bulk” O atoms include those O atoms present as part of stoichiometric  $\{111\}$  surfaces. Note that though  $\{111\}$  CNP facets are stoichiometric, their edges and corners are not. For octahedral  $\{111\}$ -terminated CNPs with no additional O atoms at edges and corners (this is the Ce-terminated case), the ratio of Ce to O atoms,  $n_{Ce}/n_O$ , is:

$$\frac{n_{Ce}}{n_O} = \frac{2N^2+1}{4(N^2-1)} \quad (2.7)$$

As above if every surface O lattice site is occupied by one O atom (the O-terminated limit) there are 24 additional O atoms at the CNP corners,  $24(N-2)$  at edges and  $4(N-2)(N-3)$  at facets. In this case the total number of O atoms becomes

$$\begin{aligned} & \frac{4N(N-1)(N+1)}{3} + 24(N-2) + 24 + \\ & 4(N-2)(N-3) = \frac{4N(N+1)(N+2)}{3} \end{aligned} \quad (2.8)$$

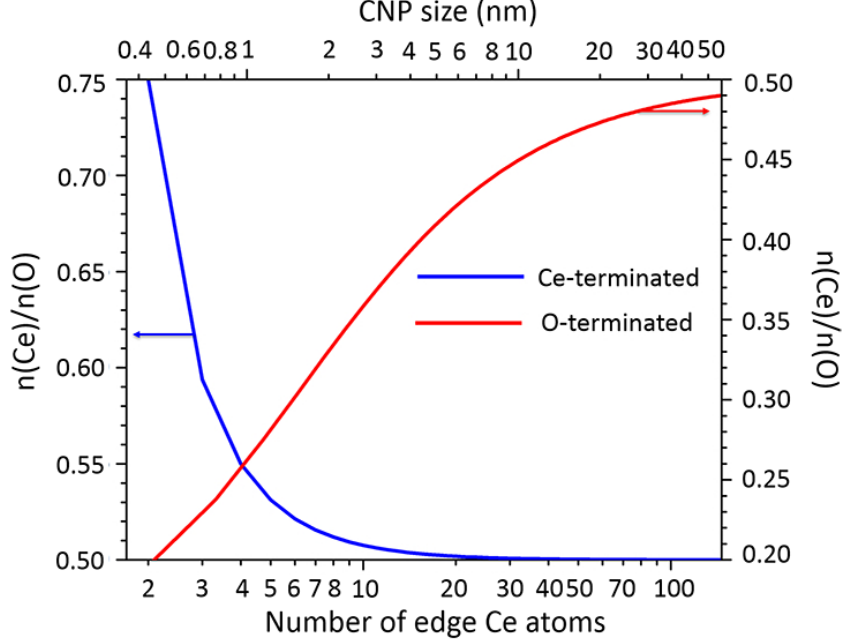


Figure 2.7:  $n(\text{Ce})/n(\text{O})$  as a function of CNP size for Ce-terminated (blue) octahedral CNPs and O-terminated (red) octahedral CNPs.

Thus, for octahedral  $\{111\}$ -terminated CNPs with all surface O lattice sites occupied by O atoms (this is the O-terminated case),  $n_{\text{Ce}}/n_{\text{O}}$  becomes

$$\frac{n_{\text{Ce}}}{n_{\text{O}}} = \frac{2N^2 + 1}{4(N + 1)(N + 2)} \quad (2.9)$$

Figure 2.7 plots  $n_{\text{Ce}}/n_{\text{O}}$  as a function of CNP size for octahedral  $\{111\}$ -terminated CNPs with either Ce- or O-terminations. As for the  $\{001\}$ -terminated CNPs discussed above, exactly stoichiometric finite-sized  $\{111\}$ -terminated CNPs can only be constructed by removing O atoms or Ce atoms from O-terminated or Ce-terminated CNPs, respectively.

### 2.8.2 Challenges to construct realistic, physically-representative uCNPs

Computing properties that are quantitatively comparable to experimental results requires the construction of realistic, physically-representative structures as calculation inputs. For bulk crystalline systems this is relatively straightforward as well-

established experimental techniques have been used to determine precise unit cell configurations for most common materials (including, of course, the two bulk structures of ceria<sup>189</sup>). Systems containing surfaces introduce the added complexity of determining (i) the local (surface) concentration of atoms and (ii) their local configuration at the surface itself. For crystal facets, these complexities are somewhat mitigated by the availability of experimental techniques (e.g. LEEM) capable of determining surface symmetry<sup>190,191</sup>. Also, the contiguous nature of bulk crystal facets generally constrains configurational complexity to identifiable rearrangements of the underlying bulk structure. Even so, surface structure (and composition) determination is an active and challenging research area<sup>26,192,193</sup>.

For nanoparticles the complexities of bulk surface systems are only exacerbated by the necessity of selecting the correct *set* of surfaces that define the three-dimensionally constrained structure. This, of course, translates as needing to know the actual shape of a nanoparticle. As an extension, not only must the local arrangements of atoms in surface facets be determined, but also the local arrangement and distribution of atoms at facet intersections (edges and corners), and the changes in atomic configurations on surface facets due to nearby edges. Finally, for small nanoparticles, large surface-to-volume ratios can even cause changes in the internal bulk atomic arrangement within the nanoparticle.

In CNPs, nanoparticle shape has been well-characterized experimentally, with TEM and XRD studies reporting octahedral, cuboctahedral and cuboidal shapes<sup>11,114,115,194–198</sup>. In addition, experimental studies primarily report that such CNPs have  $\{100\}$  and/or  $\{111\}$  facets<sup>11,114,115,194–198</sup>. In combination with calculated results for semi-infinite slabs (which find that  $\{111\}$ ,  $\{110\}$  and  $\{100\}$  surfaces have the lowest energy<sup>32,33,75,76</sup>), this existing body of experimental work has motivated quantum mechanical calculations of CNPs to focus on octahedral and cuboctahedral CNPs similar to those observed experimentally<sup>114,115,196,198</sup>. The availability of experimental results to in-

form atomistic calculations with regards to nanoparticle *shape* is in stark contrast to the lack of experimental results addressing the question of the detailed atomic arrangements and relative compositions of atoms at CNP surfaces.

The lack of experimental information regarding detailed arrangements of atoms at CNP surfaces leads immediately to a key challenge in constructing input atomic configurations for the computational modeling of CNPs. Consider building a  $\sim 1$  nm  $\{111\}$ -terminated octahedral CNP, similar to those observed experimentally<sup>114,115,196,198</sup>. Beginning with a bulk cubic fluorite  $\text{CeO}_2$  structure, we may cut eight intersecting  $\{111\}$  planes to form an octahedron with a diameter of  $\sim 1$  nm. The structure has 44 Ce atoms, and the atomic arrangement internal to the CNP is stoichiometric (as these atoms are simply arranged in the ideal bulk cubic fluorite structure). In addition, the  $\{111\}$  surfaces themselves have a stoichiometric O-termination (as observed via, e.g., STM<sup>24</sup>). But, as shown in Figure 3.4f, the edges and corners of the CNP are not stoichiometric, and require that a configurational choice be made. If all edge and corner O sites are occupied (as shown in Figure 3.4f, where blue balls are O atoms at facet, edge, and corner O lattice sites), the structure contains eighty excess O atoms ( $\text{Ce}_{44}\text{O}_{160}$ ). How do we best model real  $\{111\}$  CNPs? Previous studies focusing on ideal, bulk-terminated CNP surfaces and stoichiometric CNPs have removed all surface O atoms (blue balls in Figure 3.4f) and four (of six) arbitrarily chosen corner Ce atoms to force a stoichiometric  $\text{Ce}_{40}\text{O}_{80}$  structure. While a single result finds that CNPs with isolated excess O atoms at bulk O lattice sites are energetically unfavorable<sup>113</sup> and a number of calculations have considered partially reduced CNPs<sup>36,112,113,116–119</sup>, no comprehensive exploration of the stability of CNPs versus O facet/edge/corner concentration has been completed.

Beyond this (relatively) straightforward case of octahedral  $\{111\}$ -terminated CNPs, we must also consider other CNP shapes that have been experimentally observed, particularly those reported to have high catalytic activity. CNP cubes, for

example, are bounded by six  $\{100\}$  surfaces, have been observed experimentally, and  $\{100\}$  surfaces are reported have particularly high activity<sup>194,196,197,199,200</sup>. In this case the  $\{100\}$  surface itself does not have a stoichiometric termination, and even greater configurational gymnastics must be contemplated if we are to determine the stable CNP configuration. For example, a  $\sim 1$  nm CNP cube with all surface O lattice sites occupied has composition  $\text{Ce}_{32}\text{O}_{121}$ . To construct a stoichiometric CNP requires the removal of 57 O atoms. As there are an even number of facets, edges and corners on a cubic CNP, there is no possible way to achieve stoichiometry by removing O atoms evenly from facets, edges and/or corners!

## 2.9 Brief proposal to address the challenges in studying the surface structure of uCNPs

Ultimately, as catalysis is a surface process, understanding the atomistic concentrations and configurations at CNP surfaces is critical to accurately modeling their catalytic mechanisms. In general, it is not possible to intuit the stable concentration or configuration of surface species, as highlighted by the challenges of constructing atomistic input structures. This is even more an issue when it is noted that catalysts are both synthesized and applied in open systems where the environment the nanoparticle catalyst is in can serve as a source and/or sink of atoms or molecules. Therefore, in the absence of clear experimental information as to the detailed surface structures of real CNPs, computational attempts to characterize CNP properties must systematically investigate CNP structures without assuming particular concentrations or configurations of atoms at CNP surfaces.

In this dissertation work, we will specifically address this challenge from several points. Firstly, we will show how to construct realistic, physically-representative uCNP structures as calculation inputs based on existing experimental data and observations (see **section 3.4**). Secondly, we will systematically examine the structure

and energy of  $\sim 1\text{--}1.5$  nm CNPs with unconstrained surface concentrations and configurations of O atoms, simply to explore whether alternative surface rearrangement is possible specifically for nanoscale CNPs, while the constraint of ideal, stoichiometric, bulk-cut  $\text{CeO}_2$  surface configuration is eliminated (see **chapter 4**). Thirdly, we consider the above question dynamically and more closely to the reality of synthesizing, characterizing and applying uCNPs by taking into account the comprehensive environmental factors, for instance, temperature, partial pressure of ambient gases, and pH, etc. We will further examine whether and how surface configurations of uCNPs evolves in response to varying environmental factors (see **chapter 6**).

## Chapter 3 Theoretical backgrounds and computational methods

### 3.1 Quantum mechanical calculation methods

#### 3.1.1 Introduction

In this dissertation, we will employ density functional theory (DFT) based quantum mechanical calculations to study the structure and catalytic properties of uCNPs. Quantum mechanical calculation is basically a method to find the lowest energy state of a complicated multi-object interaction system containing numerous nuclei and electrons. Based on Born-Oppenheimer(BO) approximation and DFT, the energetics of such a complicated system can be simplified into solving a 3-dimensional Schrödinger equation interpreting the full wave function only as a function of the total electron density. Fully quantum DFT calculations allow the atomic arrangement to vary according to Coulomb forces acting on each atom determined by the distribution of valence electrons until the minimum energy distribution is reached, thus determining the relaxed atomic arrangement of studied system, i.e. the local ground state structure of studied system (here uCNPs in this research work) at 0 K. That said, to obtain the the minimum energy structure, we simply need to follow two steps: (1) find an appropriate total electron density that redistributes electrons into a lowest energy configuration, (2) based on this electron density, moving nuclei around to reach the minimum energy state. This idea is actually implemented in the commercial software we use to do calculations by going through two sets of loops: (1) electronic minimization loops, firstly fixing the positions of nuclei and allowing electrons to redistribute; and (2) ionic minimization loops, then allowing nuclei to rearrange in response to the given minimum energy electronic configuration. DFT quantum mechanical calculation is a fitting and accurate approach to explore the



minimum atomic and electronic structures of uCNPs. On the one hand, without knowing a good guess of the structure in advance, DFT calculations enable us to find (local) minimum energy atomic configurations of uCNPs through the robust relaxation algorithms, even starting from arbitrary atomic configurations of uCNPs. On the other hand, the distribution of  $\text{Ce}^{\text{III}}$  and  $\text{Ce}^{\text{IV}}$  cations within uCNPs, which is a headache in other quantum mechanical calculation methods, need not to be identified as a prior in DFT based quantum mechanical calculations, but their actual charge state and distribution are determined as an output of DFT calculations. According to thermodynamics, once we have solved the Schrödinger equation and obtained ground state energy of a uCNP structure, we can then derive mathematical formula to calculate the formation energies of various structured uCNPs. By comparing the formation energies of various structured uCNPs, the one with lowest value can be considered as the most stable uCNP structure. Furthermore, the catalytic properties of uCNPs is related to the change of structures and energies which reflect the electronic interactions that control catalysis. Information regarding electron transfer and related energetics can be extracted from analyzing the calculated charge density as well as electronic and phonon density of states of interested uCNP structures, which are all direct outputs from DFT quantum mechanical calculations.

### **3.1.2 The Schrödinger equation and Hartree-Fock approximation**

To describe the collective properties of the assembly of well-defined atoms, we need firstly to know how their energies evolve in response to the variation of their spatial arrangement. In order to locate an atom, we need to define the positions of both its nucleus and its surrounding electrons. The BO approximation is adopted to simplify this problem by separately treating the mathematical problems of the nuclei and electrons<sup>201</sup>. The BO approximation rests on the assumption that electrons respond much more rapidly than nuclei to changes in their surroundings, as electrons are

much lighter. We first fix the positions of nuclei, and solve the equations describing electron motions to obtain the lowest energy state of electrons in this given field of nuclei. Then, the ground state energy  $E$  of the collective atoms can be expressed as a function of the positions of these nuclei. The Schrödinger equation is such an equation that describes the quantum state of a physical system<sup>202</sup>.

$$\hat{H}\psi = E\psi. \quad (3.1)$$

In this equation,  $\hat{H}$  is the Hamiltonian operator and  $\psi$  is a set of solutions, or eigenstates, of the Hamiltonian. Each of these solutions,  $\psi_n$ , has an associated eigenvalue,  $E_n$ , a real number that satisfies the eigenvalue equation.

The Hartree product is used to simplifying the N-electron Schrödinger equation by approximating the N-electron wave function into a product of individual one-electron wave functions,

$$\psi = \psi_1(\mathbf{r})\psi_2(\mathbf{r}), \dots, \psi_N(\mathbf{r}). \quad (3.2)$$

The form of the N-electron wave function  $\psi$  indicates that the its exact form can not be known without finding mutually dependent individual one-electron wave function,  $\psi_i(\mathbf{r})$ <sup>203</sup>. However, the wave function for any collection of N electrons cannot be directly observed. What is interesting to us is the probability of randomly ordered N electrons at coordinates  $\mathbf{r}_1, \mathbf{r}_2, \dots, \mathbf{r}_N$ , namely, the density of electrons at a particular position in space  $n(\mathbf{r})$ , which can be observed. This can be written in terms of the individual electron wave functions as

$$n(\mathbf{r}) = 2 \sum_i \psi_i^*(\mathbf{r}) \psi_i(\mathbf{r}). \quad (3.3)$$

Several points need to be noted out in Equation 3.3. First, the term inside the summation is the probability that an electron is located at position  $\mathbf{r}$ . Second, the factor of 2 at front takes into account that two electrons with different spins can occupy same individual electron wave function. Third, this equation simplifies a very

complicated mathematical problem of solving 3N-dimensional Schrödinger equation into a simple one of solving a 3-dimensional Schrödinger equation by interpreting the full wave function only as a function of the total electron density  $n(\mathbf{r})$ .

The anti-symmetry of the wavefunction must be considered when solving the Schrödinger equation to obtain many-electron wavefunction  $\psi$ . The Slater determinant constructed from single-particle wavefunctions, as follows, obeys above principle:

$$\psi_{HF}(\mathbf{r}_1\sigma_1, \dots, \mathbf{r}_N\sigma_N) = \frac{1}{\sqrt{N!}} \begin{vmatrix} \psi_1(\mathbf{r}_1\sigma_1) & \cdots & \psi_1(\mathbf{r}_N\sigma_N) \\ \psi_2(\mathbf{r}_1\sigma_1) & \cdots & \psi_2(\mathbf{r}_N\sigma_N) \\ \vdots & \ddots & \vdots \\ \psi_N(\mathbf{r}_1\sigma_1) & \cdots & \psi_N(\mathbf{r}_N\sigma_N) \end{vmatrix}. \quad (3.4)$$

where the single electron eigenfunctions,  $\psi_i(\mathbf{r}_i\sigma_i)$ , are the solutions of an effective one-particle Hamiltonian representing a single electron in an effective potential constructed from the electrostatic field of all other electrons in the system-thus eliminating any self-interaction. While Hartree-Fock theory and the Slater determinant correctly account for the effects of electron exchange, they do not fully account for the correlation of electrons of opposite spin. As a common and successful method of doing so, let us introduce an alternative formulation for the total energy of a many body system, one based on DFT.

### 3.1.3 Density functional theory (DFT)

Kohn and Hohenberg put forward two theorems in the mid-1960s that have become the foundation of the whole DFT<sup>204</sup>. The first theorem is: *The ground-state energy from Schrödinger's equation is a unique functional of the electron density*<sup>204</sup>. This theorem shows that the ground-state wave function is directly determined by the ground-state electron density and reduces a 3N-dimensional problem to 3-dimensional problem in terms of find the ground-state energy of an N-electron system. Unfortunately, the first Hohenberg-Kohn theorem only tells us the existence of such a func-

tional of the electron density but nothing about the actual form. The second theorem states: *The electron density that minimizes the energy of the overall functional is the true electron density corresponding to the full solution of the Schrödinger equation*<sup>204</sup>. This statement provides us a way to find the electron density, i.e. varying the electron density until the energy of the overall functional reaches its nadir. The energy of a considered system can be written in terms of the single-electron wave functions  $\psi_i$  as:

$$E[\{\psi_i\}] = E_{known}[\{\psi_i\}] + E_{XC}[\{\psi_i\}]. \quad (3.5)$$

$E_{known}[\{\psi_i\}]$  is composed of four contributions:

$$\begin{aligned} E_{known}[\{\psi_i\}] = & \frac{\hbar^2}{m} \sum_i \int \psi_i^* \nabla^2 \psi_i d^3r + \int V(\mathbf{r}) n(\mathbf{r}) d^3r \\ & + \frac{e^2}{2} \int \int \frac{n(\mathbf{r}) n(\mathbf{r}')}{|\mathbf{r} - \mathbf{r}'|} d^3r d^3r' + E_{ion}, \end{aligned} \quad (3.6)$$

which in order are the electron kinetic energies, the Coulomb interactions between the electrons and the nuclei, the Coulomb interactions between pairs of electrons, and the Coulomb interactions between pairs of nuclei.  $E_{XC}[\{\psi_i\}]$ , is the exchange-correlation functional encompassing, by definition, all other quantum mechanical effects that are not included  $E_{known}[\{\psi_i\}]$ . The Kohn-Sham single-particle equations are then:

$$\left[ \frac{\hbar^2}{2m} \nabla_i^2 + V(\mathbf{r}) + V_H(\mathbf{r}) + V_{XC}(\mathbf{r}) \right] \psi_i = \varepsilon_i \psi_i. \quad (3.7)$$

$V(\mathbf{r})$  defines the interaction between an electron and all nuclei and any external field.  $V_H(\mathbf{r})$  describes the Coulomb repulsion between the electron considered and the total electron density.  $V_{XC}$  expresses exchange and correlation contributions to the single-electron equations and can be mathematically defined as:

$$V_{XC}(\mathbf{r}) = \frac{\delta E_{XC}(\mathbf{r})}{\delta n(\mathbf{r})}. \quad (3.8)$$

It is not feasible to solve the Kohn-Sham (KS) equations exactly for all points in space. Therefore a number of simplifications are undertaken when applying KS

method. The first simplification makes use of the Bloch Theorem<sup>205</sup> based on the periodic nature of crystalline materials. The domain of the KS equations is reduced from all space (real space) to a finite region of space (reciprocal space), the first Brillouin zone. A further simplification is approximating an integral over all k-points in the first Brillouin zone as a sum over some subset of special k-points in the first Brillouin zone. Monkhorst and Pack<sup>206</sup> have shown that, in reciprocal space, the rapidly varying terms in the expansion of charge density over k points may be truncated. Thus a sufficiently accurate  $n(\mathbf{r})$  may be derived from  $\psi_i$  evaluated only in reciprocal space at a set of "special k-points which are further selected to most efficiently expand  $n(\mathbf{r})$  and take advantage of the crystalline lattice symmetry<sup>207</sup>. Again to simplify the calculation, these functions are generally expanded in plane waves as:

$$\psi_{i,\mathbf{k}}(\mathbf{r}) = \sum_m c_{i,m}(\mathbf{k}) \exp(i(\mathbf{k} + \mathbf{G}_m)\mathbf{r}). \quad (3.9)$$

Here  $\mathbf{G}_m$  is a translation between reciprocal points and lattice points, and  $\mathbf{k}$  is the reciprocal points in the first Brillouin zone. The magnitude of vectors  $\mathbf{G}$  represents the kinetic energy of the plane wave described by  $\mathbf{G}$  in the expansion of  $u_{i,\mathbf{q}}(\mathbf{r})$  in plane waves  $u_{i,\mathbf{q}}(\mathbf{r}) = \sum_{\mathbf{G}} c_{i,\mathbf{q}}(\mathbf{G}) \exp(i\mathbf{G}\mathbf{r})$ . Specifying a maximum  $|\mathbf{G}|$ , equivalent to specifying the cutoff kinetic energy of plane waves included in the expansion of  $u_{i,\mathbf{q}}(\mathbf{r})$  is an additional simplification solve the KS equations.

### 3.1.4 The pseudopotential method

To further improve the computational efficiency, the number of expanded plane waves to model KS orbitals should be minimized without losing the required accuracy. This is challenging given the strongly varying potential field, and, subsequently, the strongly varying wave function, in regions near the atomic cores. Since only the valence electrons of an atom are strongly perturbed by forming/breaking chemical bonds, it is reasonable to replace the full potential of the atomic nucleus with a pseudopotential

composed of the combination of the core (non-valence) electron structure and the nucleus itself. In this way we both reduce the number of calculated orbitals and smooth the variations of the potential. Pseudopotentials are generated by a mathematically rigorous recasting of the full all-electron calculated eigenfunctions, and are known to be associated with experimentally observable properties such as scattering factors. Pseudopotentials are transferrable in that they accurately reproduce the behavior of systems of atoms in various configurations. The “softness” of a pseudopotential represents how smoothly it varies in the region of the atomic core. The softer the pseudopotential, the smaller the number of plane waves necessary to accurately expand the eigenfunctions. For elements with complex bonding characteristics, such as multiple valence configurations, care must be taken when selecting which electrons to include as part of the pseudopotential and which to treat as valence electrons. Vanderbilt<sup>208</sup> has proposed that the ionic potential can be modeled as a smoothly varying function in combination with an auxiliary function which acts near each ion core when constructing a pseudopotential.

## **3.2 Computational settings and convergence**

### **3.2.1 Introduction**

To perform self-consistent, minimum cost calculation and at the same time produce reliable computational results, we need to carefully choose a series of computational settings and keep them consistent throughout the entire research work. In the following, we will show that four settings are minimum requirements and indispensable elements to carry out reasonable computational study on uCNPs. They are k points, cutoff energy, exchange-correlation functional and Hubbard U correction. To determine whether the choice of them is appropriate, we need a consistent criterion. Basically, we need to test how the calculated ground state energy of a considered system evolves with different choices of those settings. When the calculated ground

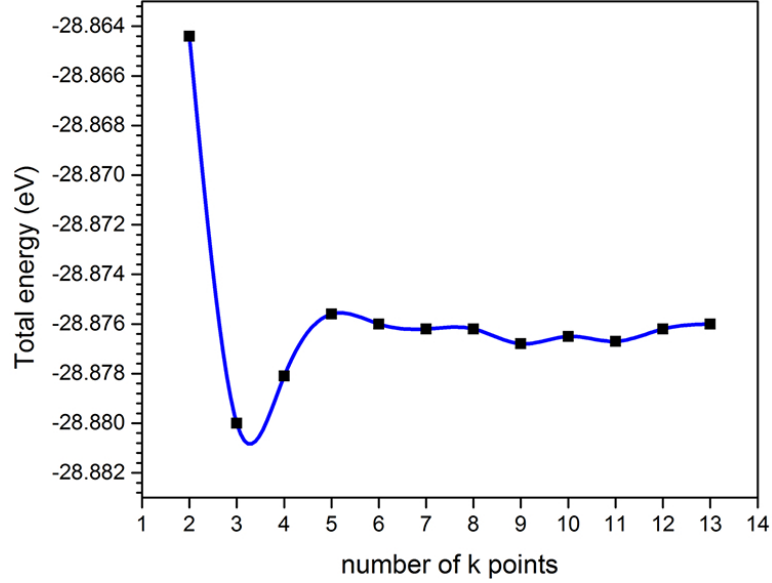


Figure 3.1: Calculated total energy as a function of the number of k points for the primitive cell of  $\text{CeO}_2$ .

state energy does not vary beyond a small scale of value, the calculation is deemed as converged, and the small scale of value is the convergence criterion of your selection.

### 3.2.2 Choice of k points

The wave function is expanded as a set of plane wave functions within the first Brillouin zone, and is integrated over a set of special k points. The number of k points used to integrate the Brillouin zone is directly related to the calculation accuracy and computation cost. We prefer to use the smallest number of k points necessary to accurately model the wave function. To choose an appropriate density of k points, a series of computational tests need to be carried out. The test is to calculate the ground state energy of the reference primitive cell of bulk ceria with different densities of k points. Since the calculated supercell is cubic, the number of k points needed to achieve a uniform density in three mutually perpendicular directions are the same. A plot of energy variation with the number of k points per reciprocal lattice vector from 1 to 10 has shown that the number of k points should use 7, which is the

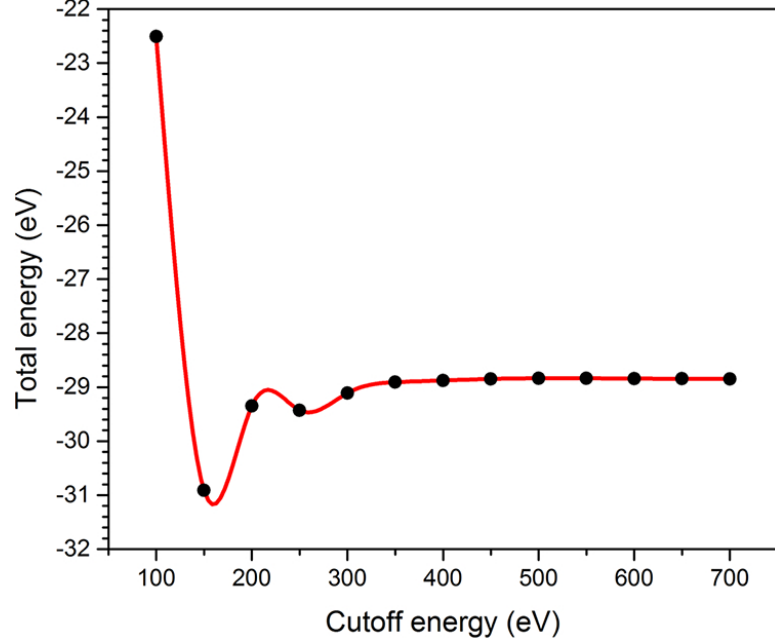


Figure 3.2: Calculated total energy as a function of the cutoff energy for the primitive cell of  $\text{CeO}_2$ .

smallest  $\mathbf{k}$  points that lead to a converged ground state energy of the primitive cell (see Figure 3.1). In actual calculation of uCNPs, the  $\mathbf{k}$ -point density is kept consistent. As the supercells used to calculate uCNPs are at least 7 times bigger than that of the primitive cell on each axis, the number of  $\mathbf{k}$  points per reciprocal lattice vector should be at most 1. Therefore, Monkhorst-Pack grid of the gamma  $\mathbf{k}$ -point only is chosen for uCNP cells.

### 3.2.3 Choice of cutoff energy

The cutoff energy  $E^{cut}$  is the kinetic energy used to expand plane waves in the first Brillouin zone, defined as:

$$E^{cut} = \frac{\hbar^2}{2m} |\mathbf{G}|^2. \quad (3.10)$$

Here,  $\mathbf{G}$  is the same as that defined in Equation 3.9 (see detailed explanation of Equation 3.9 in **section 3.1.3**). The calculation precision is the level of the convergence of calculated absolute energies. In VASP, high calculation precision will ensure that



the absolute energies are converged to a few meV. Similar to the way of determining k points in calculations, a series of convergence tests need to be carried out to decide the value of cutoff energy. Based on the principle that selecting the smallest number of cutoff energy resulting in an invariant absolute energy of the calculated primitive cell of bulk ceria (see Figure 3.2), cutoff energy of 400 eV is chosen.

### 3.2.4 Choice of exchange-correlation functional

A critical problem to solve the KS equations is that we must know the form of the exchange-correlation functional  $E_{XC}[\{\psi_i\}]$  in advance so as to use DFT. However, its exact form is simply unknown to us. Therefore, we need to find an effective approximation for such a functional. One good approximation is defining the true exchange-correlation functional as that derived for the local electron density of the homogenous electron gas—this is the local density approximation (LDA)<sup>204,209</sup>,

$$V_{XC}(r) = \int d^3\mathbf{r} n(\mathbf{r}) e_{XC}([n], \mathbf{r}). \quad (3.11)$$

Here we choose the exchange-correlation energy per electron at some point  $\mathbf{r}$ ,  $e_{XC}([n], \mathbf{r})$ , to be a function only of the local electron density,  $n(\mathbf{r})$ . Another approximation is the generalized gradient approximation (GGA)<sup>210</sup>, considering both the local electron density and the local gradient in the electron density. It is typically not possible to determine a priori which form of the exchange-correlation potential will give more accurate results. For the present work it is sufficient to point out that the LDA has proven successful and robust at predicting total energies and structures of numerous systems, including the uCNPs<sup>60,62,65,108,117</sup>. Also, the limitations of the LDA are well-documented<sup>211</sup>, and principally relate to an effective overbinding relative to other exchange-correlation approximations, an effect which can be corrected where necessary. GGA is also widely used to study ceria system, especially when it comes to systems involving H atoms<sup>48,85,88,212</sup>. In this research work, we will compare the energy variation trends using both LDA and GGA to relax uCNPs, and decide which

one is appropriate according to specific cases. In the case of LDA, exchange and correlation were described by the Ceperley-Alder functional<sup>213</sup> as parametrized by Perdew and Zunger<sup>209</sup>. While in the case of GGA, exchange and correlation were described at the level of the generalized gradient approximation (GGA), using the Perdew-Burke-Ernzerhof (PBE) formalism<sup>210</sup>.

Once a particular approximation for the exchange-correlation term has been selected, the eigenfunctions and eigenvalues of Equation 3.7 no longer specify true electron orbitals. Rather these “KS orbitals” define quasi-particle states which have no definite physical meaning. Within DFT these states have a definite mathematical meaning, as they are the derivative of total energy with respect to the occupation of a given state.

### 3.2.5 Choice of Hubbard U correction

Pure LDA and GGA often fails to accurately describe systems with localized  $d$  and  $f$  electrons. Therefore, the Hubbard U correction as formulated by Dudarev<sup>61</sup> was applied to the Ce 4f electrons with U values in the range of 1 — 5 eV considered in order to examine the effects of  $f$ -electron localization on the present results<sup>36,60,65</sup>. For detailed explanation of Hubbard U correction, please refer to section 2.2.3.

### 3.2.6 Bader charge analysis

Atomic charges are calculated according to the Bader procedure<sup>214</sup> and provide a qualitative assignment of electrons to particular ions. The charge assigned to a particular atom, on the atomic scale, is generally considered as the integration of electron densities over a selected volume surrounding the atom of interest. The way to partition the atomic volume follows the principle that the gradient of electron densities approaches zero at every point on the surface defining the boundary between two selected neighboring atomic volumes. Therefore, the macroscopic understanding on

the electronic charge of a specific atom, counting integer numbers of electrons lost or gained from a particular atom, is not quantitatively equivalent to the assigned Bader charge of that atom. However, the one-to-one mapping relationship can be both qualitatively and quantitatively obtained via the comparisons based on atoms within bulk structures.

### 3.2.7 Nudged elastic band calculation

To locate the transition state and further find reaction pathways, the nudged elastic band (NEB) method is employed if both the initial and final states of that reaction step is known beforehand. This method is primarily force based to search minimum energy path linking the initial and final states for a given reaction process. Typically, a set of intermediate states (also called as “images”) likely evolving from the initial state to the final state is constructed and subjected to NEB calculation. During the calculation, this set of images will be constrained via a string force whose intensity (similar to the elastic coefficient of a spring that connects all images along with both the initial and the final states) is specified in the calculation setting by the *SPRING* flag. Such an algorithm will facilitate locking one image into the transition state and minimizing the energy of this string of images on the whole.

### 3.2.8 Dynamical matrix calculation

Dynamical matrix (DM) calculation can be used to correct the required energy barrier of a particular reaction pathway by excluding the zero-point energy difference between the initial and the transition state. It applies the harmonic approximation to the potential to which all atoms vibrate in response, and the calculation result is analyzed to evaluate the vibration energy contribution from a specific geometry of atoms.

### 3.2.9 Relaxation convergence criterion

In the VASP calculation, iteration is used to obtain the self-consistent result. To break the iterative calculation and finish the calculation, the allowed error in calculated total energy and the break condition for ionic relaxation loop should be specified. These are also known as relaxation convergence criterion. In this research work, the allowed error in total energy is set within the range of  $10^{-5}$  —  $10^{-3}$  eV and the break condition for ionic relaxation loop is set within the range of  $10^{-4}$  —  $10^{-3}$  eV, respectively. Generally, for structural relaxation, the criterion is set towards the lower end, while for IR spectrum, NEB along with DM calculations are set towards the higher end. All considered structures were relaxed without symmetry restrictions according to the calculated interatomic forces until maximum residual atomic forces were less than  $0.04 \text{ eV } \text{\AA}^{-1}$ .

### 3.2.10 Calculation precision

DFT calculations by default have two sources of error: (1) exchange-correlation functional approximation; and (2) convergence criteria. The former error is due to the fact that the exact form of exchange-correlation functional is not known, all practically performed DFT calculations employ an approximated exchange-correlation functional. In particular for this dissertation work, both LDA and GGA are employed. Both previous work<sup>56,62,64–66</sup> and this dissertation work have tested the accuracy of DFT+U method in determining the structural and energetic properties of bulk ceria, suggesting that all computationally predicted results are within 10% variation from experimentally measured values. The latter error is determined from the choice of the researcher. As we have clearly stated in the relaxation convergence criterion, the energy convergence is set on the order of  $10^{-3}$  eV for the nanoparticle system containing around 200 atoms, thus giving the convergence accuracy on the order of  $10^{-5}$  eV per atom. Taking into account both sources of error, we are confident for

the calculation precision on all results reported to the 1st decimal point.

### 3.2.11 Other calculation settings

In this study, all calculations are implemented in planewave density function theory code VASP<sup>215</sup>. The Ce 4f5s5p5d6s, and O 2p2s electrons were treated as valence electrons, and core-electron interactions were modeled using the projector-augmented wave method<sup>216</sup>. In chapter 4, we apply DFT+U along with either local density approximation (LDA) or generalized gradient approximation (GGA) method, to accurately characterize relaxed atomic geometries, valence electron charge densities, and total energies of uCNPs with various compositions and surface configurations. All the geometry relaxation calculations (Chapters 5, 6 and 7), electronic density of states calculations (Chapters 4 and 6), IR spectrum calculations (Chapters 4 and 6), and NEB calculations (Chapter 7) are unanimously employing GGA+U methods with  $U = 5eV$ , and have all same settings as those described for geometry relaxation calculations in Chapter 4.

Partial electronic density states of states (eDOS) for all atoms within CNPs are calculated by a quick method for the determination of the spdf- and site projected wave function character of each band. The vibration frequencies of considered CNP structures were obtained by determining the Hessian matrix (i.e. a square matrix of the second-derivatives of the energy with respect to the atomic positions) either based on finite differences (under *IBRION*=5 setting) or density functional perturbation theory linear response calculation (under *IBRION*=7 setting). The matrix was constructed by the differences of the second derivatives of the total energy due to shifting each of the atoms in the species by 0.005 in all Cartesian directions from the optimized geometry. The vibration intensities of hydroxyl groups were obtained by parsing, multiplying, and collecting squares of Born effective charges (BEC) matrices. The energy barrier of reaction pathways is found via NEB calculations to locate the

transition state as well as via DM calculation to exclude zero energy difference between initial state and transition state. Both NEB and DM calculations are realized in the revised VASP code from Graeme Henkelman's group at UT-Austin.

### 3.3 Thermodynamics of uCNPs

#### 3.3.1 Introduction

The direct output from VASP calculation is the total ground state energy and associated atomic structure of considered uCNPs at 0 K. We need a way to compare the stability of various relaxed uCNP structures. Furthermore, we want to tie our computational results to experimental observations, characterizations and measurements, this requires us to account for the influence of experimental synthesis, characterization and application environments on our computational results. To accomplish all of this, we need to derive mathematical formula to evaluate the stability of various relaxed uCNP structures with respect to changing environmental parameters. In the following, the details of those exercises are shown.

#### 3.3.2 Excessive energy of formation per Ce atom of uCNPs as a function of size, shape and composition in a pure oxygen environment

To compare energies of uCNPs with different compositions (and/or shapes, surface configurations, etc.) we must define an energy of formation with a common reference. Here we focus on the relative energy of uCNPs with varying numbers of surface O-atoms. We therefore define an excess energy of formation term,  $\Delta E_f^{CNP}(n_O)$ , as referenced to the energy of a reduced  $\sim 1$  nm CNP. Changes in the excess energy of formation therefore indicate whether a particular uCNP structure is more or less stable (has lower or higher energy) than the reference uCNP structure.

$$\Delta E_f^{CNP}(n_O) \equiv E_{tot}^{CNP} - E_{tot}^{ref} - (n_O - n_O^{ref})\mu_O \quad (3.12)$$

Here  $n_O$  is the number of O atoms in the uCNP of interest, and  $n_O^{ref}$  is the number of O atoms in the reference uCNP.  $\mu_O$  is the chemical potential of O atoms (the chemical potential of  $O_2$  molecule per O atom). To facilitate comparisons between uCNPs of various sizes and shapes, we further write this excess energy of formation per Ce atom

$$\Delta e_f^{CNP}(n_O) \equiv \frac{\Delta E_f^{CNP}}{n_{Ce}} \quad (3.13)$$

Equations 3.12 and 3.13 are direct measures of the relative energy of different uCNP structures. The selection of the reference uCNP is arbitrary, and simply serves to set the zero of the energy scale. As a link to previous calculations, which have primarily focused on partially reduced uCNPs, we select the reduced  $\sim 1$  nm cubic uCNP,  $Ce_{32}O_{57}$ , as the reference uCNP structure for the present calculations of the excess energies of formation. This structure is constructed from the fully oxygenated baseline cubic uCNP ( $Ce_{32}O_{121}$ , see Figure 3.3d) by deleting all corner and edge O atoms, as well as 4 face O atoms near each uCNP corners on every  $\{001\}$  facet.

The chemical potential of O atoms appearing in Equation 3.12 characterizes the energy cost of additional O atoms, and allows the comparison of energies for uCNP structures with varying numbers of O atoms. The energy cost of O atoms in real systems is determined by the state of available O atoms from the environment surrounding the uCNP. For the present calculations, we take pure O gas as the environmental state. This is a constraint on real systems, where other atomic or molecular species are almost invariably present, but defines a tractable scope for the present work and represents a useful starting point for systematic consideration of uCNP surface configurations in open systems. Note that the chemical potential is physically related to the partial pressure of ambient gases, e.g.  $P_{O_2}$ , and more negative values of  $\mu_O$  correspond to lower  $P_{O_2}$ <sup>96</sup>. Therefore the largest energy cost ( $\mu_O^* = \frac{1}{2}E_{O_2}$ , where  $E_{O_2}$  is the calculated ground state energy of a single  $O_2$  molecule) for the addition of an O atom occurs in the dilute gas limit, and this cost represents the most negative

Table 3.1: Summary of computationally calculated (Cal.) energies and experimentally measured (Expt.) energies

Calculation	E(CeO <sub>2</sub> )	E(Ce <sub>2</sub> O <sub>3</sub> )	E(Ce)	E(O <sub>2</sub> )	$\Delta E$	$\Delta H(\text{CeO}_2)$	$\Delta H(\text{Ce}_2\text{O}_3)$
LDA(np, U = 5 eV)	-27.0182	-43.4676	-4.8469	-9.5548	0.77	-11.8465	-18.2866
LDA(sp, U = 5 eV)	-27.0182	-43.4676	-4.8469	-10.4742	-0.15	-11.8471	-18.2875
GGA(np, U = 3 eV)	-24.6554	-40.3456	-4.6046	-8.7796	-0.33	-11.6012	-18.4620
GGA(sp, U = 3 eV)	-24.6554	-40.3456	-4.6047	-9.8539	-1.40	-11.5968	-18.4554
Experiment	—	—	—	—	—	-11.3010	-18.6530

physically realizable value possible for  $\mu_O$ .

DFT calculations of metal oxide oxidation energies are known to exhibit two separate errors: an error in the O<sub>2</sub> intermolecular binding energy and an error in the change in energy upon transfer of electrons between O *2p* orbitals and metal *d* or *f* orbitals<sup>217,218</sup>. In addition, the spin state of O atoms also appreciably affects DFT calculated values of O molecules. By fitting calculated oxidation energies to experimentally determined enthalpies of formation, a net correction to the chemical potential of O atoms that addresses all of these issues has been calculated for a range of transition metal oxides<sup>217</sup>. Here we apply an analogous correction by referencing experimental formation enthalpies for bulk CeO<sub>2</sub> and Ce<sub>2</sub>O<sub>3</sub><sup>219</sup> to determine a corrected chemical potential of O atoms,  $\mu_O^*$ . Choosing  $\mu_O \equiv \mu_O^*$  therefore connects DFT calculations of CNP energies to experimentally-relevant reference values for chemical potential of O atoms and overcomes computational challenges in directly calculating such values. In other words, correcting DFT calculated O reference energies by fitting for experimental bulk enthalpies of formation gives a best-case representation of the energy cost of O atoms from real O-containing environments.

Following this reference<sup>217</sup>, the appropriate value of  $\mu_O^*$  is found by first calculating the energy of formation of O<sub>2</sub> gas ( $E(\text{O}_2)$ ) with the same calculation methodology and settings as those used to calculate uCNP energies. At the same time, the formation energies of bulk Ce ( $E(\text{Ce})$ ), bulk CeO<sub>2</sub> ( $E(\text{CeO}_2)$ ) and bulk Ce<sub>2</sub>O<sub>3</sub> ( $E(\text{Ce}_2\text{O}_3)$ ) are



calculated. The calculated formation enthalpies for bulk  $\text{CeO}_2$  and  $\text{Ce}_2\text{O}_3$  are then<sup>217</sup>:

$$\Delta H(\text{CeO}_2) = E(\text{CeO}_2) - E(\text{Ce}) - E(\text{O}_2) \quad (3.14)$$

$$\Delta H(\text{Ce}_2\text{O}_3) = \frac{2E(\text{Ce}_2\text{O}_3) - 3E(\text{O}_2)}{2} - 2E(\text{Ce}) \quad (3.15)$$

A correction  $\Delta E$  is applied to  $E(\text{O}_2)$  so that the root mean square variation of the calculated formation enthalpies for bulk  $\text{CeO}_2$  and  $\text{Ce}_2\text{O}_3$  from experimentally-measured values is minimized. Note that formation energies of  $\text{O}_2$ , bulk Ce, bulk  $\text{CeO}_2$  and bulk  $\text{Ce}_2\text{O}_3$  were calculated using both LDA+U and GGA+U approaches ( $U_{\text{eff}} = 5$  eV for LDA and  $U_{\text{eff}} = 3$  eV for GGA), as well as considering both non-spin polarized (np) and spin polarized (sp) cases. All the relevant data are summarized in Table 3.1. The corrected chemical potential of O atoms referenced to gaseous  $\text{O}_2$ ,  $\mu_{\text{O}(\text{corr})}^*$ , is evaluated via  $\mu_{\text{O}(\text{corr})}^* = \frac{1}{2}(E_{\text{O}_2} - \Delta E)$ , as -5.16 eV for LDA and -4.23 eV for GGA.

### 3.3.3 Excessive energy of formation uCNPs with different surface configurations as a function of chemical potentials of O and H atoms in a humid environment

To enable stability comparisons among uCNP structures with differing surface configurations, and to connect computed energies to physically relevant thermochemical data, the formation (binding) energy of *bulk* (cubic fluorite)  $\text{CeO}_2$ ,  $E_f^{\text{bulk}}$ , is defined as:

$$E_f^{\text{bulk}}(n_{\text{Ce}}) \equiv E_{\text{VASP}}^{\text{bulk}}(n_{\text{Ce}}) - n_{\text{Ce}}\mu_{\text{Ce}} - 2n_{\text{Ce}}\mu_{\text{O}} \quad (3.16)$$

Here,  $E_{\text{VASP}}^{\text{bulk}}(n_{\text{Ce}})$  is the calculated ground state energy of bulk cubic fluorite  $\text{CeO}_2$  with  $n_{\text{Ce}}$  Ce atoms at  $T = 0$  K.  $\mu_{\text{Ce}}$  and  $\mu_{\text{O}}$  are the chemical potentials of Ce and O atoms, respectively. The energy of formation of a uCNP with an arbitrary O- and H-containing surface configuration,  $E_f^{\text{CNP}}$ , is similarly defined as

$$E_f^{\text{CNP}}(n_{\text{Ce}}) \equiv E_{\text{VASP}}^{\text{CNP}}(n_{\text{Ce}}) - n_{\text{Ce}}\mu_{\text{Ce}} - n_{\text{O}}\mu_{\text{O}} - n_{\text{H}}\mu_{\text{H}} \quad (3.17)$$

Here,  $E_{VASP}^{CNP}(n_{Ce})$  is the calculated ground state energy of uCNP structures with  $n_{Ce}$  Ce atoms at  $T = 0$  K. Note that  $n_O$  includes both “bulk” O atoms within the uCNP and any additional O atoms present at the surface. In addition,  $\mu_O$  and  $\mu_H$  are chemical potentials of O and H atoms, and are fixed by the environment surrounding the uCNP.

For clarity, in this study we reference the energy of formation of various uCNP structures to that of bulk  $\text{CeO}_2$  with an equivalent number of Ce atoms. This gives an excess energy of formation for various uCNP structures,  $E_{ex}^{CNP}$ , which, if negative, would imply that the uCNP structure considered is more stable than bulk  $\text{CeO}_2$  *in a given environment*—where the chemical potentials of O and H atoms are determined by the environment specified. More generally, the lower the excess energy of formation of a particular uCNP structure for particular values of  $\mu_O$  and  $\mu_H$ , the more stable that uCNP structure with a specific surface configuration is.

$$\begin{aligned} E_{ex}^{CNP} &\equiv E_f^{CNP}(n_{Ce}) - E_f^{bulk}(n_{Ce}) \\ &= E_{VASP}^{CNP}(n_{Ce}) - E_{VASP}^{bulk}(n_{Ce}) - (n_O - 2n_{Ce})\mu_O - n_H\mu_H \end{aligned} \quad (3.18)$$

In an environment containing  $\text{O}_2$  gas and  $\text{H}_2\text{O}$  vapor, we can directly connect the chemical potentials of O and H atoms to experimental thermochemical data<sup>48</sup>. The chemical potential of O atoms is defined as

$$\mu_O(T, p) = 0.5\mu_{\text{O}_2}(T, p^o) + 0.5E_{VASP}^{O_2} + 0.5kT\ln(p_{\text{O}_2}/p^o) \quad (3.19)$$

in which  $E_{VASP}^{O_2}$  is the ground state energy of  $\text{O}_2$  gas at  $T = 0$  K with the same calculation parameters used for the uCNP itself.  $\mu_{\text{O}_2}(T, p^o)$  is the experimentally measured chemical potential (including vibrational and rotational contributions) at  $T$  and standard pressure  $p^o$ .  $p_{\text{O}_2}$  is the actual partial pressure of  $\text{O}_2$  gas present in the system of interest. Equation 3.19, therefore, combines the DFT-calculated ground state energy with experimentally measured thermochemical data to give the temperature- and partial-pressure-dependent  $\mu_O$  appearing in Equation 3.18. Simi-

larly, the chemical potential of H<sub>2</sub>O vapor is defined as

$$\mu_{H_2O}(T, p) = \mu_{H_2O}(T, p^o) + E_{VASP}^{H_2O} + kT \ln(p_{H_2O}/p^o) \quad (3.20)$$

again, where  $E_{VASP}^{H_2O}$  is the calculated ground state energy of H<sub>2</sub>O vapor at  $T = 0$  K,  $\mu_{H_2O}(T, p^o)$  is the experimentally measured chemical potential at  $T$  and standard pressure  $p^o$ , and  $p_{H_2O}$  is the partial pressure of H<sub>2</sub>O vapor in the system of interest.

At thermodynamic equilibrium and neutral pH,  $\mu_H$  and  $\mu_O$  must be related by

$$2\mu_H(T, p) + \mu_O(T, p) = \mu_{H_2O}(T, p) \quad (3.21)$$

Thus, in a gas phase environment containing O<sub>2</sub> gas and H<sub>2</sub>O vapor, we have:

$$2\mu_H + \mu_O = \mu_{H_2O}(T, p^o) + E_{VASP}^{H_2O} + kT \ln(p_{H_2O}/p^o) \quad (3.22)$$

Combining Equation 3.19 and Equation 3.22, we write the chemical potential of H atoms as

$$\begin{aligned} \mu_H = & 0.5\mu_{H_2O}(T, p^o) + 0.5E_{VASP}^{H_2O} + 0.5kT \ln(p_{H_2O}/p^o) - \\ & 0.25\mu_{O_2}(T, p^o) - 0.25E_{VASP}^{O_2} - 0.25kT \ln(p_{O_2}/p^o) \end{aligned} \quad (3.23)$$

Combining Equation 3.23 with Equation 3.19 gives expressions for  $\mu_H$  and  $\mu_O$ . Experimental values for  $\mu_{O_2}(T, p^o)$  and  $\mu_{H_2O}(T, p^o)$  appearing above have been obtained from the NIST-JANAF Thermochemical Tables<sup>220</sup>. Chemical potential values for temperatures not directly tabulated were linearly interpolated from values at the nearest tabulated temperatures.

In sum, the above equations give values for  $\mu_H$  and  $\mu_O$  that can be used in Equation 3.18 to determine experimentally-relevant excess energies of formation of various uCNP structures directly from knowledge of the  $T$ ,  $p_{O_2}$  and  $p_{H_2O}$  of an experimental system of interest. In this way, we combine DFT+U calculated structures and energies with experimentally measured thermochemical data to determine the relative

stability of various uCNP structures in a gas environment containing O<sub>2</sub> gas and H<sub>2</sub>O vapor.

In a pH-controlled aqueous solution, H<sub>2</sub>O molecules are ionized into H<sup>+</sup> ions and OH<sup>-</sup> ions. The equilibrium constant of the reaction  $H_2O \rightleftharpoons H^+ + OH^-$  is

$$K_{eq}(T, p) = a_{H^+} \cdot a_{OH^-}. \quad (3.24)$$

Taking natural logarithm of both sides of the above equation, we get

$$kT \ln K_{eq}(T, p) = kT \ln a_{H^+} + kT \ln a_{OH^-}. \quad (3.25)$$

According to the definition of chemical potential, we can write the expressions for the chemical potentials of H<sup>+</sup> and OH<sup>-</sup>, respectively.

$$\mu_{H^+}(T, p) = \mu_{H^+}(T, p^o) + E_{H^+} + kT \ln a_{H^+}. \quad (3.26)$$

$$\mu_{OH^-}(T, p) = \mu_{OH^-}(T, p^o) + E_{OH^-} + kT \ln a_{OH^-}. \quad (3.27)$$

Plug Equations 3.26 and 3.27 into Equation 3.25, we get

$$kT \ln K_{eq}(T, p) = \quad (3.28)$$

$$[\mu_{H^+}(T, p) - \mu_{H^+}(T, p^o)] + [\mu_{OH^-}(T, p) - \mu_{OH^-}(T, p^o)] - (E_{H^+} + E_{OH^-}).$$

At the same time,  $E_{H^+} = E_H - \mu_e$  and  $E_{OH^-} = E_H + \mu_e$ . The equilibrium constant  $K_{eq}$  is related to the ionization constant of water  $pK_w(T, p)$  via  $K_{eq} = 10^{-pK_w(T, p)}$ .

In addition,

$$\begin{aligned} \mu_{H^+}(T, p) - \mu_{H^+}(T, p^o) &= [\mu_H(T, p) - \mu_e] - [\mu_H(T, p^o) - \mu_e] = \\ &= \mu_H(T, p) - \mu_H(T, p^o). \end{aligned} \quad (3.29)$$

$$\begin{aligned} \mu_{OH^-}(T, p) - \mu_{OH^-}(T, p^o) &= \\ [\mu_{OH}(T, p) + \mu_e] - [\mu_{OH}(T, p^o) + \mu_e] &= \mu_{OH}(T, p) - \mu_{OH}(T, p^o) = \\ \mu_H(T, p) - \mu_H(T, p^o) + \mu_O(T, p) - \mu_O(T, p^o). \end{aligned} \quad (3.30)$$

Applying all above information and plugging Equations 3.29 and 3.30 into Equation 3.28, we have the relationship between  $\mu_H$  and  $\mu_{OH}$  in a pH-controlled aqueous solution

$$\begin{aligned} E_H + E_{OH} - kT \ln(10) \cdot pK_w(T, p) &= \\ 2[\mu_H(T, p) - \mu_H(T, p^o)] + [\mu_O(T, p) - \mu_O(T, p^o)]. \end{aligned} \quad (3.31)$$

in which  $E_H$  and  $E_{OH}$  are the calculated energy of formation of a H atom and a  $-OH$  group at  $T = 0K$ , respectively.

In aqueous solution, pH is defined as

$$pH = -\log_{10} a_{H^+}. \quad (3.32)$$

Applying Equation 3.32 to Equation 3.26, we have

$$\mu_{H^+}(T, p) = \mu_{H^+}(T, p^o) + E_{H^+} - kT \ln(10) \cdot pH. \quad (3.33)$$

Using  $\mu_{H^+}(T, p) = \mu_H(T, p) - \mu_e$  and  $E_{H^+} = E_H - \mu_e$ , we get the relationship between  $\mu_H$  and  $pH$

$$\mu_H = \mu_H(T, p^o) + E_H - kT \ln(10) \cdot pH. \quad (3.34)$$

In Chapter 6, the interaction of incoming H atoms with individual  $-O_x$  groups adsorbed at surfaces of  $O_x$ -terminated uCNP structures in a pH-controlled aqueous solution is in fact evaluated by the energy of formation of relaxed whole structure (uCNP structure plus one or two H atoms), mathematically defined as

$$E_f = E_{CNP+FG} - E_{CNP} - n_H \mu_H, \quad (3.35)$$

in which  $E_{CNP+FG}$  is the ground state energy of relaxed whole structure,  $E_{CNP}$  the ground state energy of the representative uCNP structure, as well as  $\mu_H$  the chemical potentials of H atoms. Applying the above expression to calculate  $\mu_H$  to Equation 3.35, the energy of formation of relaxed whole structure in various pH valued solution can be obtained.

### 3.3.4 Activation energy

When we consider a reaction pathway from one local minimum state to another, two measurands are examined to show the feasibility of such a reaction pathway, namely,

reaction energy and activation energy. Reaction energy evaluates from the thermodynamic perspective; basically whether the reaction is exothermic (releasing energy) or endothermic (absorbing energy). However, activation energy, which is the minimum energy required to start a reaction, evaluates from the kinetic perspective to examine how fast a reaction can proceed. In other word, the reaction needs to overcome an energy barrier, and its rate is determined by the height of an energy barrier. According to harmonic transition state theory (hTST), the activation energy is defined as the minimum potential barrier between two local relaxed states along a reaction pathway. The potential barrier,  $\Delta E_p$ , directly obtained from NEB calculation, does not include the vibrational energy of considered relaxed structures at 0 K. The energy contributed from harmonic atom vibration at 0 K is called zero-point energy (ZPE). To accurately describe the activation energy  $E_{ac}$ , correction from vibrational ZPE difference between initial and saddle-point states,  $\Delta F_{vib}(0)$ , must be applied<sup>221</sup>:

$$E_{ac} = \Delta E_p + \Delta F_{vib}(0) = \Delta E_p - \frac{1}{2} \left( \sum_{i=1}^{3N-1} \hbar \omega_i^S - \sum_{i=1}^{3N} \hbar \omega_i^I \right), \quad (3.36)$$

in which  $\omega_i^I$  and  $\omega_i^S$  are the vibrational frequencies of the  $i$ th mode in the initial and saddle-point states, respectively. Note that  $3N$  vibration modes are considered for the initial state, with  $N$  atoms vibrating. However, the imaginary vibrational mode along the migration coordinate in the saddle-point state is excluded; thus,  $3N - 1$  vibrational modes are considered for the saddle-point state.

### 3.4 Constructing computational cells containing uCNPs

#### 3.4.1 Experimentally reported shapes and quantitative atom counts

In this research work, we only consider uCNP structures with experimentally reported shapes. They are cubic shaped, octahedral shaped and cuboctahedral shaped uCNPs. Previous computational studies have done some work exploring the atomistic structure of octahedral shaped and cuboctahedral shaped uCNPs. However, none of the

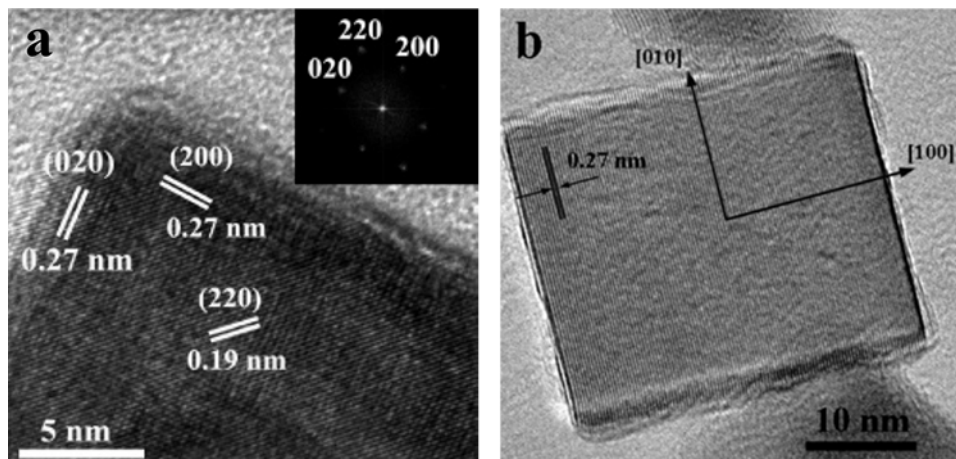


Figure 3.3: High resolution TEM images of cubic CNPs. (a) fast Fourier transform (FFT) analysis together with HRTEM image confirm cubic CNPs are single-crystalline and enclosed by  $\{200\}$  planes<sup>194</sup>; (b) interplanar spacing of 0.27 nm corresponds to  $\{001\}$  lattice fringe, indicating cubic CNPs are enclosed by  $\{100\}$  facets<sup>11</sup>.

previous computational studies have considered cubic shaped uCNPs. In this research work, we show greater interests towards cubic shaped uCNPs, mainly because (1) they have been observed experimentally (see, e.g., Figure 3.3) and (2) previous experimental studies have found that  $\{100\}$  facets exhibit greater catalytic activity than other ceria surfaces, and represent the dominant active surface in a range of nanoparticle geometries (e.g., nanoplates, nanorods, and nanowires)<sup>194,196,197,199,200</sup>. This is also supported by previous computational works showing that ceria  $\{100\}$  surfaces have lower O-vacancy formation energies, and (following the “four-step” hypothesis) are therefore expected to have greater activity<sup>32,33,75</sup>. Due to huge computational cost, we limit the size of the majority of considered uCNPs to be  $\sim 1$  nm. The mathematical derivation of quantitative atom counts can be referred to **section 2.8.1**.

For cubic shaped  $\sim 1$  nm uCNPs, it has 32 Ce atoms and 27 “bulk” O atoms. If its surface is terminated by O atoms and every lattice site is occupied by 1 O atom, it will have 8 corner O atoms, 36 edge O atoms, and 54 facet O atoms. This gives the composition of  $\sim 1$  nm cubic uCNPs as  $\text{Ce}_{32}\text{O}_{121}$  with 97 surface O sites.

For octahedral shaped  $\sim 1$  nm uCNPs, it has 44 Ce atoms and 80 “bulk” O atoms.

If its surface is terminated by O atoms and every lattice site is occupied by 1 O atom, it will have 24 corner O atoms, 48 edge O atoms, and 8 facet O atoms. This gives the composition of  $\sim 1$  nm octahedral uCNPs as  $\text{Ce}_{44}\text{O}_{160}$  with 80 surface O sites.

For cuboctahedral shaped  $\sim 1$  nm uCNPs, it is just randomly deleting Ce and O atoms at 4 out of 6 corners of octahedral shaped  $\sim 1$  nm uCNPs. By removing 4 corner Ce atoms and 16 corner O atoms, it will have 8 corner O atoms, 48 edge O atoms and 8 face O atoms. This gives the composition of  $\sim 1$  nm cuboctahedral uCNPs as  $\text{Ce}_{40}\text{O}_{144}$  with 64 surface O sites.

### 3.4.2 Construction of bulk-cut uCNP structures

Initial bulk-cut uCNP structures were constructed from cubic fluorite (space group  $\text{Fm}\bar{3}\text{m}$ ) FCC unit cells containing 1 Ce atom at the unit cell corners (where all eight cube corners are identical due to symmetry) and 3 Ce atoms at the center of the unit cell faces (where each opposite pair of faces are identical due to symmetry). Eight O atoms are located at the FCC tetrahedral interstitial sites, giving 4 Ce atoms and 8 O atoms in each unit cell (see Figure 3.4a). Initial bulk-cut uCNP structures with various sizes and shapes were constructed by repeating this unit cell in three dimensions (see, e.g., Figure 3.4b).

For cubic CNPs, its six surfaces are terminated by ceria  $\{001\}$  surfaces.  $\sim 1$  nm cubic but-cut uCNP structures are constructed by repeating the unit cell of bulk  $\text{CeO}_2$   $2 \times 2 \times 2$  (see Figures 3.4c-d). To ensure that no interactions occur between any calculated uCNP structures and minimize the computation cost, the size of the supercell is set to  $2.7 \text{ nm} \times 2.7 \text{ nm} \times 2.7 \text{ nm}$  so that neighboring uCNP structures are separated by at least 1.5 nm vacuum space when periodic boundary condition is applied (see Figure 3.4c). The ideal bulk-cut  $\sim 1$  nm cubic uCNP structure has the composition of  $\text{Ce}_{32}\text{O}_{27}$ , with 32 Ce atoms (yellow balls) and 27 “bulk” O atoms (purple balls).



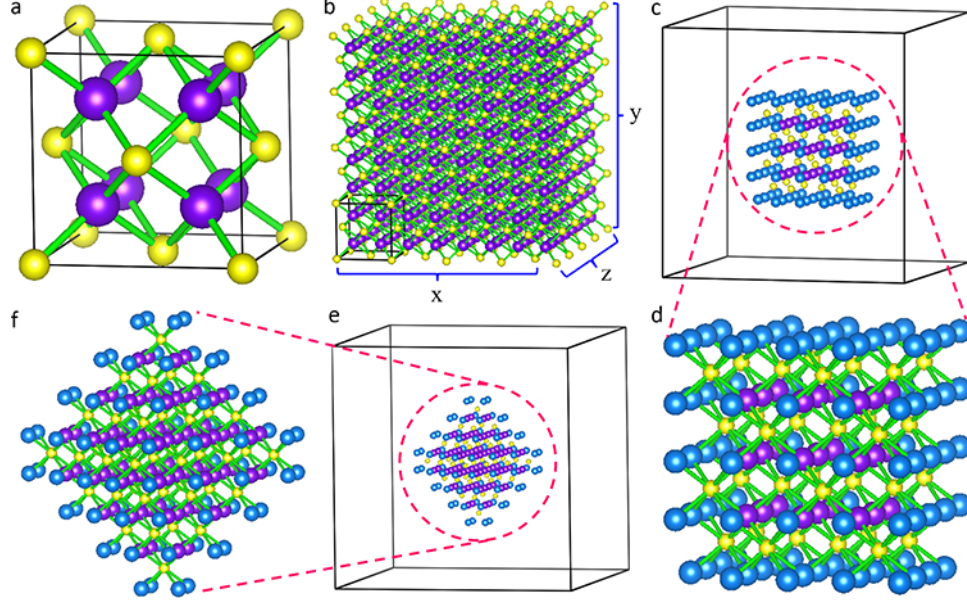


Figure 3.4: (a) Unit cell of bulk  $\text{CeO}_2$  showing cubic fluorite structure; (b) schematic illustration of building the solid atomic assembly of Ce and O atoms by randomly expanding the unit cell of bulk  $\text{CeO}_2$  (enclosed by black solid lines)  $x$ ,  $y$ , and  $z$  times in three orthonormal directions, respectively; (c) the supercell of cubic CNPs of  $\sim 1$  nm for relaxation calculation; (d) zoom-in image of the solid atomic assembly in (c) to show the atomic structure of  $\{001\}$ -terminated cubic uCNPs. (e) the supercell of octahedral CNPs of  $\sim 1$  nm for relaxation calculation; (f) zoom-in image of the solid atomic assembly in (e) to show the atomic structure of  $\{111\}$ -terminated octahedral uCNPs. Yellow balls represent Ce atoms, purple balls represent bulk O atoms, and blue balls represent all possible surface O lattice sites that can be partially or fully occupied by individual O atom.

For octahedral CNPs, all eight surfaces are terminated by ceria  $\{111\}$  surfaces.  $\sim 1$  nm but-cut octahedral uCNP structures are constructed by performing eight intersecting  $\{111\}$  bulk cuts through a  $4 \times 4 \times 4$  set of unit cells of bulk  $\text{CeO}_2$  (see Figure 3.4e-f). To ensure that no interactions occur between any calculated uCNP structures and minimize the computation cost, the size of the supercell is set to  $3.8 \text{ nm} \times 3.8 \text{ nm} \times 3.8 \text{ nm}$  so that neighboring uCNP structures are separated by at least  $1.5 \text{ nm}$  vacuum space when periodic boundary condition is applied (see Figure 3.4e). The ideal bulk-cut  $\sim 1$  nm octahedral uCNP structure has the composition of  $\text{Ce}_{44}\text{O}_{80}$ , with 32 Ce atoms (yellow balls) and 80 “bulk” O atoms (purple balls). Cuboctahedral  $\sim 1$  nm bulk-cut CNP structures are modifications of  $\sim 1$  nm bulk-cut octahedral CNP

structures and are constructed by arbitrarily deleting four out of the six corner Ce atoms<sup>113</sup>. This gives a uCNP structure with an enforced stoichiometric composition of  $\text{Ce}_{40}\text{O}_{80}$ .

### 3.4.3 Initial placement of surface groups

As we are focusing on the stability of uCNPs *as a function* of surface group concentration, we take all bulk-cut uCNP structures as structural baselines. That is, we place various surface groups (mainly  $-\text{O}_x$  and  $-\text{OH}$  groups) at surface O sites of all  $\sim 1$  nm bulk-cut uCNP structures, marked as blue balls in Figures 3.3c-f) at different pattern and concentrations. In these uCNP structures all surface O lattice sites are optional places to be occupied, including those that are symmetrically equivalent (e.g., O lattice sites on opposite facets or on corners other than the origin). In contrast, *stoichiometric* uCNP structures would have only the symmetrically distinct O lattice sites occupied. Occupying all surface O lattice sites (as is shown in Figures 3.3c-f) results in super-stoichiometric uCNP structures. For example, the ideal (bulk-cut) 1 nm  $\{100\}$ -terminated uCNP structures in Figures 3.3c-d with all surface O lattice sites occupied have the composition of  $\text{Ce}_{32}\text{O}_{121}$ —with 94 out of total 121 O atoms on the uCNP surface.

## Chapter 4 The surface configuration of ultra-small CNPs in a pure oxygen environment

Before elaborating on research results, let us again briefly review what understandings concerning the surface configuration of uCNPs have been obtained via previous experimental and computational studies. Experimentally synthesized uCNPs whose size is below 10 nm primarily exhibit two different shapes: cubic shape<sup>200</sup> and octahedral shape<sup>196</sup> (including cuboctahedral shape). However, computational studies have focused on octahedral shaped uCNPs with ideal, unreconstructed, (near-)stoichiometric, bulk-cut surface configurations. They have greatly constrained their computation models to an intuitive stable concentration or configuration of certain surface species. More importantly, they have completely ignored the influence of the environment where uCNPs are both synthesized and applied, which is an open system that can serve as a source and/or sink of atoms or molecules. Last but not least, cubic shaped uCNPs exposed with more catalytic active ceria {100} surfaces have never aroused the interest of previous researchers who apply quantum mechanical calculations to model uCNPs. Therefore, previous computational studies have failed to establish a panoramic picture regarding the surface configuration of uCNPs, especially from a dynamic perspective, though two parameters to some extent characterizing uCNPs, i.e. shape and stoichiometry, have been taken into account. In the following, we directly address above-mentioned issues. While constraining the present work to experimentally observed uCNP shapes and considering only uCNPs in a pure O environment, we systematically examine the structure and energy of  $\sim 1$  — 1.5 nm uCNPs with unconstrained surface concentrations and configurations of O atoms.

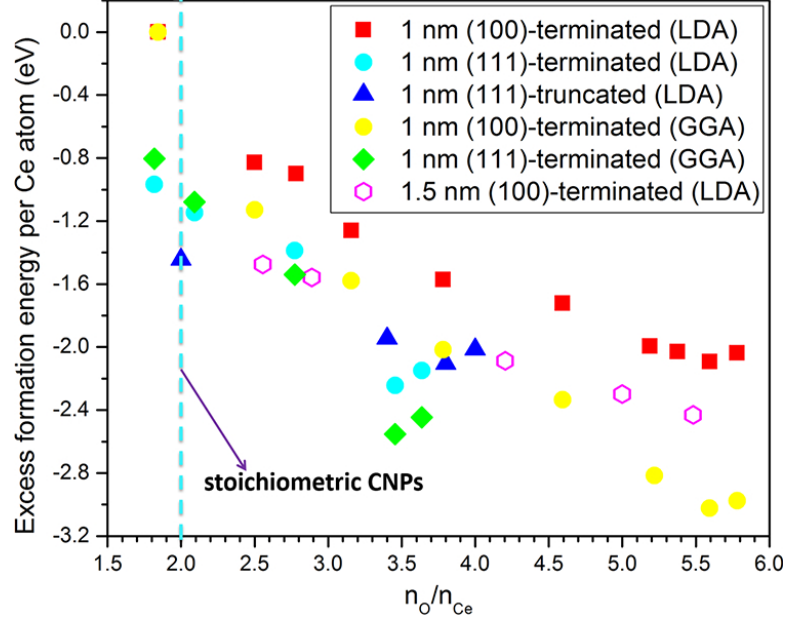


Figure 4.1: Calculated excess energies of formation per Ce atom of various sized and shaped uCNPs.  $E_f$  are referenced to the energy of formation of the same sized bulk  $\text{CeO}_2$  as a function of  $n_{\text{O}}/n_{\text{Ce}}$  in various uCNPs at the corrected chemical potential of O atoms.

#### 4.1 Excess energy of formation per Ce atom of uCNPs as a function of oxygen concentration

We now turn to the question of determining the stable surface configuration of various uCNPs when the surface O concentration and configuration are allowed to vary from that of the underlying bulk. Beginning with constructed initial uCNP structures (see **section 3.4**, we have relaxed various  $\{100\}$ -terminated cubic uCNPs with diameters of  $\sim 1$ – $1.5$  nm and a range of surface O concentrations as well as  $\{111\}$ -terminated octahedral and cuboctahedral uCNPs with diameters of  $\sim 1$  nm and a range of surface O concentrations. Using Equations 3.16 and 3.17, the excess energy of formation per Ce atom has been calculated for each uCNP structure. Figure 4.1 shows the results of these calculations in the O-lean limit (that is, at the corrected chemical potential of O,  $\mu_{\text{O}}^*$ ). For considered uCNPs of all shapes, Figure 4.1 shows that uCNPs can reduce their excess energy of formation by increasing the O concentration at their surfaces.

Because the chemical potential of O atoms only increases for increasing partial pressures of  $O_2$  ( $p_{O_2}$ )—that is, the energy cost of O atoms *decreases* as the environment moves from the O-lean limit towards the O-rich limit—Figure 4.1 demonstrates that oxidized uCNPs ( $CeO_{2+x}$ ) are more stable in both O-lean ( $\mu_O \equiv \mu_O^* = -5.16$  eV for LDA and -4.23 eV for GGA) and O-rich ( $\mu_O > -5.16$  eV for LDA and -4.23 eV for GGA) environments. In the latter case, O-enriched uCNPs even more stable with respect to reduced uCNPs, as the cost of the additional O atoms is less. Note that both LDA and GGA results exhibit the same trend in excess energy of formation per Ce atom as a function of  $n_O/n_{Ce}$  for  $\{001\}$ -terminated cubic uCNPs and  $\{111\}$ -terminated octahedral uCNPs. In addition, while Figure 4.1 only shows results for  $U_{\text{eff}} = 5$  and 3 eV (for LDA and GGA, respectively), calculations for  $U_{\text{eff}} = 1$  and 3 eV (LDA) and  $U_{\text{eff}} = 1$  and 5 eV (GGA) also reveal the same trend: that increased surface O concentration reduces excess energy of formation for uCNPs.

Addressing the possible special case of exactly stoichiometric CNPs, the excess energy of formation for the  $\sim 1$  nm cuboctahedral uCNP with composition  $Ce_{40}O_{80}$  is explicitly included in Figure 4.1. While the stoichiometric cuboctahedral uCNP does exhibit a local minimum in energy with respect to O composition, numerous oxidized uCNPs, including oxidized cuboctahedral uCNPs of the same shape and size, have lower excess energies of formation. That is, even relative to exactly stoichiometric uCNPs, oxidized uCNPs with enhanced surface O concentrations have lower excess energies of formation. These results demonstrate that the thermodynamically stable structure that a sufficiently small CNP begins in and returns to before and after catalyzing a redox reaction is not stoichiometric, rather the surfaces of thermodynamically stable CNPs that are sufficiently small are O-enriched.

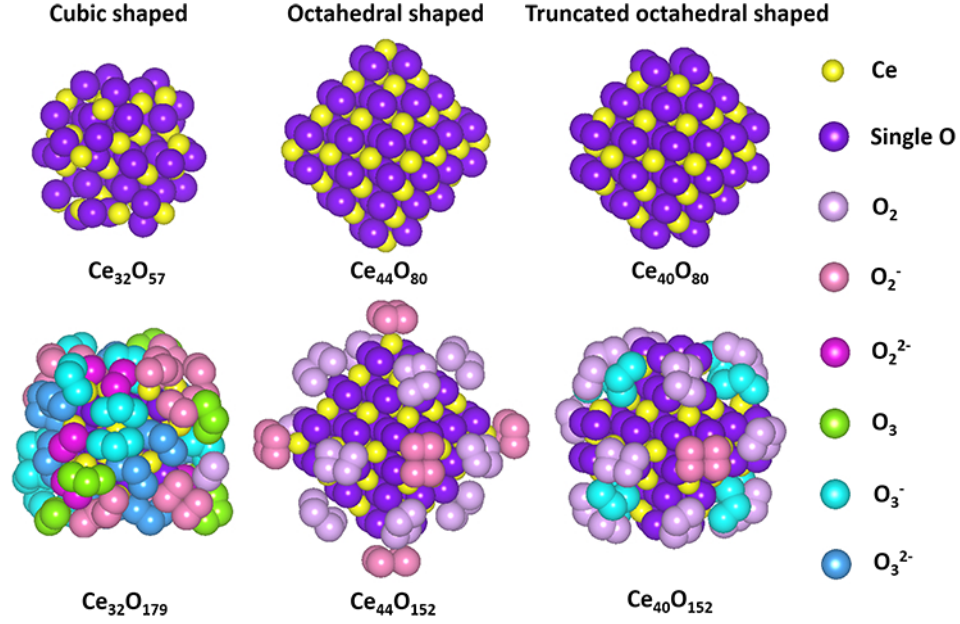


Figure 4.2: Atomic structures of various shaped uCNPs with reduced, stoichiometric and oxidized chemical compositions. Yellow balls represent Ce atoms while larger sized balls represent O atoms and they are colored according to their type and charge states.

## 4.2 Atomic structures of uCNPs

Figure 4.2 shows the atomic structures of representative relaxed cubic, octetedral and cuboctetedral CNPs with reduced, stoichiometric and oxidized net compositions. Excess energies of formation for these structures are all included in Figure 4.2. It is apparent that stoichiometrically “excess” O atoms in oxidized uCNP structures appear at the CNP corners, edges and  $\{100\}$  facets in the form of either O pairs or O triples. These structures represent substantial rearrangements of O atoms relative to the initial (input) uCNP structures, which in all cases had individual O atoms initially located at ideal O lattice sites. Individual (crystalline) O lattice atoms only appear in reduced or stoichiometric uCNP (in general  $\text{CeO}_{2-x}$ ,  $0 \leq x < 2$ ) structures, while O pairs and triples only appear in oxidized CNP structures that are sufficiently small. That is, while the assumption of bulk-like surface configuration is valid for reduced or stoichiometric uCNPs, thermodynamically stable uCNPs are in real O-containing

environments (all of which are oxidized) do not exhibit bulk-like arrangements of surface O atoms.

Table 4.1: Properties of assigned  $-\text{O}_x$  surface groups in representative uCNP structures.

Type	Bond length (Å)	Bond angle (°)	Bader charge	Molecule Assignment
$\text{Ce}_{32}\text{O}_{179}$	1.24	—	$-0.18 \pm 0.02$	$\text{O}_2$
	$1.31 \pm 0.03$	—	$-0.53 \pm 0.16$	$\text{O}_2^-$
	$1.42 \pm 0.02$	—	$-1.07 \pm 0.05$	$\text{O}_2^{2-}$
	$1.33 \pm 0.02, 1.30 \pm 0.01$	$111.96 \pm 0.38$	$-0.39 \pm 0.04$	$\text{O}_3$
	$1.40 \pm 0.04, 1.31 \pm 0.02$	$108.57 \pm 1.55$	$-0.64 \pm 0.10$	$\text{O}_3^-$
	$1.42 \pm 0.03, 1.40 \pm 0.02$	$105.36 \pm 1.24$	$-1.11 \pm 0.11$	$\text{O}_3^{2-}$
$\text{Ce}_{44}\text{O}_{152}$	1.25	—	$-0.24 \pm 0.03$	$\text{O}_2$
	$1.28 \pm 0.01$	—	$-0.39 \pm 0.03$	$\text{O}_2^-$
$\text{Ce}_{40}\text{O}_{152}$	1.25	—	$-0.19 \pm 0.02$	$\text{O}_2$
	1.27	—	$-0.35 \pm 0.01$	$\text{O}_2^-$
	$1.42 \pm 0.02, 1.30 \pm 0.01$	$110.97 \pm 0.70$	$-0.76 \pm 0.03$	$\text{O}_3^-$

For every O pair or triple present on a relaxed uCNP, the distance between at least one O atom in each pair or triple and a Ce atom is within the range of Ce-O bond lengths observed in bulk  $\text{CeO}_2$  or  $\text{Ce}_2\text{O}_3$ . Table 4.1 compares calculated O-O bond lengths, angles, and local charge (assigned per atom following the method of Bader<sup>214</sup>, which provides a qualitative assignment of electrons to particular atoms) for O pairs and triples on oxidized uCNPs and the calculated properties of isolated  $\text{O}_2$ ,  $\text{O}_2^-$ ,  $\text{O}_2^{2-}$ ,  $\text{O}_3$ ,  $\text{O}_3^-$ , and  $\text{O}_3^{2-}$  molecules. Based on these results we conclude that the excess O atoms present on oxidized uCNPs are variously charged  $\text{O}_x^{q-}$  surface groups chemically adsorbed at CNP corners, edges and  $\{100\}$  facets.

While more clear for the  $\{111\}$ -terminated uCNPs, negatively charged  $\text{O}_2^-$  or  $\text{O}_3^-$  surface groups are preferentially adsorbed at CNP corners while neutral  $\text{O}_2$  or  $\text{O}_3$  groups are apt to be adsorbed at CNP edges. In addition, for all studied oxidized uCNP structures, the removal of all O atoms present after relaxation *in the form of adsorbed  $\text{O}_x^{q-}$  surface groups* leaves net reduced uCNP structures. This suggests that low-energy uCNP structures (all of which are oxidized, see Figure 4.1) can be considered reduced CNP structures passivated with adsorbed  $\text{O}_x^{q-}$  surface groups.

This picture is directly supported by a recent extensive analysis by Preda, et al.<sup>222</sup>, of the energetics and electronic effects of the adsorption a single O<sub>2</sub> molecule on the surface of reduced uCNPs and is consistent with previous experimental studies<sup>223</sup> reporting spectroscopic evidence for the adsorption of superoxo and peroxo species on reduced ceria surfaces.

Since the Ce<sup>III</sup>–Ce<sup>IV</sup> redox couple is the engine driving the catalytic properties of CNPs, the oxidation states of Ce cations in various relaxed uCNP structures have also been probed. As above, atomic charges are calculated via the Bader procedure<sup>214</sup>. Ce atoms in reduced uCNP structures exhibit a range of charge states generally intermediate between the charge states of Ce<sup>III</sup> and Ce<sup>IV</sup> as determined from calculations of bulk Ce<sub>2</sub>O<sub>3</sub> and CeO<sub>2</sub>. Lower Hubbard  $U$  parameters (which reduce the  $U$  energy penalty against extended states) decrease the net positive charge on each Ce atom, but do not change the qualitative distribution of charges. Increased O concentration (from reduced CeO<sub>2- $x$</sub>  to super-oxidized CeO<sub>2+ $x$</sub>  uCNP structures) shifts the charge distribution of Ce atoms in considered uCNP structures towards Ce<sup>IV</sup>, but produces no Ce atoms with net charges significantly greater than Ce<sup>IV</sup>. Table 4.2 summarizes calculated average Bader charges of Ce atoms in a set of cubic uCNP structures as an example, and their oxidation states can be analyzed by comparing to the calculated average Bader charge of Ce atoms in bulk CeO<sub>2</sub> and Ce<sub>2</sub>O<sub>3</sub>.

We are now in a position to comment on why the formation of O <sub>$x$</sub>  <sup>$q-$</sup>  surface groups substantially reduces the excess energy of formation for uCNPs. As a rare earth oxide with negative enthalpy of formation (see Table 3.1), we expect CeO<sub>2</sub> to prefer O-terminated surfaces in O-containing environments. This is supported by STM studies of ceria {111} surface<sup>24</sup> and atomistic calculations<sup>64,96</sup>. In fact, if this were not so, Ce metal would be expected to be more stable relative to CeO<sub>2</sub> in O environments. While ceria {111} surface has a stoichiometric O-terminated structure, O-termination of CNP corners, edges and {001} facets requires a super-saturation of O atoms.



Table 4.2: Average Bader charge of Ce atoms in cubic uCNPs with different O concentrations obtained from LDA+U calculations (U = 5 eV).

uCNPs with different O concentrations	Average charge of Ce atoms	uCNP type
Ce <sub>32</sub> O <sub>59</sub>	2.185 ± 0.067	reduced
Ce <sub>32</sub> O <sub>89</sub>	2.291 ± 0.032	oxidized
Ce <sub>32</sub> O <sub>101</sub>	2.302 ± 0.039	oxidized
Ce <sub>32</sub> O <sub>121</sub>	2.309 ± 0.038	oxidized
Ce <sub>32</sub> O <sub>147</sub>	2.314 ± 0.033	oxidized
Ce <sub>32</sub> O <sub>169</sub>	2.321 ± 0.028	oxidized
Ce <sub>32</sub> O <sub>179</sub>	2.331 ± 0.028	oxidized
bulk Ce <sub>2</sub> O <sub>3</sub>	~ 1.98	—
bulk CeO <sub>2</sub>	~ 2.35	—

Therefore, for uCNPs, O-termination of CNP corners, edges and {001} facets implies that the overall uCNP be super-oxidized (CeO<sub>2+x</sub>). In turn, excess O implies either the presence of Ce atoms oxidized beyond Ce<sup>IV</sup>—a situation not observed in the present study—or, that not all O atoms are doubly reduced. This last is the case as observed here, as highlighted in Table 4.1. In a structure with excess O atoms that have *not* relaxed to form O<sub>x</sub><sup>q-</sup> surface groups, individual O atoms that are *not* doubly reduced (that is O<sub>1</sub><sup>-1</sup> anions) are most likely to be under-coordinated at uCNP corners, edges or {001} facets. An under-coordinated corner/edge/facet O atom with unfilled *p* orbitals (that is, not doubly reduced) is highly reactive. Interaction with other O atoms allows reactive O<sub>1</sub><sup>-1</sup> anions to form more stable O<sub>2</sub>/O<sub>2</sub><sup>-</sup>/O<sub>2</sub><sup>2-</sup> and O<sub>3</sub>/O<sub>3</sub><sup>-</sup>/O<sub>3</sub><sup>2-</sup> surface groups. These then appear as adsorbed O<sub>x</sub><sup>q-</sup> surface groups on uCNP corners, edges and {001} facets.

For CNPs with bulk portions that are stoichiometric CeO<sub>2</sub>, this effect (that excess O implies Ce atoms oxidized beyond Ce<sup>IV</sup> or O atoms that are not doubly reduced) would be present at all particle sizes. But as bulk CeO<sub>2</sub> prefers a partially reduced form (that is, some fraction of Ce atoms are Ce<sup>III</sup> at finite temperature)<sup>189</sup>, large enough particles (e.g., particles with sufficient internal bulk volume) can sustain the additional O atoms necessary to yield O<sub>x</sub>-terminated surfaces while remaining net

reduced ( $\text{CeO}_{2-x}$ )—and hence not requiring Ce atoms oxidized beyond  $\text{Ce}^{\text{IV}}$  or O atoms that are not doubly reduced. For even larger ceria samples, sufficient O-vacancies exist in the bulk that, via diffusion, an equilibrium concentration of surface O-vacancies will appear at finite temperature. In this way, the present picture is completely consistent with previous calculations and experiments showing that large ceria particles (and bulk  $\text{CeO}_2$ ) are partially reduced<sup>26</sup>.

### 4.3 Electronic density of states

To further understand the properties of oxidized uCNPs, we need to explore the underlying electronic properties. Calculating the electronic density of states (eDOS) of uCNPs is a good way to reveal their electronic structures and predict their potential electronic properties. For the convenience of comparison, calculated eDOS of two typical bulk ceria, one typical reduced uCNP and three oxidized uCNPs of different shapes and thermodynamically stable surface configurations are plotted in Figure 4.3.

This plot actually shows the projected eDOS for some interested atomic orbitals with LDA+U ( $U = 5$  eV) calculation. Fermi energy ( $E_f$ ) is set to zero, as the reference energy to which relative positions of energy bands are shifted. In general, for all structures, projected eDOS can be divided into three parts: (1) the valence bands (VB) mainly composed of *Ce 5p* and *O 2p* bands in character at lower energy region; (2) the conduction band (CB) primarily formed by *Ce 5d* band in character at higher energy region and (3) gap between VB and CB sit *Ce 4f* band in character.

In bulk  $\text{CeO}_2$ , each Ce atom is coordinated with 8 neighboring O atoms and each O atom is coordinated with 4 neighboring Ce atoms. From pure chemistry perspective, each Ce atom shows the valence of 4+ and each O atom shows the valence of 2-. The eDOS accordingly exhibits features of energy bands associated with  $\text{Ce}^{\text{IV}}$  cations and  $\text{O}^{\text{II}}$  anions: (1) Ce 4f orbitals locate above Fermi level and (2) *O 2p* orbitals overlap with *Ce 4f* orbitals and *Ce 5d* orbitals. Calculated band gap for bulk  $\text{CeO}_2$  is  $\approx 5.2$

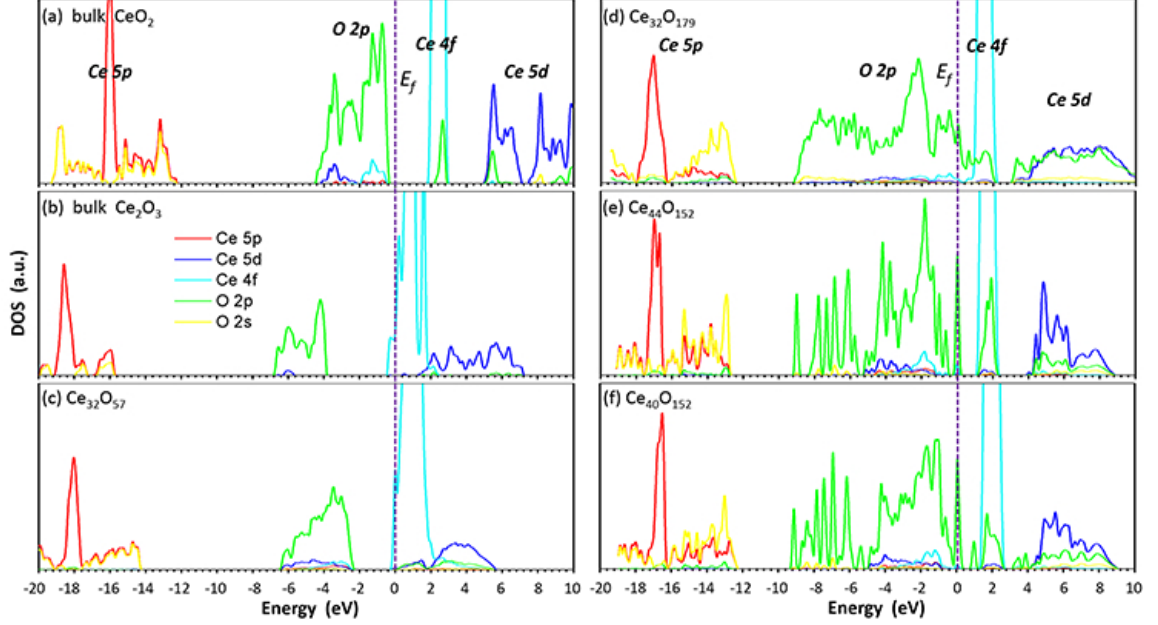


Figure 4.3: Calculated projected electronic density of states (eDOS) of some interested atomic orbitals for (a) bulk  $\text{CeO}_2$ ; (b) bulk  $\text{H-Ce}_2\text{O}_3$ ; (c)  $\text{Ce}_{32}\text{O}_{57}$ ; (d)  $\text{Ce}_{32}\text{O}_{179}$ ; (e)  $\text{Ce}_{44}\text{O}_{152}$  and (f)  $\text{Ce}_{40}\text{O}_{152}$  under LDA+U algorithm.

eV ( $\approx 3.2$  eV measured experimentally<sup>224</sup>).

In bulk  $\text{Ce}_2\text{O}_3$ , each Ce atom is coordinated with 7 neighboring O atoms. One third of O atom is coordinated with 6 neighboring Ce atoms while rest two thirds are individually coordinated with 4 neighboring Ce atoms. From pure chemistry perspective, each Ce atom on average shows the valence of 3+ and each O atom on average shows the valence of 2-. The corresponding eDOS exhibits features of energy bands associated with  $\text{Ce}^{\text{III}}$  cations and  $\text{O}^{\text{II}}$  anions: (1) partial  $\text{Ce } 4f$  orbitals locate below Fermi level; (2) no overlapping between  $\text{O } 2p$  orbitals and  $\text{Ce } 4f$  orbitals and (3)  $\text{Ce } 4f$  orbitals overlap with  $\text{Ce } 5d$  orbitals. Calculated band gap for bulk  $\text{Ce}_2\text{O}_3$  is  $\approx 4.8$  eV ( $\approx 2.4$  eV measured experimentally<sup>225</sup>).

Generally speaking, eDOS of bulk  $\text{CeO}_2$  together with bulk  $\text{Ce}_2\text{O}_3$  capture the internal electronic properties of  $\text{Ce}^{\text{IV}}$  and  $\text{Ce}^{\text{III}}$  cations within ceria, and can be used as the reference to identify these two distinct oxidation states of Ce cations in uC-NPs. Let us first look at the eDOS of a typical reduced uCNP structure,  $\text{Ce}_{32}\text{O}_{57}$

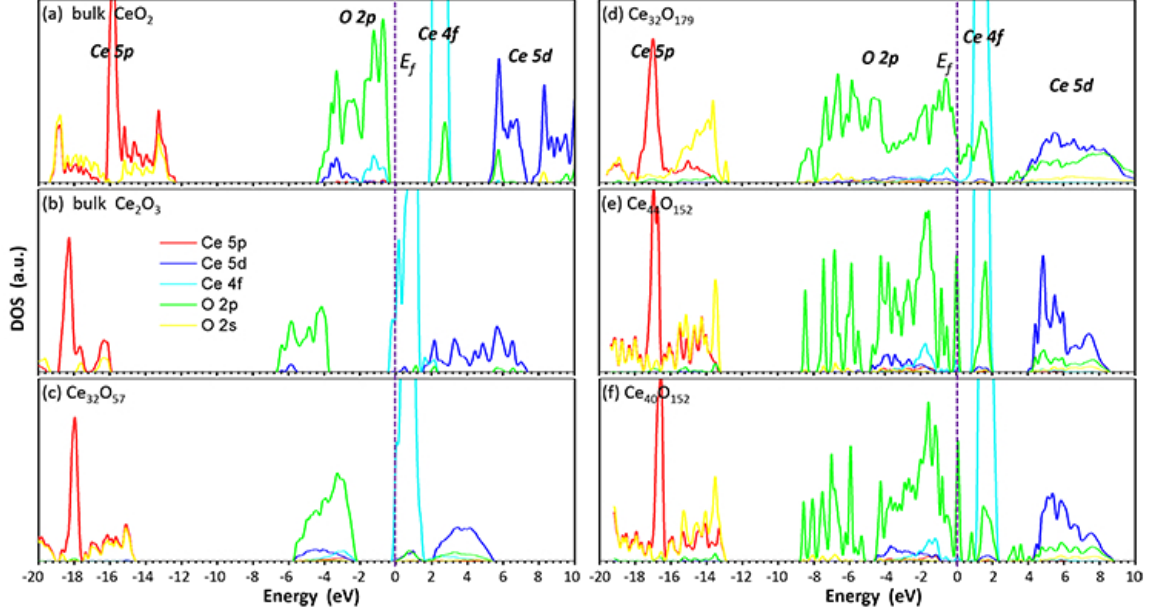


Figure 4.4: Calculated projected electronic density states (eDOS) of some interested atomic orbitals for (a) bulk  $\text{CeO}_2$ ; (b) bulk  $\text{H-Ce}_2\text{O}_3$ ; (c)  $\text{Ce}_{32}\text{O}_{57}$ ; (d)  $\text{Ce}_{32}\text{O}_{179}$ ; (e)  $\text{Ce}_{44}\text{O}_{152}$  and (f)  $\text{Ce}_{40}\text{O}_{152}$  under GGA+U algorithm.

in Figure 4.3(c). It is well acknowledged that some  $\text{Ce}^{\text{III}}$  cations are present in reduced uCNPs. The calculated eDOS for  $\text{Ce}_{32}\text{O}_{57}$  apparently exhibit features similar to that of calculated eDOS for bulk  $\text{Ce}_2\text{O}_3$ , suggesting that it is very likely that  $\text{Ce}^{\text{III}}$  cations are present in  $\text{Ce}_{32}\text{O}_{57}$ . This is further confirmed via Bader charge analysis on Ce atoms within  $\text{Ce}_{32}\text{O}_{57}$ , showing a good agreement with previously established understanding.

In contrast, it is very interesting that no obvious feature of calculated eDOS for bulk  $\text{Ce}_2\text{O}_3$  has been observed in oxidized uCNPs (i.e.  $\text{Ce}_{32}\text{O}_{179}$ ,  $\text{Ce}_{44}\text{O}_{152}$ , and  $\text{Ce}_{40}\text{O}_{152}$ ), with three representative shapes of experimentally synthesized uCNPs. Their eDOS patterns shown in Figures 4.3d-f unanimously express the typical feature of calculated eDOS for bulk  $\text{CeO}_2$ , especially the relative positions between  $\text{Ce } 4f$  and  $\text{Ce } 5d$  orbitals and their positions relative to the Fermi level. This strongly indicates that  $\text{Ce}^{\text{III}}$  cations are not expected to appear in those oxidized uCNPs, which is further confirmed via Bader charge analysis showing that all Ce are  $\text{Ce}^{\text{IV}}$  cations.

More delicate electronic structural information of oxidized uCNPs can be extracted from calculated eDOS. As  $O\ 2p$  orbitals expand, the edge of CB moves significantly closer towards the edge of VB, leading to apparent band gap reduction, particularly for  $Ce_{32}O_{179}$ . Two sets of eDOS patterns corresponding to two chemical states of O atoms in oxidized uCNPs are convoluted and overlapped to different degrees in uCNPs of different shapes, giving rise to  $O\ 2p$  orbital expansion. A set of O atoms are basically “bulk-like” O lattice atoms bonded to Ce atoms involving electronic interactions only between Ce orbitals and O orbitals, while others are bonded not only to neighboring O atoms within  $-O_x$  surface groups involving electronic interactions between O orbitals of different O atoms but also to surface Ce atoms involving electronic interactions between Ce orbitals and O orbitals. This is quite complicated that eDOS of  $O\ 2p$  orbitals can not be distinguished as two parts that exactly reflect above described two chemical states of O atoms; however, bands at higher energy and closer to  $Ce\ 5d$  orbitals at CB are primarily contributed from “bulk-like” O lattice atoms, whose pattern on the whole resembles that of  $O\ 2p$  orbitals in bulk  $CeO_2$ , while bands at lower energy and towards  $Ce\ 5p$  orbitals, are mainly contributed from O atoms within  $-O_x$  groups bonded to surface Ce atoms. The greatly reduced energy difference between  $O\ 2p$  orbitals and  $Ce\ 5d$  orbitals may indicate that electrons can be more easily excited from VB to CB, as a result of the pathway established by surface chemically adsorbed  $-O_x$  groups for oxidized uCNPs.

We have used GGA+U ( $U = 3\text{ eV}$ ) algorithm to calculate eDOS of all above mentioned bulk ceria and uCNP structures as well. The results are plotted in Figure 4.4. Apart from insignificant band shifts relative to the Fermi level, the patterns of calculated eDOS for all considered structures almost remains exactly the same as those obtained from LDA+U ( $U = 5\text{ eV}$ ) calculation. On the one hand, it suggests that atomic and electronic structural features of uCNPs are well captured by our calculation, and our results are reliable. On the other hand, it shows that both LDA

and GGA algorithms to some extent are robust and accurate enough to study the atomic and electronic structures of uCNPs.

#### 4.4 Infrared spectrum

Adsorbed functional groups at solid surfaces can be effectively detected with carefully designed infrared (IR) spectrum experiment. This provides us a straightforward means to validate our atomistic picture concerning the surface configuration of oxidized uCNPs, which primarily features various adsorbed  $-O_x$  surface groups.

The IR absorption properties of individual free  $-O_x$  groups like  $O_2$  and  $O_3$  have been well characterized by previous experiments. However, the vibration of  $-O_x$  groups free from any chemical restriction along with their featured vibration frequencies cannot simply serve as the fingerprint to identify the chemical status of  $-O_x$  groups adsorbed at solid surfaces. This is because at the interface between gas environment and the solid surface, various degrees of limitations are compounded to the force governing the vibrational behavior of these  $-O_x$  groups, which directly affects their vibration frequencies and associated vibration intensities. This is exactly the case in our oxidized uCNPs that  $-O_x$  groups are chemically bonded to the surface. Thus, we need not only tractable IR characterization from the experiment to verify our computationally predicted surface configuration of oxidized uCNPs, but also available data/information directly obtained from the computation to assist assigning an experimentally measured vibration frequency to a specific vibration mode of an adsorbed  $-O_x$  group. Thus, we are capable of mapping collective vibration frequencies to individual vibration modes of present  $-O_x$  groups at surfaces of uCNPs and better understanding the surface configuration of uCNPs via the IR spectrum. This demonstrates that experimental measurement and computational prediction serve as a mutually promotive, integrated tool to explore and substantiate the surface configuration of uCNPs.

VASP (our computational tool) provides an approach to calculate the complete IR spectrum of a particular structure, and we take advantage of this to calculate the IR spectrum of oxidized uCNPs. One big hurdle of practically applying this method to our uCNPs system is the enormous computation cost. To be specific, obtaining the complete calculated IR spectrum (including vibration frequency and vibration intensity) based on density functional perturbation theory to calculate Hessian matrix requires *IBRION*=7 setting with demanding reciprocal space projection, all atoms in the system under consideration, and non-gamma point, memory consuming calculation. In contrast, switching to *IRHION*=5 setting based on finite differences to determine Hessian matrix, we can rely on fully automatic-optimized real space projection, a portion of interested atoms under consideration, and gamma-point memory reducing calculation, which alleviates at least 75 % of total computation cost, in other words, at least three times faster. In addition, compared to vibration frequency, vibration intensity is a secondary and often half-empirical factor in terms of identifying vibration mode and type of a particular surface functional groups, it is more important to accurately locate the position of IR adsorption peaks than their intensities. To estimate how much predicted vibration frequencies obtained from *IBRION*=5 calculation where only atoms within adsorbed  $-O_x$  groups are movable are off from *IBRION*=7 calculation without any fixed atoms, we use a relatively simple yet representative uCNP structure,  $Ce_{32}O_{101}$ .

In  $Ce_{32}O_{101}$ , there are three kinds of  $-O_x$  surface groups, i.e.  $O_2^-$  laying at corners,  $O_3$  bridging at edges, and  $O_3^-$  standing at edges. In general,  $-O_x$  groups adsorbed at surfaces of uCNPs can take one of the three spatial orientation: (1) laying; (2) bridging; and (3) standing, as shown in Figure 4.5. For a diatomic  $O_x$  surface group, like  $O_2$ ,  $O_2^-$  and  $O_2^{2-}$ , laying refers to the case that both O atoms are bonded to the same Ce atom, bridging refers to the case that each O atom is bonded to one or two Ce atoms at a time separately with overall molecule spanning over two neighboring

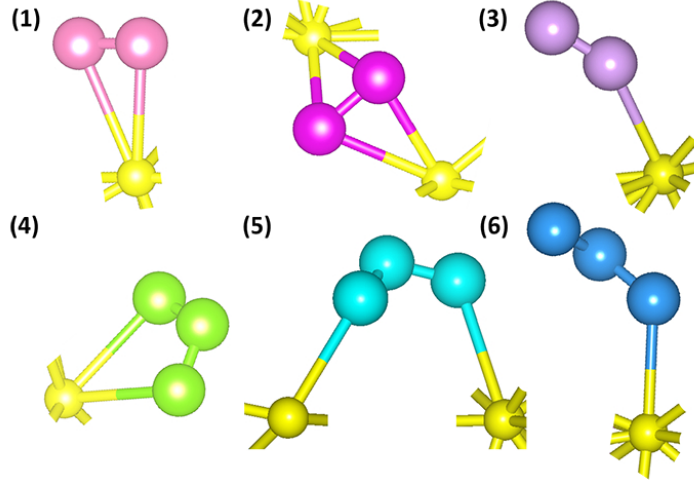


Figure 4.5: Spatial orientation for diatomic and triatomic  $-O_x$  groups adsorbed at surfaces of uCNPs: (1)  $O_2^-$  laying; (2)  $O_2^{2-}$  bridging; (3)  $O_2$  standing; (4)  $O_3$  laying; (5)  $O_3^-$  bridging and (6)  $O_3^{2-}$  standing. Note that yellow balls represent Ce atoms, while other colored balls represent O atoms within different  $-O_x$  surface groups, and the coloring is consistent with Figure 4.2.

Table 4.3: Comparison of calculated vibration frequencies under  $IBRION=5$  and  $IBRION=7$  settings and assigned vibration modes to  $-O_x$  surface groups in a representative oxidized uCNP structure,  $Ce_{32}O_{101}$ .

$O_x$ surface Groups	Special Orientation	Vibration Mode	Vibration Frequency Range ( $cm^{-1}$ ) <sup>a</sup>	
			$IBRION=5$	$IBRION=7$
$O_2^-$	laying	stretching	1157.30	1137.73
$O_3$	bridging	symmetric stretching	1102.86	1084.61
		asymmetric stretching	1008.90	997.00
		bending	688.94	689.23
$O_3^-$	standing	symmetric stretching	1285.47	1263.88
		bending	700.27	705.52
$O_3^{2-}$	bridging	symmetric stretching	910.64	899.17
		asymmetric stretching	769.39	773.80
		bending	575.64	570.68

<sup>a</sup>Note: Vibration frequency listed within  $IBRION=5$  column are the average values, while those listed within  $IBRION=7$  column are estimated absorption peak positions.

Ce atoms, and standing refers to the case that only one end of O atom is bonded to a single Ce atom. In the same manner, for a triatomic  $O_x$  surface group, like  $O_3$ ,  $O_3^-$  and  $O_3^{2-}$ , laying refers to the case that two-end O atoms are bonded to the same Ce atom, bridging refers to the case that each O atom at one end is bonded to one or two



Ce atoms at a time separately with overall molecule spanning over two neighboring Ce atoms, and standing refers to the case that only one-end O atom is bonded to a single Ce atom.

The calculated vibration frequencies and assigned vibration modes corresponding to those  $-O_x$  surface groups are summarized in Table 4.3. It can be seen that a tiny difference (around  $20\text{ cm}^{-1}$  higher) in vibration frequency occurs in *IBRION*=5 calculation compared to *IBRION*=7 calculation. This strongly suggests that much more efficient *IBRION*=5 calculation is reliable and accurate enough to produce results of similar quality obtained via computationally expansive *IBRION*=7 calculation.

Let us move on to examine possible vibration modes and IR absorption properties of  $-O_x$  groups at surfaces of three thermodynamically stable structures representing cubic, octahedral and cuboctahedral shaped uCNPs. Vibration frequencies together with vibration modes assigned to corresponding  $-O_x$  surface groups with dissimilar chemical bonding status as well as spacial orientation are tabulated in Table 4.4. The detailed information presented in Table 4.4 can be used together with experimentally measured IR spectra as a handy reference to map out which type of  $-O_x$  groups are likely present at surfaces of uCNPs, and further to predict their adsorption location and orientation. The adsorption location refers to available surface sites of uCNPs expressed via both abstract spatial relation, for instance, corner and specific crystallographic direction, for instance,  $\langle 100 \rangle$  direction. The adsorption orientation mainly refers to the spatial relation between  $-O_x$  surface groups and neighboring Ce atoms, for instance, laying (see Figure 4.5 for details).

For octahedral and cuboactahedral uCNPs, due to the stoichiometry of  $\{111\}$  facet, edges and corners except  $\{111\}$  facets of uCNPs are available adsorption sites for  $-O_x$  surface groups. This in turn simplifies vibration modes of  $Ce_{44}O_{152}$  and  $Ce_{40}O_{152}$ . As a result, we can predict that for  $Ce_{44}O_{152}$ , roughly two sets of IR absorption peaks belonging to vibration of  $O_2$  and  $O_2^-$  surface groups respectively will

show up in experimentally measured IR spectrum. Similarly, no more than three sets of IR absorption peaks are expected for  $\text{Ce}_{40}\text{O}_{152}$ . In contrast, ceria  $\{100\}$  facets are non-stoichiometric by nature, thus, experimentally measured IR spectrum will be expected to be much more complicated due to multiple available adsorption sites and varied types of  $-\text{O}_x$  surface groups, which has already been reflected by calculation. What specific vibration mode can we predict to be observed in experimentally measured IR spectrum of uCNPs? For diatomic  $-\text{O}_x$  surface groups, stretching along the axis of two vibrating atoms is the only vibration mode that is likely to be detected by experimental IR measurement. For triatomic  $-\text{O}_x$  surface groups, the possible detectable vibration modes include symmetric stretching, antisymmetric stretching and bending. Normally,  $\text{O}_2$  will not show IR absorption as symmetric stretching is the only vibration mode that does not induce a dipole moment within  $\text{O}_2$ ; however, symmetric stretching of adsorbed  $\text{O}_2$  surface group may exhibit IR adsorption peak, as the local environment of adsorbed  $\text{O}_2$  surface group could induce a dipole moment within otherwise unpolarized  $\text{O}_2$  molecules. The same principle may apply to the symmetric stretching of adsorbed  $\text{O}_3$  surface group. Meanwhile,  $-\text{O}_x$  groups adsorbed at surfaces of octahedral and cuboctahedral uCNPs are often paired, resulting in new patterns of vibration, for instance, synchronized stretching (i.e. two paired  $\text{O}_x$  surface groups vibrating at same pace and in the same direction) and contrary stretching (i.e. two paired  $\text{O}_x$  surface groups vibrating at same pace but in the opposite direction).

Not every  $-\text{O}_x$  surface groups can occupy any adsorption site and/or choose any adsorption orientation. As a matter of fact, they follow certain patterns.  $\text{O}_2$  surface groups preferably adsorb to edge Ce atoms along  $\langle 110 \rangle$  in a standing orientation, while  $\text{O}_2^-$  surface groups preferably adsorb to corner/edge Ce atoms within  $\{100\}$  plane in a laying orientation.  $\text{O}_2^{2-}$  surface groups tends to adsorb to facet Ce atoms within  $\{100\}$  plane in a bridging orientation.  $\text{O}_3$  surface groups primarily adsorb to corner Ce atoms within  $\{100\}$  plane and edge Ce atoms along  $\langle 110 \rangle / \langle 100 \rangle$  in a

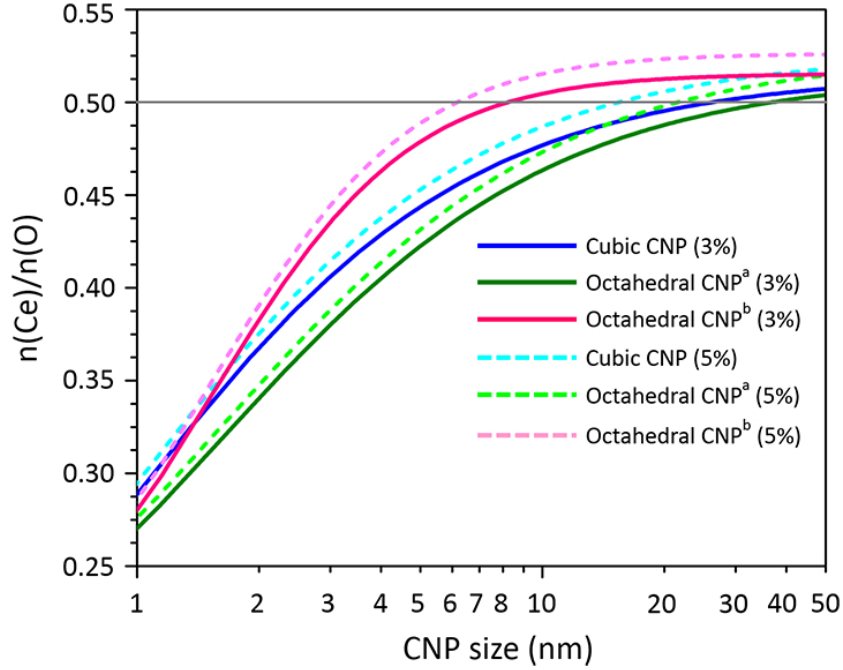


Figure 4.6: Ratio of Ce to O atoms in cubic and octahedral CNPs as a function of CNP size. Cubic CNP and octahedral CNP<sup>a</sup> structures are fully oxidized, while octahedral CNP<sup>b</sup> structures exhibit stoichiometric  $\{111\}$  facets, but fully coordinated (oxidized) edges and corners.

laying orientation (minority at corners/edges in a standing orientation).  $\text{O}_3^-$  surface groups typically adsorb to edge Ce atoms along  $\langle 110 \rangle / \langle 100 \rangle$  in a bridging orientation with a small portion at corners in a laying orientation.  $\text{O}_3^{2-}$  surface groups, like  $\text{O}_2^{2-}$  surface groups, tends to adsorb to facet Ce atoms within  $\{100\}$  plane in a bridging orientation.

Furthermore, the vibration frequency of an  $-\text{O}_x$  surface group is highly dependent on its adsorption location and orientation.  $-\text{O}_x$  surface groups adsorbed at corners or edges exhibit higher vibration frequencies than those adsorbed towards/at facets. For diatomic  $-\text{O}_x$  surface groups, their overall vibration frequency in terms of spatial orientation is in the following order: standing > laying > bridging. For triatomic  $-\text{O}_x$  surface groups, those in a standing/bridging orientation tend to exhibit higher vibration frequencies than those in a laying orientation. Within a specific  $-\text{O}_x$  surface

group in a particular spatial orientation, vibration frequency in terms of vibration modes is generally in the following order: symmetric (synchronized) stretching > asymmetric (contrary) stretching > bending, which is well consistent with common knowledge of molecular IR spectroscopy. Clearly, vibration frequency assigned to a specific vibration mode of  $-\text{O}_x$  surface groups is not randomly distributed but in a general order as follows:  $\text{O}_2 > \text{O}_2^- > \text{O}_3 > \text{O}_3^- > \text{O}_2^{2-} > \text{O}_3^{2-}$ .

#### 4.5 Size-dependent surface terminations

By assuming a net bulk O-vacancy concentration of 5%<sup>24,226</sup> and leveraging geometrical rules for the number of Ce and O atoms present in CNPs of various shapes (see **section 2.8.1**), the net Ce/O ratio can be estimated as a function of the size for O-terminated cubic and octahedral CNPs. Figure 4.6 shows that the transition from larger, reduced (and therefore bulk-terminated) CNPs to smaller, CNPs with surface configuration of various adsorbed  $\text{O}_x^{q-}$  surface groups occurs at critical sizes between 8 and 35 nm, depending on the CNP geometry. These critical sizes are the result of two competing effects—bulk thermodynamic effects driving net reduction of  $\text{CeO}_2$ , and surface configurations driving net oxidation of  $\text{CeO}_2$ . Decreases (or increases) in the net O-vacancy concentration do not alter this qualitative result, but rather lead to small increases (or decreases) in the critical size (e.g., from 25 to 15 nm for {100}-terminated CNPs after a decrease in O-vacancy concentration to 3%).

#### 4.6 Summary

Below a critical size, uCNPs in a pure O environment do not exhibit bulk-like surface configuration. Instead, they exhibit stable surface reconstructions consisting of  $-\text{O}_x^{q-}$  ( $0 \leq q \leq 2$ ,  $x=2,3$ ) surface groups chemically adsorbed at uCNP corners, edges, and {001} facets. Those  $-\text{O}_x$  surface groups can be well characterized by computationally obtained eDOS as well as experimentally measured IR spectrum. Calculated IR

spectrum can serve as a fingerprint to facilitate analyzing experimentally measured IR spectrum and further to judge the type and chemical status of present  $-\text{O}_x$  surface groups. The formation of these  $-\text{O}_x$  surface groups reduces the energy of uCNPs by increasing the coordination of near surface Ce cations, while allowing for low-energy  $-\text{O}_x$  surface groups with charges more positive than 2-. The existence of this balance (increased cation coordination and  $-\text{O}_x$  surface groups) is necessitated by the non-stoichiometry of uCNP corners, edges and (as considered here)  $\{100\}$  facets. For larger CNPs with larger internal (and therefore bulk) volumes, the presence of intrinsic O-vacancies can offset the excess corner, edge and facet  $-\text{O}_x$  surface groups required to increase near-surface Ce cation coordination. This leads to a shape-dependent critical size (estimated here as  $\sim 15$  and  $\sim 3$  nm for  $\{100\}$ - and  $\{111\}$ -terminated uCNPs) for a transition from atomic-O-(bulk-like) surface configuration to  $\text{O}_x^{q-}$  surface group populated surface configuration.

The presence of directly adsorbed  $\text{O}_x^{q-}$  groups at surfaces of uCNP structures strongly suggests the possibility of catalytic mechanisms of uCNPs that do not involve the formation and/or migration of bulk O-vacancies. Hence, for instance, reaction rates for catalytic oxidation of CO or NO over uCNPs may not be limited by the thermodynamics and kinetics of bulk and surface O-vacancies. Extending the picture introduced above of stable uCNP structures in pure oxygen environments as reduced “core” with oxidized “shell” (passivated with  $\text{O}_x^{q-}$  surface groups), we note that the uCNP stabilization effects reported here due to adsorbed  $\text{O}_x^{q-}$  surface groups could also be realized by  $-\text{OH}$  or peroxide surface groups, or a host of other anionic surface groups. In turn, this suggests the possibility of tailoring the catalytic mechanisms of uCNPs for specific reactions—e.g., stabilizing uCNPs with  $-\text{OH}$  surface groups for application in water splitting or the water-gas shift reaction. Such mechanisms would represent direct reaction pathways that do not depend on the annihilation and regeneration of O-vacancies in bulk ceria and ceria exhibiting ideal, unreconstructed,

stoichiometric bulk-like terminations.

Table 4.4: Comparison of calculated vibration frequencies under IBRION=5 settings and assigned vibration modes to  $-O_x$  surface groups in three representative oxidized uCNP structures, cubic shaped  $Ce_{32}O_{179}$ , octahedral shaped  $Ce_{44}O_{152}$ , and cuboctahedral shaped  $Ce_{40}O_{152}$  obtained via LDA+U calculations (U=5 eV).

Type of uCNP	$O_x$ Surface Groups	Special Orientation	Vibration Mode	Vibration Frequency Range ( $cm^{-1}$ )
$Ce_{32}O_{179}$	$O_2$	standing	stretching	1461.15 — 1439.12
	$O_2^-$	standing	stretching	1319.16
		laying	stretching	1308.51 — 1233.41 1202.22 — 1171.75
		bridging	stretching	1208.89, 1170.61 1138.51 — 1124.69 1116.86, 1112.01, 1074.25
	$O_2^{2-}$	bridging	stretching	1021.45 — 982.88 971.07 — 964.48, 954.49
	$O_3$	standing	symmetric stretching asymmetric stretching bending	1202.61 840.75 652.50
		laying	symmetric stretching	1108.97 — 1076.90, 1073.23
			asymmetric stretching	1049.75, 1047.69 1046.65 — 1022.80
			bending	722.83, 722.18, 709.04, 707.16 702.53, 700.37, 681.39
	$O_3^-$	bridging	symmetric stretching	1167.76 — 1144.12, 1118.85
			asymmetric stretching	960.66, 942.04, 934.40 902.32 — 873.86, 839.02 806.04, 753.77, 744.33
			bending	744.33, 723.66, 723.04, 713.11 705.73, 684.52, 669.51, 653.90 615.63, 604.17, 583.60, 572.38
		laying	symmetric stretching asymmetric stretching bending	1055.70, 1047.26 960.66, 942.03 681.67, 670.93
	$O_3^{2-}$	bridging	symmetric stretching	973.43, 963.73, 961.64 958.67, 953.90 — 944.66 941.60, 939.56 — 924.98
			asymmetric stretching	858.40 — 849.84, 829.67 819.38, 796.23, 773.73 750.77, 746.20, 733.60, 729.71
			bending	644.96 — 621.85, 604.61 594.24, 589.35, 580.54 576.70, 571.04
$Ce_{44}O_{152}$	$O_2$	standing	synchronized stretching contrary stretching	1423.71 — 1388.79 1333.28 — 1324.59
	$O_2^-$	laying	synchronized stretching contrary stretching	1353.38 — 1337.89 1287.09 — 1261.51
$Ce_{40}O_{152}$	$O_2$	standing	synchronized stretching contrary stretching	1450.55 — 1393.31 1375.49 — 1358.51
	$O_2^-$	laying	synchronized stretching contrary stretching	1357.11 — 1356.60 1288.76 — 1288.14
	$O_3^-$	bridging	symmetric stretching	1157.91 — 1066.36
			asymmetric stretching	808.19 — 741.16 721.48 — 707.36
			bending	631.76 — 551.84

## Chapter 5 Direct oxidation of CO over ultra-small CNPs terminated with $-\text{O}_x$ surface groups

In the previous chapter, we have systematically explored the surface configuration of uCNPs in a pure oxygen environment. Our study has rendered a new perspective on their surface configuration, in direct contrast to conventional perspectives concerning the surface configuration of bulk ceria, ceria surfaces, and larger-sized CNPs. That is, regardless of their shape, the surface of uCNPs are populated with various  $-\text{O}_x$  surface groups. Instead of relying on the thermodynamics and kinetics of O-vacancies in ceria systems with bulk-like surface configuration, the catalytic behavior of uCNPs are expected to be dominated by their surface chemistry, i.e.  $-\text{O}_x$  surface groups to be specific here. To test our hypothesis and assess the performance of uCNPs obtained from our computation, we have chosen the carbon monoxide (CO) oxidation reaction, a widely investigated catalytic reaction over ceria systems both experimentally and computationally. More importantly, this reaction is actually adopted in industry to control the pollutants released to our living environment.

### 5.1 Catalytic properties of uCNPs terminated with $-\text{O}_x$ surface groups

On the whole, for ceria catalysts with bulk-like surface configuration, the “four-step” hypothesis described in **section 1.2** is the only possible pathway that CO oxidation reaction can take. However, our study presents a different scenario concerning the surface configuration of uCNPs in a pure oxygen environment, that is, numerous  $-\text{O}_x$  groups are chemically adsorbed at surfaces. For uCNPs with such a surface configuration, we expect a utterly dissimilar catalytic behavior in terms of oxidizing CO, which heavily involves the direct exchange of atomic O between  $-\text{O}_x$  surface groups and CO at uCNP surfaces. In the following, we will show that the catalytic



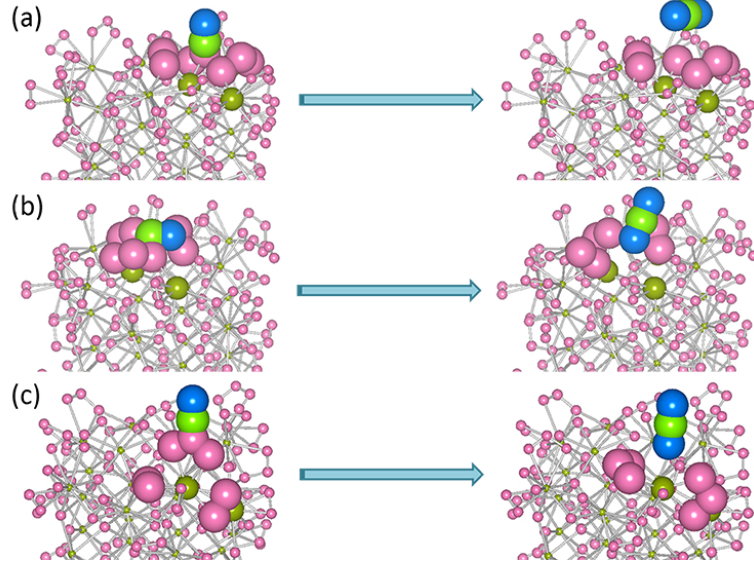


Figure 5.1: Three different situations of an incoming CO molecule attacking the surface of uCNPs. These are zoom-in pictures showing the reaction sites pertaining to partial surface of considered uCNPs. Yellow greenish balls represent Ce atoms, pink balls represent O atoms within considered uCNP structures, light green balls represent C atoms, and blue balls represent O atoms bound to C atoms. Some balls are enlarged to clearly show the atoms actively participating in the CO oxidation process.

behavior of uCNPs terminated with  $-O_x$  surface groups is in fact distinct from reduced ceria systems with bulk-like surface configuration. Generally speaking, uCNPs can spontaneously oxidize CO to  $CO_2$  relying on various adsorbed  $-O_x$  groups at surfaces rather than thermally-activated lattice O-vacancies.

Figure 5.1 shows three dissimilar situations of an incoming CO molecule attacking the surface of  $\sim 1$  nm uCNPs. These scenarios revealed on the atomic scale give us a hint to understand the interaction between CO molecules and uCNPs. Figure 5.1a presents the case of a CO molecule attacking one end of an  $-O_3$  surface group. It is apparent that the attacked  $-O_3$  surface group donates one O atom to the CO molecule and oxidizes it to a free  $CO_2$  molecule, while itself is reduced to an  $-O_2$  surface groups formed by two remaining O atoms. The whole reaction can be expressed as

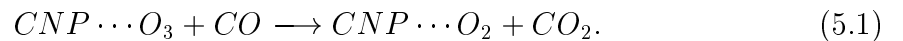


Figure 5.1b illustrates the case of a CO molecule attacking one end of an  $-O_2$  surface group. Similarly, the attacked  $-O_2$  surface group donates one O atom to the CO molecule and oxidizes it to a free  $CO_2$  molecule. In this case, a single O atom is left behind, It is thus energetically favorable to form a surface O lattice atom to link two separate Ce atoms rather than to combine with another  $O_2$  molecule via traveling a long distance. The whole reaction can be expressed as

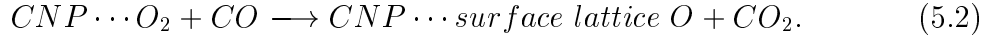


Figure 5.1c exhibits the case of a CO molecule attacking the middle atom of an  $-O_3$  surface group. In this case, the  $O_3$  surface group splits into three separate O atoms. The middle O atom is donated to the CO molecule and oxidizes it to a free  $CO_2$  molecule. The other two-end O atoms combine with neighboring  $-O_2$  surface groups to reform another two  $-O_3$  surface groups. The whole reaction can be expressed as



All above three scenarios unanimously indicates that uCNPs terminated with  $-O_x$  surface groups are able to spontaneously oxidize CO to  $CO_2$  without thermally overcoming certain energy barrier.

To verify the successful conversion of incoming CO molecules to free  $CO_2$  molecules by  $\sim 1$  nm uCNPs, the energy of formation of relevant relaxed structures are calculated and along with structural information summarized in Table 5.1. Above all, the C-O bond length, O-C-O bond angle and total charge of yielded carbon oxide listed in the table fall in the range of  $1.17 \pm 0.01 \text{ \AA}$ ,  $179.44 \pm 0.20^\circ$  and  $15.99 \pm 0.01$ , respectively, which are very close to those of a free  $CO_2$  molecule, i.e.  $1.20 \text{ \AA}$ ,  $180^\circ$  and  $16.00$ , respectively. Furthermore, the difference between the energy of overall relaxed structure ( $CO_2 + \text{uCNP}$ ) and that of the remaining uCNP structure only is  $-22.96 \pm 0.36 \text{ eV}$ , quite close to the calculated energy of formation of a free  $CO_2$  molecule,  $-22.98 \text{ eV}$ . In addition, the distance of yielded  $CO_2$  molecule to the

Table 5.1: The information on the relaxed structure of  $\sim 1$  nm cubic uCNPs interacting with an incoming CO molecule

$O_x$ surface groups attacked by CO molecules	Type	$O_3$	$O_3^-$	$O_3^-$	$O_2^-$	$O_3$
	reaction site	less negatively charged end atom	less negatively charged end atom	more negatively charged end atom	less negatively charged end atom	slightly positively charged middle atom
Yielded carbon oxides	C-O bond length ( $\text{\AA}$ )	1.17	1.17	1.17	1.18	1.17
	O-C-O bond angle ( $^\circ$ )	1.18	1.18	1.18	1.18	1.18
		179.53	179.42	179.14	179.41	179.68
	Total charge	15.99	16.00	15.98	16.01	15.98
	Distance from nearest Ce atoms ( $\text{\AA}$ )	2.82	3.27	2.79	3.90	2.88
CNP+CO reaction	Energy of overall relaxed structure (eV)	-1226.13	-1232.11	-1231.95	-1232.13	-1225.50
	Energy of relaxed uCNP by subtracting the formed carbon oxide (eV)	-1202.88	-1209.08	-1208.89	-1209.10	-1203.19
	Energy difference of above two (eV)	-23.25	-23.03	-23.07	-23.03	-22.31
	Formation energy of pure $CO_2$ (eV)	-22.98	-22.98	-22.98	-22.98	-22.98

nearest Ce atom at the surface of relaxed uCNP structure is beyond the Ce-O bond length in ceria, which again confirms that  $CO_2$  molecule is unbound to the surface of uCNP. All suggests that uCNPs are capable of spontaneously oxidizing an incoming CO molecule to a free  $CO_2$  molecule.

It is worth noting that not all  $-O_x$  surface groups can oxidize CO into  $CO_2$ . Firstly, the oxidation reaction never occurs when a CO molecule approaches a neutral  $-O_2$  surface group. Secondly, once a CO molecule approaches either end of an  $-O_3^-$  surface group or a less negatively charged end of a neutral  $-O_3$  surface group, and the oxidation reaction occurs and follows the pathway shown in Equation 5.1. Thirdly, whenever a CO molecule approaches a less negatively charged end of a  $-O_2^-$  surface group, the reaction also occurs and follows the pathway shown in Equation 5.2. Lastly,

as soon as a CO molecule approaches the middle atom of a neutral  $-\text{O}_3$  surface group, the reaction immediately occurs and follows the pathway shown in Equation 5.3. The possible explanation is the stabilization of surface O atoms. For a neutral  $-\text{O}_2$  surface group, it is most stable; otherwise a single O separating from a neutral  $-\text{O}_2$  surface group is highly reactive. For a  $-\text{O}_2^-$  surface group, the more negatively charged O atom is more strongly bound to that of an O lattice atom compared to the other less negatively charged one. Therefore, it is energetically favorable for the less negatively charged to combine with the incoming CO molecule and the more negatively charged to form a surface O lattice atom. For a neutral  $-\text{O}_3$  surface group, it is more reasonable for the most negatively charged as the primary electron donor to form a stable  $-\text{O}_2$  surface group with the remaining less negatively charged or slightly positively charged middle O atom when either one is taken away by the incoming CO molecule. For an  $-\text{O}_3^-$  surface group, if the middle atom is captured by the incoming CO molecule, the newly formed  $\text{CO}_2$  molecule will be somewhat positively charged while the remaining two O atoms will form somewhat negatively charged  $-\text{O}_2$  surface group. The strong Coulomb interaction between  $\text{CO}_2^+$  and  $\text{O}_2^-$  surface group will be strongly likely to combine together, which is consistent with the result of our DFT calculation. Therefore, it is favorable for either remaining end O atom of an  $-\text{O}_3^-$  surface group to form a stable  $-\text{O}_2$  surface group with the middle O atom. The panoramic picture of oxidizing CO into  $\text{CO}_2$  by uCNPs is that a particular O atom in an absorbed  $-\text{O}_x$  surface group will donate itself to the approaching CO molecule to form a  $\text{CO}_2$  molecule. As a result, the formed  $\text{CO}_2$  molecule detaches from the surface and becomes a free  $\text{CO}_2$  molecule while the uCNP loses one surface atomic O and adjusts its overall structure to a more energetically favorable structure.

In direct contrast to the O-vacancy dominated catalytic behavior of reduced bulk ceria and ceria surfaces that require relatively longer times to enable the generation, migration and annihilation of O-vacancies both at “bulk” part and surfaces, uCNPs

terminated with  $-O_x$  surface groups can effectively enhance the kinetics of such oxidation reaction given the readily available active  $-O_x$  surface groups. In addition, the presence of  $-O_x$  surface groups necessarily implies lower oxidation temperature of CO by uCNPs compared to reduced bulk ceria and ceria surfaces that requires higher activation temperature of O-vacancies. All the above evidences strongly indicate that uCNPs are potentially more efficient catalyst materials in terms of oxidizing CO than bulk ceria and ceria surfaces.

## 5.2 Summary

Ultra-small ceria nanoparticles (uCNPs) terminated with  $-O_x$  surface groups exhibit different catalytic behavior in the CO oxidation process compared to ceria systems with ideal, unreconstructed, stoichiometric, bulk-like surface configurations. Instead of relying on the “four-step” hypothesis (see **section 1.2**), which is intrinsically driven via thermodynamics and kinetics of O-vacancies, uCNPs fully take advantage of various adsorbed  $-O_x$  surface groups. To be more specific, in a gas environment containing CO and  $O_2$ ,  $-O_x$  groups adsorbed at surfaces of uCNPs can directly donate an atomic O to incoming reactants, enabling uCNPs to spontaneously oxidize the incoming CO molecule. Dissimilar pathways are required to accomplish the oxidation process in case of which  $-O_x$  surface group and surface site the incoming CO molecule approaches. Nevertheless, once such an oxidation reaction proceeds, it needs no activation energy, in direct contrast to processes depending on kinetics of O-vacancies, which definitely needs to overcome an activation energy barrier. In a word, though an idealized case (that only consider a gas environment containing CO and  $O_2$ ) is investigated here to explore the catalytic mechanism of CO oxidation reaction over uCNPs, our calculations strongly suggest that uCNPs offer an alternative catalytic pathway (or mechanism) to oxidize CO molecules, which further implies that uCNPs are potentially more efficient catalytic materials than ceria systems with ideal,

unreconstructed, stoichiometric, bulk-like surface configurations.

## Chapter 6 The surface configuration of ultra-small CNPs in a humid environment

In the previous chapter, we have discussed a simple and ideal case, the surface configuration of uCNPs in a pure oxygen environment. We realize that for uCNPs, they are covered with various chemically adsorbed  $-O_x$  surface groups. The overall structure of uCNPs can be viewed as a “core-shell” structure, with *reduced*  $CeO_{2-x}$  *core* and *oxidized*  $-O_x$  surface group *shell*. As catalysis is usually expected to occur at surfaces, such a layer of  $-O_x$  surface groups is likely to be the active sites for catalytic reactions and dominates the catalytic behavior of uCNPs. However, in practice, uCNPs are typically synthesized in aqueous solution and applied in a humid environment. The role of  $H_2O$ , in other words, the influence of  $H_2O$  on the surface configuration of uCNPs cannot be simply neglected and must be taken into account while examining the structure-property relationship of uCNPs and exploring the detailed process of catalytic reactions over uCNPs.

The awareness of notable impacts on the surface configuration of catalysts from  $H_2O$  has driven several computational studies based on DFT to examine the interplay between  $H_2O$  and bulk metal oxide surfaces including bulk ceria surfaces<sup>48,227–230</sup> on the atomic scale. In general, they have found that  $H_2O$  either favorably adsorbed over the top of a metal atom or dissociated into OH and H at O-vacancy sites. In spite of these insightful conclusions, none of them has investigated the influence of  $H_2O$  on the surface configuration of nanoparticulate metal oxide systems, in particular uCNPs as our focus in this study here. Thus, several concerns remain to be addressed regarding the surface configuration of uCNPs in a humid environment: (1) will  $H_2O$  affect the surface configuration of uCNPs in a similar way that  $H_2O$  affects bulk ceria surfaces? (2) will such a layer of  $-O_x$  surface groups remain at surfaces of uCNPs in

an environment containing  $\text{H}_2\text{O}$ ? (3) will the surface configuration of uCNPs vary in response to different humid environments? If so, how? Those are the questions that we will further discuss and explore in this chapter.

The simplest thought to approach these questions is creating a supercell, in which a uCNP is surrounded with a finite number of  $\text{H}_2\text{O}$  molecules to simulate a humid environment and relaxing the overall supercell to see whether there is any interplay between  $\text{H}_2\text{O}$  molecules and uCNP surface. This is at first sight a facile and elegant idea except that the computation cost is too expensive to afford. On the one hand, we know that in a humid environment, a  $\text{H}_2\text{O}$  molecule can be weakly ionized into  $\text{H}^+$  and  $\text{OH}^-$  ions. On the other hand, the considered system is overall neutral and DFT relaxation calculations automatically handle the electron distribution, thus the interaction between ionized species and adsorbed  $-\text{O}_x$  surface groups can be simply treated as neutral H atoms or neutral  $-\text{OH}$  surface groups interacting with neutral uCNPs. As an alternative, we can decompose the general question into two separate problems: (1) examining the case that individual  $-\text{O}_x$  surface group is attacked by one H atom or two and deducing the pattern or law from examined cases to make a general prediction about the interaction between  $\text{H}_2\text{O}$  molecules and  $-\text{O}_x$  groups adsorbed at surfaces of uCNPs; and (2) probing the possible surface configuration of uCNPs subjected to different humid environments based on the general prediction from problem (1).

### **6.1 Individual $-\text{O}_x$ group at surfaces of uCNPs interacting with H atoms**

The first step is to examine the evolution of the surface configuration of  $\text{O}_x$ -terminated uCNPs attacked by H atoms in a humid environment. Since previous experimental studies on the properties of uCNPs are primarily carried out in aqueous solution, and have shown that pH is an important factor controlling their properties<sup>1,9</sup>, we hereby set pH-controlled solution as the environment. We further choose two  $\sim 1$  nm



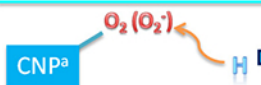
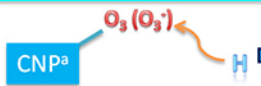




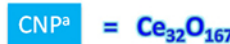
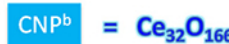
Structural Evolution		pH	Formation Energy (eV)
		3	-3.8334 (-3.9400)
		11	-3.3618 (-3.4684)
		3	-4.2042 (-4.2880)
		11	-3.7326 (-3.8164)
		3	-8.3360
		11	-7.1453
		3	-9.0273
		11	-7.8366
		3	-8.9818
		11	-7.7911
		3	-8.6158
		11	-7.4251
			

Figure 6.1: Evolution of the surface configuration of  $O_x$ -terminated uCNPs when approached by H atoms. Those cases corresponding to singular H atom interacting with negative charged  $-O_x$  surface groups are shown in the parenthesis.

cubic uCNP structures close to local energy minimum,  $Ce_{32}O_{166}$  and  $Ce_{32}O_{167}$ , as representative uCNP structures subjected to such an examination. We put a single H atom close to an  $-O_x$  group at surfaces of  $Ce_{32}O_{166}$  and relax the whole structure to explore interaction between an  $-O_x$  surface groups and one H atom. This simulates the case that a  $H_2O$  molecule provide one of its H atoms to an  $-O_x$  surface group. In the same manner, two H atoms are put close to an  $-O_x$  surface group at the surface of  $Ce_{32}O_{167}$  and relax the whole structure to explore whether  $-O_x$  surface groups interact with two H atoms. This simulates a  $H_2O$  molecule give both H atoms to an  $-O_x$  surface group, or that two  $H_2O$  molecules simultaneously/sequentially approach an  $-O_x$  surface group.

The dissimilar scenarios showing interaction between H atoms and individual  $-O_x$  group at surfaces of representative uCNP structures together with corresponding

formation energies in both typical acidic solution ( $pH=3$ ) and typical basic solution ( $pH=11$ ) are summarized in Figure 6.1. Interestingly, the interplay between individual  $-O_x$  surface groups and H atoms is not random but follows a certain pattern. When a H atom attacks an  $-O_2$  surface group, one O atom captures the H atom and overall turns into a  $-OOH$  surface group; whereas a H atom attacks an  $-O_3$  surface group, O atom at one end seizes the H atom and departs from other two O atoms to form a  $-OH$  surface group alone. In this case, we observe two patterns. One, the surplus charge is always preserved within the O atom of  $-O_x$  surface groups that captures the incoming H atom. For example, if an  $-O_3^-$  surface group is attacked by a H atom, after relaxation, it becomes a  $-OH^-$  surface group and keeps the surplus negative charge originally from  $-O_3^-$  surface groups. Two, after capturing one H atom, the energy of formation of the overall structure is lowered great than 3 eV, no matter the solution is acid or basic, which strongly suggests that passivating  $-O_x$  surface groups with H atoms greatly stabilizes uCNP structures.

The case becomes more complicated once two H atoms come along simultaneously. If the target is a net neutral  $-O_2$  surface group, these two H atoms will combine with the  $-O_2$  surface group to forms a  $-H_2O_2$  surface group. If the target is a  $-O_2^-$  surface group, the whole molecule will split into two  $-OH$  surface groups with one negatively charged. If the target is a net neutral  $-O_3$  surface group, the whole molecule will decompose and separately form a net neutral  $-O_2$  surface group and a  $H_2O$  molecule. If the target is an  $-O_3^-$  surface group, the surface group will dissociate to form a  $-OOH$  surface group and a negatively charged  $-OH$  surface group. In spite of the complexity, two patterns observed in the case of a single H atom attacking  $-O_x$  surface groups still apply to the case of two H atoms.

All the above scenarios unanimously suggest that passivating O atoms within  $-O_x$  surface groups with H atoms significantly stabilizes uCNP structures regardless of the acidity of applied aqueous solution. This could be applicable to surface O lattice

atoms as well. In general, it is likely that the more surface O atoms are passivated by H atoms, the lower energy of formation of the resultant uCNP structure has, and the more stable the overall uCNP structure is, based on the fact that adding one H atom almost linearly lowers the energy of formation of the overall uCNP structure by  $\sim 3$  eV. This strongly indicates the possibility that in a pH-controlled aqueous solution or in a humid environment, the surface configuration of uCNP structures is a combined arrangement of  $-\text{OH}$  and/or  $-\text{O}_x$  surface groups depending on the detailed environmental conditions.

## 6.2 Surface configuration of uCNPs in a humid environment

The second step is probing the surface configuration of uCNPs subjected to varied humid environments according to our understanding of the interaction between H atoms and individual  $-\text{O}_x$  group at surfaces of uCNPs. For this reason, we have constructed a series of cubic uCNP structures with different surface configurations — a combination of  $-\text{OH}$  and  $-\text{O}_x$  surface groups and relax them to lowest energy structures using quantum mechanical calculations based on DFT.

The stability of various relaxed uCNP structures is compared by calculating their excess energies of formation according to Equations 3.18, 3.19 and 3.23. In determining relevant values for  $\mu_{\text{O}}$  and  $\mu_{\text{H}}$ , we note that uCNP synthesis is typically conducted in the presence of both  $\text{O}_2$  gas and  $\text{H}_2\text{O}$  vapor, and that the ambient temperature and relative partial pressures of  $\text{O}_2$  gas and  $\text{H}_2\text{O}$  vapor completely determine both  $\mu_{\text{O}}$  and  $\mu_{\text{H}}$  (see detailed in **section 3.3.3**). For experimentally relevant temperatures ( $25 - 650$  °C) and pressures ( $10^{-16}$  to  $10^2$ ) atm,  $\mu_{\text{O}}$  ( $\mu_{\text{H}}$ ) varies between  $-4.65$  and  $-6.90$  eV ( $-4.75$  and  $-6.93$  eV). As the DFT calculated energy is not an absolute quantity, we take  $\mu_{\text{Ce}} = 0$  eV as a global reference energy.

In calculating the excess energies of formation of uCNP structures with various mixed surface configurations of  $-\text{OH}$  and  $-\text{O}_x$  surface groups, we invoke the fact that

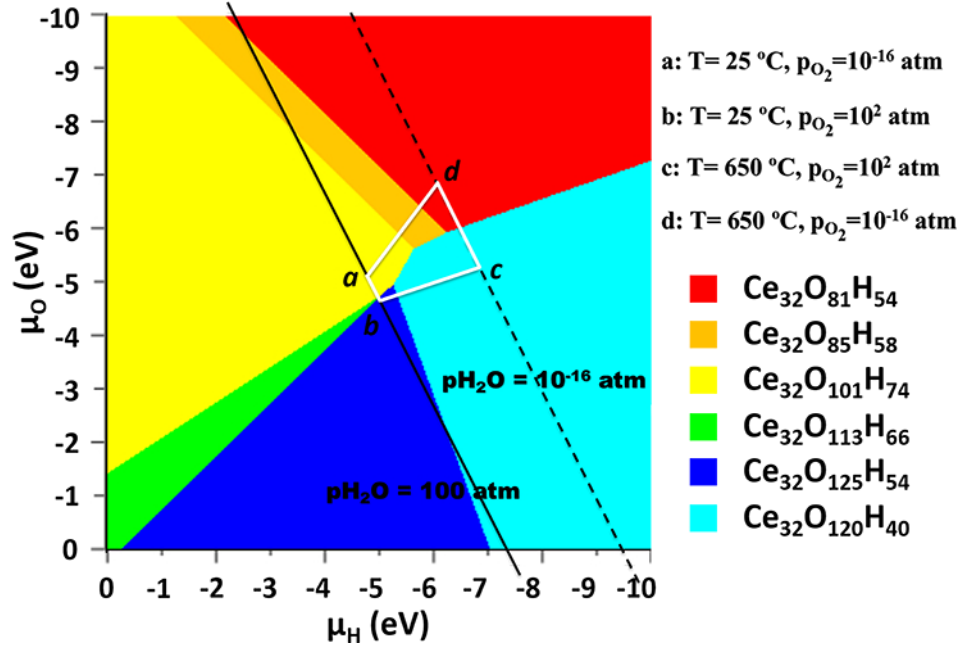


Figure 6.2: Phase diagram of ground state surface configurations for a series of considered uCNP structures as a function of  $\mu_O$  and  $\mu_H$  in a gas phase environment containing  $\text{O}_2$  gas and  $\text{H}_2\text{O}$  vapor. Warm colors indicate structures terminated solely with  $-\text{OH}$  surface groups (see atomic structures in Figure 6.3). Cool colors indicate structures terminated with mixed  $-\text{OH}$  and  $-\text{O}_x$  surface groups (see atomic structures in Figure 6.4). Black parallel lines indicate the experimentally relevant limits of the partial pressure of  $\text{H}_2\text{O}$  vapor. The white trapezoid  $abcd$  indicates the region of experimental conditions most relevant for the synthesis and application of uCNP structures.

in an equilibrium gas phase environment containing both  $\text{O}_2$  gas and  $\text{H}_2\text{O}$  vapor,  $\mu_O$  and  $\mu_H$  are not independent, but must satisfy the relation  $2\mu_H + \mu_O = \mu_{\text{H}_2\text{O}}$ , with  $\mu_{\text{H}_2\text{O}}$  as the chemical potential of  $\text{H}_2\text{O}$  vapor. Moreover, the chemical potential values considered can be connected to experimentally measured enthalpies of  $\text{O}_2$  gas and  $\text{H}_2\text{O}$  vapor as a function of ambient temperature ( $T$  and the partial pressures of  $\text{O}_2$  gas ( $p_{\text{O}_2}$ ) and  $\text{H}_2\text{O}$  vapor ( $p_{\text{H}_2\text{O}}$ ). In this way, experimental values of  $T$ ,  $p_{\text{O}_2}$  and  $p_{\text{H}_2\text{O}}$  (that is, the measured conditions under which a uCNP is synthesized or applied) can be mapped into chemical potential values that define an experimentally relevant range of conditions. The mapping of environmental conditions ( $T$ ,  $p_{\text{O}_2}$  and  $p_{\text{H}_2\text{O}}$ ) unto sets of chemical potential values is non-linear, and defined by Equations 3.19

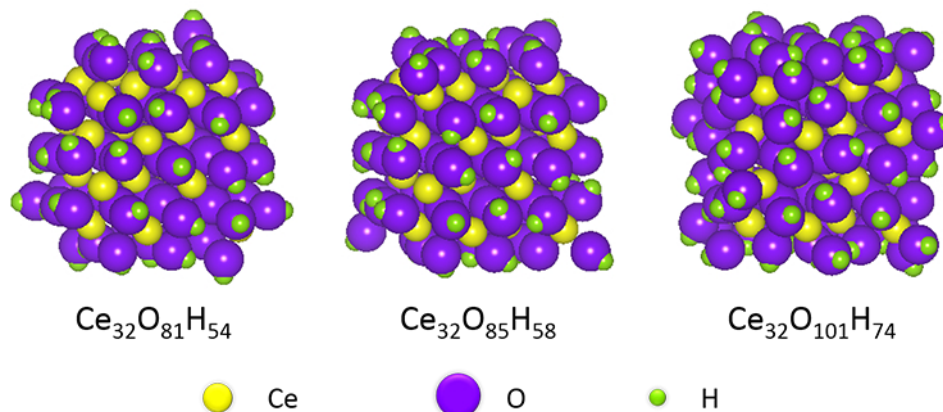


Figure 6.3: The relaxed, ground-state atomic structures of three OH-terminated cubic uCNPs with different densities of  $-\text{OH}$  surface groups. Yellow balls represent Ce atoms, purple balls represent O atoms, and green balls represent H atoms. For increasing densities of  $-\text{OH}$  surface groups,  $-\text{OH}$  groups are first adsorbed on uCNP  $\{001\}$  facets, then edges and corners.

and 3.23. Furthermore, the relative stability of these uCNP structures with various surface configurations is determined from Equation 3.18. Together, this leads to a phase diagram of the stable surface configuration of uCNPs as a function of  $\mu_{\text{O}}$  and  $\mu_{\text{H}}$ , as plotted in Figure 6.2. To facilitate use of the phase diagram in Figure 6.2, a tool implementing Equations 3.19 and 3.23 has been made available to convert experimental conditions to chemical potential values. The tool allows input of  $T$ ,  $p_{\text{O}_2}$  and  $p_{\text{H}_2\text{O}}$  values and returns  $\mu_{\text{O}}$  and  $\mu_{\text{H}}$  values for the specified conditions. In this way the computationally-predicted stable surface configuration of uCNP structures for any given experimental condition can be determined directly from Figure 6.2.

Considering Figure 6.2 itself, we note that within the upper half the phase diagram  $|\mu_{\text{O}}|$  is high, and stable uCNPs are terminated solely with  $-\text{OH}$  surface groups (structures indicated by warm colors in Figure 6.2). Figure 6.3 shows the atomic structures of relaxed OH-terminated uCNPs and highlights the distribution of bound  $-\text{OH}$  surface groups at uCNP  $\{001\}$  facets, edges and corners. As a matter of fact, for hydrothermal synthesis conditions of small CNPs (typically  $T < 200^\circ\text{C}$ ,  $p_{\text{O}_2} < 1\text{ atm}$ , and  $p_{\text{H}_2\text{O}} < 1\text{ atm}$ ), the excess energy of formation for OH-terminated CNPs *decreas-*

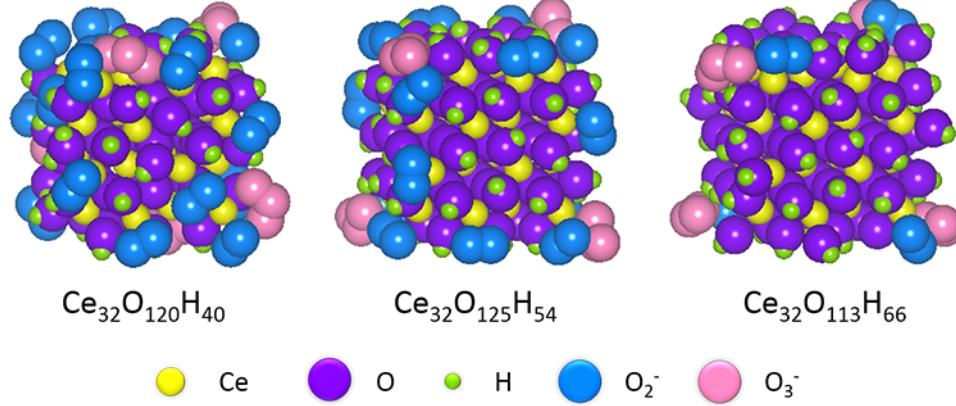


Figure 6.4: The relaxed, ground-state atomic structures of three cubic uCNPs terminated with mixed  $-\text{OH}$  and  $-\text{O}_x$  surface groups. Yellow balls represent Ce atoms, purple balls represent either bulk O atoms or O atoms in  $-\text{OH}$  surface groups, green balls represent H atoms, blue balls represent O atoms in  $-\text{O}_2^-$  surface groups, and pink balls represent O atoms in  $-\text{O}_3^-$  surface groups. For increasing numbers of adsorbed  $-\text{O}_x$  surface groups,  $-\text{O}_x$  groups are first adsorbed on uCNP corners, then edges and  $\{001\}$  facets.

es with *increasing* numbers of bound  $-\text{OH}$  surface groups, and achieves a minimum for 74  $-\text{OH}$  surface groups ( $\text{Ce}_{32}\text{O}_{101}\text{H}_{74}$ ). Figure 6.3 shows relaxed OH-terminated uCNPs structures, including the low energy  $\text{Ce}_{32}\text{O}_{101}\text{H}_{74}$  structure, and highlights the distribution of bound  $-\text{OH}$  surface groups to CNP  $\{001\}$  facets, edges and corners. The 74  $-\text{OH}$  surface groups are all negatively charged, each exhibiting Bader charges consistent with a formal oxidation state of  $-1$ . All 27 “bulk-like” O lattice atoms (single O atoms within the uCNP and each coordinated to 4 Ce atoms) are also negatively charged, exhibiting Bader charges consistent with formal oxidation state of  $-2$ , and all 32 Ce atoms are positively charged, each with Bader charges consistent with a formal oxidation state of  $+4$ . This leads to a straightforward explanation for the low-energy number of bound  $-\text{OH}$  groups at the surface of uCNP structures: that is, the number required to fully oxidize all Ce atoms in the uCNP. Hence,  $\text{Ce}_{32}\text{O}_{101}\text{H}_{74}$  uCNPs have 128 net (formal) positive charges (from the 32 Ce  $+4$  atoms) and 54 negative charges (from the 27 “bulk” O  $-2$  atoms), therefore requiring exactly 74 negatively charged  $-\text{OH}$  surface groups to give a net neutral uCNP. Finally, we note

that the uCNP geometries considered here have  $\sim 1$  nm side lengths, and therefore  $\sim 6$  nm<sup>2</sup> of surface area, giving a predicted stable density of bound  $-\text{OH}$  surface groups of  $\Omega_{\text{OH}}^{\text{calc}} = 12.3 \text{ nm}^{-2}$ .

In contrast, within the lower half of the phase diagram, where  $|\mu_{\text{O}}|$  is low, stable uCNP structures exhibit surface configuration of mixed  $-\text{OH}$  and  $-\text{O}_x$  surface groups (structures indicated by cool colors in Figure 6.2, and atomic structures in Figure 6.4). Low energy uCNP structures have  $-\text{O}_2$  and  $-\text{O}_3$  surface groups preferentially adsorbed at uCNP corners, edges and  $\{001\}$  facets, as shown in Figure 6.4. Based on Bader charge analysis, the oxidation state of  $-\text{O}_x$  surface groups can be determined by the same procedure applied above for OH-terminated uCNPs. For the  $\text{Ce}_{32}\text{O}_{125}\text{H}_{54}$  and  $\text{Ce}_{32}\text{O}_{113}\text{H}_{66}$  structures, all surface groups ( $-\text{OH}$  and  $-\text{O}_x$  groups) have formal charges of -1, while for the  $\text{Ce}_{32}\text{O}_{120}\text{H}_{40}$  structure, a subset of  $-\text{O}_x$  surface groups have formal charges of -2. In all cases the sum of formal negative charges ( $-\text{OH}$  plus  $-\text{O}_x$  surface groups) equals the sum of formal positive charges from fully oxidized Ce (+4) atoms. Hence, the evolution of stable surface configurations is simply a reallocation of  $-\text{OH}$  and  $-\text{O}_x$  surface groups in response to changes in the combinations of  $\mu_{\text{O}}$  and  $\mu_{\text{H}}$  such that the charge neutrality of all considered uCNP structures is maintained.

From an experimental perspective we note that increasing the magnitude of  $|\mu_{\text{O}}|$  (or  $|\mu_{\text{H}}|$ ), e.g. by lowering  $p_{\text{O}_2}$  (or  $p_{\text{H}_2\text{O}}$ ), represents increasing difficulty of obtaining O (or H) atoms from the environment. Similarly, increasing the temperature increases the difficulty of binding O or H atoms from the environment, and therefore increases the magnitude of both  $|\mu_{\text{O}}|$  and  $|\mu_{\text{H}}|$ . Under typical experimental conditions for synthesizing, characterizing and applying uCNPs, the temperature is held between  $25^\circ\text{C}$  and  $650^\circ\text{C}$ , and partial pressures of  $\text{O}_2$  and  $\text{H}_2\text{O}$  vapor range between  $10^2$  and  $10^{-16}$  atm. These pressures constrain accessible chemical potential values between black solid and dotted lines in Figure 6.2. Further, the temperature constraints limit the accessible phase space to that enclosed by the white trapezoid  $abcd$ —precisely

the chemical potential range within which transitions in the stable uCNP surface configurations are concentrated.

Specifically in terms of experimental synthesis conditions, when  $\text{H}_2\text{O}$  vapor is the major source of H atoms (as assumed here), OH-terminated uCNPs can be fabricated by constraining temperatures to below  $350^\circ\text{C}$  and handling uCNPs under relatively high partial pressures of  $\text{H}_2\text{O}$  vapor (e.g., ambient humidity levels). In contrast, uCNP terminated with mixed  $-\text{OH}$  and  $-\text{O}_x$  surface groups are expected from synthesis occurring above  $350^\circ\text{C}$  and under relatively low partial pressures of  $\text{H}_2\text{O}$  vapor (e.g., dry air). In addition, increasing  $p_{\text{O}_2}$  directly (e.g., to greater than 1 atm) favors the formation of uCNPs terminated with mixed  $-\text{OH}$  and  $-\text{O}_x$  surface groups, and increasing temperature generally leads to reduced number of adsorbed  $-\text{OH}$  surface groups and increased numbers of adsorbed  $-\text{O}_x$  surface groups.

### 6.3 Densities of $-\text{OH}$ surface groups bound to cubic uCNPs as a function of particle size

We note that OH-terminated cubic uCNP structures considered here have  $\sim 1$  nm side lengths, and therefore  $6\text{ nm}^2$  of surface area, giving a predicted stable density of bound  $-\text{OH}$  surface groups of  $\Omega_{\text{OH}}^{\text{calc}} = 12.3\text{ nm}^{-2}$ . If such a surface configuration represents that of experimentally synthesized cubic uCNP structures, we can predict the density of  $-\text{OH}$  surface groups bound to any-sized cubic uCNPs.

Considering cubic uCNP structures with sizes of 1 nm, 1.5 nm and 2 nm reveals the relationship between the number of Ce/O atoms and CNP size. For a CNP with a size of  $N$  nm (and therefore containing approximately  $(2N)^3$  ceria unit cells), the number of Ce atoms scales as approximately  $32N^3$  and the number of “bulk” O atoms (O atoms internal to the CNP) scales as approximately  $(4N - 1)^3$ . Since the formal positive charge is contributed from Ce atoms, in the case that each Ce atom is fully oxidized (+4), CNPs will have  $128N^3$  net formal positive charges. Similarly, the net



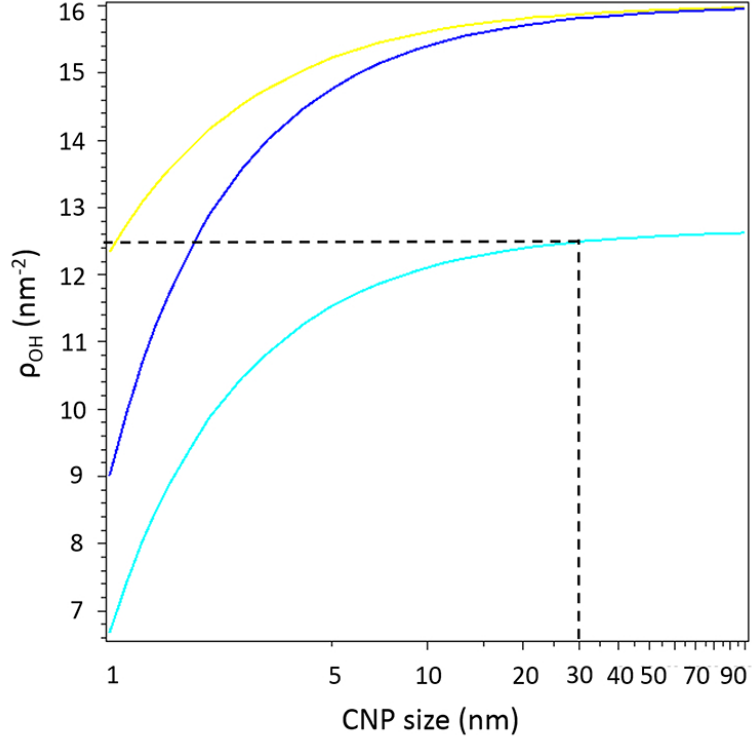


Figure 6.5: Density of adsorbed  $\text{-OH}$  surface groups as a function of cubic CNP size calculated from the scaling relationship invoking full oxidation of Ce atoms (see text for details). Yellow, blue and cyan curves are plotted for cubic CNPs of surface configurations consistent with the  $\text{Ce}_{32}\text{O}_{101}\text{H}_{74}$ ,  $\text{Ce}_{32}\text{O}_{125}\text{H}_{54}$  and  $\text{Ce}_{32}\text{O}_{120}\text{H}_{40}$  structures, respectively. In addition, the yellow curve represents the case where  $\text{-OH}$  surface groups are the only surface group to balance net positive charges from  $\text{Ce}^{\text{IV}}$  cations, while blue and cyan curves represent the case where both  $\text{-OH}$  and  $\text{-O}_x$  surface groups are present. Colors have been selected to match subsequent figure (Figure 6.2).

formal negative charge contributed from “bulk” O atoms is  $2(4N - 1)^3$ , with each “bulk” O atom contributing -2. Therefore, if all remaining formal positive charges in a fully oxidized CNP (that is,  $128N^3 - 2(4N - 1)^3$ ) are balanced with *surface*  $\text{-OH}$  groups each contributing a formal charge of -1, we may calculate the density of  $\text{-OH}$  surface groups bound to OH-terminated cubic uCNPs,  $\Omega_{\text{OH}}^{\text{calc}}$ , as:

$$\Omega_{\text{OH}}^{\text{calc}} = \frac{128N^3 - 2(4N - 1)^3}{6N^2} = \frac{96N^2 - 24N + 2}{6N^2}. \quad (6.1)$$

In the limit of large CNPs ( $N \rightarrow \infty$ ), therefore, fully oxidized and OH-terminated CNPs have  $\Omega_{\text{OH}}^{\text{calc}} = 16$ , or one  $\text{-OH}$  group per ceria  $\{001\}$  surface O lattice site. This is

intuitively correct, as ceria  $\{001\}$  surface anion lattice sites are four-fold coordinated, with half the cation neighbors of “bulk” anion sites. Finite sized CNPs, particular those with sizes  $\sim 30$  nm and smaller, have *lower* densities of  $-\text{OH}$  surface groups, even when fully oxidized. Specifically, the density of bound  $-\text{OH}$  surface groups as a function of CNP size is predicted to be  $12.3 \text{ nm}^{-2}$  for  $\sim 1$  nm CNPs, and  $15.8 \text{ nm}^{-2}$  for CNPs with side lengths of  $\sim 30$  nm (see yellow curve in Figure 6.5). Therefore, based on results for OH-terminated  $\sim 1$  nm cubic CNPs, calculations predict a surface hydroxyl group density of  $15.8 \text{ nm}^{-2}$  for  $\sim 30$  nm cubic CNPs, a surface density  $\sim 33\%$  higher than the experimentally measured value of  $12.9 \text{ nm}^{-2}$  (result from Dr. Grulk’s research group). Partial reduction of such CNPs can reduce the density of  $-\text{OH}$  surface groups in proportion to the percentage of  $\text{Ce}^{\text{IV}}$  cations reduced to  $\text{Ce}^{\text{III}}$  cations. Achieving quantitative agreement between calculated and experimentally observed density of  $-\text{OH}$  surface groups entirely through CNP reduction, therefore, would require that  $\sim 33\%$  of  $\text{Ce}^{\text{IV}}$  cations be reduced to  $\text{Ce}^{\text{III}}$  cations.

Scaling calculated densities of  $-\text{OH}$  surface groups from  $\sim 1$  nm OH-terminated cubic CNPs yields predicted density of  $-\text{OH}$  surface groups for  $\sim 30$  nm CNPs that is  $\sim 33\%$  higher than the experimentally measured value ( $\Omega_{\text{OH}}^{\text{calc}} = 15.8 \text{ nm}^{-2} > \Omega_{\text{OH}}^{\text{exp}} = 12.9 \text{ nm}^{-2}$ ). This discrepancy can be attributed to a number of factors, including (i) kinetic limitations preventing removal of all  $-\text{OH}$  surface groups (arising because at low surface densities,  $-\text{OH}$  surface group removal is limited by the requirement that two bound  $-\text{OH}$  surface groups combine to form the desorbed  $\text{H}_2\text{O}$  molecule), (ii) misidentification of some chemically bound  $-\text{OH}$  surface groups as physisorbed (as noted above, we have assumed that all mass loss during TGA occurring below  $110^\circ\text{C}$  is solely due to physisorbed  $-\text{OH}$  surface groups), (iii) the possibility that at finite temperature as-synthesized uCNPs are not fully oxidized (as is the case for bulk ceria samples, see examples<sup>24,231</sup>), or (iv) that more tightly bound surface functional groups *other than  $-\text{OH}$  surface groups* are present on as-synthesized uCNPs.

While all of these effects are likely influencing the measured densities of  $-\text{OH}$  surface groups bound to cubic uCNPs reported here, the last explanation—that surface functional groups other than  $-\text{OH}$  surface groups may be present on as-synthesized uCNPs—highlights the fact that uCNPs are generally synthesized and applied in environments where both  $\text{O}_2$  gas and  $\text{H}_2\text{O}$  vapor are abundant. This suggests that O-containing surface groups other than  $-\text{OH}$  surface groups, e.g.  $-\text{O}$ ,  $-\text{O}_2$  and/or  $-\text{O}_3$  surface groups, may be present as surface adsorbed anions, reducing the effective density of  $-\text{OH}$  surface groups. Accounting for negative charges provided by  $-\text{O}_x$  surface groups in addition to  $-\text{OH}$  surface groups (e.g., as in the  $\text{Ce}_{32}\text{O}_{120}\text{H}_{40}$  and  $\text{Ce}_{32}\text{O}_{125}\text{H}_{54}$  structures), the density of  $-\text{OH}$  surface groups will be reduced compared to the case where only  $-\text{OH}$  groups are present at the surface. From the pattern of adsorbed surface groups on the  $\text{Ce}_{32}\text{O}_{120}\text{H}_{40}$  and  $\text{Ce}_{32}\text{O}_{125}\text{H}_{54}$  structures found here (Figure 6.4) and the results of Bader charge analysis, we can develop expressions for the density of  $-\text{OH}$  surface groups bound to cubic uCNPs terminated with mixed  $-\text{OH}$  and  $-\text{O}_x$  surface groups analogous to Equation 6.1.

For  $\text{Ce}_{32}\text{O}_{125}\text{H}_{54}$ ,  $-\text{O}_x$  surface groups appear only at CNP corners and edges, and all have Bader charges indicating formal charges of -1. For CNPs with side lengths of  $N$  nm, four corner Ce atoms are present, each binding 2  $-\text{O}_x^-$  surface groups. In addition, a single  $-\text{O}_x^-$  surface group binds on each of 12  $N$  nm lengths of CNP edges. This gives a total negative contribution from  $-\text{O}_x$  surface groups of  $-1 \cdot (4 \cdot 2 + 12N)$ . This leaves net negative charge of  $128N^3 - 2(4N - 1)^3 - 8 - 12N$  to be accounted for by  $-\text{OH}$  surface groups, yielding a density of bound  $-\text{OH}$  surface groups,  $\Omega_{OH}^{calc}$  of

$$\begin{aligned}\Omega_{OH}^{calc} &= \frac{128N^3 - 2(4N - 1)^3 - 8 - 12N}{6N^2} \\ &= \frac{96N^2 - 36N - 6}{6N^2}.\end{aligned}\tag{6.2}$$

For  $\text{Ce}_{32}\text{O}_{120}\text{H}_{40}$ , some  $\{001\}$  facet sites are also occupied by  $-\text{O}_x$  surface groups. There are 5 facet sites occupied by  $-\text{O}_x^{2-}$  surface groups (that is,  $-\text{O}_x$  surface groups

with Bader charges consistent with formal charges of -2). Similar to the  $\text{Ce}_{32}\text{O}_{125}\text{H}_{54}$  structure, 4 corner sites and 10 edge sites are also occupied by  $-\text{O}_x^-$  surface groups. Assuming the relative ratio of all  $-\text{O}_x$  surface groups remains unchanged as CNP size is increased, total net negative charge provided by all  $-\text{O}_x$  surface groups will be  $4+10N+10N^2$ . This leaves net negative charge of  $128N^3-2(4N-1)^3-4-10N-10N^2$  to be accounted for by  $-\text{OH}$  surface groups, yielding a density of bound  $-\text{OH}$  surface groups,  $\Omega_{\text{OH}}^{\text{calc}}$  of

$$\begin{aligned}\Omega_{\text{OH}}^{\text{calc}} &= \frac{128N^3 - 2(4N - 1)^3 - 4 - 10N - 10N^2}{6N^2} \\ &= \frac{76N^2 - 34N - 2}{6N^2}.\end{aligned}\tag{6.3}$$

For the experimental conditions used to synthesize sin20–40 nm CNPs from Dr. Grulke’s research group (finally dried at  $T = 75^\circ\text{C}$  and  $p_{\text{O}_2} = 0.2 \text{ atm}$   $p_{\text{H}_2\text{O}} = 10^{-7} \text{ atm}$ ),  $\mu_{\text{O}}$  is calculated as -4.78 eV and  $\mu_{\text{H}}$  as -5.30 eV. These chemical potentials are predicted to yield a  $\text{Ce}_{32}\text{O}_{120}\text{H}_{40}$  structure terminated with mixed surface configuration of  $-\text{OH}$  and  $-\text{O}_x$  groups (see Figure 6.4), which, due to the presence of  $-\text{O}_x$  surface groups, is expected to have a lower effective density of bound  $-\text{OH}$  surface groups than  $\text{OH}$ -terminated CNP structures. This is consistent with the fact that computationally predicted density of  $-\text{OH}$  surface groups bound to  $\sim 30 \text{ nm}$  CNPs are  $\sim 33\%$  higher than experimentally measured values. Applying Equation 6.3, we find that  $\sim 30 \text{ nm}$  CNPs with surface configurations consistent with the  $\text{Ce}_{32}\text{O}_{120}\text{H}_{40}$  structure are predicted to have  $\Omega_{\text{OH}}^{\text{calc}} \approx 12.5$  bound  $-\text{OH}$  surface groups per  $\text{nm}^2$  (see cyan curve in Figure 6.5)—extremely close to the experimentally measured value of  $\Omega_{\text{OH}}^{\text{exp}} = 12.9 \text{ nm}^{-2}$ .

#### 6.4 Electronic density of states of OH-terminated uCNPs

Figure 6.6 shows plots of the calculated projected eDOS of bulk  $\text{CeO}_2$ , bulk  $\text{H-Ce}_2\text{O}_3$ ,  $\text{Ce}_{32}\text{O}_{81}\text{H}_{54}$ , and  $\text{Ce}_{32}\text{O}_{101}\text{H}_{74}$  for some atomic orbitals of interest. For the convenience

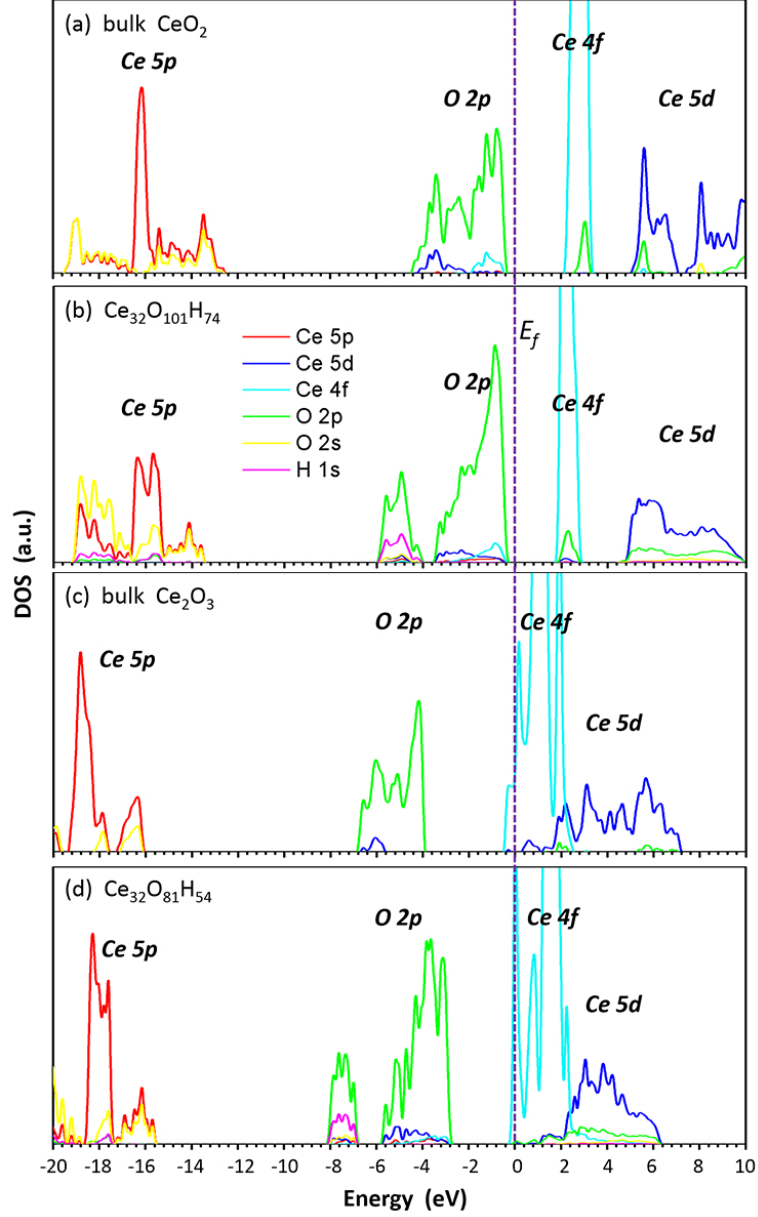


Figure 6.6: Calculated projected electronic density states (eDOS) of some interested atomic orbitals for (a) bulk  $\text{CeO}_2$ ; (b)  $\text{Ce}_{32}\text{O}_{101}\text{H}_{74}$ ; (c) bulk  $\text{H-Ce}_2\text{O}_3$  and (d)  $\text{Ce}_{32}\text{O}_{81}\text{H}_{54}$ .

of comparing the relative positions of energy bands, eDOS of each structure is shifted by setting Fermi energy ( $E_f$ ) to zero as the reference energy. Calculated eDOS of all considered structures can be generally divided into three parts: (1) the valence band (VB) mainly composed of  $\text{Ce } 5p$  and  $\text{O } 2p$  orbitals in character at lower energy region;

(2) the conduction band (CB) primarily formed by *Ce 5d* orbitals in character at higher energy region and (3) gap between VB and CB sit *Ce 4f* orbitals in character.

In bulk  $\text{CeO}_2$ , each Ce atom is coordinated with 8 neighboring O atoms and each O atom is coordinated with 4 neighboring Ce atoms. Thus, every atom is fully saturated in terms of coordination and charge. Compared to bulk  $\text{CeO}_2$ , despite the existence of  $-\text{OH}$  surface groups, each atom in  $\text{Ce}_{32}\text{O}_{101}\text{H}_{74}$  is also saturated in terms of coordination and charge in a different pattern. The delicate structural information is well manifested through eDOS. The eDOS of  $\text{Ce}_{32}\text{O}_{101}\text{H}_{74}$  share some common “bulk” features with that of bulk  $\text{CeO}_2$  while explicitly show its unique feature. For instance, the position of HOMO (top of *O 2p* orbitals) for  $\text{Ce}_{32}\text{O}_{101}\text{H}_{74}$  is the same as that of bulk  $\text{CeO}_2$ , but the position of LUMO (bottom of *Ce 5d* orbitals) slightly blue-shifts towards HOMO in  $\text{Ce}_{32}\text{O}_{101}\text{H}_{74}$  relative to bulk  $\text{CeO}_2$ . The former is determined by “bulk part” Ce and O atoms which is almost the same for both  $\text{Ce}_{32}\text{O}_{101}\text{H}_{74}$  and bulk  $\text{CeO}_2$ , while the latter is likely related to the surface states of Ce and O atoms in  $\text{Ce}_{32}\text{O}_{101}\text{H}_{74}$ . Such phenomenon becomes more salient for  $\text{Ce}_{32}\text{O}_{81}\text{H}_{54}$  and its overall band blue-shifts significantly. As both  $\text{Ce}_{32}\text{O}_{101}\text{H}_{74}$  and  $\text{Ce}_{32}\text{O}_{81}\text{H}_{54}$  have two kinds of O atoms, eDOS of *O 2p* orbitals split and directly reflect two sets of atomic O bonding states, that is, “bulk part” O atoms each coordinating with 4 neighboring Ce atoms as well as surface O atoms each coordinating with 2 neighboring Ce atoms and 1 H atom. In addition, *Ce 4f* orbitals in  $\text{Ce}_{32}\text{O}_{81}\text{H}_{54}$  split and directly reflect two different states of surface Ce atoms, that is, those located at corners and edges with unsaturated coordination and charge as well as those at facets with saturated coordination and charge. Those unsaturated Ce atoms further cause *Ce 4f* orbitals to fall below Fermi level, indicating that *Ce 4f* orbitals are partly occupied by electrons. The fact that its eDOS are quite similar to that of bulk  $\text{H-Ce}_2\text{O}_3$  further confirms that some portion of  $\text{Ce}^{\text{IV}}$  cations are reduced to  $\text{Ce}^{\text{III}}$  cations, most of which are likely located at corners and edges, since they are under-coordinated. On the whole,

the eDOS of  $\text{Ce}_{32}\text{O}_{81}\text{H}_{54}$  exhibit characteristics of bulk  $\text{H-Ce}_2\text{O}_3$  and  $\text{Ce}_{32}\text{O}_{101}\text{H}_{74}$ , and the combination of both thereof.

We will further discuss how passivating surface O atoms with H atoms in OH-terminated uCNPs influences their electronic structure. The intensity of eDOS in OH-terminated uCNP structures is greatly enhanced in contrast to that of two typical bulk ceria structures, and this is simply the nanoscale effect as the surface-to-volume ratio of uCNPs is much greater than that of bulk ceria. Our calculation shows that for OH-terminated uCNPs, the contribution from *Ce 4f* orbitals increases relative to *Ce 5p* and *Ce 5d* orbitals, indicating that more states of *Ce 4f* orbitals are available to be occupied. This suggests that in a Ce-O-H tri-element system, Ce atoms gives away more electrons to O atoms and are oxidized even more in OH-terminated uCNPs compared to bulk ceria, which is further confirmed by Bader charge analysis on Ce atoms in these two different structures. Moreover, the portion of eDOS contributed from *O 2p* orbitals at higher energy relative to lower energy increases in OH-terminated uCNPs, again suggesting that surface O atoms accept additional electrons from H atoms compared to “bulk ” O atoms. Meanwhile, this is supported by Bader charge analysis on O atoms within OH-terminated uCNPs showing the presence of two sets of O atoms with distinct charge states (7.2 for “bulk” O atoms and 7.6 for O atoms within  $-\text{OH}$  surface groups). Passivating surface O atoms with H atoms in OH-terminated uCNPs enables surface O atoms to exhibit rather strong electronegativity to attract electrons from both Ce atoms and H atoms to compensate its under-coordinated state. In contrast to bulk ceria, the band gap between VB and CB of hydroxylated uCNPs is reduced, which facilitates electron excitation between *O 2p* and *Ce 5d* orbitals. In summary, it is possible that hydroxylated uCNPs are more stable and catalytic active than bulk ceria.

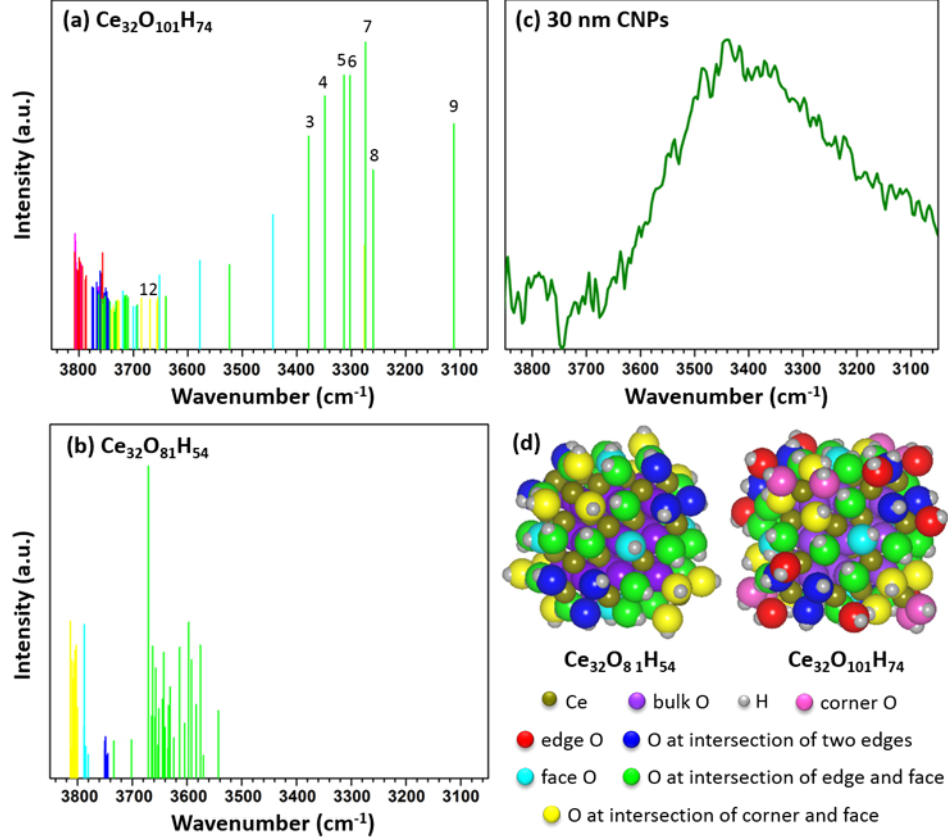


Figure 6.7: Calculated IR absorption spectra for  $\text{Ce}_{32}\text{O}_{81}\text{H}_{54}$  (a) and  $\text{Ce}_{32}\text{O}_{101}\text{H}_{74}$  (b); (c) experimental measured IR absorption spectrum for as-synthesized  $\sim 30$  nm CNPs; (d) relaxed atomic structures of  $\text{Ce}_{32}\text{O}_{81}\text{H}_{54}$  and  $\text{Ce}_{32}\text{O}_{101}\text{H}_{74}$ .

## 6.5 Infrared spectrum

Step on from eDOS, the IR absorption spectra of both  $\text{Ce}_{32}\text{O}_{81}\text{H}_{54}$  and  $\text{Ce}_{32}\text{O}_{101}\text{H}_{74}$  are calculated and shown in Figure 6.7, respectively. The calculated IR absorption spectra can be clearly divided into two parts, separately located at higher energy region and lower energy region. Those peaks above  $3000\text{ cm}^{-1}$  correspond to the stretching ( $\nu\text{-OH}$ ) vibration of  $\text{-OH}$  surface groups<sup>123</sup> while those below  $900\text{ cm}^{-1}$  correspond to the bending ( $\pi\text{-OH}$ ) vibration of  $\text{-OH}$  surface groups. In the light of the calculated absorption peak of Ce-O bond at  $459\text{ cm}^{-1}$  in bulk ceria, the absorption peak at  $\sim 459\text{ cm}^{-1}$  in calculated IR absorption spectra for OH-terminated uCNPs can be attributed to the vibration of Ce-O bond as well. On bulk ceria surface,



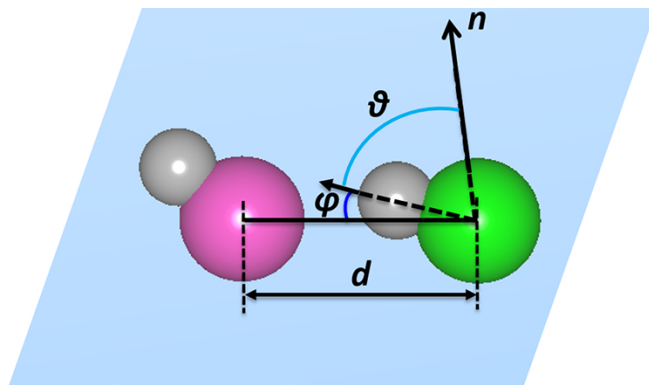


Figure 6.8: Schematic illustration of three measurands used to describe the status of a facet  $\text{-OH}$  group. The green ball represent an O atom as the base of a  $\text{-OH}$  surface group under consideration, which is leaning towards a nearest  $\text{-OH}$  surface group adsorbed at edges/corners whose base O atom is colored in purple. Their spatial relationship is determined by the distance between the centers of these two base O atoms,  $d$ , the angle between the O-H vector of a considered facet  $\text{-OH}$  group and the vector normal to the surface ( $n$ ),  $\theta$ , and the angle between the O-H vector of this considered facet  $\text{-OH}$  group and the direction lining up the centers of these two base O atoms,  $\phi$ .

three kinds of  $\text{-OH}$  surface groups have been identified by IR analysis and designated OH(I), OH(II), and OH(III) with the numeral in parenthesis giving the number of coordinated Ce atoms and with corresponding stretching vibration frequency decreases in such order<sup>19</sup>. In OH-terminated uCNPs, only OH(I) and OH(II) are present, but the case is much more complicated. Generally, it follows two rules: (1) stretching vibration of OH(I) exhibits higher vibration frequencies than that of OH(II), which is consistent with the trend observed on bulk ceria surface; (2)  $\text{-OH}$  surface groups located at/towards corners and edges exhibit higher vibration frequencies than those located at/towards facets, which is possibly due to different degree of freedom; (3) among  $\text{-OH}$  surface groups located at facets, the vibration frequency of a particular  $\text{-OH}$  surface group is determined by the distance to a nearest  $\text{-OH}$  surface group at edges/corners and its spatial orientation.

We want to elaborate on the last point here because those  $\text{-OH}$  surface groups turn out to be characteristic of fully oxidized OH-terminated uCNPs, exhibiting the

broad peak around  $3440\text{ cm}^{-1}$  in calculated IR absorption spectrum of  $\text{Ce}_{32}\text{O}_{101}\text{H}_{74}$ . What causes such an apparently intensified IR absorption properties for  $\text{Ce}_{32}\text{O}_{101}\text{H}_{74}$ ? We found that the reason lies in their pattern of stretching vibration and local environment. Those  $-\text{OH}$  surface groups are primarily located at facet sites quite close to edges and corners. When H atom stretches, it moves towards the nearest  $-\text{OH}$  surface group at edges/corners to form a pseudo  $\text{H}_2\text{O}$  structure ( $\text{H}-\text{O}\cdots\text{H}\cdots\text{O}$ ). Such an energetically favorable attraction between a positively charged  $\text{H}^+$  nucleus from the vibrating  $-\text{OH}$  surface group and a nearby negatively charged  $\text{OH}^-$  surface group induces a significant dipole change within the vibrating  $-\text{OH}$  surface group, thus exhibiting strong IR absorption properties. To clearly describe such a vibration process and capture the spatial relationship of those  $-\text{OH}$  surface groups relative to nearby  $-\text{OH}$  surface groups at edges/corners, we need three key measurands and they are schematically illustrated in Figure 6.8. The green atom is the O atom as the base of a  $-\text{OH}$  surface group under consideration, which is leaning towards a nearest  $-\text{OH}$  surface group at edges/corners whose base O atom is colored in purple. Their spatial relationship is determined by the distance between the centers of these two base O atoms,  $d$ , the angle between the O-H vector of a considered  $-\text{OH}$  surface group and the vector normal to the surface ( $n$ ),  $\theta$ , and the angle between the O-H vector of this considered  $-\text{OH}$  surface group and the direction lining up the centers of these two base O atoms,  $\phi$ .  $d$  is the most important parameter, directly showing how far a considered  $-\text{OH}$  surface group is apart from a neighboring  $-\text{OH}$  surface group at edges/corners.  $\theta$  measures the degree of a considered  $-\text{OH}$  surface group titling away from its base plane and  $\phi$  estimates the extent of a considered  $-\text{OH}$  surface group titling away from the nearest  $-\text{OH}$  surface group at edges/corners. Three measurands depicting the status of  $-\text{OH}$  surface groups marked from number 1 to number 9 in Figure 6.7a are tabulated in Table 6.1. From this table, we generally observe two governing rules: (1) the importance of three measurands are in the following order,  $d$

Table 6.1: Summary of required measurands used to describing two neighboring facet -OH groups

No.	wavenumber ( $\text{cm}^{-1}$ )	intensity (a.u.)	$d$ ( $\text{\AA}$ )	$\theta$ ( $^\circ$ )	$\phi$ ( $^\circ$ )
1	3685.40	0.061	2.36	23.42	56.11
2	3669.67	0.059	2.26	22.14	52.52
3	3378.33	0.572	1.92	66.75	15.77
4	3348.64	0.698	1.88	58.25	17.27
5	3313.36	0.764	1.85	62.72	15.14
6	3302.57	0.763	1.81	48.30	22.20
7	3259.82	0.465	1.80	74.55	13.93
8	3273.84	0.868	1.84	74.89	14.33
9	3111.74	0.611	1.73	77.12	12.45

$> \theta > \phi$ ; (2) smaller  $d$ , smaller  $\phi$ , and larger  $\theta$  result in stronger vibration intensities.

Experimentally measured IR absorption spectrum of synthesized  $\sim 30$  nm CNPs (result from Dr. Grulke's research group) features the broad peak from  $3750 \text{ cm}^{-1}$  to  $3000 \text{ cm}^{-1}$  centering  $3440 \text{ cm}^{-1}$  (see Figure 6.7 and narrow peak centering  $1590 \text{ cm}^{-1}$  corresponding to the stretching ( $\nu$ -OH) and in-plane bending vibration ( $\delta$ -OH) of -OH group, as well as intensified peaks around  $600 \text{ cm}^{-1}$  corresponding to the vibration of Ce-O bond<sup>232</sup>. Note that the broad peak shown here is not a unique feature of our sample. It has been observed that small CNP samples with bound -OH surface groups synthesized via different methods exhibit similar broad peak pattern in measured IR absorption spectrum as well<sup>233,234</sup>. Calculated IR absorption spectrum for fully oxidized OH-terminated uCNPs ( $\text{Ce}_{32}\text{O}_{101}\text{H}_{74}$ ) perfectly matches experimentally measured IR absorption spectrum for synthesized  $\sim 30$  nm CNPs. In contrast, partially reduced OH-terminated uCNPs ( $\text{Ce}_{32}\text{O}_{81}\text{H}_{54}$ ) show apparently different IR absorption spectrum. In reduced OH-terminated uCNPs, all -OH surface groups at edges and corners are gone. Hence, the condition required for -OH surface groups bound at facets to exhibit high intensified IR absorption properties can no longer be satisfied. This is an excellent example showing that structural change of small CNPs on the atomic scale can be reflected via change in macroscopic properties, such as IR absorption properties examined here. In turn, IR absorption spectrum

Table 6.2: Comparison of calculated vibration frequencies under IBRION=5 and IBRION=7 settings and assigned vibration modes to  $-O_x$  surface groups in two representative cubic uCNP structures terminated with mixed  $-OH$  and  $-O_x$  surface groups.

Type of uCNP	$O_x$ Surface Groups	Special Orientation	Vibration Mode	Vibration Frequency Range ( $cm^{-1}$ )	
				IBRION=5	IBRION=7
$Ce_{32}O_{125}H_{54}$	$O_2^-$	laying	stretching	1079.01, 1155.72	1194.45, 1180.95
				1149.59 — 1072.13	1146.18 — 1081.86
	$O_3^-$	standing	symmetric stretching	1190.16, 1176.01	1171.63, 1165.93
			asymmetric stretching	1171.94, 1162.45	1161.46, 1160.96
			bending	674.62, 672.14 672.08, 670.93	692.81, 680.41 679.32, 678.16
$Ce_{32}O_{120}H_{40}$	$O_2^-$	laying	stretching	1201.90 — 1066.21	1189.80 — 1053.03
				1055.36, 1020.98	1046.97, 999.74
	$O_2^{2-}$	bridging	stretching	901.48, 879.22	938.62, 915.91
				876.53, 873.49 870.07, 868.78 861.87	890.52, 887.57 886.05, 884.63 881.44
	$O_3^-$	laying	symmetric stretching	1027.62, 997.03	1029.18, 1024.86
			asymmetric stretching	888.05, 873.74	893.53, 884.01
			bending	661.39, 628.71	663.17, 649.17
	$O_3^{2-}$	bridging	symmetric stretching	1006.12	1010.80
			asymmetric stretching	858.50, 836.65	872.32, 859.94
				710.01	729.16
			bending	701.13, 697.96	716.57, 707.65
				574.73	588.12
				564.02, 552.33	567.19, 558.95

featuring broad absorption peak around  $3440\text{ cm}^{-1}$  can serve as a fingerprint to determine whether a OH-terminated uCNP is fully oxidized or not.

Above are the discussion on IR absorption properties of OH-terminated uCNPs. For uCNPs terminated with mixed  $-OH$  and  $-O_x$  surface groups, their IR absorption spectra can be viewed as the combination of both OH-terminated and  $O_x$ -terminated uCNPs. Actually, it is those features associated with  $-O_x$  surface groups that makes uCNPs with surface configurations of mixed  $-OH$  and  $-O_x$  surface groups interesting.

Vibration frequencies together with vibration modes assigned to corresponding  $-O_x$  surface groups with dissimilar chemical bonding status as well as spacial orientation for two representative cubic uCNPs terminated with mixed  $-OH$  and  $-O_x$  surface groups are tabulated in Table 6.2. Results obtained from both *IBRION=5* and *IBRION=7* calculations are listed in the table. Again, we see that fixed-atom calculation (*IBRION=5*) is a reliable estimation and further simplification of all-atom based

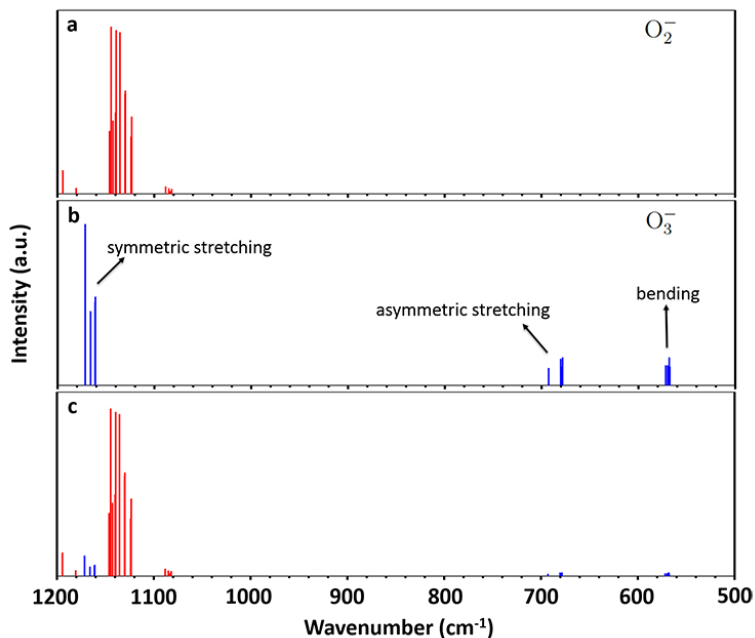


Figure 6.9: Calculated IR absorption spectrum of  $\text{Ce}_{32}\text{O}_{125}\text{H}_{54}$  within the vibration frequency range of adsorbed  $-\text{O}_x$  surface groups: (a)  $\text{O}_2^-$ ; (b)  $\text{O}_3^-$ ; and (c) combined.

yet time-consuming calculation ( $\text{IBRION}=7$ ), similar to the case we have shown for  $\text{Ce}_{32}\text{O}_{101}$ ,  $\text{O}_x$ -terminated uCNP (see **section 4.4**), where we have discussed the IR absorption spectrum of  $-\text{O}_x$  surface groups in detail. Now we will only briefly point out something worth noting on the IR absorption spectrum of uCNPs terminated with mixed  $-\text{OH}$  and  $-\text{O}_x$  surface groups here. First of all, the patterns of different  $-\text{O}_x$  surface groups arranging themselves towards preferable adsorption location and orientation at surfaces of  $\text{O}_x$ -terminated uCNPs all apply here. Meanwhile, similar vibration frequency range pertaining to a vibration mode of a particular  $-\text{O}_x$  surface group shown in uCNPs terminated with mixed  $-\text{OH}$  and  $-\text{O}_x$  surface groups, on the one hand, validates our previous results on  $\text{O}_x$ -terminated uCNPs, and on the other hand can be used as the fingerprint to determine whether  $-\text{O}_x$  groups are present at surfaces of experimentally synthesized uCNPs and even their types and chemical statuses.

From the computational perspective, we appreciate the convenience, relatively

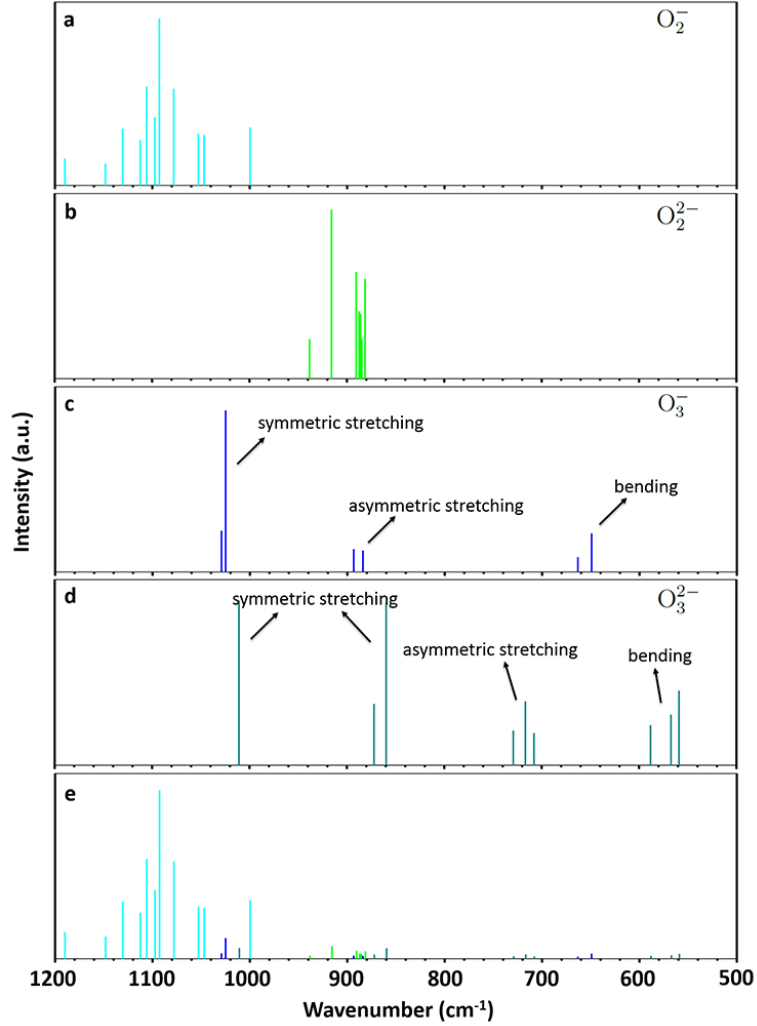


Figure 6.10: Calculated IR absorption spectrum of  $\text{Ce}_{32}\text{O}_{120}\text{H}_{40}$  within the vibration frequency range of adsorbed  $-\text{O}_x$  surface groups: (a)  $\text{O}_2^-$ ; (b)  $\text{O}_2^{2-}$ ; (c)  $\text{O}_3^-$ ; (d)  $\text{O}_3^{2-}$  and (e) combined.

cheap computational cost and reliability of  $\text{IBRION}=5$  calculation. However, it only generates vibration frequency, possible vibration peak positions. The complete IR absorption spectrum requires the relative intensity of each vibration peaks besides their positions, which can only be obtained from  $\text{IBRION}=7$  calculation. To establish a general sense of which vibration mode is more likely to be observed in experimentally measured IR absorption spectrum of synthesized uCNPs, we still need to analyze  $\text{IBRION}=7$  calculation results.

Since we mainly care the vibration of adsorbed  $-O_x$  surface groups, a portion of the complete calculated IR absorption spectra i.e. within the vibration frequency range of adsorbed  $-O_x$  surface groups for  $Ce_{32}O_{125}H_{54}$  and  $Ce_{32}O_{120}H_{40}$  are shown in Figures 6.9 and 6.10, respectively. For negatively charged  $-O_x$  surface groups, their vibration frequency range is between  $1200\text{ cm}^{-1}$  and  $500\text{ cm}^{-1}$ . Obviously, the stretching of  $-O_2^-$  surface groups exhibits much stronger intensity than any vibration mode of  $-O_2^{2-}$ ,  $-O_3^-$  and  $-O_3^{2-}$  surface groups, and locates within  $1200 - 1000\text{ cm}^{-1}$ , centering around  $1100\text{ cm}^{-1}$ . Thus, if all those negatively charged  $-O_x$  surface groups are present in uCNPs, vibration information of  $-O_2^{2-}$ ,  $-O_3^-$  and  $-O_3^{2-}$  surface groups are more than likely to be overridden by that of  $-O_2^-$  surface groups. To consider the case where  $-O_2^-$  surface groups are not present, we have separated vibration frequency of each  $-O_x$  surface group to observe their pattern. Consistent with common knowledge of molecular IR absorption spectroscopy, for triatomic molecules, our calculated results show that symmetric stretching exhibits stronger intensity than that of asymmetric stretching and bending, and that their frequency order is as follows: symmetric stretching > asymmetric stretching > bending.

We should pay attention to triatomic  $-O_x$  surface groups, because they have three separate sets of IR absorption peaks in three range, namely,  $1100 - 900\text{ cm}^{-1}$ ,  $850 - 700\text{ cm}^{-1}$ , and  $650 - 550\text{ cm}^{-1}$ . Interestingly, these regions are commonly neglected by experimentalists when they do IR spectrum measurement on uCNPs, but the highly probable evidence to verify the presence of triatomic  $-O_x$  groups adsorbed at surfaces of uCNPs. Together with Table 4.4, without the influence of other carbon-, nitrate- and sulfid-based molecular species, we can confidently assign peaks appearing in experimentally measured IR absorption spectrum of uCNPs within this window of  $1200 - 500\text{ cm}^{-1}$  to certain  $-O_x$  surface groups. For instance, IR absorption peaks around  $1050\text{ cm}^{-1}$  can be asymmetric stretching of laying  $-O_3$  surface groups or symmetric stretching of laying  $-O_3^-$  surface groups, while peaks around  $850\text{ cm}^{-1}$

can be asymmetric stretching of standing  $-\text{O}_3$  surface groups, asymmetric stretching of bridging  $-\text{O}_3^-$  surface groups, or asymmetric stretching of bridging  $-\text{O}_3^{2-}$  surface groups. In order to precisely assign a (or a set of) vibration frequency to a particular  $-\text{O}_x$  surface group, we need to comprehensively examine the related frequency and intensity of other vibration modes.

## 6.6 Summary

Moving forward from the investigation of the surface configuration of uCNPs in a pure oxygen environment, an idealized case, we have further explored the surface configuration of uCNPs in a humid environment, a more complicated but realistic case. In addition to various  $-\text{O}_x$  surface groups, like the idealized case,  $-\text{OH}$  surface groups are also found to be present at surfaces of uCNPs. The presence of adsorbed  $-\text{OH}$  surface groups is consistent with the experimental characterization of small CNPs. However, experiments cannot reveal the atomic scale arrangement of adsorbed surface groups. Atomistic quantum mechanical calculations have been used not only to determine the surface configuration of uCNPs, but more importantly to investigate how it varies in response to a particular environment, for instance, the temperature and partial pressure of ambient gaseous atmosphere. Combining calculated excess energies of formation for uCNPs with mixed surface configurations of  $-\text{OH}$  and  $-\text{O}_x$  surface groups with previously tabulated thermochemical data yields a phase diagram for uCNP surface configurations as a function of  $\mu_H$  and  $\mu_O$ . These results demonstrate that tuning the environmental conditions under which uCNPs are synthesized and/or applied can have a significant impact on the surface configuration of uCNPs. For conditions involving  $\text{O}_2$  gas and  $\text{H}_2\text{O}$  vapor, we have shown that the distribution of adsorbed  $-\text{OH}$  and  $-\text{O}_x$  surface groups can be varied by changing the temperature and partial pressures of  $\text{O}_2$  gas and  $\text{H}_2\text{O}$  vapor. These results not only provide an initial map for the design of uCNPs with controlled surface configurations, but



demonstrate that combined computational and experimental studies can be leveraged to reveal the detailed structure and properties of uCNPs.

As adsorbed  $-OH$  surface groups are experimentally considered an important structural feature of uCNPs, we have specifically examined (1) the density of  $-OH$  surface groups bound to uCNPs and (2) IR absorption spectrum of  $OH$ -terminated uCNPs. Assuming  $-OH$  surface groups as the only surface functional group present at uCNP facets, edges and corners results in the computationally predicted density of  $-OH$  surface groups  $\sim 33\%$  higher than the experimentally measured value. This discrepancy can be rectified by considering the possibility that both  $-OH$  and  $-O_x$  groups are present at surfaces of uCNPs. Furthermore, calculated IR absorption spectra of uCNPs have shown that the detailed information concerning the surface configuration of uCNPs can be reflected in their IR absorption spectra. This information includes whether uCNPs are fully oxidized or not, what surface functional groups are present, and the possible atomic arrangement of present surface functional groups, which again demonstrates that combined computational and experimental studies can be leveraged to reveal the detailed structure and properties of uCNPs.

## Chapter 7 Water-gas shift reaction over OH-terminated ultra-small CNPs

### 7.1 Catalytic pathway of WGS reaction over pure OH-terminated uCNPs

As we have discussed in Chapter 6, the surface of as-synthesized uCNPs are typically populated with numerous  $-OH$  surface groups. When they are applied in WGS reaction, those  $-OH$  surface groups are still likely to be present in the application environment. Note that traditional viewpoint of ceria catalyzing WGS reaction considers the metal to be crucial for breaking incoming  $H_2O$  and generating  $-OH$  surface groups. In addition, it is suggested that  $H_2O$  dissociation is the overall rate determining step and quite energy-consuming. In retrospect, OH-terminated uCNPs seem have already met these conditions. It is interesting to examine the possible catalytic pathway of WGS reaction over OH-terminated uCNPs. For simplicity, we choose a thermodynamic stable cubic uCNP structure,  $Ce_{32}O_{101}H_{74}$ , as the representative structure to conduct this investigation.

To find out possible pathways, we have first explored the interaction between  $H_2O/CO$  and surface of uCNPs and have identified a series of relaxed structures with local minimum energy. By comparing the relative energy of those relaxed structures, we have further paired some relaxed structures that have local minimum energies and probed the energetics and kinetics of elementary steps connecting those paired structures to form complete reaction pathways. In general, we found two possible mechanisms, i.e. formate mechanism and dehydrogenation mechanism.

#### 7.1.1 Formate mechanism

Typical formate mechanism over metal/ceria catalysts involves two key steps, i.e. dissociating adsorbed  $H_2O$  molecules at metal/ceria interface into adsorbed H atoms

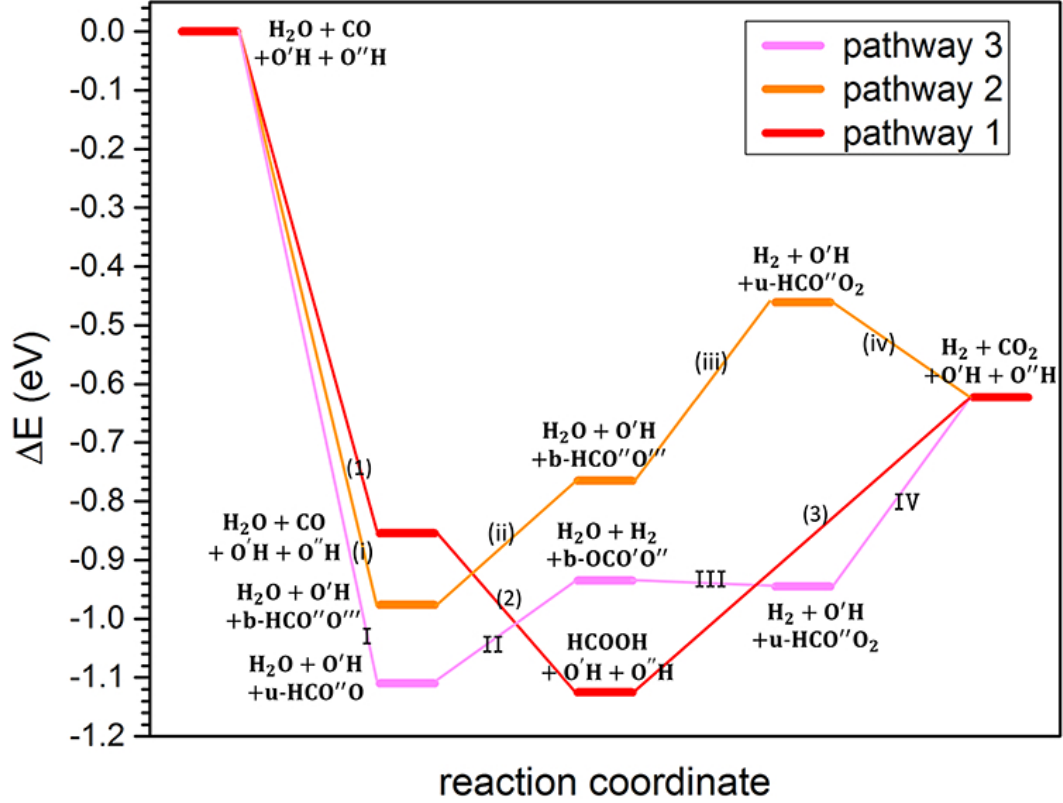


Figure 7.1: Three possible WGS reaction pathways realized via OH-terminated uCNPs following formate mechanism. Chemical elements marked with single/double/triple prime symbols represent atoms adsorbed to different surface Ce atoms of OH-terminated uCNPs. Letter “u” stands for “unidentate” and letter “b” stands for “bidentate”.

on the metal surface and adsorbed  $\text{-OH}$  groups on ceria surface, as well as combining adsorbed CO molecules on the metal surface and adsorbed  $\text{-OH}$  groups on the ceria surface to form the intermediate—formate. Here, we call it formate mechanism primarily recognizing the formation of formate as the intermediate, and showing how OH-terminated uCNPs fulfill both catalytic functions the metal/ceria system.

Three dissimilar pathways all having formate as the intermediate have been identified and relative energies of pertinent local minimum energy structures are plotted in Figure 7.1. For the convenience of comparing energy differences among those relaxed structures, we set the starting system, which is  $\text{H}_2\text{O}$ , CO and the OH-terminated uCNP, as the reference system, and its total ground state energy (calculated from VASP

at  $T = 0$  K) to be zero. In pathway 1, incoming  $\text{H}_2\text{O}$  and  $\text{CO}$  molecules, without interacting with the surface of the OH-terminated uCNP, directly form a formic acid by themselves, lowering the total energy of the system by 0.85 eV [see step (1)]. It then adjust its spatial orientation to be ready to interact with a  $-\text{OH}$  group at the surface of the OH-terminated uCNP (see Figure 7.2(1)), which lowers the total energy of the system by another 0.27 eV. Now the energy of the system reaches its bottom for this particular reaction pathway [see step (2)]. The final big step is using this  $-\text{OH}$  surface group to assist the formate acid decomposing into  $\text{H}_2$  and  $\text{CO}_2$  molecules to accomplish WGS reaction, ending up with increasing the total energy of the system by 0.5 eV (see [step (3)]). In pathway 2, a  $\text{CO}$  molecule firstly approaches a  $-\text{OH}$  surface group to form a bidentate formate adsorbed to two different surface Ce atoms of the OH-terminated uCNP (see Figure 7.3(1)), which lowers the total energy of the system by 0.98 eV [see step (i)]. Once the formate is formed, a  $\text{H}_2\text{O}$  molecule comes along ready to attack the adsorbed formate. Note that instead of traveling a long distance to interact with the adsorbed formate,  $\text{H}_2\text{O}$  molecule strategically passes a H atom to a nearby  $-\text{OH}$  surface group sitting between itself and the adsorbed formate and then switches position with that  $-\text{OH}$  surface group. The  $-\text{OH}$  surface group originally sitting at the surface O lattice site receives a H atom from the  $\text{H}_2\text{O}$  molecule which later turns into another  $-\text{OH}$  surface group and itself ends up with becoming a new  $\text{H}_2\text{O}$  molecule close enough to the targeted adsorbed formate [see step (ii)]. This increases the total energy of the system by 0.21 eV. Then this newly formed  $\text{H}_2\text{O}$  molecule attacks the adsorbed formate with each donating a H atom to form a  $\text{H}_2$  molecule. Their residuals together form a unidentate bicarbonate, increasing the total energy of the system by another 0.30 eV [see step (iii)]. Finally, the unidentate bicarbonate adjusts its structure (see Figure 7.3(5)) and dissociates into  $\text{CO}_2$  molecule and a  $-\text{OH}$  surface group to accomplish WGS reaction and recover the original surface configuration of the OH-terminated uCNP (see Figure 7.3(6)), which

lowers the total energy of the system by 0.16 eV [see step (iv)]. In pathway 3, the first step is similar to that in pathway 2, which is a CO molecule interacts with a  $\text{-OH}$  surface group but form a unidentate formate adsorbed at one surface O lattice site of the OH-terminated uCNP. Due to different bonding status of the formed formate, this time the total energy of the system is lowered even more, by 1.11 eV [see step I]. Next, this unidentate formate leans towards a neighboring  $\text{-OH}$  surface group and interacts with it by each donating a H atom to form a  $\text{H}_2$  molecule. Their residuals together form a bidentate carbonate adsorbed to two different surface Ce atoms of the OH-terminated uCNP, resulting in an increase of the total energy of the system by 0.17 eV [see step II]. Then an incoming  $\text{H}_2\text{O}$  molecule approaches and further passes a H atom to one of two O atoms within the bidentate carbonate bonded to surface Ce atoms, causing the bidentate carbonate to become a unidentate bicarbonate (see Figure 7.4(4)) as well as itself to refill the surface O lattice site of the uCNP left behind by the newly formed unidentate bicarbonate [see step III]. This process slightly lowers the total energy of the system by 0.01 eV. Finally, it goes through a step similar to the last step in pathway 2, that is the unidentate bicarbonate adjusts its structure (see Figure 7.4(5)) and dissociates into a  $\text{CO}_2$  molecule and a  $\text{-OH}$  surface group to accomplish WGS reaction (see Figure 7.4(6)) and recover the original surface configuration of the OH-terminated uCNP [see step IV]. The difference is that, at this time, the total energy of the system is increased by 0.32 eV.

All the above discussion on the reaction energy for different pathways does not consider the kinetic factor, i.e. the activation energy defining the rate of each step. The step having largest activation energy is considered the rate determining step of the overall pathway. However, if the activation energy of one step is too large, that step in practice is very unlikely to happen, no matter how energetically close the beginning state is to the end state within that step. Now we especially engage in this point to examine whether an assumed particular step within a pathway can actually

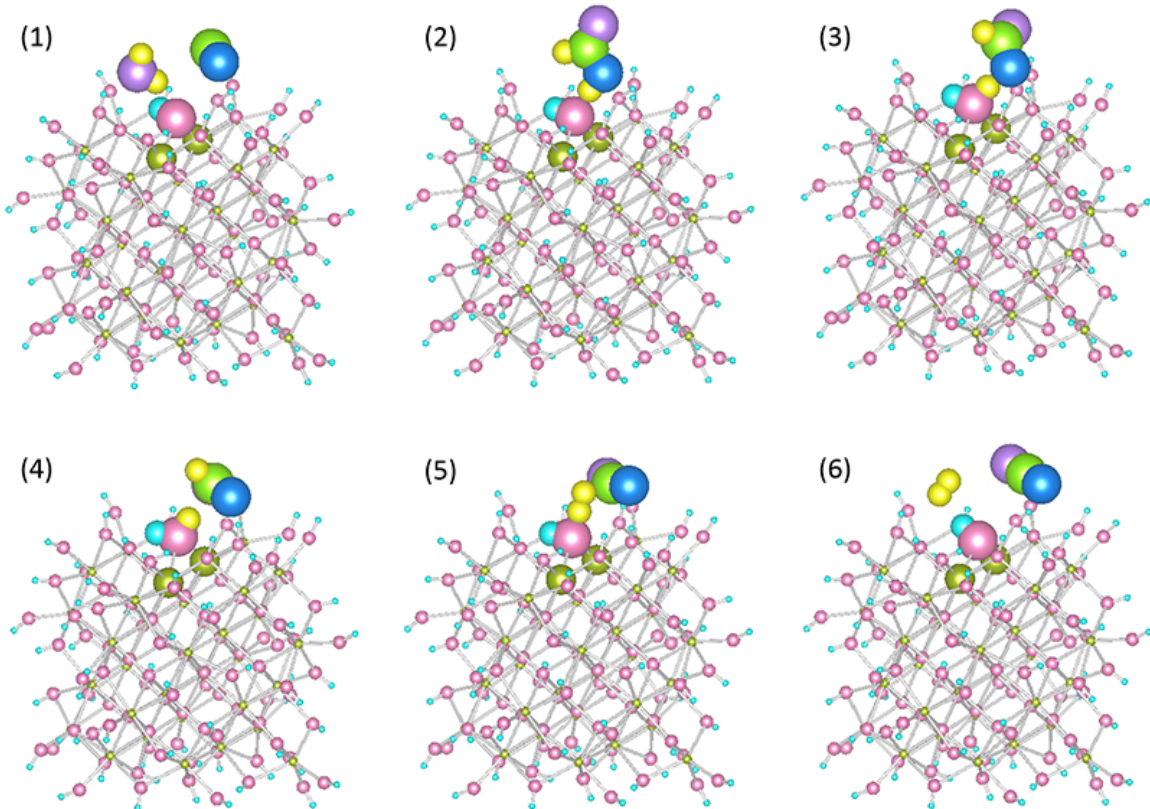


Figure 7.2: Key products during WGS reaction along pathway 1 following the formate mechanism. Yellow greenish balls represent Ce atoms, pink balls represent O atoms of the OH-terminated uCNP, cyan balls light green balls represent C atoms, blue balls represent O atoms from the CO molecule, light purple balls represent O atoms from the H<sub>2</sub>O molecule, and yellow balls represent H atoms from the H<sub>2</sub>O molecule. Some balls are enlarged to clearly show the atoms actively participating in the WGS reaction. Note that different color is also used to track the movement of interested atoms.

happen within a reasonable and finite period of time.

In pathway 1, NEB calculation shows that step (1) together with step (2) generally brings down the total energy of the considered system. To accomplish these two steps, it requires overcoming a little energy barrier (no more than 0.20 eV), indicating that reaction rate for step (1) and step (2) is very fast. Step (3) is the crucial step for the overall pathway because it involves how the OH-terminated uCNP functions to facilitate dissociating formic acid into the final products of WGS reaction. Firstly, the formic acid passes a H atom to a -OH group at the surface of the OH-terminated

uCNP. As a result, the formic acid itself becomes formate by losing a H atom, and the  $-OH$  surface group becomes a surface adsorbed  $H_2O$  molecule by gaining a H atom (Figure 7.2(2)). Secondly, the formate intermediate gradually adjusts its orientation to reach a point that its H atom is appropriately positioned to reap off another H atom from the surface adsorbed  $H_2O$  molecule (Figure 7.2(3)). Thirdly, both the formate and  $H_2$  molecule give up a H atom and ready to interact with each other. In this process, a transition state is that one H atom is in the middle of leaving the  $H_2O$  molecule while approaching another H atom which is in the middle of leaving the formate (Figure 7.2(4)). Lastly, both H atoms completely escape from their hosts and combine into a single  $H_2$  molecule; at the same time, the formate turns into a  $CO_2$  molecule, and the newly formed  $-OH$  surface group recovers the original surface configuration of the OH-terminated uCNP (Figure 7.2(5)). The activation energy of step (3) is 1.42 eV.

In pathway 2, NEB calculation shows that step (i) and step (iv) brings down the total energy of the considered system by overcoming a small energy barrier (0.08 eV and 0.42 eV, respectively). Steps (ii) and (iii) are energy climbing steps that need to be carefully examined. Step (ii) is simply an incoming  $H_2O$  molecule pushing and giving a H atom to a  $-OH$  surface group to form a new  $H_2O$  molecule away from the surface of the OH-terminated uCNP while itself becoming a  $-OH$  surface group to reoccupy that surface site of the OH-terminated uCNP (Figure 7.3(2)). The activation energy required to accomplish this step is 0.53 eV, suggesting its rate is fast. Step (iii) is quite similar to step (3) in pathway 1, that is a  $H_2O$  molecule interacts with the adsorbed formate to generate a single  $H_2$  molecule. And a transition state is that one H atom is in the middle of leaving the  $H_2O$  molecule while approaching another H atom which is in the middle of leaving the bidentate formate (Figure 7.3(3)). As we know from pathway 1, demanding both a  $H_2O$  molecule and an adsorbed formate to give up a H atom is rather energy consuming, it is expected that the activation energy

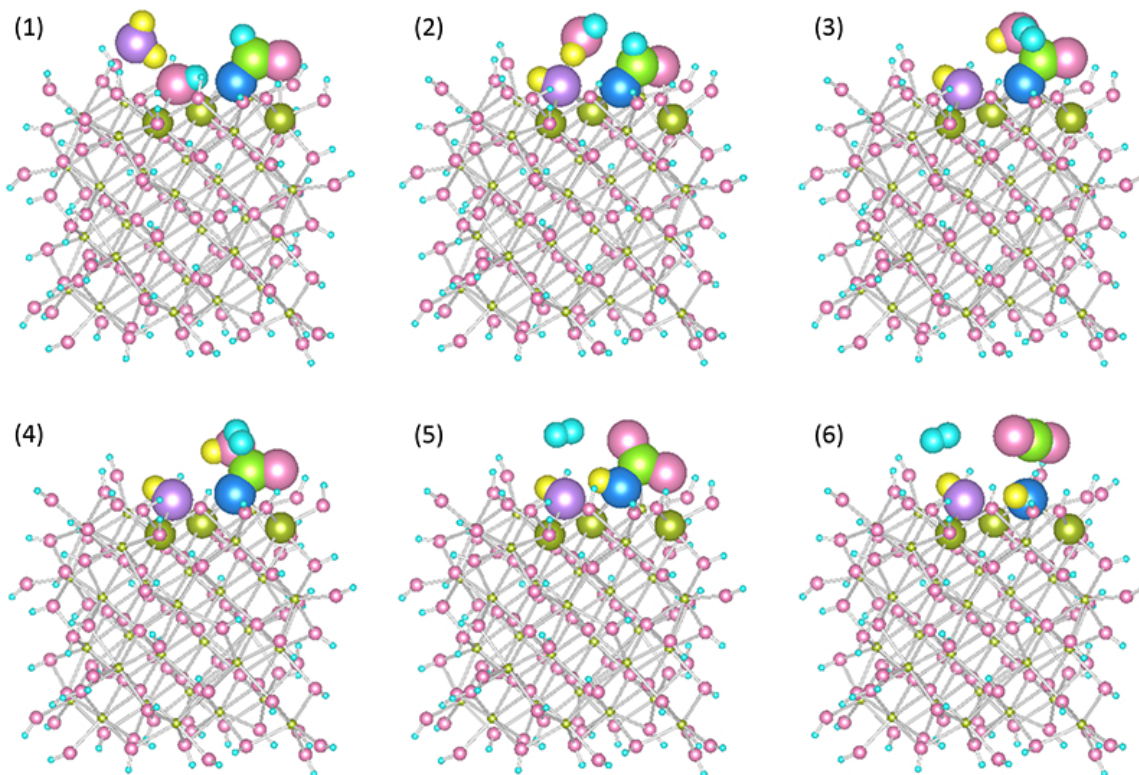


Figure 7.3: Key products during WGS reaction along pathway 2 following the formate mechanism. Yellow greenish balls represent Ce atoms, pink balls represent O atoms of the OH-terminated uCNP, cyan balls light green balls represent C atoms, blue balls represent O atoms from the CO molecule, light purple balls represent O atoms from the H<sub>2</sub>O molecule, and yellow balls represent H atoms from the H<sub>2</sub>O molecule. Some balls are enlarged to clearly show the atoms actively participating in the WGS reaction. Note that different color is also used to track the movement of interested atoms.

should be high. The difference is that the newly formed –OH surface group from the H<sub>2</sub>O molecule losing a H atom further combines with the residual of the bidentate formate to form a unidentate bicarbonate (Figure 7.3(4)), instead of recovering the –OH surface group of the OH-terminated uCNP. This leads to a much higher activation energy, 2.66 eV, which indicates this step is very unlikely to happen under applied reaction condition.

In pathway 3, step I is quite similar to step (i) in pathway 2. An incoming CO<sub>2</sub> molecule interacts with a –OH surface group of the OH-terminated uCNP to form a unidentate formate (Figure 7.4(1)) rather than a bidentate formate. It is within our



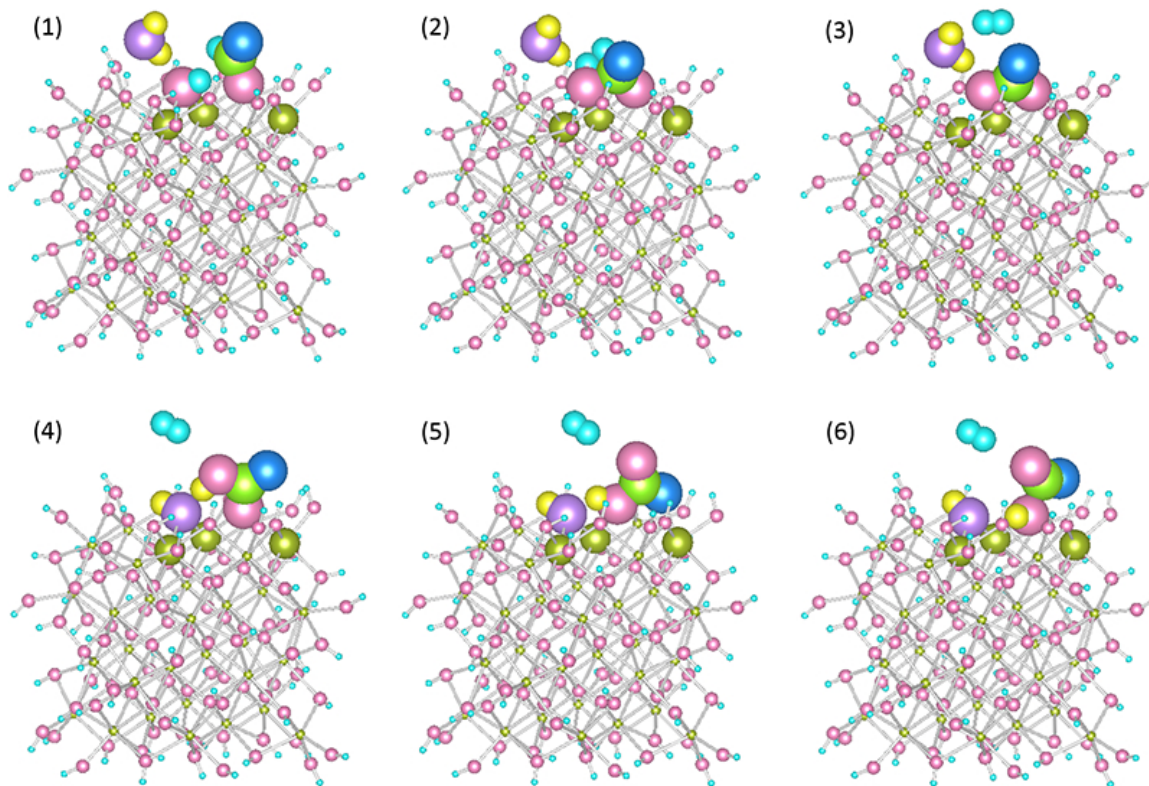


Figure 7.4: Key products during WGS reaction along pathway 3 following the formate mechanism. Yellow greenish balls represent Ce atoms, pink balls represent O atoms of the OH-terminated uCNP, cyan balls light green balls represent C atoms, blue balls represent O atoms from the CO molecule, light purple balls represent O atoms from the H<sub>2</sub>O molecule, and yellow balls represent H atoms from the H<sub>2</sub>O molecule. Some balls are enlarged to clearly show the atoms actively participating in the WGS reaction. Note that different color is also used to track the movement of interested atoms.

expectation, the energy barrier for this step is quite small (0.03 eV). Again step II is generating a single H<sub>2</sub> molecule and a transition state is that one H atom is in the middle of leaving the –OH surface group while approaching another H atom which is in the middle of leaving the unidentate formate (Figure 7.4(2)). Instead of relying on a formate interacting with a surface adsorbed H<sub>2</sub>O molecule, a H<sub>2</sub> molecule is generated via the interaction between a unidentate formate and a neighboring –OH surface group both adsorbed at the surface of the OH-terminated uCNP. This leads to the formation of a bidentate carbonate (Figure 7.4(3)) and a expected high activation

energy of 2.76 eV, which again indicates this step is very unlikely to happen under applied reaction condition.

In sum, formate mechanism requires formate intermediate as one source to provide a H atom and a  $\text{H}_2\text{O}$  molecule (or a  $-\text{OH}$  surface group) as another source to offer another H atom so as to generate a single  $\text{H}_2$  molecule. Such a way of breaking a O-H bond is very energy demanding, to some extent confirming the viewpoint from previous investigations of WGS reaction on metal/ceria catalyst system. Meanwhile, the advantage of readily available  $-\text{OH}$  groups at the surface of uCNP is not taken in an energy efficient way.

### 7.1.2 Dehydrogenation mechanism

Here, dehydrogenation mechanism is a new terminology we invent here to highlight two important dehydrogenation steps within this particular reaction pathway to realize WGS reaction specifically over a OH-terminated uCNP. The ground state relaxed structures comprising the overall pathway have been identified and their relative energies are plotted in Figure 7.5. For the convenience of comparing energy differences among those relaxed structures, we set the starting system, which is  $\text{H}_2\text{O}$ , CO and the OH-terminated uCNP, as the reference system, and its total ground state energy (calculated from VASP at  $T = 0$  K) to be zero.

The first half of step (a) is more or less a repetition of step I in pathway 3 following formate mechanism, which is a  $\text{CO}_2$  molecule interacting with a  $-\text{OH}$  surface group of the OH-terminated uCNP. The second half of step (a) is that newly formed formate intermediate abandons its H atom and becomes a  $\text{CO}_2$  molecule while the H atom left behind sits right at a surface O lattice site between two surface Ce atoms of the OH-terminated uCNP. This time, the newly formed formate intermediate is not adsorbed to the surface of the OH-terminated uCNP and then ready to go through subsequent steps so as to generate a single  $\text{H}_2$  molecule, but is directly transformed into a  $\text{CO}_2$

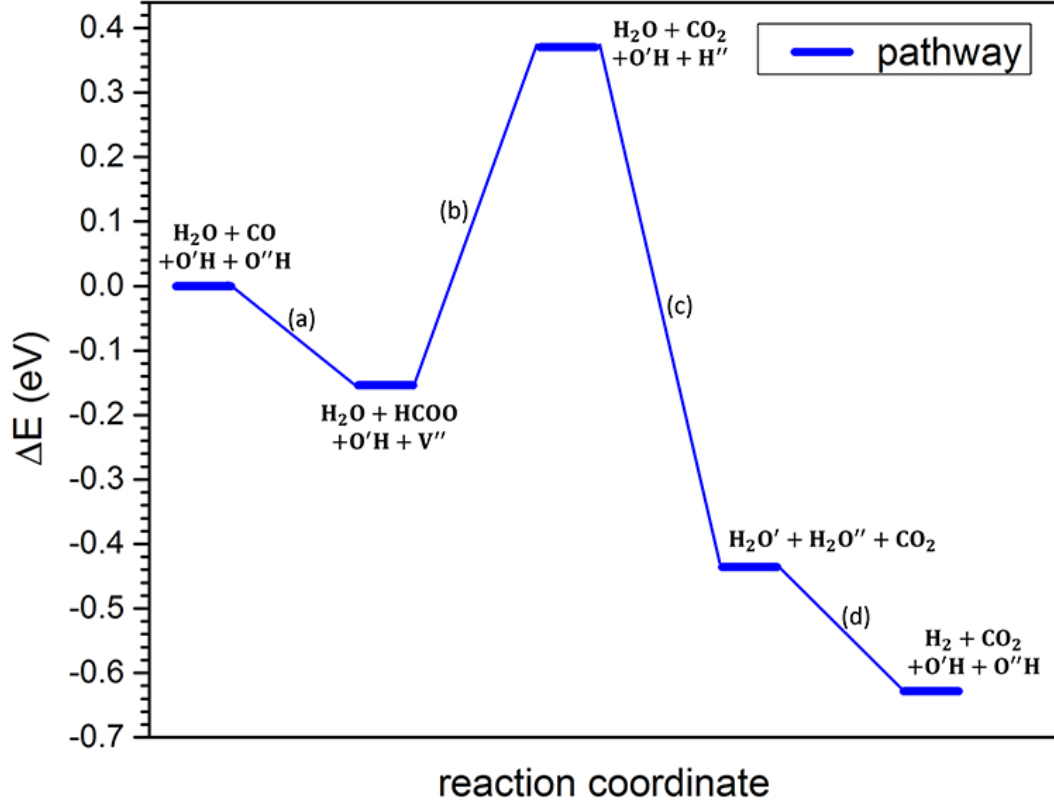


Figure 7.5: The possible WGS reaction pathway realized via OH-terminated uC-NPs following dehydrogenation mechanism. Chemical elements marked with single/double prime symbols represent atoms adsorbed to different surface Ce atoms of OH-terminated uCNPs.

molecule. The total energy of the system is marginally lowered by  $\sim 0.15$  eV, much less compared to the first step in three different pathways of formate mechanism that lowers the total energy of the system by at least 0.85 eV. However, this seemingly uneffective energy-reducing step in fact sets a higher energy starting point for the next energy climbing step, which in turn effectively lowers the activation energy of the next step to some extent. Starting from step (b), an incoming  $\text{H}_2\text{O}$  molecule gradually gets close to the H atom dissociated from the formate and a neighboring  $-\text{OH}$  surface group of the OH-terminated uCNP, which increases the total energy of the system by 0.52 eV. In step (c), the  $\text{H}_2\text{O}$  molecule donates one H atom to a  $-\text{OH}$  surface group, which is transformed into a surface adsorbed  $\text{H}_2\text{O}$  molecule, and combines itself with the H atom dissociated from the formate to form another

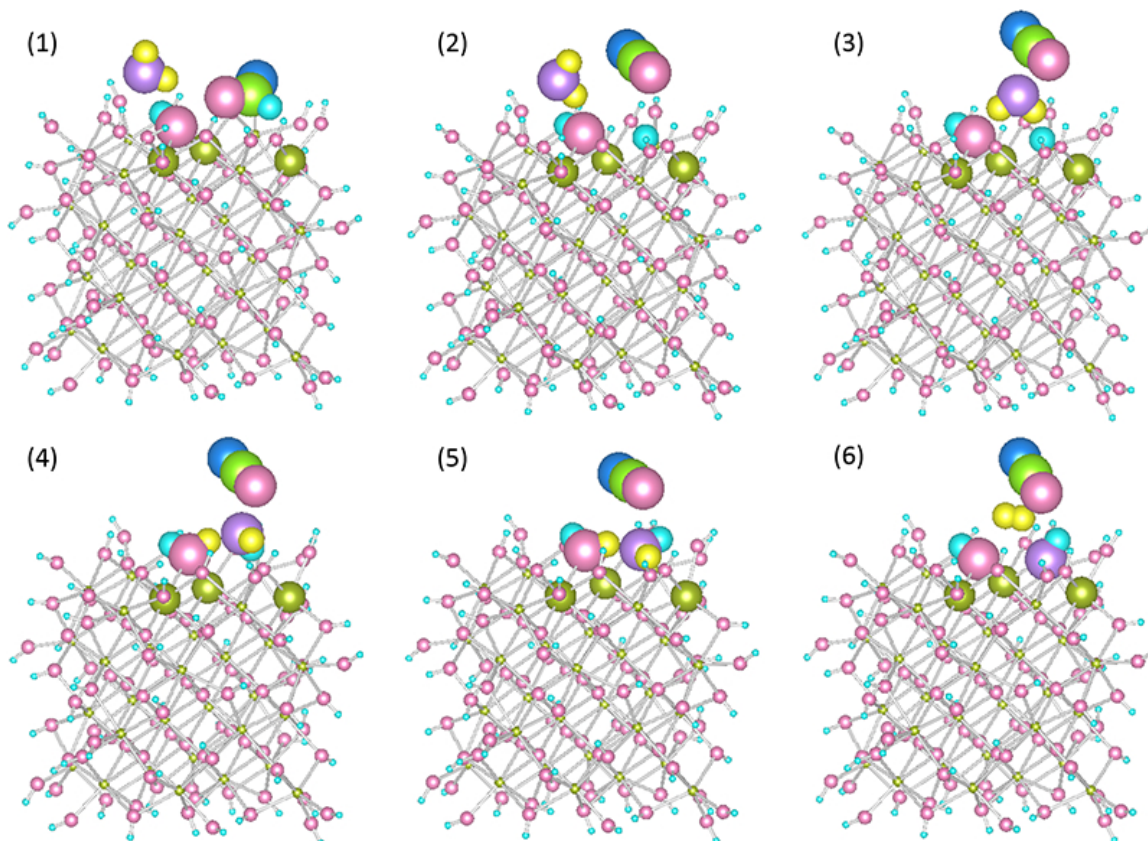


Figure 7.6: Key products during WGS reaction along the pathway following the dehydrogenation mechanism. Yellow greenish balls represent Ce atoms, pink balls represent O atoms of the OH-terminated uCNP, cyan balls light green balls represent C atoms, blue balls represent O atoms from the CO molecule, light purple balls represent O atoms from the H<sub>2</sub>O molecule, and yellow balls represent H atoms from the H<sub>2</sub>O molecule. Some balls are enlarged to clearly show the atoms actively participating in the WGS reaction. Note that different color is also used to track the movement of interested atoms.

surface adsorbed H<sub>2</sub>O molecule (see Figure 7.6(4)). This lowers the total energy of the system by 0.81 eV. In the final step (d), these two neighboring surface adsorbed H<sub>2</sub>O molecules each gives up one H atom to generate a single H<sub>2</sub> molecule and meanwhile recover the surface configuration of the OH-terminated uCNP to accomplish WGS reaction, lowering the total energy of the system by another 0.19 eV.

In the same token, we need to take the kinetic factor into account to assess whether the assumed pathway is energetically practical or not. In Step (a), the formate intermediate that is desorbed from the surface of the OH-terminated uCNP

is the transition state (Figure 7.6(1)). To complete forming the formate intermediate and further dissociating the formate into a  $\text{CO}_2$  molecule and a surface adsorbed H atom (Figure 7.6(2)), it requires overcoming a moderate energy barrier, calculated as 0.31 eV. When  $\text{H}_2\text{O}$  molecule approaches closer and closer to the surface of the OH-terminated uCNP in step (b), the total energy of the system is generally increasing until the system reaches its transition state (Figure 7.6(3)), where the  $\text{H}_2\text{O}$  molecule is facing downward with closest distance to both the  $-\text{OH}$  group and the H atom at the surface of uCNP. The activation energy of this step is 0.67 eV. Once two surface adsorbed  $\text{H}_2\text{O}$  molecules are formed at two surface O lattice sites of the OH-terminated uCNP (Figure 7.6(5)), the energy of the system is dropped significantly, leading to a lower energy starting point for the last step. The last step is also a energy climbing one, with two H atoms each from a surface adsorbed  $\text{H}_2\text{O}$  molecule getting together to form a single  $\text{H}_2$  molecule as the transition state (Figure 7.6(6)). The activation energy of this step is 0.34 eV. It turns out that step (b) is the biggest energy barrier required to overcome in this dehydrogenation mechanism, suggesting that this is the rate determining step.

## 7.2 Summary

We have explored the possibility of a widely proposed WGS reaction mechanism, formate mechanism, and a new WGS reaction mechanism specific in this study, dehydrogenation mechanism, for the OH-terminated uCNP. In retrospect, for this particular structured uCNP, reaping off H atoms both from the formate intermediate and a  $\text{H}_2\text{O}$  molecule or a  $-\text{OH}$  surface group is very energy demanding. However, direct transformation of the formate intermediate into a  $\text{CO}_2$  molecule by dropping a H atom to the surface of uCNP only requires a moderate energy cost. As a result, dehydrogenation mechanism is more likely to be the pathway of WGS reaction over the OH-terminated uCNP in practice. Another advantage of dehydrogenation

mechanism is that it fully uses the nature of two surface adsorbed  $\text{H}_2\text{O}$  molecules to generate the  $\text{H}_2$  molecule, another energy inexpensive pathway particular to the OH-terminated uCNP to simultaneously realize the recovery of its surface structure and the formation of one final product of WGS reaction ( $\text{H}_2$  molecules). Note that the realization of such a catalytic mechanism seems only depend on  $-\text{OH}$  surface groups; however, as a matter of fact, Ce atoms function as the electron acceptor, which is in stark contrast to the conventional view regarding the function of Ce atoms (served as the electron donor).

WGS reaction is only investigated over a OH-terminated uCNP in this study. It seems that this is a special case study; however, it reveals some crucial ideas in the dehydrogenation mechanism that can be generalized to uCNPs of various surface configurations. It is simply because that  $-\text{OH}$  surface groups are one of the key surface functional groups unanimously present in uCNPs with any surface configuration. This well demonstrates that combined computational and experimental studies can be leveraged to reveal the detailed structure and catalytic properties of uCNPs.

## Chapter 8 Conclusions and future work

### 8.1 Concluding results of this research work

The design and development of low-cost but highly active and selective catalysts continues to be a major focus of efforts in materials chemistry. Ceria-based materials, particularly, ultra-small ceria nanoparticles (uCNPs) are increasingly becoming the focus of interdisciplinary researchers, due to their excellent catalytic potentials in energy and biomedical applications. Understanding the surface structure of uCNPs and catalytic behavior thereof is to harness and functionalize uCNPs for the realization of the maximum efficacy in catalyzing desirable reactions.

Over the past 30 years, explanations for the mechanism of ceria catalysis have, to date, assumed ideal, stoichiometric bulk-cut surface configurations, or minor perturbations thereof. This long standing viewpoint has in fact become a stumbling block to understand the surface structure and catalytic properties of uCNPs, perplexing experimentalists devoting to improving, controlling and designing better functionalized uCNPs in diversified energy and biomedical applications. By lifting such a constraint and not assuming particular concentrations or configurations of atoms at uCNP surfaces, a comprehensive exploration of the stability of uCNPs with various surface configurations versus environmental factors has been completed. We have first examined the surface configuration of uCNPs in a pure oxygen environment (an idealized case) and then in a humid environment (a more complicated but realistic case). This leads to a groundbreaking finding that uCNPs are covered with various surface functional groups, for instance,  $-\text{OH}$  and  $-\text{O}_x$  surface groups in this study. Moreover, the type and atomic arrangement of those surface functional groups are internally varied with and determined by the synthesis and application environment of uCNPs. Such a dynamic picture about the surface configuration of uCNPs, not

only to some extent explains the seemingly controversial experimental observation on the behavior of uCNPs, which is uCNPs sometimes behave as an oxidizing agent and sometimes as a reducing agent, but more importantly provides a recipe for experimentalists to tune the functionalization of uCNPs via controlling their surface configurations in a targeted way.

Besides environmental factors governing the surface configuration of uCNPs, we have also investigated the intrinsic reason of forming those functional groups at surfaces of uCNPs. Above all, it is due to the nature of under-coordinated corners, edges, and  $\{100\}$  facets depending on the shape of considered uCNPs. The number (or density) of surface functional groups, which increases the coordination of near surface Ce atoms, is offset by intrinsic O-vacancies within the “bulk” part, which decreases the coordination of internal Ce atoms. When the size of uCNPs is sufficiently large, the nanoscale induced surface effect is replaced by the bulk surface property, shown as the size-dependent surface termination transition in **section 4.5**. Moreover, it is controlled by the charge neutrality of considered uCNPs. The “bulk” part is generally positively charged as positive charges contributed from Ce cations exceed negative charges contributed from “bulk” O anions, the rest positive charges need to be balanced by negatively charged functional groups at surfaces of uCNPs. Again, this balance is size-dependent, shown as varying density of  $-OH$  surface groups as a function of CNP size in **section 6.3**. In a word, uCNPs can be viewed as a “core-shell” structure, with positively charged *reduced core* and a finite number of under-coordinated Ce atoms as well as negatively charged *oxidized shell* and a finite number of super-coordinated Ce atoms. Their surface configuration is intrinsically dominated by both non-stoichiometry nature of corners, edges and  $\{100\}$  facets as well as charge neutrality requirement, both of which are size-dependent. Thus, non-bulk like surface configurations is only limited to CNPs below a certain size, and it is purely a nanoscale effect.



Two typical reactions catalyzed by ceria, namely CO oxidation and water-gas shift reaction, has been used to computationally assess uCNP structures. In general, surface functional groups have been shown to be essential active components that direct and drive the proceeding of those catalytic reactions. They directly interact with incoming species to be catalyzed and function as the building block to establish energetically favorable pathways. This is in stark contrast to conventional picture regarding the catalytic mechanism of uCNPs that O-vacancies are the dominate factor and it is energetically more favorable to form O-vacancies in uCNPs.

In addition, we have calculated IR absorption spectra of some interested uCNP structures. Calculated IR absorption spectra together with experimentally measured IR absorption spectra not only can be used as the fingerprint to determine the surface configuration of synthesized uCNPs and uCNPs applied in a specific environment, but also can identify the type of present functional groups, and even predict their chemical status and distribution at surfaces of uCNPs.

## 8.2 Future research directions

This work opens up many opportunities for further practical applications of uCNPs in energy, environment, and health-related fields. For instance, this work will help maximize uCNPs' ability to split  $\text{H}_2\text{O}$  molecules to produce  $\text{H}_2$  molecules as an alternative green energy substitute for fossil fuels, to convert toxic gas (e.g., CO) to nontoxic gas (e.g.,  $\text{CO}_2$ ) for mitigating automobile exhausts, and to reduce oxidative stress (a key precursor state to many chronic diseases) in the human body. All of these applications rely on successfully preventing the agglomeration of uCNPs and enhancing various functionalities of uCNPs, which are potentially my future research directions. Current experimental studies have examined a series of organic molecules called surfactants to evaluate their effects on preventing the agglomeration of uCNPs. However, those organic molecules either improve the agglomeration but weaken

the functionalities of uCNPs or vice versa. This work to date has laid down all the foundation necessary to understand how surfactants influence the atomic and electronic structures of uCNPs, how to collect associated data from both computational and experimental studies, and most importantly, to effectively design surfactants and fabrication processes to produce uCNPs of specific reactive surface configurations.

### 8.3 Overall conclusions

From this research work, we can clearly see that the structure and catalytic properties of uCNPs is completely different from bulk ceria materials. The current perspective concerning the structure and catalytic behavior of uCNPs needs an urgent and paradigm shift. Our results unambiguously show that studying uCNPs has nothing to do with intrinsic O-vacancies, but everything to do with surface functional groups. If one wants to design a functional uCNP, the first thing to be aware of is that the surface configuration (e.g., the type, density and distribution of potentially present surface functional groups) of uCNPs is very sensitive to the synthesizing and processing environment. One must carefully control their synthesizing and processing conditions in order to obtain uCNPs with the desired surface configurations. In today's applications of uCNPs, surfactants are crucial elements to functionalize uCNPs. After knowing the potential surface configurations of uCNPs via joint experimental and computational study, one needs to smartly choose one or a series of desirable surfactants. For instance, if uCNPs are decorated with negatively charged  $-OH$  and  $-O_x$  surface groups, employing polarized surfactants with positively charged end will likely to form strong Coulomb interaction or even forming new chemical bonding with  $-OH$  surface groups, while those surfactants with functional groups exhibiting reducing properties will likely be oxidized by  $-O_x$  surface groups or even form new chemical bonding to the surface of uCNPs. Likewise, if one wants to separate a surfactant from the surface of uCNPs, such a surfactant should not contain any func-

tional group that potentially exhibits strong interaction or even forms new chemical bonding with surface functional groups of uCNPs, and vice versa. To carry out an efficient research, one needs to associate what computational studies are capable of intimately with what experimental studies are capable of. Finding where they are connected and start from the joint point is the key step to move forward.

## Appendix: Exemplary input files for DFT calculations performed in this study

Following are exemplary INCAR files taken as computation inputs by the computational tool (VASP) employed in this dissertation work to perform all calculations.

Direct relaxation calculation

```
PREC = High
ENCUT = 400
ALGO = Fast
LREAL = A
NPAR = 12
NSIM = 4
ISTART = 0
ICHARG = 1
ISMEAR = 0
SIGMA = 0.1
EDIFF = 1e-4
EDIFFG = 1e-3
IBRION = 2
ISYM = 0
MAXMIX = 60
IALGO = 48
NSW = 100
NELM = 100
POTIM = 0.5
LASPH = .TRUE.
LDAU = .TRUE.
LDAUL = 3 -1 -1 -1
LDAUU = 5 0 0 0
LMAXMIX = 6
```

## Electronic density of states calculation

```
PREC = High
ENCUT = 400
ALGO = Fast
ISTART = 0
ICHARG = 1
LREAL = A
NPAR = 12
NSIM = 4
ISMEAR = 0
SIGMA = 0.1
EDIFF = 1e-5
EDIFFG = 1e-4
IBRION = 2
ISYM = 0
MAXMIX = 60
IALGO = 48
LCHARG = .FALSE.
LWAVE = .FALSE.
LORBIT = 11
EMIN = -25
EMAX = 20
NEDOS = 4500
NSW = 0
NELM = 120
NELMIN = 6
NBANDS = 1392
POTIM = 0.8
LDAU = .TRUE.
LDAUL = 3 -1 -1
LDAUU = 5 0 0
LMAXMIX = 6
```

## IR absorption spectrum calculation

```
PREC = High
ENCUT = 400
ALGO = Fast
LREAL = .FALSE.
ISTART = 0
ICHARG = 1
NPAR = 12
NSIM = 4
ISMear = 0
SIGMA = 0.1
EDIFF = 1e-6
EDIFFG = 1e-6
IBRION = 7
LEPSILON = .TRUE.
ADDGRID = .TRUE.
ISYM = 0
MAXMIX = 60
IALGO = 48
NSW = 1
NWRITE = 3
NELMIN = 10
LWAVE = .FALSE.
LCHARG = .FALSE.
POTIM = 0.005
LASPH = .TRUE.
LDAU = .TRUE.
LDAUL = 3 -1 -1
LDAUU = 5 0 0
LMAXMIX = 6
```

Nudged elastic band calculation

```
SYSTEM = NEB
PREC = High
ENCUT = 400
ALGO = Fast
SPRING = -5
IMAGES = 6
LREAL = A
NPAR = 8
NSIM = 4
ISMEAR = 0
SIGMA = 0.1
EDIFF = 1e-3
EDIFFG = 1e-3
LCLIMB = .TRUE.
IBRION = 3
SMASS = 2
ISYM = 0
MAXMIX = 60
IALGO = 48
NSW = 1000
NELMIN = 5
NELM = 80
POTIM = 0.1
LASPH = .TRUE.
LDAU = .TRUE.
LDAUL = 3 -1 -1 -1
LDAUU = 5 0 0 0
LMAXMIX = 6
```

## Dynamical matrix calculation

```
PREC = High
ENCUT = 400
ALGO = Fast
NPAR = 16
NSIM = 4
ISMEAR = 0
SIGMA = 0.1
MAXMIX = 60
IALGO = 48
LASPH = .TRUE.
LDAU = .TRUE.
LDAUL = 3 -1 -1 -1
LDAUU = 5 0 0 0
LMAXMIX = 6
IBRION = 3
POTIM = 0.0
ISYM = 0
NSW = 115
EDIFF = 1E-7
EDIFFG = -1E-6
LREAL = A
LWAVE = .FALSE.
LCHARG = .FALSE.

# DIMER PARAMETERS
ICHAIN = 1

# OPTIMIZER PARAMETERS
IOPT=2
```



## Bibliography

- [1] A. Asati, S. Santra, C. Kaittanis, S. Nath, and J. M. Perez, "Oxidase-like activity of polymer-coated cerium oxide nanoparticles," *Angew. Chem. Int. Ed.*, vol. 48, no. 13, pp. 2308–2312, 2009.
- [2] J. Chen, S. Patil, S. Seal, and J. F. McGinnis, "Rare earth nanoparticles prevent retinal degeneration induced by intracellular peroxides," *Nat. Nanotechnol.*, vol. 1, no. 2, pp. 142–150, 2006.
- [3] M. Das, S. Patil, N. Bhargava, J. F. Kang, L. M. Riedel, S. Seal, and J. J. Hickman, "Auto-catalytic ceria nanoparticles offer neuroprotection to adult rat spinal cord neurons," *Biomaterials*, vol. 28, no. 10, pp. 1918–1925, 2007.
- [4] S. M. de Lima, A. M. Silva, U. M. Graham, G. Jacobs, B. H. Davis, L. V. Mattos, and F. B. Noronha, "Ethanol decomposition and steam reforming of ethanol over  $\text{CeZrO}_2$  and  $\text{Pt/CeZrO}_2$  catalyst: Reaction mechanism and deactivation," *Appl. Catal. A-Gen*, vol. 352, no. 1–2, pp. 95–113, 2009.
- [5] H. N. Evin, G. Jacobs, J. Ruiz-Martinez, U. M. Graham, A. Dozier, G. Thomas, and B. H. Davis, "Low temperature water-gas shift: The effect of alkali doping on the CH bond of formate over  $\text{Pt/ZrO}_2$  catalysts," *Catal. Lett.*, vol. 122, no. 1–2, pp. 9–19, 2007.
- [6] G. Jacobs, L. Williams, U. Graham, D. Sparks, and B. H. Davis, "Low-temperature water-gas shift: In-situ DRIFTS-reaction study of a  $\text{Pt/CeO}_2$  catalyst for fuel cell reformer applications," *J. Phys. Chem. B*, vol. 107, no. 38, pp. 10 398–10 404, 2003.

- [7] C. Korsvik, S. Patil, S. Seal, and W. T. Self, "Superoxide dismutase mimetic properties exhibited by vacancy engineered ceria nanoparticles," *Chem. Commun.*, no. 10, pp. 1056–1058, 2007.
- [8] E. P. Murray, T. Tsai, and S. A. Barnett, "A direct-methane fuel cell with a ceria-based anode," *Nature*, vol. 400, no. 6745, pp. 649–651, 1999.
- [9] J. M. Perez, A. Asati, S. Nath, and C. Kaittanis, "Synthesis of biocompatible dextran-coated nanoceria with pH-dependent antioxidant properties," *Small*, vol. 4, no. 5, pp. 552–556, 2008.
- [10] R. W. Tarnuzzer, J. Colon, S. Patil, and S. Seal, "Vacancy engineered ceria nanostructures for protection from radiation-induced cellular damage," *Nano Lett.*, vol. 5, pp. 2573–2577, 2005.
- [11] Z. Yang, K. Zhou, X. Liu, Q. Tian, D. Lu, and S. Yang, "Single-crystalline ceria nanocubes: size-controlled synthesis, characterization and redox property," *Nanotechnology*, vol. 18, p. 185606, 2007.
- [12] L. Yue and X. M. Zhang, "Texture stability of mesoporous ceria made from nanoparticles assembly," *Ceram. Int.*, vol. 35, pp. 847–853, 2009.
- [13] J. G. Park, T. Katoh, W. M. Lee, H. Jeon, and U. Paik, "Surfactant effect on oxide-to-nitride removal selectivity of nano-abrasive ceria slurry for chemical mechanical polishing," *Jpn. J. Appl. Phys., Part1*, vol. 42, pp. 5420–5425, 2003.
- [14] J. C. Summers and S. A. Ausen, "Interaction of cerium oxide with noble metals," *J. Catal.*, vol. 58, pp. 131–143, 1979.
- [15] G. Kim, "Ceria-promoted three-way catalysts for auto exhaust emission control," *Ind. Eng. Chem. Prod. Res. Dev.*, vol. 21, pp. 267–274, 1982.

- [16] S. P. Ray, A. S. Nowick, and D. E. Cox, "X-ray and neutron diffraction study of intermediate phases in nonstoichiometric cerium dioxide," *J. Solid State Chem.*, vol. 15, pp. 344–351, 1975.
- [17] M. Ricken, J. Nölting, and I. Riess, "Specific heat and phase diagram of non-stoichiometric ceria ( $\text{CeO}_{2-x}$ )," *J. Solid State Chem.*, vol. 54, pp. 89–99, 1984.
- [18] R. Körner, M. Ricken, J. Nölting, and I. Riess, "Phase transformations in reduced ceria: Determination by thermal expansion measurements," *J. Solid State Chem.*, vol. 78, pp. 136–147, 1989.
- [19] A. Laachir, V. Perrichon, A. Badri, J. Lamotte, E. Catherine, J. C. Lavalley, J. E. Fallah, L. Hilaire, F. Le Normand, E. Quéméré, G. N. Sauvion, and O. Touret, "Reduction of  $\text{CeO}_2$  by hydrogen. magnetic susceptibility and fourier-transform infrared, ultraviolet and X-ray photoelectron spectroscopy measurements," *J. Chem. Soc., Faraday Trans.*, vol. 87, pp. 1601–1609, 1991.
- [20] V. Perrichon, A. Laachir, G. Bergeret, L. Fréty, G. and Tournayan, and O. Touret, "Reduction of cerias with different textures by hydrogen and their reoxidation by oxygen," *J. Chem. Soc., Faraday Trans.*, vol. 90, pp. 773–781, 1994.
- [21] A. Trovarelli, "The utilization of ceria in industrial catalysis," *Catal. Today*, vol. 50, pp. 353–367, 1999.
- [22] H. C. Yao and Y. F. Yu Yao, "Ceria in automotive exhaust catalysts," *J. Catal.*, vol. 86, pp. 254–265, 1984.
- [23] M. Ozawa, M. Kimura, and A. Isogai, "The application of Ce-Zr oxide solid solution to oxygen storage promoters in automotive catalysts," *J. Alloys Compd.*, vol. 193, pp. 73–75, 1993.

- [24] F. Esch, S. Fabris, L. Zhou, T. Montini, C. Africh, P. Fornasiero, G. Comelli, and R. Rosei, “Electron localization determines defect formation on ceria substrates,” *Science*, vol. 309, no. 5735, pp. 752–755, 2005.
- [25] U. M. Graham, R. A. Khatri, D. A., G. Jacobs, and B. Davis, “3D ridge-valley structure of a Pt-ceria catalyst: HRTEM and EELS spectrum imaging,” *Catal. Lett.*, vol. 132, pp. 335–341, 2009.
- [26] Q. Yuan, H. H. Duan, L. L. Li, L. D. Sun, Y. W. Zhang, and C. H. Yan, “Controlled synthesis and assembly of ceria-based nanomaterials,” *J. Colloid. Interf. Sci.*, vol. 335, no. 2, pp. 151–167, 2009.
- [27] P. Burroughs, A. Hamnett, A. F. Orchard, and G. Thornton, “Satellite structure in the X-ray photoelectron spectra of some binary and mixed oxides of lanthanum and cerium,” *J. Chem. Soc., Dalton Trans.*, pp. 1686–1698, 1976.
- [28] F. Le Normand, L. Hilaire, K. Kili, G. Krill, and G. Maire, “Oxidation state of cerium in cerium-based catalysts investigated by spectroscopic probes,” *J. Phys. Chem.*, vol. 92, pp. 2561–2568, 1988.
- [29] D. Mullins, S. Overbury, and D. Huntley, “Electron spectroscopy of single crystal and polycrystalline cerium oxide surfaces,” *Surf. Sci.*, vol. 409, pp. 307–319, 1998.
- [30] C. Binet, M. Daturi, and J. C. Lavalley, “Ir study of polycrystalline ceria properties in oxidised and reduced states,” *Catal. Today*, vol. 50, pp. 207–225, 1999.
- [31] G. Praline, B. E. Koel, R. L. Hance, H. I. Lee, and J. M. White, “X-ray photoelectron study of the reaction of oxygen with cerium,” *J. Electron Spectrosc. Relat. Phenom.*, vol. 21, pp. 17–30, 1980.

- [32] T. X. T. Sayle, S. Parker, and C. R. A. Catlow, "The role of oxygen vacancies on ceria surfaces in the oxidation of carbon monoxide," *Surf. Sci.*, vol. 316, pp. 329–336, 1994.
- [33] J. C. Conesa, "Computer modeling of surfaces and defects on cerium dioxide," *Surf. Sci.*, vol. 339, pp. 337–352, 1995.
- [34] H. Cordatos, D. Ford, and R. J. Gorte, "Simulated annealing study of the structure and reducibility in ceria clusters," *J. Phys. Chem.*, vol. 100, pp. 18 128–18 132, 1996.
- [35] S. Vyas, R. W. Grimes, D. H. Gay, and A. L. Rohl, "Structure, stability and morphology of stoichiometric ceria crystallites," *J. Chem. Soc., Faraday Trans.*, vol. 94, pp. 427–434, 1998.
- [36] A. Migani, K. M. Neyman, F. Illas, and S. T. Bromley, "Exploring  $\text{Ce}^{3+}/\text{Ce}^{4+}$  cation ordering in reduced ceria nanoparticles using interionic-potential and density-functional calculations," *J. Chem. Phys.*, vol. 131, no. 6, p. 064701, 2009.
- [37] E. H. Teunissen, A. P. J. Jansen, R. A. van Santen, R. Orlando, and R. Dovesi, "Adsorption energies of  $\text{NH}_3$  and  $\text{NH}_4^+$  in zeolites corrected for the longrange electrostatic potential of the crystal," *J. Chem. Phys.*, vol. 101, pp. 5865–5874, 1994.
- [38] M. A. Nygren and L. G. M. Pettersson, " $\text{H}_2\text{O}$  interaction with the polar  $\text{Cu}_2\text{O}$  (100) surface: a theoretical study," *J. Phys. Chem.*, vol. 100, pp. 1874–1878, 1996.
- [39] A. Redlack and J. Grindlay, "Coulombic potential lattice sums," *J. Phys. Chem. Solids*, vol. 36, pp. 73–82, 1975.

- [40] A. M. Burow, M. Sierka, J. Dobler, and J. Sauer, “Point defects in  $\text{CaF}_2$  and  $\text{CeO}_2$  investigated by the periodic electrostatic embedded cluster method,” *J. Chem. Phys.*, vol. 130, no. 17, p. 174710, 2009.
- [41] K. N. Kudin and G. E. Scuseria, “Revisiting infinite lattice sums with the periodic fast multipole method,” *J. Chem. Phys.*, vol. 121, pp. 2886–2890, 2004.
- [42] C. A. Whitem and M. Head-Gordon, “Derivation and efficient implementation of the fast multipole method,” *J. Chem. Phys.*, vol. 101, pp. 6593–6605, 1994.
- [43] C. Müller, C. Freysoldt, M. Baudin, and K. Hermansson, “An ab initio study of CO adsorption on ceria (110),” *Chem. Phys.*, vol. 318, pp. 180–190, 2005.
- [44] B. Herschend, M. Baudin, and K. Hermansson, “Electronic structure of the  $\text{CeO}_2$  (110) surface oxygen vacancy,” *Surf. Sci.*, vol. 599, pp. 173–186, 2005.
- [45] ———, “CO adsorption on  $\text{CeO}_2$  (110) using hybrid-DFT embedded-cluster calculations,” *Chem. Phys.*, vol. 328, pp. 345–353, 2006.
- [46] C. Müller and K. Hermansson, “Assessment methods for embedding schemes – ceria as an example,” *Surf. Sci.*, vol. 603, pp. 3329–3338, 2009.
- [47] J. C. Conesa, “Surface anion vacancies on ceria: Quantum modelling of mutual interactions and oxygen adsorption,” *Catal. Today*, vol. 143, pp. 315–325, 2009.
- [48] M. Fronzi, S. Piccinin, B. Delley, E. Traversa, and C. Stampfl, “Water adsorption on the stoichiometric and reduced  $\text{CeO}_2$  (111) surface: a first-principles investigation,” *Phys. Chem. Chem. Phys.*, vol. 11, pp. 9188–9199, 2009.
- [49] M. V. Ganduglia-Pirovano, J. L. F. Da Silva, and J. Sauer, “Density-functional calculations of the structure of near-surface oxygen vacancies and electron localization on  $\text{CeO}_2$  (111),” *Phys. Rev. Lett.*, vol. 102, p. 026101, 2009.

- [50] S. Gennard, F. Corà, , and C. R. A. Catlow, “Comparison of the bulk and surface properties of ceria and zirconia by ab initio investigations,” *J. Phys. Chem. B*, vol. 103, pp. 10 158–10 170, 1999.
- [51] N. V. Skorodumova, R. Ahuja, S. I. Simak, I. A. Abrikosov, B. Johansson, and B. I. Lundqvist, “Electronic, bonding, and optical properties of  $\text{CeO}_2$  and  $\text{Ce}_2\text{O}_3$  from first principles,” *Phys. Rev. B*, vol. 64, p. 115108, 2001.
- [52] N. V. Skorodumova, S. I. Simak, B. I. Lundqvist, I. A. Abrikosov, and B. Johansson, “Quantum origin of the oxygen storage capability of ceria,” *Phys. Rev. Lett.*, vol. 89, p. 166601, 2002.
- [53] J. C. Conesa, “Computer modeling of local level structures in (Ce, Zr) mixed oxide,” *J. Phys. Chem. B*, vol. 107, pp. 8840–8853, 2003.
- [54] N. V. Skorodumova, M. Baudin, and K. Hermansson, “Surface properties of  $\text{CeO}_2$  from first principles,” *Phys. Rev. B*, vol. 69, p. 075401, 2004.
- [55] Z. Yang, T. K. Woo, M. Baudin, and K. Hermansson, “Atomic and electronic structure of unreduced and reduced  $\text{CeO}_2$  surfaces: A first-principles study,” *J. Chem. Phys.*, vol. 120, pp. 7741–7749, 2004.
- [56] D. A. Andersson, S. I. Simak, B. Johansson, I. A. Abrikosov, and N. V. Skorodumova, “Modeling of  $\text{CeO}_2$ ,  $\text{Ce}_2\text{O}_3$ , and  $\text{CeO}_{2x}$  in the LDA+U formalism,” *Phys. Rev. B*, vol. 75, p. 035109, 2007.
- [57] V. I. Anisimov, J. Zaanen, and O. K. Andersen, “Band theory and Mott insulators: Hubbard U instead of Stoner I,” *Phys. Rev. B*, vol. 44, pp. 943–954, 1991.
- [58] J. P. Perdew, M. Ernzerhof, and K. Burke, “Rationale for mixing exact exchange with density functional approximations,” *J. Chem. Phys.*, vol. 105, pp. 9982–9985, 1996.

- [59] P. J. Hay, R. L. Martin, J. Uddin, and G. E. Scuseria, “Theoretical study of  $\text{CeO}_2$  and  $\text{Ce}_2\text{O}_3$  using a screened hybrid density functional,” *J. Chem. Phys.*, vol. 125, p. 034712, 2006.
- [60] J. L. F. Da Silva, M. V. Ganduglia-Pirovano, J. Sauer, V. Bayer, and G. Kresse, “Hybrid functionals applied to rare-earth oxides: The example of ceria,” *Phys. Rev. B*, vol. 75, p. 045121, 2007.
- [61] S. L. Dudarev, G. A. Botton, S. Y. Savrasov, C. J. Humphreys, and A. P. Sutton, “Electron-energy-loss spectra and the structural stability of nickel oxide: An LSDA+U study,” *Phys. Rev. B*, vol. 57, pp. 1505–1509, 1998.
- [62] C. Loschen, J. Carrasco, K. M. Neyman, and F. Illas, “First-principles LDA+U and GGA+U study of cerium oxides: Dependence on the effective U parameter,” *Phys. Rev. B*, vol. 75, p. 035115, 2007.
- [63] M. Cococcioni and S. de Gironcoli, “Linear response approach to the calculation of the effective interaction parameters in the LDA+U method,” *Phys. Rev. B*, vol. 71, p. 035105, 2005.
- [64] Y. Jiang, J. B. Adams, and M. van Schilfhaarde, “Density-functional calculation of  $\text{CeO}_2$  surfaces and prediction of effects of oxygen partial pressure and temperature on stabilities,” *J. Chem. Phys.*, vol. 123, p. 064701, 2005.
- [65] C. W. Castleton, J. Kullgren, and K. Hermansson, “Tuning LDA+U for electron localization and structure at oxygen vacancies in ceria,” *J. Chem. Phys.*, vol. 127, p. 244704, 2007.
- [66] M. Nolan, S. Grigoleit, D. C. Sayle, S. C. Parker, and G. W. Watson, “Density functional theory studies of the structure and electronic structure of pure and defective low index surfaces of ceria,” *Surf. Sci.*, vol. 576, pp. 217–229, 2005.



- [67] J. F. Herbst, R. E. Watson, and J. W. Wilkins, “Relativistic calculations of 4f excitation energies in the rare-earth metals: Further results,” *Phys. Rev. B*, vol. 17, pp. 3089–3098, 1978.
- [68] V. I. Anisimov and O. Gunnarsson, “Density-functional calculation of effective coulomb interactions in metals,” *Phys. Rev. B*, vol. 43, pp. 7570–7574, 1991.
- [69] I. V. Solovyev and P. H. Dederichs, “Ab initio calculations of Coulomb U parameters for transition-metal impurities,” *Phys. Rev. B*, vol. 49, pp. 6736–6740, 1994.
- [70] M. Nolan, S. C. Parker, and G. W. Watson, “The electronic structure of oxygen vacancy defects at the low index surfaces of ceria,” *Surf. Sci.*, vol. 595, pp. 223–232, 2005.
- [71] ———, “Reduction of NO<sub>2</sub> on ceria surfaces,” *J. Phys. Chem. B*, vol. 110, pp. 2256–2262, 2006.
- [72] Z. Yang, G. Luo, Z. Lu, and K. Hermansson, “Oxygen vacancy formation energy in Pd-doped ceria: A DFT+U study,” *J. Chem. Phys.*, vol. 127, p. 074704, 2007.
- [73] Z. Yang, Z. Lu, G. Luo, and K. Hermansson, “Oxygen vacancy formation energy at the Pd/CeO<sub>2</sub> (111) interface,” *Phys. Lett. A*, vol. 369, pp. 132–139, 2007.
- [74] S. Lutfalla, V. Shapovalov, and A. T. Bell, “Calibration of the DFT/GGA+U method for determination of reduction energies for transition and rare earth metal oxides of Ti, V, Mo, and Ce,” *J. Chem. Theory Comput.*, vol. 7, pp. 2218–2223, 2011.
- [75] T. X. T. Sayle, S. Parker, and C. R. A. Catlow, “Surface oxygen vacancy formation on CeO<sub>2</sub> and its role in the oxidation of carbon-monoxide,” *J. Chem. Soc., Chem. Commun.*, vol. 14, pp. 997–998, 1992.

- [76] M. Baudin, M. Wójcik, and K. Hermansson, “Dynamics, structure and energetics of the (111), (011) and (001) surfaces of ceria,” *Surf. Sci.*, vol. 468, pp. 51–61, 2000.
- [77] A. Gotte, K. Hermansson, and M. Baudin, “Molecular dynamics simulations of reduced CeO<sub>2</sub>: bulk and surfaces,” *Surf. Sci.*, vol. 552, pp. 273–280, 2004.
- [78] Z. Yang, T. K. Woo, and K. Hermansson, “Strong and weak adsorption of CO on CeO<sub>2</sub> surfaces from first principles calculations,” *Chem. Phys. Lett.*, vol. 396, pp. 384–392, 2004.
- [79] S. Fabris, G. Vicario, G. Balducci, S. de Gironcoli, and S. Baroni, “Electronic and atomistic structures of clean and reduced ceria surfaces,” *J. Phys. Chem. B*, vol. 109, pp. 22 860–22 867, 2005.
- [80] S. Kumar and P. K. Schelling, “An ab initio study of CO adsorption on ceria (110),” *J. Chem. Phys.*, vol. 125, p. 204704, 2006.
- [81] M. Nolan, S. C. Parker, and G. W. Watson, “CeO<sub>2</sub> catalysed conversion of CO, NO<sub>2</sub> and NO from first principles energetics,” *Phys. Chem. Chem, Phys.*, vol. 8, pp. 216–218, 2006.
- [82] D. H. Mei, N. A. Deskins, M. Dupuis, and Q. F. Ge, “Methanol adsorption on the clean CeO<sub>2</sub> (111) surface: A density functional theory study,” *J. Phys. Chem. C*, vol. 111, pp. 10 514–10 522, 2007.
- [83] D. H. Mei, N. A. Deskins, and M. Dupuis, “A density functional theory study of formaldehyde adsorption on ceria,” *Surf. Sci.*, vol. 601, pp. 4993–5001, 2007.
- [84] H. T. Chen, Y. M. Choi, M. L. Liu, and M. C. Lin, “A first-principles analysis for sulfur tolerance of CeO<sub>2</sub> in solid oxide fuel cells,” *J. Phys. Chem. C*, vol. 111, pp. 11 117–11 122, 2007.

- [85] ———, “A theoretical study of surface reduction mechanisms of  $\text{CeO}_2$  (111) and (110) by  $\text{H}_2$ ,” *Chem. Phys. Chem.*, vol. 8, pp. 849–855, 2007.
- [86] M. Huang and S. Fabris, “Role of surface peroxo and superoxo species in the low-temperature oxygen buffering of ceria: Density functional theory calculations,” *Phys. Rev. B*, vol. 75, p. 081404, 2007.
- [87] S. Torbrügge, M. Reichling, A. Ishiyama, S. Morita, and O. Custance, “Evidence of subsurface oxygen vacancy ordering on reduced  $\text{CeO}_2$  (111),” *Phys. Rev. Lett.*, vol. 99, p. 056101, 2007.
- [88] M. B. Watkins, A. S. Foster, and A. L. Shluger, “Hydrogen cycle on  $\text{CeO}_2$  (111) surfaces: density functional theory calculations,” *J. Phys. Chem. C*, vol. 111, pp. 15 337–15 341, 2007.
- [89] D. R. Beste, A. and Mullins, S. H. Overbury, and R. J. Harrison, “Adsorption and dissociation of methanol on the fully oxidized and partially reduced (111) cerium oxide surface: Dependence on the configuration of the cerium 4f electrons,” *Surf. Sci.*, vol. 602, pp. 162–175, 2008.
- [90] M. Huang and F. Stefano, “CO adsorption and oxidation on ceria surfaces from DFT+U calculations,” *J. Phys. Chem. C*, vol. 112, pp. 8643–8648, 2008.
- [91] M. M. Branda, C. Loschen, M. K. Neyman, and F. Illas, “Atomic and electronic structure of cerium oxide stepped model surfaces,” *J. Phys. Chem. C*, vol. 112, pp. 17 643–17 651, 2008.
- [92] D. Knapp and T. Ziegler, “Methane dissociation on the ceria (111) surface,” *J. Phys. Chem. C*, vol. 112, pp. 17 311–17 318, 2008.
- [93] A. D. Mayernick and M. J. Janik, “Methane activation and oxygen vacancy formation over  $\text{CeO}_2$  and Zr, Pd substituted  $\text{CeO}_2$  surfaces,” *J. Phys. Chem. C*, vol. 112, pp. 14 955–14 964, 2008.

- [94] D. H. Mei, N. A. Deskins, M. Dupuis, and Q. F. Ge, “Density functional theory study of methanol decomposition on the CeO<sub>2</sub> (110) surface,” *J. Phys. Chem. C*, vol. 112, pp. 4257–4266, 2008.
- [95] H. T. Chen, J. G. Chang, H. L. Chen, and S. P. Ju, “Identifying the O<sub>2</sub> diffusion and reduction mechanisms on CeO<sub>2</sub> electrolyte in solid oxide fuel cells: A DFT+U study,” *J. Comput. Chem.*, vol. 30, pp. 2433–2442, 2009.
- [96] M. Fronzi, A. Soon, B. Delley, E. Traversa, and C. Stampfl, “Stability and morphology of cerium oxide surfaces in an oxidizing environment: A first-principles investigation,” *J. Chem. Phys.*, vol. 131, p. 104701, 2009.
- [97] W. O. Gordon, Y. Xu, D. R. Mullins, and S. H. Overbury, “Temperature evolution of structure and bonding of formic acid and formate on fully oxidized and highly reduced CeO<sub>2</sub> (111),” *Phys. Chem. Chem. Phys.*, vol. 11, pp. 11 171–11 183, 2009.
- [98] Z. X. Yang, X. H. Yua, Z. S. Lu, S. F. Li, and K. Hermansson, “Oxygen vacancy pairs on CeO<sub>2</sub> (110): A DFT+U study,” *Phys. Lett. A*, vol. 373, pp. 2786–2792, 2009.
- [99] C. Zhang, A. Michaelides, D. A. King, and S. J. Jenkins, “Oxygen vacancy clusters on ceria: Decisive role of cerium f electrons,” *Phys. Rev. B*, vol. 79, p. 075433, 2009.
- [100] B. T. Teng, S. Y. Jiang, Z. X. Yang, M. F. Luo, and Y. Z. Lan, “A density functional theory study of formaldehyde adsorption and oxidation on CeO<sub>2</sub> (111) surface,” *Surf. Sci.*, vol. 604, pp. 68–78, 2009.
- [101] M. M. Branda, R. M. Ferullo, M. Causá, and F. Illas, “Relative stabilities of low index and stepped CeO<sub>2</sub> surfaces from hybrid and GGA+U implementations of density functional theory,” *J. Phys. Chem. C*, vol. 115, pp. 3716–3721, 2011.

- [102] H. Y. Li, H. F. Wang, Y. L. Guo, G. Z. Lu, and P. Hu, “Exchange between sub-surface and surface oxygen vacancies on  $\text{CeO}_2$  (111): a new surface diffusion mechanism,” *Chem. Commun.*, vol. 47, pp. 6105–6107, 2011.
- [103] F. Chen, D. Liu, J. Zhang, P. Hu, X. Q. Gong, and G. Z. Lu, “A DFT+U study of the lattice oxygen reactivity toward direct CO oxidation on the  $\text{CeO}_2$  (111) and (110) surfaces,” *Phys. Chem. Chem. Phys.*, vol. 14, pp. 16 573–16 580, 2012.
- [104] T. Désaunay, A. Ringuedé, M. Cassir, F. Labat, and C. Adamo, “Modeling basic components of solid oxide fuel cells using density functional theory: Bulk and surface properties of  $\text{CeO}_2$ ,” *Surf. Sci.*, vol. 606, pp. 305–311, 2012.
- [105] T. X. T. Sayle, S. C. Parker, and D. C. Sayle, “Shape of  $\text{CeO}_2$  nanoparticles using simulated amorphisation and recrystallisation,” *Chem. Commun.*, pp. 2438–2439, 2004.
- [106] X. Feng, D. C. Sayle, Z. L. Wang, M. S. Paras, B. Santora, A. C. Sutorik, T. X. T. Sayle, Y. Yang, Y. Ding, X. Wang, and Y. S. Her, “Converting ceria polyhedral nanoparticles into single-crystal nanospheres,” *Science*, vol. 312, pp. 1504–1508, 2006.
- [107] S. Tsunekawa, J. T. Wang, and Y. Kawazoe, “Lattice constants and electron gap energies of nano- and subnano-sized cerium oxides from the experiments and first-principles calculations,” *J. Alloys Compd.*, vol. 408-412, pp. 1145–1148, 2006.
- [108] S. F. Li, H. Lu, P. Li, Z. Yang, and Z. X. Guo, “First-principles local density approximation (generalized gradient approximation)+U study of catalytic  $\text{Ce}_n\text{O}_m$  clusters: U value differs from bulk,” *J. Chem. Phys.*, vol. 128, no. 16, p. 164718, 2008.

- [109] J. Zhang, Z. Fu, Z. Yang, and S. Li, "The highly active Ce<sub>4</sub>O<sub>8</sub> nanoparticle for CO oxidation," *Phys. Lett. A*, vol. 376, no. 45, pp. 3235–3240, 2012.
- [110] H. L. Chen, M. H. Weng, S. P. Ju, J. G. Chang, H. T. Chen, and C. S. Chang, "Structural and electronic properties of Ce<sub>n</sub>O<sub>2n</sub> (n = 15) nanoparticles: A computational study," *J. Mol. Struct.*, vol. 963, no. 1, pp. 2–8, 2010.
- [111] R. Parr and W. Yang, "Density functional approach to the frontier-electron theory of chemical reactivity," *J. Am. Chem. Soc.*, vol. 106, pp. 4049–4050, 1984.
- [112] C. Loschen, S. T. Bromley, K. M. Neyman, and F. Illas, "Understanding ceria nanoparticles from first-principles calculations," *J. Phys. Chem. C*, vol. 111, pp. 10 142–10 145, 2007.
- [113] C. Loschen, A. Migani, S. T. Bromley, F. Illas, and K. M. Neyman, "Density functional studies of model cerium oxide nanoparticles," *Phys. Chem. Chem. Phys.*, vol. 10, pp. 5730–5738, 2008.
- [114] Z. L. Wang and X. Feng, "Polyhedral shapes of CeO<sub>2</sub> nanoparticles," *J. Phys. Chem. B*, vol. 107, pp. 13 563–13 566, 2003.
- [115] F. Zhang, Q. Jin, and S. W. Chan, "Ceria nanoparticles: Size, size distribution, and shape," *J. Appl. Phys.*, vol. 95, pp. 4319–4326, 2004.
- [116] A. Migani, C. Loschen, F. Illas, and K. M. Neyman, "Towards size-converged properties of model ceria nanoparticles: Monitoring by adsorbed CO using DFT+U approach," *Chem. Phys. Lett.*, vol. 465, pp. 106–109, 2008.
- [117] T. M. Inerbaev, S. Seal, and A. E. Masunov, "Density functional study of oxygen vacancy formation and spin density distribution in octahedral ceria nanoparticles," *J. Mol. Model*, vol. 16, no. 10, pp. 1617–1623, 2010.

- [118] A. Migani, G. N. Vayssilov, S. T. Bromley, F. Illas, and K. M. Neyman, “Greatly facilitated oxygen vacancy formation in ceria nanocrystallites,” *Chem. Commun.*, vol. 46, no. 32, pp. 5936–5938, 2010.
- [119] —, “Dramatic reduction of the oxygen vacancy formation energy in ceria particles: a possible key to their remarkable reactivity at the nanoscale,” *J. Mater. Chem.*, vol. 20, no. 46, pp. 10 535–10 546, 2010.
- [120] A. Migani, K. M. Neyman, and S. T. Bromley, “Octahedrality versus tetrahedrality in stoichiometric ceria nanoparticles,” *Chem. Commun.*, vol. 48, no. 35, pp. 4199–4201, 2012.
- [121] M. Zawadzki, “Preparation and characterization of ceria nanoparticles by microwave-assisted solvothermal process,” *J. Alloys Compd.*, vol. 454, pp. 347–351, 2008.
- [122] M. L. Dos Santos, R. C. Lima, C. S. Riccardi, R. L. Tranquilin, P. R. Bueno, J. A. Varela, and E. Longo, “Preparation and characterization of ceria nanospheres by microwave-hydrothermal method,” *Mater. Lett.*, vol. 62, pp. 4509–4511, 2008.
- [123] M. Molinari, S. S. Parker, D. C. Sayle, and M. S. Islam, “Water adsorption and its effect on the stability of low index stoichiometric and reduced surfaces of ceria,” *J. Phys. Chem. C*, vol. 116, pp. 7073–7082, 2012.
- [124] B. H. Wang, P. Wu, R. A. Yokel, and E. A. Grulke, “Influence of surface charge on lysozyme adsorption to ceria nanoparticles,” *Appl. Surf. Sci.*, vol. 258, pp. 5332–5341, 2012.
- [125] T. Shimada, K. Aoki, Y. Shinoda, T. Nakamura, N. Tokunaga, S. Inagaki, and T. Hayashi, “Functionalization on silica gel with allylsilanes. a new method of

- covalent attachment of organic functional groups on silica gel,” *J. Am. Chem. Soc.*, vol. 125, pp. 4688–4689, 2003.
- [126] W. Calleja, C. Falcony, A. Torres, M. Aceves, and R. Osorio, “Optical properties of non-stoichiometric  $\text{SiO}_2$  as a function of excess silicon content and thermal treatments,” *Thin Solid Films*, vol. 270, pp. 114–117, 1995.
- [127] W. O. R. Horacio and E. Bergna, *Colloidal silica: fundamentals and applications*. London, New York: CRC Press, Taylor & Francis Group, 2006.
- [128] V. Kanniah, B. H. Wang, Y. Yang, and E. A. Grulke, “Graphite functionalization for dispersion in a two-phase lubricant oligomer mixture,” *J. Appl. Polym. Sci.*, vol. 125, pp. 165–174, 2012.
- [129] L. Chen, P. Fleming, V. Morris, J. D. Holmes, and M. A. Morris, “Size-related lattice parameter changes and surface defects in ceria nanocrystals,” *J. Phys. Chem. C*, vol. 114, pp. 12 909–12 919, 2007.
- [130] T. X. T. Sayle, S. C. Parker, and D. C. Sayle, “Oxidising CO to  $\text{CO}_2$  using ceria nanoparticles,” *Phys. Chem. Chem. Phys.*, vol. 7, pp. 2936–2941, 2005.
- [131] D. Valechha, S. Lokhande, M. Klementova, J. Subrt, S. Rayalua, and N. Labhsetwar, “Study of nano-structured ceria for catalytic CO oxidation,” *J Mater. Chem.*, vol. 21, pp. 3718–3725, 2011.
- [132] Z. X. Yang, Z. M. Fu, Y. N. Zhang, and R. Q. Wu, “Direct CO oxidation by lattice oxygen on Zr-doped ceria surfaces,” *Catal. Lett.*, vol. 141, pp. 78–82, 2011.
- [133] N. J. Lawrence, J. R. Brewer, L. Wang, T. S. Wu, J. Wells-Kingsbury, M. M. Ihrig, G. H. Wang, Y. L. Soo, W. N. Mei, and C. L. Cheun, “Defect engineering in cubic cerium oxide nanostructures for catalytic oxidation,” *Nano Lett.*, vol. 11, pp. 2666–2671, 2011.



- [134] C. Ho, C. Y. Jimmy, K. Tszyan, C. M. Angelo, and L. Sukyin, “Morphology-controllable synthesis of mesoporous CeO<sub>2</sub> nano- and microstructures,” *Chem. Mater.*, vol. 17, pp. 4514–4522, 2005.
- [135] D. E. Zhang, X. J. Zhang, X. M. Ni, J. M. Song, and H. G. Zheng, “Fabrication of novel threefold shape CeO<sub>2</sub> dendrites: Optical and electrochemical properties,” *Chem. Phys. Lett.*, vol. 430, pp. 326–329, 2006.
- [136] C. Pana, D. Zhang, and L. Shi, “CTAB assisted hydrothermal synthesis, controlled conversion and CO oxidation properties of CeO<sub>2</sub> nanoplates, nanotubes, and nanorods,” *J. Solid State Chem.*, vol. 181, pp. 1298–1306, 2008.
- [137] X. S. Huang, H. Sun, L. C. Wang, Y. M. Liu, K. N. Fan, and Y. Cao, “Morphology effects of nanoscale ceria on the activity of Au/CeO<sub>2</sub> catalysts for low-temperature CO oxidation,” *Appl. Catal. B*, vol. 90, pp. 224–2941, 2009.
- [138] W. Shan, X. Dong, N. Ma, S. Yao, and Z. Feng, “The synthesis of three-dimensional CeO<sub>2</sub> and their catalytic activities for CO oxidation,” *Catal. Lett.*, vol. 131, pp. 350–355, 2009.
- [139] L. González-Rovira, J. M. Sánchez-Amaya, M. López-Haro, E. del Rio, A. B. Hungria, P. Midgley, J. J. Calvino, S. Bernal, and F. J. Botana, “Single-step process to prepare CeO<sub>2</sub> nanotubes with improved catalytic activity,” *Nano Lett.*, vol. 9, pp. 1395–1400, 2009.
- [140] C. Rhodes, G. J. Hutchings, and A. M. Ward, “Water-gas shift reaction: finding the mechanistic boundary,” *Catal. Today*, vol. 23, pp. 43–58, 1995.
- [141] C. Ratnasamy and J. P. Wagner, “Water gas shift catalysis,” *Catal. Rev. Sci. Eng.*, vol. 51, pp. 325–440, 2009.

- [142] E. F. Armstrong and T. P. Hilditch, "A study of catalytic actions at solid surfaces. iv. the interaction of carbon monoxide and steam as conditioned by iron oxide and by copper," *Proc. Roy. Soc. A*, vol. 97, pp. 265–273, 1920.
- [143] R. Mezaki and S. Oki, "Locus of the change in the rate-determining step," *J. Catal.*, vol. 30, pp. 488–489, 1973.
- [144] S. Hilaire, X. Wang, T. Luo, R. Gorte, and J. Wagner, "A comparative study of water-gas-shift reaction over ceria supported metallic catalysts," *Appl. Catal. A*, vol. 215, pp. 271–278, 2001.
- [145] M. C. Ribeiro, G. Jacobs, L. Lingniso, K. G. Azzam, U. M. Graham, and B. H. Davis, "Low temperature water gas shift: Evaluation of Pt/HfO<sub>2</sub> and correlation between reaction mechanism and periodic trends in tetravalent (Ti, Zr, Hf, Ce, Th) metal oxides," *ACS Catal.*, vol. 1, pp. 1375–1383, 2011.
- [146] R. Burch, "Gold catalysts for pure hydrogen production in the watergas shift reaction: Activity, structure and reaction mechanism," *Phys. Chem. Chem. Phys.*, vol. 8, pp. 5483–5500, 2006.
- [147] R. Leppelt, B. Schumacher, V. Plzak, M. Kinne, and R. J. Behm, "Kinetics and mechanism of the low-temperature watergas shift reaction on Au/CeO<sub>2</sub> catalysts in an idealized reaction atmosphere," *J. Catal.*, vol. 244, pp. 137–152, 2006.
- [148] P. O. Graf, D. M. de Vlieger, B. L. Mojet, and L. Lefferts, "New insights in reactivity of hydroxyl groups in water gas shift reaction on Pt/ZrO<sub>2</sub>," *J. Catal.*, vol. 262, pp. 181–187, 2009.
- [149] C. M. Kalamaras, P. Panagiotopoulou, D. I. Kondarides, and A. M. Efstathiou, "Kinetic and mechanistic studies of the water-gas shift reaction on Pt/TiO<sub>2</sub> catalyst," *J. Catal.*, vol. 264, pp. 117–129, 2010.

- [150] J. B. Park, J. Graciani, J. Evans, D. Stacchiola, S. D. Senanayake, L. Barrio, P. Liu, J. F. Sanz, J. Hrbek, and J. A. Rodriguez, “Gold, copper, and platinum nanoparticles dispersed on  $\text{CeO}_x/\text{TiO}_2$  (110) surfaces: High water-gas shift activity and the nature of the mixed-metal oxide at the nanometer level,” *J. Am. Chem. Soc.*, vol. 132, pp. 356–363, 2010.
- [151] C. M. Kalamaras, I. D. Gonzalez, R. M. Navarro, J. L. G. Fierro, and A. M. Efstathiou, “Effects of reaction temperature and support composition on the mechanism of water-gas shift reaction over supported-pt catalysts,” *J. Phys. Chem. C*, vol. 115, pp. 11 595–11 610, 2011.
- [152] J. Vecchietti, S. Collins, J. J. Delgado, M. Malecka, E. del Rio, X. W. Chen, S. Bernal, and A. Bonivardi, “Gold catalysts supported on ceriumgallium mixed oxide for the carbon monoxide oxidation and water gas shift reaction,” *Top. Catal.*, vol. 54, pp. 201–209, 2011.
- [153] D. Mendes, V. Chibante, A. Mendes, and L. M. Madeira, “Determination of the low-temperature water-gas shift reaction kinetics using a Cu-based catalyst,” *Ind. Eng. Chem. Res.*, vol. 49, pp. 11 269–11 279, 2010.
- [154] P. Liu, “Water-gas shift reaction on oxide/Cu (111): Rational catalyst screening from density functional theory,” *J. Chem. Phys.*, vol. 133, p. 204705, 2010.
- [155] X. M. Liu, Z. M. Ni, P. Yao, Q. Xu, J. H. Mao, and Q. Q. Wang, “Comparison of three reaction mechanisms for the water gas shift feaction on Au (111) surface,” *Acta Phys.-Chim. Sin.*, vol. 26, pp. 1599–1606, 2010.
- [156] J. A. Rodriguez, J. Evans, J. Graciani, J. B. Park, P. Liu, J. Hrbek, and J. Fdez Sanz, “High water-gas shift activity in  $\text{TiO}_2$  (110) supported Cu and Au nanoparticles: Role of the oxide and metal particle size,” *J. Phys. Chem. C*, vol. 113, pp. 7364–7370, 2009.

- [157] S. F. Peng and J. J. Ho, "The mechanism of the water-gas shift reaction on Cu/TiO<sub>2</sub> (110) elucidated from application of density-functional theory," *Phys. Chem. Chem. Phys.*, vol. 13, pp. 20 393–20 400, 2011.
- [158] K. G. Azzam, I. Babich, K. Seshan, and L. Lefferts, "Bifunctional catalysts for single-stage watergas shift reaction in fuel cell applications.: Part 1. effect of the support on the reaction sequence," *J. Catal.*, vol. 251, p. 153, 2007.
- [159] Y. Li, Q. Fu, and M. Flytzani-Stephanopoulos, "Low-temperature water-gas shift reaction over Cu- and ni-loaded cerium oxide catalysts," *Appl. Catal. B*, vol. 27, pp. 179–191, 2000.
- [160] W. Deng and M. Flytzani-Stephanopoulos, "On the issue of the deactivation of Au-ceria and Pt-ceria water-gas shift catalysts in practical fuel-cell applications," *Angew. Chem., Int. Ed.*, vol. 45, pp. 2285–2289, 2006.
- [161] J. Lamotte, J. Lavalley, D. Druet, and E. Freund, "Infrared study of acidbase properties of thorium dioxide," *J Chem. Soc. Faraday Trans.*, vol. 79, pp. 2219–2227, 1983.
- [162] J. Kondo, Y. Sakata, K. Domen, K. Maruya, and T. Onishi, "Infrared study of hydrogen adsorbed on ZrO<sub>2</sub>," *J Chem. Soc. Faraday Trans.*, vol. 86, pp. 397–401, 1990.
- [163] T. Shido and Y. Iwasawa, "Regulation of reaction intermediate by reactant in the water-gas shift reaction on CeO<sub>2</sub>, in relation to reactant-promoted mechanism," *J. Catal.*, vol. 136, pp. 493–503, 1992.
- [164] G. Jacobs, P. M. Patterson, U. Graham, D. Sparks, and B. Davis, "Low temperature water-gas shift: kinetic isotope effect observed for decomposition of surface formates for Pt/ceria catalysts," *Appl. Catal. A*, vol. 269, pp. 63–73, 2004.

- [165] G. Jacobs, U. M. Graham, E. Chenu, P. M. Patterson, D. A., and B. Davis, “Low-temperature water-gas shift: impact of Pt promoter loading on the partial reduction of ceria and consequences for catalyst design,” *J. Catal.*, vol. 229, pp. 499–512, 2005.
- [166] E. Chenu, G. Jacobs, A. Crawford, R. Keogh, P. Patterson, D. Sparks, and B. Davis, “Water-gas shift: an examination of Pt promoted Mgo and tetragonal and monoclinic  $\text{ZrO}_2$  by in situ drifts,” *Appl. Catal. B*, vol. 59, pp. 45–56, 2005.
- [167] H. Cordatos, T. Bunluesin, J. Stubenrauch, J. M. Vohs, and R. J. Gorte, “Effect of ceria structure on oxygen migration for Rh/ceria catalysts,” *J. Phys. Chem.*, vol. 100, pp. 785–789, 1996.
- [168] T. Bunluesin, R. J. Gorte, and G. W. Graham, “Studies of the water-gas-shift reaction on ceria-supported Pt, Pd, and Rh: Implications for oxygen-storage properties,” *Appl. Catal. B*, vol. 15, pp. 107–114, 1998.
- [169] Q. Fu, A. Weber, and M. Flytzani-Stephanopoulos, “Nanostructured  $\text{AuCeO}_2$  catalysts for low-temperature water-gas shift,” *Catal. Lett.*, vol. 77, pp. 87–95, 2001.
- [170] Q. Fu, H. Saltsburg, and M. Flytzani-Stephanopoulos, “Active nonmetallic Au and Pt species on ceria-based water-gas shift catalysts,” *Science*, vol. 301, pp. 935–938, 2003.
- [171] T. Shido and Y. Iwasawa, “Reactant-promoted reaction mechanism for water-gas shift reaction on Rh-doped  $\text{CeO}_2$ ,” *J. Catal.*, vol. 141, pp. 71–81, 1993.
- [172] Y. Chen, J. Cheng, P. Hu, and H. F. Wang, “Examining the redox and formate mechanisms for water-gas shift reaction on  $\text{Au/CeO}_2$  using density functional theory,” *Surf. Sci.*, vol. 602, pp. 2828–2834, 2008.

- [173] G. Jacobs, L. Williams, U. Graham, G. A. Thomas, D. E. Sparks, and B. H. Davis, “Low temperature water-gas shift: kinetic isotope effect observed for decomposition of surface formates for Pt/ceria catalysts,” *Appl. Catal. A*, vol. 252, pp. 107–118, 2003.
- [174] G. Jacobs, P. A. Patterson, U. M. Graham, D. E. Sparks, and B. H. Davis, “Water-gas shift catalysis: kinetic isotope effect identifies surface formates in rate limiting step for Pt/ceria catalysts,” *Appl. Catal. A*, vol. 268, pp. 255–266, 2004.
- [175] G. Jacobs, E. Chenu, P. M. Patterson, L. Williams, D. Sparks, G. Thomas, and B. H. Davis, “Water-gas shift: comparative screening of metal promoters for metal/ceria systems and role of the metal,” *Appl. Catal. A*, vol. 258, pp. 203–214, 2004.
- [176] G. Jacobs, P. M. Patterson, U. Graham, A. C. Crawford, A. Dozier, and B. H. Davis, “Catalytic links among the water-gas shift, water-assisted formic acid decomposition, and methanol steam reforming reactions over Pt-promoted thorium,” *J. Catal.*, vol. 235, pp. 79–91, 2005.
- [177] C. I. Vignatti, M. S. Avila, C. R. Apestegua, and T. F. Garetto, “Study of the water-gas shift reaction over Pt supported on CeO<sub>2</sub>-ZrO<sub>2</sub> mixed oxides,” *Catal. Today*, vol. 171, pp. 297–303, 2011.
- [178] J. Pigos, C. Brooks, G. Jacobs, and B. Davis, “Low temperature water-gas shift: Characterization of Pt-based ZrO<sub>2</sub> catalyst promoted with Na discovered by combinatorial methods,” *Appl. Catal. A*, vol. 319, pp. 47–57, 2007.
- [179] Y. Denkwitz, A. Karpenko, V. Plzak, R. Leppelt, B. Schumacher, and R. Behm, “Influence of CO<sub>2</sub> and H<sub>2</sub> on the low-temperature water-gas shift reaction on

- Au/CeO<sub>2</sub> catalysts in idealized and realistic reformat,” *J. Catal.*, vol. 246, pp. 74–90, 2007.
- [180] D. Tibiletti, A. Goguet, F. C. Meunier, J. P. Breen, and R. Burch, “On the importance of steady-state isotopic techniques for the investigation of the mechanism of the reverse water-gas-shift reaction,” *Chem. Commun.*, pp. 1636–1637, 2004.
- [181] J. A. Rodriguez, J. Graciani, J. Evans, J. B. Park, F. Yang, D. Stacchiola, S. D. Senanayake, S. Ma, M. Pérez, P. Liu, J. Fdez Sanz, and J. Hrbek, “Water-gas shift reaction on a highly active inverse CeO<sub>x</sub>/Cu (111) catalyst: unique role of ceria nanoparticles,” *Angew. Chem., Int. Ed.*, vol. 48, no. 43, pp. 8047–8050, 2009.
- [182] S. D. Senanayake, D. Stacchiola, J. Evans, M. Estrella, L. Barrio, M. Pérez, J. Hrbek, and J. A. Rodriguez, “Probing the reaction intermediates for the watergas shift over inverse CeO<sub>x</sub>/Au (111) catalysts,” *J. Catal.*, vol. 271, pp. 392–400, 2010.
- [183] A. A. Gokhale, J. A. Dumesic, and M. Mavrikakis, “On the mechanism of low-temperature water gas shift reaction on copper,” *J. Am. Chem. Soc.*, vol. 130, pp. 1402–1414, 2008.
- [184] Z. P. Liu, S. J. Jenkins, and D. A. King, “Origin and activity of oxidized gold in water-gas-shift catalysis,” *Phys. Rev. Lett.*, vol. 94, p. 196102, 2005.
- [185] J. A. Rodriguez, P. Liu, J. Hrbek, J. Evans, and M. Perez, “Water gas shift reaction on Cu and Au nanoparticles supported on CeO<sub>2</sub> (111) and ZnO (000 $\bar{1}$ ): Intrinsic activity and importance of support interactions,” *Angew. Chem., Int. Ed.*, vol. 46, pp. 1329–1332, 2007.

- [186] Y. Chen, H. F. Wang, R. Burch, C. Hardacre, and P. Hu, “New insight into mechanisms in water-gas-shift reaction on Au/CeO<sub>2</sub> (111): A density functional theory and kinetic study,” *Faraday Discuss.*, vol. 152, pp. 121–133, 2011.
- [187] L. C. Grabow, A. A. Gokhale, S. T. Evans, J. A. Dumesic, and M. Mavrikakis, “Mechanism of the water gas shift reaction on Pt: first principles, experiments, and microkinetic modeling,” *J. Phys. Chem. C*, vol. 112, pp. 4608–4617, 2008.
- [188] L. Barrio, P. Liu, J. A. Rodriguez, J. M. Campos-Martin, and J. L. G. Fierro, “A density functional theory study of the dissociation of H<sub>2</sub> on gold clusters: Importance of fluxionality and ensemble effects,” *J. Chem. Phys.*, vol. 125, p. 164715, 2006.
- [189] A. Trovarelli, *Catalysis by Ceria and Related Materials*. Imperial College Press, 2002.
- [190] S. D. Senanayake, J. T. Sadowski, J. Evans, S. Kundu, S. Agnoli, F. Yang, D. Stacchiola, J. I. Flege, J. Hrbek, and J. A. Rodriguez, “Nanopatterning in CeO<sub>x</sub>/Cu (111): A new type of surface reconstruction and enhancement of catalytic activity,” *J. Phys. Chem. Lett.*, vol. 3, pp. 839–843, 2012.
- [191] D. C. Grinter, C. M. Yim, C. L. Pang, B. Santos, T. O. Montes, A. Locatelli, and G. Thornton, “Oxidation state imaging of ceria island growth on Re(0001),” *J. Phys. Chem. C*, vol. 117, pp. 16 509–16 514, 2013.
- [192] C. T. Campbell, “Chemistry: Oxygen vacancies and catalysis on ceria surfaces,” *Science*, vol. 309, pp. 713–714, 2005.
- [193] C. W. Sun, H. Li, and L. Q. Chen, “Nanostructured ceria-based materials: synthesis, properties, and applications,” *Energ. Environ. Sci.*, vol. 5, no. 9, pp. 8475–8505, 2012.



- [194] H. X. Mai, L. D. Sun, Y. W. Zhang, R. Si, W. Feng, H. P. Zhang, H. C. Liu, and C. H. Yan, “Shape-selective synthesis and oxygen storage behavior of ceria nanopolyhedra, nanorods, and nanocubes,” *J. Phys. Chem. B*, vol. 109, no. 51, pp. 24 380–24 385, 2005.
- [195] K. Kaneko, K. Inoke, B. Freitag, A. B. Hungria, P. A. Midgley, T. W. Hansen, J. Zhang, S. Ohara, and T. Adschiri, “Structural and morphological characterization of cerium oxide nanocrystals prepared by hydrothermal synthesis,” *Nano Lett.*, vol. 7, pp. 421–425, 2007.
- [196] Tana, M. Zhang, J. Li, H. Li, Y. Li, and W. Shen, “Morphology-dependent redox and catalytic properties of CeO<sub>2</sub> nanostructures: Nanowires, nanorods and nanoparticles,” *Catal. Today*, vol. 148, no. 1-2, pp. 179–183, 2009.
- [197] W. Q. Han, W. Wen, J. C. Hanson, X. Teng, N. Marinkovic, and J. A. Rodriguez, “One-dimensional ceria as catalyst for the low-temperature water-gas shift reaction,” *J. Phys. Chem. C*, vol. 113, pp. 21 949–21 955, 2009.
- [198] I. Florea, C. Feral-Martin, J. Majimel, D. Ihiawakrim, C. Hirlimann, and O. Ersen, “Three-dimensional tomographic analyses of CeO<sub>2</sub> nanoparticles,” *Cryst. Growth Des.*, vol. 13, pp. 1110–1121, 2013.
- [199] X. Zhou, K. and Wang, X. Sun, Q. Peng, and Y. Li, “Enhanced catalytic activity of ceria nanorods from well-defined reactive crystal planes,” *J. Catal.*, vol. 229, pp. 206–212, 2005.
- [200] C. Pan, D. Zhang, L. Shi, and J. Fang, “Template-free synthesis, controlled conversion, and CO oxidation properties of CeO<sub>2</sub> nanorods, nanotubes, nanowires, and nanocubes,” *Eur. J. Inorg. Chem.*, pp. 2429–2436, 2008.
- [201] M. Bohn and J. R. Oppenheimer, “Zur quantentheorie der molekeln,” *Ann. Physik (Berlin)*, vol. 389, pp. 457–484, 1927.

- [202] E. Schrödinger, “An undulatory theory of the mechanics of atoms and molecules,” *Phys. Rev.*, vol. 28, pp. 1049–1070, 1926.
- [203] D. R. Hartree, *The calculation of atomic structures*. John Wiley and Sons, New York, 1957.
- [204] P. Hohenberg and W. Kohn, “Inhomogeneous electron gas,” *Phys. Rev.*, vol. 136, pp. B864–B871, 1964.
- [205] F. Bloch, “ber die quantenmechanik der elektronen in kristallgittern,” *Z. Physik*, vol. 52, pp. 555–600, 1929.
- [206] H. J. Monkhorst and J. D. Pack, “Special points for brillouin-zone integrations,” *Phys. Rev. B*, vol. 13, pp. 5188–5192, 1976.
- [207] J. Moreno and J. M. Soler, “Optimal meshes for integrals in real- and reciprocal-space unit cells,” *Phys. Rev. B*, vol. 45, pp. 13 891–13 898, 1992.
- [208] D. Vanderbilt, “Soft self-consistent pseudopotentials in a generalized eigenvalue formalism,” *Phys. Rev. B*, vol. 41, pp. 7892–7895, 1990.
- [209] J. P. Perdew and A. Zunger, “Self-interaction correction to density-functional approximations for many-electron systems,” *Phys. Rev. B*, vol. 23, no. 10, pp. 5048–5079, 1981.
- [210] J. P. Perdew, K. Burke, and M. Ernzerhof, “Generalized gradient approximation made simple,” *Phys. Rev. Lett.*, vol. 77, pp. 3865–3868, 1996.
- [211] A. van de Walle and G. Cedar, “Correcting overbinding in local-density-approximation calculations,” *Phys. Rev. B*, vol. 59, pp. 14 992–15 001, 1999.
- [212] H. L. Chen, W. T. Peng, J. J. Ho, and H. M. Hsieh, “Density-functional calculation of the adsorption and reaction of CO and H<sub>2</sub>O molecules over a 4Rh/CeO<sub>2</sub> (111) surface,” *Chem. Phys.*, vol. 348, pp. 161–1168, 2008.

- [213] D. M. Ceperley and B. J. Alder, “Ground state of the electron gas by a stochastic method,” *Phys. Rev. Lett.*, vol. 45, no. 7, pp. 566–569, 1980.
- [214] E. Sanville, S. D. Kenny, R. Smith, and G. Henkelman, “Improved grid-based algorithm for bader charge allocation,” *J. Comput. Chem.*, vol. 28, no. 5, pp. 899–908, 2007.
- [215] G. Kresse and J. Furthmüller, “Efficiency of ab-initio total energy calculations for metals and semiconductors using a plane-wave basis set,” *Comput. Mater. Sci.*, vol. 6, no. 1, pp. 15–50, 1996.
- [216] P. E. Blöchl, “Projector augmented-wave method,” *Phys. Rev. B*, vol. 50, pp. 17 953–19 979, 1994.
- [217] L. Wang, T. Maxisch, and G. Ceder, “Oxidation energies of transition metal oxides within the GGA+U framework,” *Phys. Rev. B*, vol. 73, p. 195107, 2006.
- [218] Y. L. Lee, J. Kleis, J. Rossmeisl, and D. Morgan, “Ab initio energetics of  $\text{LaBO}_3$  (001) ( $B = \text{Mn}$ ,  $\text{Fe}$ ,  $\text{Co}$ , and  $\text{Ni}$ ) for solid oxide fuel cell cathodes,” *Phys. Rev. B*, vol. 80, p. 224101, 2009.
- [219] O. Kubaschewski, C. Alcock, and P. Spencer, *Materials Thermochemistry, 6th ed.* Pergamom Press, Oxford, 1993.
- [220] M. W. Chase, Jr., *NIST-JANAF Thermochemical Tables, Fourth Edition.* American Chemical Society and the American Institute of Physics for the National Institute of Standards and Technology, 1998.
- [221] L. F. Huang, M. Y. Ni, X. H. Zheng, W. H. Zhou, L. Y. G., and Z. Zeng, “Ab initio simulations of the kinetic properties of the hydrogen monomer on graphene,” *J. Phys. Chem. C*, vol. 114, pp. 22636–22643, 2010.

- [222] G. Preda, A. Migani, K. M. Neyman, S. T. Bromley, F. Illas, and G. Pacchioni, “Formation of superoxide anions on ceria nanoparticles by interaction of molecular oxygen with  $\text{Ce}^{3+}$  sites,” *J. Phys. Chem. C*, vol. 115, pp. 5817–5822, 2011.
- [223] V. V. Pushkarev, V. I. Kovalchuk, and J. L. d’Itri, “Probing defect sites on the  $\text{CeO}_2$  surface with dioxygen,” *J. Phys. Chem. B*, vol. 108, pp. 5341–5348, 2004.
- [224] Z. C. Orel and B. Orel, “Optical properties of pure  $\text{CeO}_2$  and mixed  $\text{CeO}_2/\text{SnO}_2$  thin film coatings,” *Phys. Stat. Sol. B*, vol. 186, pp. K33–K36, 1994.
- [225] A. V. Prokofiev, A. I. Shelykh, and B. T. Melekh, “Periodicity in the band gap variation of  $\text{Ln}_2\text{X}_3$  ( $\text{X} = \text{O}, \text{S}, \text{Se}$ ) in the lanthanide series,” *J. Alloys Compd.*, vol. 242, pp. 41–44, 1996.
- [226] P. Dutta, S. Pal, M. S. Seehra, Y. Shi, E. M. Eyring, and R. D. Ernst, “Concentration of  $\text{Ce}^{3+}$  and oxygen vacancies in cerium oxide nanoparticles,” *Chem. Mater.*, vol. 18, no. 21, pp. 5144–5146, 2006.
- [227] Q. Sun, K. Reuter, and M. Scheffler, “Effect of a humid environment on the surface structure of  $\text{RuO}_2$  (110),” *Phys. Rev. B*, vol. 67, p. 205424, 2003.
- [228] A. V. Bandura, J. O. Sofo, and J. D. Kubicki, “Derivation of force field parameters for  $\text{SnO}_2\text{-H}_2\text{O}$  surface systems from plane-wave density functional theory calculations,” *J. Phys. Chem. B*, vol. 110, pp. 8386–8397, 2006.
- [229] C. Chizallet, G. Costentin, M. Che, F. Delbecq, and P. Sautet, “Infrared characterization of hydroxyl groups on mgo:a periodic and cluster density functional theory study,” *J. Am. Chem. Soc.*, vol. 129, pp. 6442–6452, 2007.
- [230] F. Zasada, W. Piskorz, S. Cristol, J. F. Paul, A. Kotarba, and Z. Sojka, “Periodic density functional theory and atomistic thermodynamic studies of cobalt spinel nanocrystals in wet environment: Molecular interpretation of water adsorption equilibria,” *J. Phys. Chem. C*, vol. 114, pp. 22 245–22 253, 2010.

- [231] S. Babu, R. Thanneeru, T. Inerbaev, R. Day, A. E. Masunov, A. Schulte, and S. Seal, “Dopant-mediated oxygen vacancy tuning in ceria nanoparticles,” *Nanotechnology*, vol. 20, p. 085713, 2009.
- [232] J. F. Li, G. Z. Lu, H. F. Li, Y. Q. Wang, Y. Guo, and Y. L. Guo, “Facile synthesis of 3D flowerlike CeO<sub>2</sub> microspheres under mild condition with high catalytic performance for CO oxidation,” *J. Colloid. Interf. Sci.*, vol. 360, pp. 93–99, 2011.
- [233] A. A. Athawale, M. S. Bapata, and P. A. Desai, “Hydroxide directed routes to synthesize nanosized cubic ceria (CeO<sub>2</sub>),” *J. Alloy Compd.*, vol. 484, pp. 211–217, 2009.
- [234] X. D. Li, J. G. Li, D. Huo, Z. M. Xiu, and X. D. Sun, “Facile synthesis under near-atmospheric conditions and physicochemical properties of hairy CeO<sub>2</sub> nanocrystallines,” *J. Phys. Chem. C*, vol. 113, pp. 1806–1811, 2009.

## Vita

### Education

2009.8–2014.2 Chemical and Materials Engineering University of Kentucky

PhD (2014) Materials Science and Engineering

Dissertation: Structure and catalytic properties of ultra-small  
ceria nanoparticles

Advisor: Dr. Matthew J. Beck

Committee members: Dr. Eric A. Grulke, Dr. Bruce J. Hinds, Dr. Yang-Tse  
Cheng, Dr. Gang Cao, Dr. Kaveh A. Tagavi

2006.9–2009.6 Materials Science and Engineering Wuhan University of Technology

Master of Engineering Materials Science

Thesis: Study on the synthesis of complicated hematite nanostructures

2002.9–2006.6 Materials Science and Engineering Wuhan University of Technology

Bachelor of Engineering (2006) Materials Science and Engineering

Thesis: Synthesis and performance of TiO<sub>2</sub>-PTFE compounded hydrophobic  
thin films

### Presentations

1. **Structure of ultra-small ceria nanoparticles from first-principles**

*MRS Spring Meeting, San Francisco, CA, 2011.*

2. **Ultra-small ceria nanoparticles stabilized by absorbed molecular oxygen**

*Center for Advanced Materials, Lexington, KY, 2011.*

3. **Novel catalytic behavior of ultra-small ceria nanoparticles for water splitting through DFT investigation**

*MS&T Conference and Exhibition, Columbus, OH, 2011.*

4. **Catalytic mechanism of ultra-small ceria nanoparticles for water splitting through DFT Investigation**

*MRS Spring Meeting, San Francisco, CA, 2012.*

**Publications**

1. Tong, G. X.; Guan, J. G.; Xiao, Z. D; Huang, X; and Guan, Y. In situ generated gas bubble-assisted modulation of the morphologies, photocatalytic, and magnetic properties of ferric oxide nanostructures synthesized by thermal decomposition of iron nitrate. *Journal of Nanoparticle Research*, 2010, 12, 3025–3037.
2. Huang, X.; Guan, J. G.; Xiao, Z. D; Tong, G. X; Mou, F. Z; and Fan, X. A. Flower-like porous hematite nanoarchitectures achieved by complexation-mediated oxidation-hydrolysis reaction. *Journal of Colloid Interface and Science*, 2011, 357, 36-45.
3. Huang, X.; Wang, B. H; Beck, M. J; and Grulke, E. A. Toward tuning the surface functionalization of small ceria nanoparticles. *Journal of Chemical Physics*, 2014, 140, 074703.
4. Huang, X.; and Beck, M. J. Surface termination of catalytically-active ceria nanoparticle. *Physical Review Applied* (submitted).
5. Huang, X.; and Beck, M. J. Oxidation state of small OH-terminated ceria nanoparticles from IR spectra. *Applied Physics Letters* (submitted).
6. Huang, X.; and Beck, M. J. Spontaneous oxidizing CO to CO<sub>2</sub> by ultra-small ceria nanoparticles. (in preparation)
7. Huang, X.; and Beck, M. J. Catalytic mechanism of photocatalytic water splitting over ultra-small ceria nanoparticles. (in preparation)
8. Huang, X.; and Beck, M. J. Catalytic mechanism of water-gas shift reaction over ultra-small ceria nanoparticles. (in preparation)

**Honors and Awards**

2012 *Best Materials Science & Engineering Poster Award*

- University of Kentucky Department of Chemical and Materials Engineering
- 2012 *Center for Advanced Materials Graduate Fellowship*  
University of Kentucky Center for Advanced Materials
- 2011 *Graduate Excellence in Materials Science*  
The American Ceramic Society
- 2011 *Kentucky Opportunity Fellowship*  
University of Kentucky Graduate School
- 2006-2009 *National Scholarship for Graduate Student*  
Hubei Provincial Department of Education
- 2007 *Scholarship for Excellent Graduate Student*  
Wuhan University of Technology
- 2007 *Excellent Graduate Student Leader*  
Wuhan University of Technology
- 2007 *Hubei Province Excellent Bachelor's Degree Thesis*  
Hubei Provincial Department of Education
- 2006 *Excellent Graduate of Wuhan University of Technology*  
Wuhan University of Technology
- 2003-2005 *Scholarship for Excellent Undergraduates*  
Wuhan University of Technology